Targeting CXCR4 with immuno-modified iron oxide nanoparticles for cancer treatment with magnetically-induced hyperthermia

An *in vitro* approach

Vânia Filipa Esteves Vilas Boas

Tese do 3º Ciclo de Estudos Conducente ao grau de Doutoramento em Ciências Farmacêuticas, na especialidade de Toxicologia

PhD thesis of the 3rd Cycle of Studies in Pharmaceutical Sciences on the Specialty of Toxicology

Trabalho realizado sob a orientação de
Elaborated under supervision of

Professor Doutor Félix Dias Carvalho

Doutora Begoña Espiña

Doutora Verónica Romão

Janeiro 2017

Recomeça…
Se puderes,
Sem angústia e sem pressa.
E os passos que deres,
Nesse caminho duro
Do futuro,
Dá-os em liberdade.
Enquanto não alcances
Não descanses.
De nenhum fruto queiras só metade.
E, nunca saciado,
Vai colhendo
Ilusões sucessivas no pomar
E vendo
Acordado,
O logro da aventura.
És homem, não te esqueças!
Só é tua a loucura
Onde, com lucidez, te reconheças.

Miguel Torga, Diário XIII

Aos meus pais

Acknowledgments/ Agradecimentos

Gostaria de agradecer a algumas pessoas cuja contribuição para o desenvolvimento deste trabalho foi essencial, tanto a nível científico, como a nível pessoal.

Primeiramente, quero agradecer ao meu Orientador, Professor Félix Carvalho, por ter tido a ousadia de percorrer este caminho comigo. Em particular, quero agradecer o seu entusiasmo nas nossas discussões científicas, que me deixavam sempre mais otimista em relação ao meu trabalho. A sua atitude positiva e a sua serenidade são contagiantes. Muito obrigada por toda a orientação e por ter me ter indicado sempre o caminho certo para navegar..

To my co-supervisor, Dr. Begoña Espiña, I thank all the dedication to this work, all the good advises and all the brilliant ideas. You really are that person that fully understands what I say, even when I speak just half of the words, which demonstrates how much this work is also yours. I should apologize to Suzo and Leo for all the days you went home late because of me…

Agradeço à minha co-orientadora, Doutora Verónica Romão, por me ter recebido tão bem e com tanta atenção no INL e por me ter introduzido ao campo das nanopartículas e da sua funcionalização. Mesmo estando longe, os teus conselhos foram sempre pertinentes e sábios. Obrigada por sempre me tratares como igual e, principalmente, por seres minha amiga.

Não posso deixar de agradecer ao Professor Paulo Freitas por me ter aceitado no INL e me dar todas as condições para desenvolver este trabalho. Agradeço também as discussões científicas muito produtivas e o seu genuíno interesse neste trabalho.

Agradeço à Professora Lurdes por me deixar ser parte do seu laboratório desde há vários anos, e por sempre me receber tão bem de cada vez que regresso ao laboratório de Toxicologia. A sua constante alegria e a forma como lidera o laboratório são admiráveis.

Ao Professor Fernando Remião agradeço o facto de me ter cativado para o trabalho científico ao me aceitar como aluna de Mestrado. Foi consigo que tudo isto começou…

À Sra. Engenheira pelo seu exemplo de dinamismo, alegria e senso de organização que nos marca a todos. Obrigada por todo o carinho.

Ao Professor José Alberto Duarte agradeço a imediata disponibilidade para a participação neste trabalho e para a revisão dos manuscritos. Obrigada também à Dona Celeste pela disponibilidade para a receção e preparação das amostras.

Agradeço do fundo do coração às minhas queridas “Biogirls”, Lili e Raquel, pelo companheirismo, pelo apoio constante, pelas conversas, pelas sugestões... Ao Nelson agradeço o incentivo constante, os lanches e pausas no trabalho contínuo, que ajudam à manutenção da sanidade mental... Agradeço também à Martinha e à Diana pela ajuda e pelo carinho.

I thank Yury for all the help with the nanoparticles and your constant good mood in the lab; nobody’s sad around you! ☺ I thank Manolo for the introduction to magnetic hyperthermia and the days we stayed working late.

To Dmitri I thank all the prompt help and long discussions… I learned a lot! My work and scientific view are certainly enriched by our conversations.

I thank **everybody** at INL, the place where I spent these last four years, for the opportunity of working in such an enriching environment, with top researchers and state of the art equipment. In particular, I would like to thank:

- my “open space” colleagues: Elisabete, Marisa, Chícharo, Carla e Alejandro, for always being available to help and for the good environment that dominates our work place;
- Hongyan, who I thank for the friendship and consideration. I deeply admire you for having the courage of embracing these last months of the INL challenge with your family. I wish we could meet again in the future!
- Maitê, Vasi, and Jana, for giving me the opportunity to collaborate with them, allowing me to apply my knowledge and improve my skills;
- Adelino, Zé Gonçalves, Hugo, and Cassiano for always being available to help and enjoy some (lunch) moments just having fun;
- Adelaide Pinheiro, for all the care and attention you have dedicated to me since my beginning at INL;
- Marta Prado, Pablo, Pieter, Leonard, Cláudia Sousa, Elvira, Silvina, Noélia, Diogo, Tareq and João Piteira, for the companionship, help and words of encouragement;
- to Jerome for the explanations on magnetism and for your example of dedication to work. I believe you have no notion of how fascinating a human being you are.

Aos meus colegas e amigos da FFUP, Ana, Teresa, Juliana e Luciana agradeço a vossa amizade e incentivo, os almocinhos, as conversas, as saudades... Peço à vida que nos volte a juntar em breve! À Márcia e à Maria João, estou muito grata pelo carinho e por estarem sempre disponíveis para me ajudar, tanto na ciência como na burocracia ☺. À Cátia e à Margarida, agradeço a disponibilidade para ajudar sempre que precisei.

Agradeço à Doutora Emília e à Sara Cravo pela ajuda nas análises de FTIR. Espero um dia poder compensar a vossa disponibilidade imediata em ajudar-me. Obrigada!

Às “miúdas da FFUP”, Rita Ribeiro, Rita Ferreira, Sarocas, Ana, Ju e Fátima, agradeço a amizade, os momentos bem passados, os lanchinhos de Domingo (aos quais falto muitas vezes), as vossas famílias lindas... À Anabela quero agradecer a cumplicidade e a amizade, desde os tempos da República Checa! Obrigada a todas por se lembrarem sempre de mim e desculpem as ausências, que espero poder compensar...

Aos meus amigos de longa data: Carlos, Nuno, Paulo Sousa, Paulo Campos, Raúl e Marlene, e Clarinha. Passamos tanto tempo juntos!.. Obrigada por todas as chatices e gargalhadas, pelos momentos hilariantes que recordaremos para sempre!...

Ao meu amigo Filipe agradeço todo o carinho com que sempre me tratou. As tuas palavras doces aquecem-me sempre o coração! Fico sempre mais feliz depois de falar contigo!

À minha família próxima agradeço a presença, a ajuda e o incentivo. Felizmente, as batalhas que temos enfrentado têm-nos tornado mais fortes e unidos. Acrescento aqui um agradecimento à Romy, amiga de tão longa data que considero parte da família, por tudo o que sempre fez por mim. Tens estado sempre presente nos momentos importantes da nossa vida. Espero que assim continue a ser! Deixo um agradecimento especial ao meu avô e às minhas avós, que tanto fizeram para hoje sermos quem somos. Deles herdei o “feitiozinho” que muitos em mim reconhecem...

À professora Conceição Rego, minha professora primária, agradeço o incentivo que sempre me deu em prosseguir uma vida na ciência. “Tu sempre disseste que querias ser cientista!” ☺ A sua atenção e dedicação ao ensino básico são um exemplo que deve ser seguido!

Ao Diogo, por todo o carinho e apoio incansável, pela tua crença ilimitada em mim e nas minhas capacidades. A vida separou-nos mas o coração mantém-nos unidos.

À Sofia, agradeço a amizade pura e sem cobranças. A certeza desta amizade e do teu apoio incondicional traz-me serenidade e força. A tua capacidade de trabalho e

dedicação são admiráveis! Só espero que a vida te consiga trazer tudo o que tu mereces, pessoal e profissionalmente. Estarás para sempre no meu coração.

A ti Renata agradeço a amizade forte e toda a ajuda que sempre me prestaste. Em tudo: no laboratório, nas conversas que ajudam a descomprimir e a clarificar ideias, na infindável formatação desta tese, enfim!.. Foi contigo que me iniciei no trabalho de laboratório, e a visão do trabalho que aprendi de ti mantém-se hoje e há de manter-se para sempre! Muito obrigada por tudo, Re! De coração!... Depois apareceu o Danielinho, aquele ser que trabalha das 7 às 19h e que tem SDs que parecem SEMs!!! E aí se completou o triângulo... Que saudades de partilhar convosco o laboratório! Como eram divertidos esses tempos!.. Quem sabe um dia?! Obrigada, Danielinho pelas tuas palavras constantes de incentivo, pelos telefonemas, por te lembrares sempre de mim. A forma serena como encaras a tua vida é admirável! Vocês são a minha inspiração sempre que estou no laboratório!

A ti, Marinazinha, agradeço a amizade sincera, que foi crescendo na confiança e na alegria que nos caracteriza. És a pessoa mais altruísta que conheço e, talvez por isso, aceitaste a que fizesse parte do teu grupo de amigos. É um privilégio ser parte desse grupo, já que tu cuidas e alimentas as amizades como se fossem flores (na verdade, muito melhor do que tratas as flores! :P). Como te admiro!!.. Estiveste sempre lá para mim, nos bons e maus momentos, e isso não tem preço. Mereces tudo de bom na vida. Que ela te saiba compensar por tudo de bom que fazes pelos outros.

To Tim, I thank for all the care, patience and incitement. Simultaneously, I thank you for all the scientific discussions, which made my thoughts so much clearer. I am deeply fascinated by your intelligence and the enthusiastic way you embrace each conversation. I must apologize for being late so many times…

Aos meus pais agradeço o apoio incansável, a confiança cega nas minhas decisões, a ajuda sempre pronta, a paciência infinita... Tudo teria sido ainda mais difícil sem vocês por perto. Desculpem as ausências e os silêncios. Agradeço também aos meus irmãos, Necas e Ni, por confiarem em mim e por acreditarem que é possível manter a família unida. Ao Necas e à Sandrinha agradeço a bênção que é a Carlota. O génio que herdou do pai e a feminilidade da mãe fazem dela o pequeno ser humano mais adorável do mundo!

À Cati, um exemplo de força e coragem, agradeço o amor, o carinho e as palavras de incentivo. O presente maior chegou há pouco, com toda a vivacidade e alegria de

alguém que é uma parte de ti... Obrigada a ti e ao Mika por este presente maravilhoso que é a princesa Francisca.

Há um sem número de outras pessoas que também contribuíram para o desenvolvimento deste trabalho, tanto a nível profissional como pessoal. Na impossibilidade de agradecer a cada uma individualmente, deixo um agradecimento geral, mas de coração, a todas estas pessoas cujo nome não mencionei anteriormente.

Agradeço à FCT pela Bolsa de Doutoramento que me possibilitou a realização deste trabalho [SFRH/BD/82556/2011].

Publications

Manuscripts in international peer-review journals

V. Vilas-Boas, N. Guldris, E. Carbó-Argibay, D. G. Stroppa, M. F. Cerqueira, B. Espiña, J. Rivas, C. Rodríguez-Abreu and Y. V. Kolen'ko (2015). Straightforward phase-transfer route to colloidal iron oxide nanoparticles for protein immobilization. *RSC Advances*, 2015, 5, 47954-47958.

Manuscripts submitted to international peer-review journals

V. Vilas-Boas, B. Espiña, Y. V. Kolen'ko, M. Bañobre-Lopez, J. A. Duarte, V. Martins, D. Y. Petrovykh, P. Freitas and F. Carvalho. Combining the iron loading of CXCR4-targeted and non-targeted nanoparticles to efficiently kill Jurkat cells via unassisted magnetically-induced hyperthermia

Unsubmitted manuscripts

V. Vilas-Boas, B. Espiña, V. Martins, Y. V. Kolen'ko, M. Bañobre-Lopez, P. Freitas and F. Carvalho. Optimizing magnetic nanoparticle's functionalization with biomolecules for targeted magnetically-induced hyperthermia in cancer cells.

V. Vilas-Boas, B. Espiña, Y. V. Kolen'ko, M. Bañobre-Lopez, M. Brito, V. Martins, J. A. Duarte, D. Petrovykh, P. Freitas and F. Carvalho. A mono-therapeutic magnetic hyperthermia treatment to kill glioblastoma cells based on CXCR4 targeting.

Awards

Best poster awarded by the European Society of Toxicology *In Vitro* (ESTIV) to the poster presented at EUROTOX 2016, in Seville: V. Vilas-Boas, B. Espiña, Y. V. Kolen'ko, M. Bañobre Lopez, V. Martins, P. Freitas and F. Carvalho (2016) Targeting chemokine receptor CXCR4 with magnetic particles to eliminate leukaemia cells with magnetic hyperthermia. The 52nd Congress of the European Societies of Toxicology (EUROTOX), Seville, Spain, 4–7 September.

ABSTRACT

Abstract

Magnetic hyperthermia (MHT) therapy is a cancer treatment that takes advantage of the ability of magnetic nanoparticles (MNPs) to produce heat when exposed to an alternating magnetic field (AMF). The use of targeted (functionalized) MNPs for MHT has been explored, but generally with limited efficiency. In many cases, a combination with chemotherapeutic agents was suggested to improve MHT outcome (and vice-versa). The use of MHT to treat glioblastoma multiforme (GBM, a very aggressive type of brain tumour) has been approved by the European Medicines Agency. Yet, the improvement on the overall survival of GBM patients, although significant, is insufficient, and death is still the most probable outcome within less than 2 years after diagnosis. The overexpression of the chemokine receptor, CXCR4, in a range of cancer cells, namely, GBM and leukaemia, among others, has been related to tumour development, growth and metastasis, making CXCR4 an appealing target for cancer diagnosis and treatment. Particularly, CXCR4-targeted MNPs have been tested for cancer diagnosis, but still have not been tested for cancer treatment. With this in mind, it was our purpose to functionalize MNPs with anti-CXCR4 antibodies (targeted particles) to produce highly efficient cytotoxic MHT in cancer cells, while minimizing the toxicity in normal cells.

We optimized the conditions for the functionalization of the MNPs with anti-CXCR4 by testing direct covalent binding of antibodies to poly(acrylic acid)-coated MNPs, or by affinity binding of antibodies to proteins (streptavidin (STR) or protein A (PA)) covalently immobilized on the MNPs surface (STR– or PA–MNPs). Our results demonstrated successful covalent binding of proteins to the MNPs, a process that depended on the concentration of coupling agents and protein. STR and PA on the MNPs allowed the affinity immobilization of antibodies, showing the linker protein functionality was not compromised during conjugation. However, PA–MNPs maintained higher stability, probably due to the oriented binding of the antibody. Thus, PA–MNPs further functionalized with anti-CXCR4 antibodies were selected to set-up the conditions for MHT treatments. These MNPs proved to be insufficient for obtaining efficient temperature rise in MHT studies, so bigger particles (MPs) with the same linker protein were selected for the targeted MHT experiments.

The studies on Jurkat cells showed that a purely CXCR4-targeted approach underperformed in the MHT studies, resulting in limited toxicity in cancer cells. The efficiency of this approach was then improved by providing cells with a boost of magnetic material of a non-targeted origin (SPIONs). The cells internalized a sufficient amount of SPIONs to increase the magnetic material, boosting the heating during an optimized AMF

application of 1 h. This way, remarkable decreases in cell viability were observed, following two distinct death pathways depending on the temperature conditions during the MHT treatment. When a necrotic pathway was followed, a long-lasting, null cell viability was maintained, while for the apoptotic samples a slight recovery was observed, supporting a more efficient outcome for the necrotic route. This strategy was subsequently applied to a GBM *in vitro* model, adjusting the magnetic content with SPIONs due to lower surface expression of CXCR4. Again, the MHT treatment established herein resulted in long-lasting, null cell viability, and only features of a necrotic signature were observed. Furthermore, the developed strategy proved safe for normal cells, as demonstrated by control experiments on normal cells from human kidney, HK-2 cell line.

Overall, the combination of targeted and non-targeted nanoparticles for MHT resulted in remarkable toxicity in cancer cells, while keeping normal cells nearly undamaged. This strategy is a rare example of efficient MHT in a mono-therapeutic context, proving interesting and promising for future *in vivo* studies.

Keywords: magnetic hyperthermia, CXCR4, cancer treatment, targeted-nanoparticles

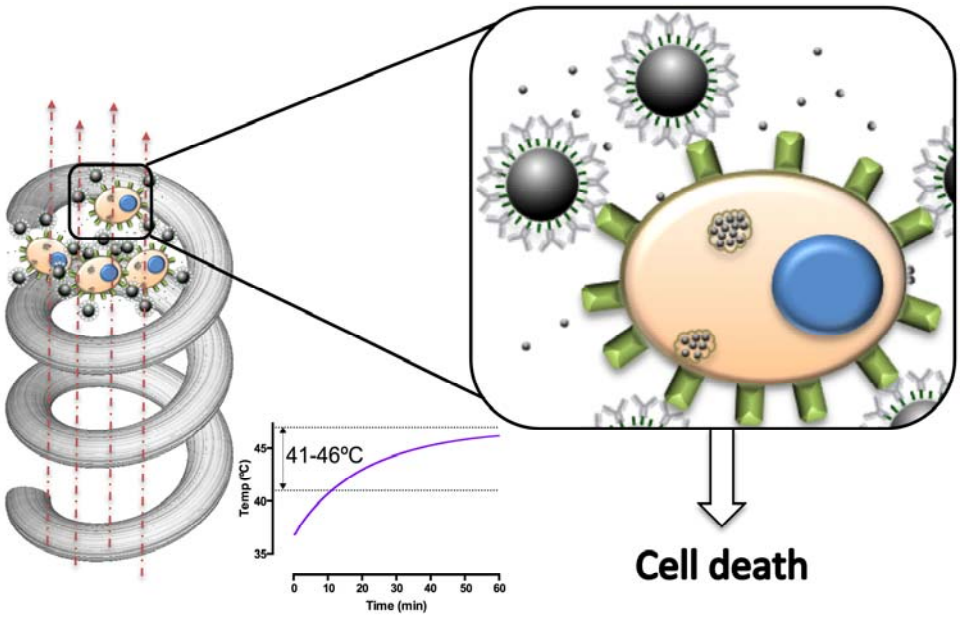

RESUMO

Resumo

A hipertermia magnética (MHT) é um tratamento anticancerígeno que explora a produção de calor por nanopartículas magnéticas (MNPs) expostas a um campo magnético alternado (AMF). A utilização de MNPs direcionadas (funcionalizadas) em MHT tem sido estudada, mas geralmente tem eficácia limitada. Em muitos casos, a combinação com agentes quimioterapêuticos foi sugerida como forma de melhorar o efeito da MHT (e vice-versa). O uso de MHT para o tratamento do glioblastoma multiforme (GBM, um tipo de tumor do cérebro muito agressivo) foi aprovado pela Agência Europeia do Medicamento. Ainda assim, a melhoria da sobrevida dos pacientes com GBM não é suficiente, e a morte, em menos de 2 anos após o diagnóstico, ainda é o desfecho mais provável. A sobre-expressão do recetor de quimiocinas, CXCR4, em vários tipos de tumores, nomeadamente GBM e leucemia, entre outros, foi associada a desenvolvimento e crescimento tumoral e, ainda, a metastização, fazendo do CXCR4 um alvo apelativo para o diagnóstico e tratamento do cancro. Em particular, MNPs direcionadas para o CXCR4 foram testadas em diagnóstico do cancro, mas não para o tratamento de tumores. Sendo assim, foi nosso objetivo funcionalizar MNPs com anticorpos anti-CXCR4 (partículas direcionadas) para produzir MHT citotóxica, de elevada eficácia em células tumorais, com toxicidade mínima em células normais.

As condições de funcionalização das MNPs com anticorpos anti-CXCR4 foram otimizadas testando a ligação covalente de anticorpos a MNPs revestidas com ácido poliacrílico, ou por química de afinidade entre os anticorpos e as proteínas (streptavidina (STR) ou Proteína A (PA)) imobilizadas covalentemente à superfície das MNPs. Os resultados demonstraram que a ligação covalente de proteínas às MNPs foi bem sucedida, num processo dependente das concentrações de reagentes de acoplamento e de proteína. A STR e a PA das MNPs permitiram a imobilização de anticorpos por afinidade, demonstrando que a funcionalidade da proteína de ligação não foi comprometida durante o processo de imobilização. No entanto, as PA–MNPs mantiveram maior estabilidade, provavelmente devido à ligação orientada do anticorpo à PA. Portanto, as PA–MNPs funcionalizadas com anticorpos anti-CXCR4 foram selecionadas para estabelecer as condições para os estudos de MHT. Estas MNPs não conduziram a um aquecimento suficiente nesses estudos pelo que, consequentemente, selecionamos MNPs maiores com a mesma proteína de ligação para os estudos subsequentes de MHT direcionada.

Os estudos em células Jurkat demonstraram que uma estratégia puramente direcionada para o CXCR4 não funcionou nos testes de MHT, resultando em toxicidade

limitada em células cancerígenas. A eficácia desta estratégia foi, portanto, incrementada utilizando um impulso de material magnético de origem não-direcionada (SPIONs). As células internalizaram quantidade suficiente de SPIONs para aumentar o seu material magnético, impulsionando o aquecimento durante uma aplicação do AMF optimizador, durante 1 h. Como consequência, foram observados decréscimos notáveis na viabilidade celular, seguindo duas vias de morte celular distintas, de acordo com as condições de temperatura atingidas durante o tratamento de MHT. Enquanto a morte celular por necrose conduziu a uma viabilidade celular nula e prolongada, para as amostras apoptóticas, foi observada uma pequena recuperação, o que sugere maior eficácia para a morte por necrose. Esta estratégia foi subsequentemente aplicada a um modelo *in vitro* de GBM, ajustando o conteúdo magnético com SPIONs devido à menor expressão de CXCR4 neste modelo. Da mesma forma, o tratamento de MHT desenvolvido neste trabalho, resultou em viabilidade celular nula e prolongada, observando-se apenas características de necrose. Adicionalmente, a estratégia desenvolvida provou ser segura para células normais, como se demonstra com os testes em células normais de rim humano, HK-2.

No geral, a combinação de MNPs direcionadas e não-direcionadas para MHT resultou numa toxicidade extraordinária em células cancerígenas, mantendo as células normais praticamente sem danos. Esta estratégia constitui um raro exemplo de MHT eficaz num contexto de mono-terapia, interessante e promissora para futuros estudos *in vivo*.

Palavras-chave: hipertermia magnética, CXCR4, tratamento do cancro, nanopartículas direcionadas

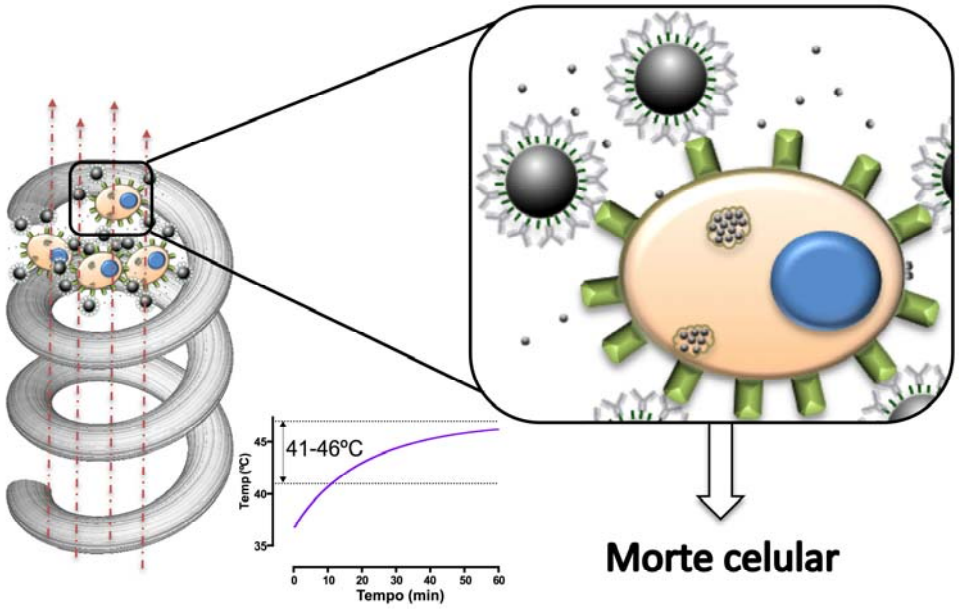

TABLE OF CONTENTS

Table of Contents

INDEX OF FIGURES

Index of Figures

INDEX OF TABLES

Index of Tables

LIST OF ABBREVIATIONS

List of Abbreviations

ALL – Acute lymphoblastic leukaemia

AMF – Alternating magnetic field

AML – Acute myeloid leukaemia

CLL – Chronic lymphocytic leukaemia

CML – Chronic myeloid leukaemia

CNS – Central nervous system

CXCR4 – C-X-C chemokine receptor type 4

D-Gal – D-galactosamine

DNA – Deoxyribonucleic acid

EDC – 1-ethyl-3-(-3-dimethylaminopropyl) carbodiimide hydrochloride

EGFR – Epidermal growth factor receptor

EMA – European Medicines Agency

EPR – Enhanced permeability retention

FDA – Food and Drug Administration

GBM – Glioblastoma multiforme

HSCT – Hematopoietic stem cell transplantation

HSP – Heat shock protein

IONP – Iron oxide nanoparticles

IT – Intratumoural

IV – Intravenous

LDH – Lactate dehydrogenase

LHRH – Luteinizing Hormone–Releasing Hormone

MHT – Magnetic hyperthermia

MNC – Magnetic nanocluster

MNP – Magnetic nanoparticle

MP – Magnetic particle

MRI – Magnetic resonance imaging

PA – Protein A from Staphylococcus aureus

PAA – Poly(acrylic acid)

pAb – Polyclonal antibody

PDT – Photodynamic therapy

PTT – Photothermal therapy

PEG – Poly(ethylene glycol)

RES – Reticuloendothelial system

RT –Room temperature

SAR – Specific absorption rate

SDF-1 – Stromal cell-derived factor-1

SPION – Superparamagnetic iron oxide nanoparticles

STR – Streptavidin

T – Temperature

TMZ – Temozolomide

Outline of the Thesis

This thesis is divided in four chapters:

Chapter I – General Introduction and Main Objectives the Thesis

In this chapter, general concepts that are important for the understanding of the work in magnetic hyperthermia are explained. Some cancer facts are provided and the *in vitro* models selected for the experimental part are described. A number of *in vitro*, *in vivo*, and clinical studies are discussed to provide an insight on the current knowledge and the main needs on this topic.

The main objectives of the thesis are described at the end of this section.

Chapter II – Experimental Section, Results and Partial Discussions

The manuscripts produced under the scope of this dissertation, either submitted or not, are presented in this chapter.

Chapter III – Integrated Discussion and Conclusions

This chapter provides an integrative discussion of the main results obtained, and their relevance within the framework of magnetic hyperthermia for cancer treatment.

The final part of this chapter includes the main conclusions that may be drawn from the studies included in this dissertation.

Chapter IV – References

The literature cited in chapters I and III is listed in this chapter.

CHAPTER I

General Introduction and Main Objectives

General Introduction

Plenty of the currently on-going scientific research in the field of medicine is devoted to cancer, namely its prevention, detection and treatment. Notwithstanding the small progress observed in the past decade, cancer has escalated to one of the leading causes of death worldwide, being one of the most important and dreadful contemporary problems of mankind. Cancer treatments are sometimes very difficult to endure due to the elevated incidence of important and debilitating secondary effects. Therefore, further efforts are needed to fight this complex disease in a more efficient and less toxic way. Innovative treatments have been recently proposed to treat cancer, among them magnetically-induced hyperthermia, which employs the heating ability of magnetic nanoparticles under the influence of an alternating magnetic field to kill cancer cells. The use of targeted strategies, i.e., therapies directed to cancer cells, offers the opportunity of minimizing the side effects, which are common in conventional cancer therapies. In summary, directing magnetic nanoparticles to accumulate in tumours so that cancer cells can be “cooked” to death sounds promising and appealing. As a researcher, it is particularly gratifying to have the possibility of contributing, even slightly, to improve the current armoury to fight this devastating condition.

In this section, the thematic of this work is introduced and the latest developments are described to better understand the motivation and the purpose of the work herein presented.

1. Cancer at a glance

Cancer is a generic term referring to a group of diseases that can affect any part of our body, characterized by rapid and uncontrolled cell growth. Although the precise origin of cancer is yet to unveil, it generally arises from a single cell that suffers DNA damage (mutation), escapes the repair mechanisms and becomes abnormal, rapidly multiplying as abnormal cells. This transformation is dependent both on genetic and environmental causes (exposure to chemical, physical and biological carcinogens). Ageing is also a risk factor for developing cancer. Some types of cancer have a tendency to spread to other locations, a process called metastization. The presence of metastases is normally associated with worse prognosis.

1.1. Cancer statistics

The most recent worldwide data collection on cancer refers to the year 2012, and was performed by the International Agency for Cancer Research, the cancer agency of the World Health Organization, under the GLOBOCAN project (Ferlay et al. 2015). This project aimed at granting a contemporary estimation of cancer incidence, mortality and prevalence for 184 countries worldwide. Overall, in 2012 only, an estimated 14.1 million new cancer cases were diagnosed, and 8.2 million people died with cancer (Ferlay et al. 2015). In the United States (US), cancer is the second leading cause of death, right after heart disease, eventually ranking first if considering the age group between 40 and 80 years old (Siegel et al. 2015). Annual cases of cancer are expected to rise to over 22 million by 2030 (Bray et al. 2012). These data suggest that advances in prevention, (early) diagnosis, and treatment of cancer are urgently needed to avoid such statistics to be maintained or even aggravated.

According to GLOBOCAN estimations, lung cancer was the most frequent and deadly type of cancer worldwide (Ferlay et al. 2015) —if considering women only, or, interestingly, Europe only (Ferlay et al. 2013), breast cancer was the most common one. Notably, when considering the individual age groups, higher death rates are found for leukaemia and brain tumours, in particular in US patients aged below 20 (Siegel et al. 2015). In this introductory section, leukaemia and glioblastoma multiforme (GBM, the most common and most aggressive brain cancer) will be especially addressed, as we believe that magnetically-induced hyperthermia may become an important asset to treat these types of cancer.

1.2. Leukaemia

Leukaemia is a group of cancers of the hematopoietic and lymphoid tissues that generally begins at the bone marrow, resulting in increased numbers of white blood cells. Considering the cell type of origin, there are lymphoid and myeloid types of leukaemia. While lymphoid leukaemia affects cells committed to lymphoid lineages (namely T-lymphocytes, B-lymphocytes, and natural killer cells), the myeloid type affects cells committed to myeloid lineages (namely megakaryocytes and erythrocytes, as well as granulocytes and macrophages). Depending on the speed of the onset of the disease, acute and chronic subtypes are described. Therefore, the majority of the leukaemia cases are categorized as Acute Lymphoblastic Leukaemia (ALL), Acute Myeloid Leukaemia (AML), Chronic Lymphocytic Leukaemia (CLL) and Chronic Myeloid Leukaemia (CML). An overview of the haematopoiesis and the set points of each of these types of leukaemia are provided in Figure 1.

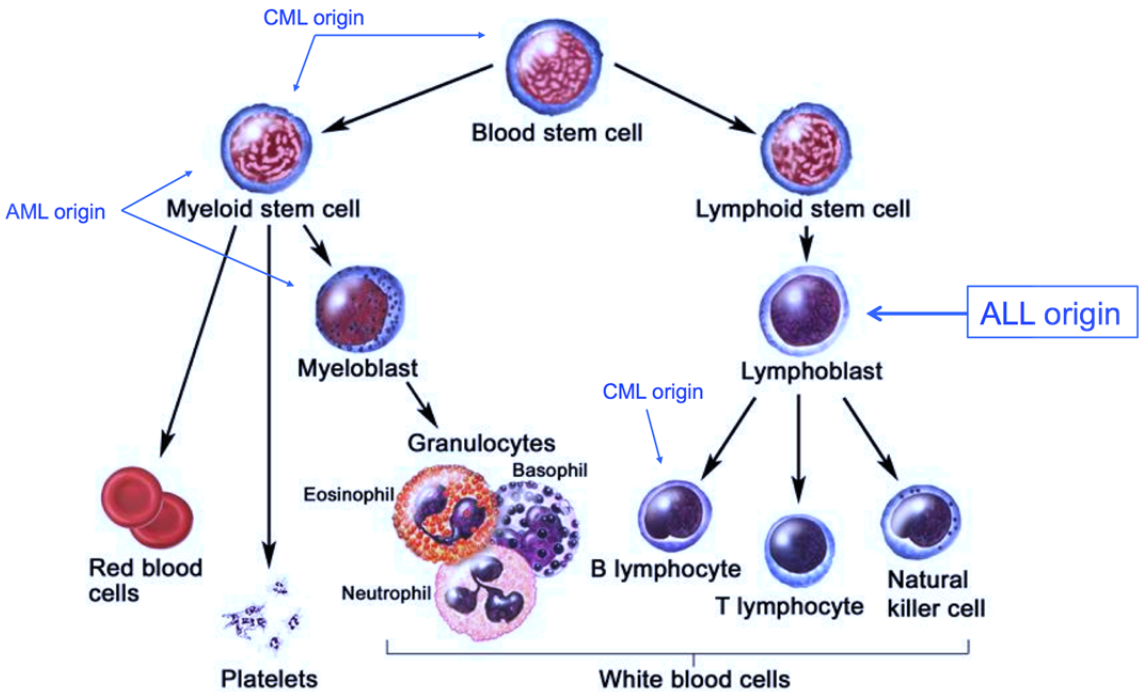

Figure 1 - Leukaemia set points during haematopoiesis.
Adapted from National Cancer Institute (https://www.cancer.gov/types/leukemia/patient/child-all-treatment-pdq).

Nearly 352,000 new leukaemia cases, and more than 265,000 deaths, were reported worldwide, in 2012 (Ferlay et al. 2015). Leukaemia is the most frequent type of cancer affecting children, with ALL at the top of the list. ALL is characterized by the overproduction of immature lymphocyte precursors, called lymphoblasts, which

accumulate and prevent the development of normal B- or T-lymphocytes (B-ALL or T-ALL, respectively). These blasts normally represent 1–2 % of bone marrow cells, but in ALL patients this percentage raises to more than 20 % and blasts are also found in peripheral blood, or even invading other organs, as a result of their uncontrolled proliferation.

1.2.1. Available ALL therapies

Modern ALL therapy uses high-dose chemotherapy, allogeneic haematopoietic stem-cell transplantation (HSCT) and targeted therapies, and comprises three phases: remission-induction (4–6 weeks), consolidation (20–30 weeks) and maintenance (2 years or longer) (Inaba et al. 2013). However, ALL has a wide biological heterogeneity, which leads to different treatment needs depending on the patient's age and overall status, ALL's immunophenotype, and genetic studies (Bassan and Hoelzer 2011). A variety of chemotherapeutic drugs can be used for ALL treatment, normally in combination (namely vincristine, asparaginase, daunorubicin, methotrexate, cytarabin, etoposide, some glucocorticoids, such as dexamethasone or prednisone), under a number of different protocols (Inaba et al. 2013). Allogeneic HSCT is considered for patients with very high risk ALL. It refers to the use of haematopoietic pluripotent stem-cells collected from compatible healthy donors that are transplanted to the patient, normally after chemotherapy has destroyed the immune system (Bassan and Hoelzer 2011). For some ALL subtypes, targeted therapies with tyrosine-kynase inhibitors, such as imatinib or nilotinib, may be useful. Surgery, radiation and monoclonal antibodies may be interesting approaches in special cases.

Higher incidence of ALL is reported in children (6 in each 10 cases), but an estimated 80 % of deaths from ALL occur in adults (4 in each 5 deaths), showing the need for more efficient approaches to eradicate ALL.

1.2.2. Jurkat cells as an *in vitro* model of T-cell leukaemia

Around 1500 models of leukaemia are available for *in vitro* studies, 600 of which are well characterized and have been considered robust *in vitro* models (Drexler et al. 2000, MacLeod and Drexler 2008). In particular, Jurkat cell line (clone E6-1, ATCC® TIB-152™) is one of the most frequently used acute lymphoblastic leukaemia model for mechanistic studies. This immortalized cell line was collected and maintained from the peripheral blood of a 14-year old boy relapsing from T-ALL (Schneider et al. 1977). Its easy manipulation and evident response in the context of apoptosis, for example, makes it an appealing model for many types of studies, such as the staining with the early apoptosis

marker, Annexin-V, for flow cytometry (Martin et al. 1995). Figure 2 shows microscopy images of Jurkat cells at different cell densities.

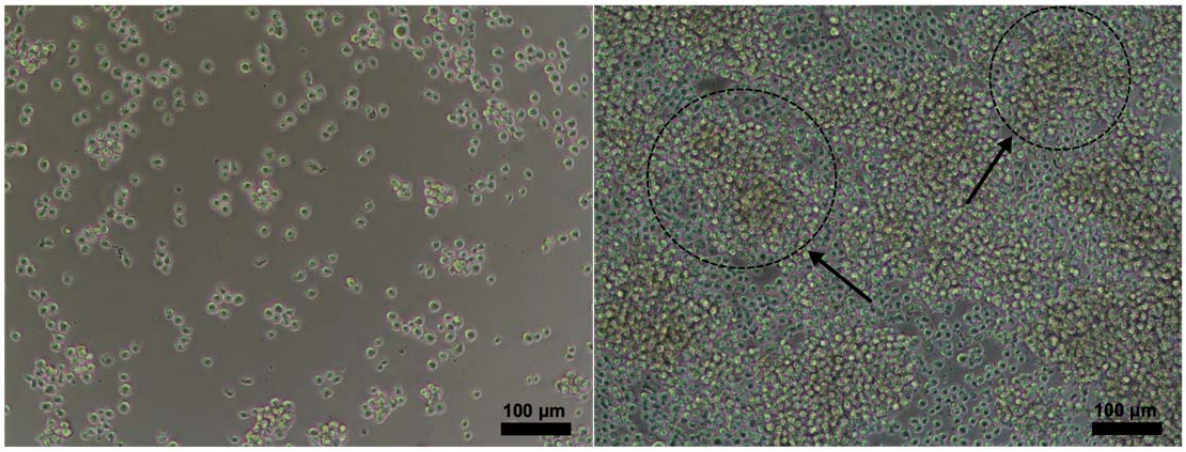

Figure 2 - Bright field images of Jurkat cells at low (left) and high (right) cellular density. The circles and arrows highlight the cell agglomerates formed when cells multiply to high density.

The mechanisms of action and the therapeutic effects on ALL of many chemotherapeutic agents have been studied *in vitro* using Jurkat cells. As an example, a study by da Silva *et al.* has shown that methotrexate, doxorubicin, daunorubicin and vincristine, many of which are currently used in ALL treatment, induced pronounced apoptotic cell death in Jurkat cells (da Silva et al. 1996). The same study demonstrated lack of efficiency of 6-mercaptopurine and prednisolone for ALL treatment. More recently, lapatinib—an inhibitor of the tyrosine-kinase activity of the epidermal growth factor receptor (EGFR) family members, which has been approved in 2007 by the Food and Drug Administration (FDA) for the treatment of breast cancer—has been tested in Jurkat cells, demonstrating its potential to be used in leukaemia therapy (Chen et al. 2016b). Another example is the recent suggestion of Articulatin-D, a ribosome-inactivating protein extracted from the mistletoe (*Viscum articulatum*), as a promising agent for leukaemia treatment (Mishra et al. 2016). The studies performed in Jurkat cells and, in parallel, in peripheral blood mononuclear cells demonstrated selective cytotoxicity in cancer cells (Mishra et al. 2016). These recent studies highlight the present reliability on Jurkat cells as suitable *in vitro* models of ALL.

1.3. Glioblastoma multiforme

The cancers of the brain and the central nervous system (CNS) accounted for around 256,000 new cases worldwide (1.8 % of total new cases), nearly 74 % of which resulted in death in 2012 (Ferlay et al. 2015). These numbers show that, even though their incidence

rate is low, these cancers have a very high mortality rate. Amongst the various types of brain tumours, glioblastoma multiforme (GBM, Figure 3), also called glioblastoma, stands out as the most frequent and most malignant type of primary brain tumours. They are also known as high-grade (i.e. fast-growing; grade IV) astrocytomas as they arise from star-shaped cells called astrocytes. The presence of necrotic cells and increased blood flow (angiogenesis) around the tumour are key histological features of GBM (ABTA 2016). GBM's malignancy is related to their ability to metastasize inside the brain, but these tumours rarely spread outside the CNS. Although a small amount of GBM can be called secondary, as they develop from less malignant (grades II or III) astrocytoma forms, most GBM (90–95 %) are called primary or *de novo* as they are diagnosed without a known less malignant precursor lesion. These types are also associated with different age groups: while secondary glioblastomas predominate in patients aged under 45, primary glioblastomas are more frequent in patients aged over 55 (ABTA 2016).

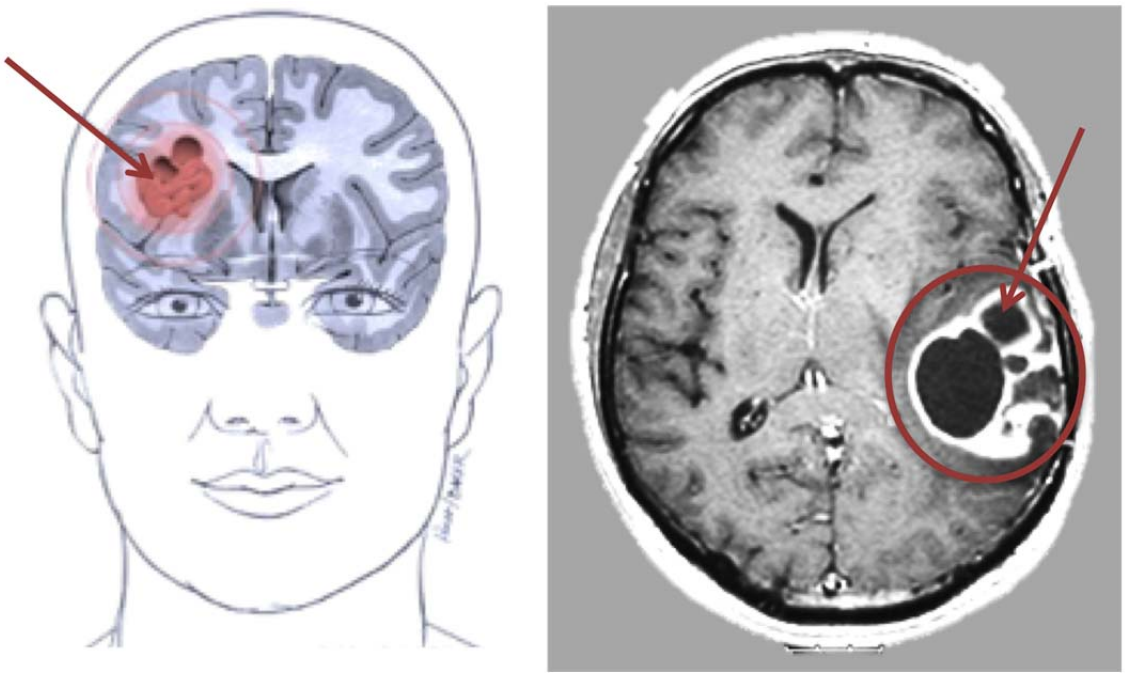

Figure 3 - Glioblastoma multiforme: schematic representation and magnetic resonance imaging.
The red arrows indicate the tumour mass, appearing red in the schematic representation and appearing as black masses in the magnetic resonance imaging. Adapted from http://mayfieldclinic.com/PE-Glioma.htm

1.3.1. Clinically available glioblastoma therapies

The high malignancy and fast-growth of GBM demand a very aggressive treatment approach, generally combining resection surgery, radiation and chemotherapy as first line treatment (Stupp et al. 2005, Weller et al. 2014).

Surgery is a fundamental element in the management of GBM treatment, both for diagnostic (biopsy) and therapeutic purposes. Maximal resection of the tumour mass, specially its core that can be resistant to radiation and chemotherapy, helps diminishing the incidence of symptoms arising from the presence of the tumour, but generally a complete resection is not possible due to the tentacle-shaped cells composing it (Weller et al. 2014). Chemotherapy, radiation and immunotherapy are then used, combined or not, to control the growth of the remaining tumour cells (ABTA 2014).

Radiotherapy is directed to the tumour and surrounding area, and it can be boosted with localized radiation, which is more protective of normal cells. It generally lasts for 5–6 weeks (5× a week) (Stupp et al. 2005).

The most used chemotherapeutic agent to treat GBM is temozolomide (TMZ). Since 2005, the standard treatment combines a 6-week course of TMZ with radiation therapy, followed by TMZ alone for 6–12 cycles (Stupp et al. 2005). Other alkylating agents have been approved for the treatment of GBM, namely Carmustine (1,3-Bis(2-chloroethyl)-1-nitrosourea), and Lomustine (N-(2-chloroethyl)-N'-cyclohexyl-N-nitrosourea). Patients whose tumours display O-6-methylguanine-DNA methyltransferase (MGMT) promoter methylation have better prognosis, as they are more responsive to these alkylating agents (Hegi et al. 2005). Because chemotherapeutic agents can affect normal cells as well, chemotherapy is normally associated to high incidence of adverse effects.

Other innovative therapies have been proposed for the treatment of GBM, namely immunotherapy and magnetic hyperthermia (see Section 2), a therapy that has been certified in the European Union to treat glioblastoma with NanoTherm® Therapy (MagForce 2016a). Phase II clinical trials showed a 7.2–8.6 month increase in overall survival of GBM patients (Maier-Hauff et al. 2011).

Despite the plethora of combined treatments for GBM, the prognosis for this type of cancer remains very unfavourable. Median survival of adult patients with GBM treated with concurrent TMZ and radiation therapy is about 14.6 months; the two-year median survival rate is 27 %. Overall five-year survival is 10 % (Stupp et al. 2009). These numbers confirm the urgent need for new and more efficient treatments for GBM.

1.3.2. LN229 cells as an *in vitro* model of glioblastoma

A number of glioblastoma cell lines from human origin are available, which can be grown in 2D or 3D configuration, for *in vitro* studies on the physiology, the diagnosis and the therapy of this aggressive type of brain cancer (Grotzer et al. 2016). Despite the

advantages of *in vitro* 3D cultures, the 2D models still represent a good starting point for therapeutic studies due to their affordable price, easiness of handling, and compatibility with high throughput screening (Das et al. 2015). The advantages and disadvantages of 2D and 3D *in vitro* cultures are summarized in Table 1.

Table 1 - Advantages and limitations of 2D and 3D *in vitro* cell culture

***In vitro* culture method**	**Advantages**	**Limitations**
2D	Easiness of culturing; Good viability levels; Easiness of imaging; Suitable for endpoint assays; Highly suitable with high throughput screening; Affordable when compared with other systems; Significant availability of 2D data.	Lack of cell–cell and cell–stroma interactions; Lack of histological morphology of tumour of origin; Do not replicate heterogeneity seen in tumour regions; Different genetic makeup from the original tissue.
3D	Oxygen and nutrient gradient of tumours; Cell–cell and cell–stroma interactions; Histological morphology different from the tumour of origin; Hypoxia-induced cell cycle alterations reflecting microregions of tumours; High throughput-compatible 3D culture plates available.	Assays are laborious; Requires higher drug concentrations compared with 2D cultures; Requires advanced imaging systems; Relatively expensive compared with 2D cultures; High throughput screening compatibility still under development.

Adapted from (Das et al. 2015)

In particular, the LN229 cell line (ATCC® CRL-2611™) was first established in 1979 from cells collected from a 60 year-old female patient with right frontal parieto-occipital GBM. This adherent, highly tumorigenic, cell line is commonly used in studies involving apoptosis, and is capable of growing in 2D or 3D configuration (Figure 4). The LN229 cell line has been genetically characterized and its resistance/ sensitivity to a number of chemotherapeutic drugs has been established (Weller et al. 1998).

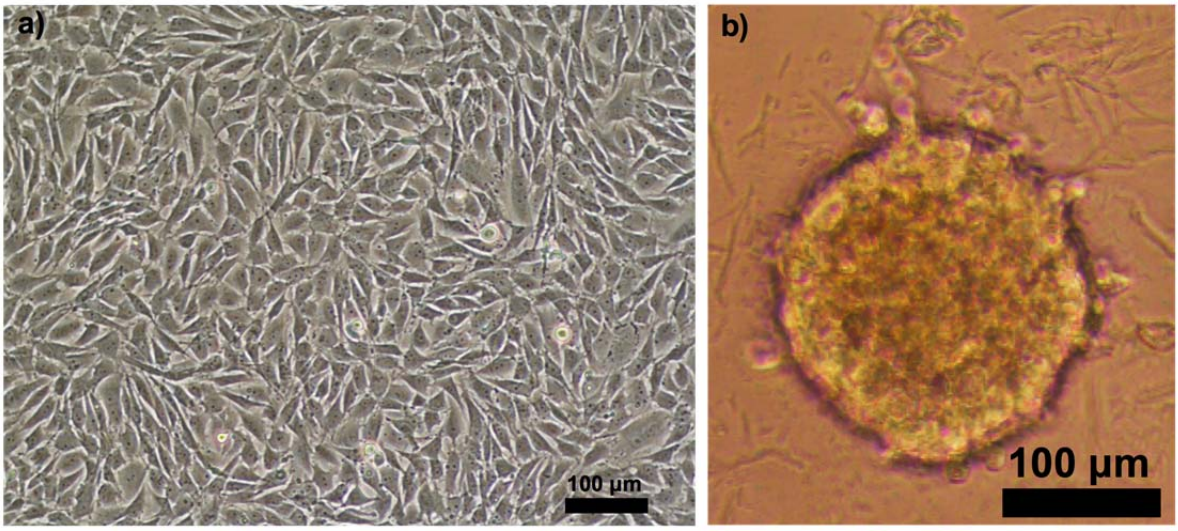

Figure 4 - LN229 cells cultured in 2D or 3D configurations.
a) Bright field microscopy image of a high-density monolayer of LN229 cells. b) a 48-h LN229 3D culture (spheroid).

This cell line has been extensively used in previous reports as an *in vitro* model of GBM, in particular, in the search for therapeutic improvements to the current standard protocols for GBM treatment, which are highly fallible. For example, Combs *et al.* found that LN229 cells are highly resistant to radiation therapy alone, and higher therapeutic efficiency was observed for a combination of TMZ and cetuximab, an anti-EGFR antibody (Combs et al. 2007). This cell surface receptor was found to be overexpressed in many GBM samples collected from patients (Shinojima et al. 2003). More recently, Elhag *et al.* demonstrated that the effects of TMZ in LN229 cells could be potentiated by silibinin, a hepatoprotective drug, via down-regulation of the inhibitor of apoptosis, survivin (Elhag et al. 2015). Another interesting study used nanoparticles as nanocarriers, serving as transfection agents, of an antisense microRNA to silence the microRNA21, an oncogene overexpressed in many cancer cells. The resulting knockdown of microRNA21 in LN229 cells significantly potentiated TMZ effect in this cell line (Ananta et al. 2015).

1.4. CXCR4 expression and cancer

The ability of cells to migrate directionally is often moved by the secretion of small molecules (chemokines) that bind to a subset of G-protein-coupled receptors at the cell membrane (chemokine receptors), a process called chemotaxis. One of such receptors, CXCR4, is a seven transmembrane protein that is endogenously activated by the stromal cell-derived factor-1 (SDF-1 or CXCL12), which can rapidly induce receptor endocytosis to initiate the signalling cascade (Signoret et al. 1997). The CXCR4 has been initially described as a co-receptor for CD4-independent HIV infection (Endres et al. 1996, Feng

et al. 1996). Further studies established an important role for the CXCL12/CXCR4 axis in haematopoiesis, leukocyte chemotaxis and cerebellar development (Zou et al. 1998).

The CXCR4 antagonist, AMD3100, also known as Plerixafor, has been clinically tested as a stem cell mobilizer, in combination with granulocyte-colony-stimulating factor, after chemotherapy in lymphoma or multiple myeloma patients, with good results and low toxicity (Jagirdar et al. 2015). Later, CXCR4 was found to be overexpressed in many types of cancer, such as leukaemia (Mohle et al. 1998), GBM (Sehgal et al. 1998), breast cancer (Muller et al. 2001) and prostate cancer (Taichman et al. 2002), among others. In this sense, CXCR4 overexpression is related with increased tumour aggressiveness, proliferation, metastization and, consequently, bad prognosis (reviewed in (Zlotnik 2006, Domanska et al. 2013)). CXCR4 has consequently been proposed as a potential target for ALL (de Lourdes Perim et al. 2015) and GBM treatment (Terasaki et al. 2011). A recent work reports the use of AMD3100 as part of the therapeutic regimen of a 66-year old patient diagnosed with GBM that has been in clinical and radiological remission 30 months from initiating the adjuvant treatment (Rios et al. 2016).

The leukaemia and glioblastoma *in vitro* models previously described, i.e., Jurkat and LN229 cells, express different levels of CXCR4, as assessed by western blotting using a monoclonal anti-human-CXCR4 antibody (Figure 5). When compared to another GBM cell line, U87MG (ATCC® HTB-114™), LN229 cells display intermediate levels of that chemokine receptor while Jurkat cells exhibit the highest levels of CXCR4, in line with a previous study (Huang et al. 2014). The discrepancy in CXCR4 expression between suspension and adherent cell lines has been previously discussed (Huang et al. 2014). The exposed facts confirm the suitability of those cell lines for *in vitro* studies in the scope of CXCR4 targeting for leukaemia and GBM treatment.

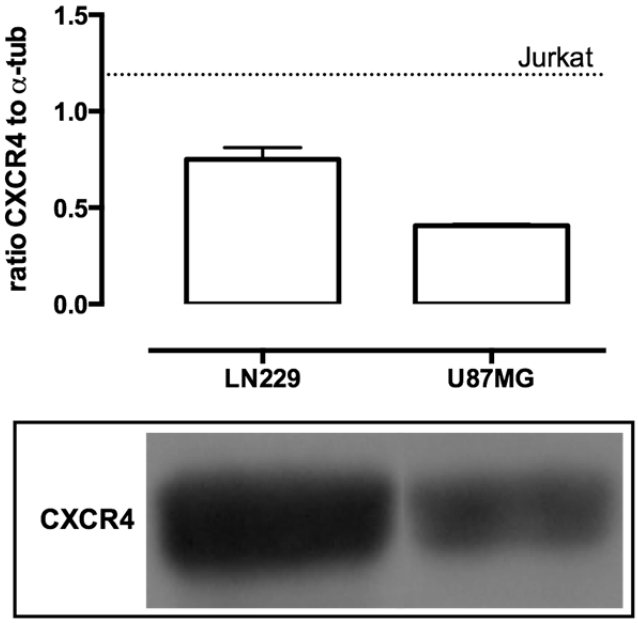

Figure 5 - CXCR4 expression in two human glioblastoma cell lines, LN229 and U87MG, assessed by western blot.
The dashed line represents CXCR4 expression in the positive control, Jurkat cell line.

2. Magnetic hyperthermia for cancer treatment

"Quæ medicamenta non sanant, ferrum sanat; quæ ferrum non sanat, ignis sanat; quæ vero ignis non sanat, insanabilia reputari oportet." – Hippocrates

"Those diseases which medicines do not cure, the knife cures; those which the knife cannot cure, fire cures; and those which fire cannot cure, are to be reckoned wholly incurable."

2.1. Introducing the (magnetic) hyperthermia concept

The term "hyperthermia" refers to the local, regional, or generalized increase in body temperature (*T*). This concept has been put in practice centuries ago by the ancient civilizations and has been applied for cancer treatment since the 19th century (Moyer and Delman 2008). Cancer cells are known to be more sensitive than normal cells to elevated *T*, in the range of 41–43 ºC, due to their faster cellular division rate, entering a programmed cell death mode (apoptosis) (Hervault and Thanh 2014). Although the cellular targets of hyperthermia are not yet fully understood, it is known that it affects the membranes, the cytoskeleton, protein synthesis and, even, DNA repair (reviewed in (Hildebrandt et al. 2002)). Some genes were found overexpressed after hyperthermia treatment, namely the heat-shock protein (HSP) family, a situation known to generate

thermo-resistance, also called thermo-tolerance, that results in impaired cell death through hyperthermia. At a *T* below 42 ºC, tumour blood flow is increased, which may be useful for the simultaneous delivery of chemotherapeutic agents, enhancing their anti-tumour effect (Wust et al. 2002). Furthermore, increased blood flow results in increased oxygenation, a factor known to enhance radiosensitivity (Maier-Hauff et al. 2011). At a *T* above 42 ºC the tumour's blood flow decreases, while increasing in the normal tissues, which leads to lower dissipation rate and, therefore, faster *T* rise in tumours, compared to normal tissues (Song 1984). In the case of thermoablation, when the *T* rises above 46 ºC, the cell death mode changes to a necrotic cell death (generally accompanied by inflammation), which may affect normal cells, as well (Hildebrandt et al. 2002).

Since the late 1950s, magnetic implants have been proposed for cancer treatment, as thermo-seeds, under an alternating magnetic field (AMF), a process called magnetic hyperthermia (MHT) (Gilchrist et al. 1957). Later, in 1979, Gordon *et al.* were the first to introduce the concept of "intracellular" MHT by using dextran-coated magnetite submicron particles, which were internalized by cancer cells *in vivo*, to increase the *T* of tumours submitted to a strong AMF (Gordon et al. 1979). These authors suggested that cell membranes efficiently act as thermal insulators, preventing the heat generated by the internalized particles from dissipating to the surroundings. This concept, therefore, implied that, when an external magnetic field is applied, the heat generated by a single particle inside a cell could effectively kill it.

The first clinical trials on MHT were undertaken in Japan, in the 1990s, by Kobayashi and Kida, in malignant glioma patients locally implanted with a FePt metal alloy, reporting encouraging results, in particular for the generally considered unresectable tumours (Kobayashi and Kida 1990). More recently, many MHT studies have been performed using magnetic nanoparticles (MNPs) as magnetic heaters, testing different sizes, coatings, targeting systems, cancer cells, and AMF parameters to reach the best protocol to induce cancer-cell death. Andreas Jordan and co-workers have reported consistent and pioneering studies, performing *in vitro*, *in vivo*, and clinical studies on MHT for cancer treatment. He founded the company MagForce Nanotechnologies AG, which currently detains an European Medicines Agency (EMA) approval for using and testing MHT as cancer treatment (NanoTherm™ therapy), in particular primary and recurrent GBM (MagForce 2016a). So far, the results collected from phase II clinical trials were promising and indicated a significant 8-month prolongation of patient life (Maier-Hauff et al. 2011). More studies were conducted to test MHT's efficacy and safety for the treatment of prostate cancer (Johannsen et al. 2007). Figure 6 shows a schematic representation of magnetic hyperthermia treatment.

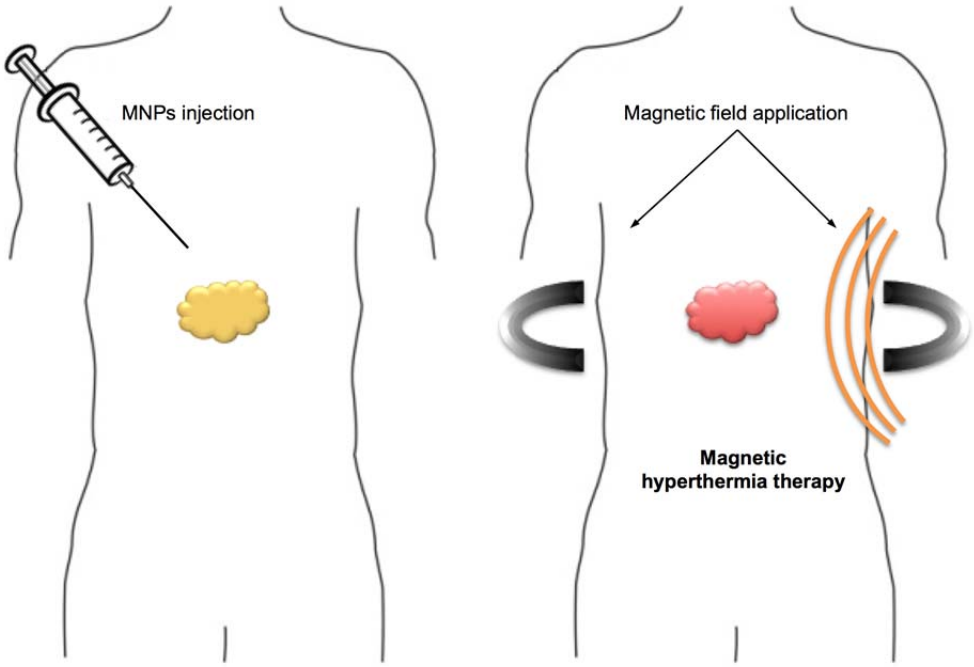

Figure 6 – Schematic representation of a magnetically-induced hyperthermia treatment using magnetic nanoparticles.
The MNPs may be injected directly into the tumour or intravenously, with the possibility of being magnetically or biologically guided to the tumour. The application of an alternating magnetic field generates heat that kills tumours cells, shrinking or eradicating the tumour. Adapted from (Andrade et al. 2011)

Although MHT is mostly used for cancer treatment, some other interesting applications have been recently suggested, namely the treatment and control of bacterial (Chen et al. 2016a), fungal (Chudzik et al. 2016) and parasitic (Grazu et al. 2012) infections, or as a disruptor of β-amyloid protein aggregates that trigger Alzheimer's disease (Loynachan et al. 2015). A search in Pubmed.gov under the keywords "magnetic hyperthermia cancer" showed that around 2100 reports have been published since its introduction in 1950, nearly half of which in the past six years (since 2010). Therefore, MHT for cancer treatment has been experiencing increased interest by the scientific community in recent years. This fact was particularly promoted by the expansion and growth of nanotechnology era, through the development of new and efficient materials for MHT, followed by its application to *in vitro, in vivo* and clinical studies.

2.2. Magnetic nanoparticles for MHT

The magnetic properties of some naturally occurring materials, such as loderstone, have been noticed thousands of years ago due to their rare ability to attract iron. These rocks, also called *magnetes* or *magnetis* back then, because they were extracted in a region named *Magnesia*, are mainly composed of magnetite (Fe_3O_4) and maghemite (γ-

Fe_2O_3). Their natural orientation towards the earth's geographical poles led to their use as direction tools, that later gave rise to the compass (Du Trémolet de Lacheisserie 2005).

The magnetic properties of the materials arise from their basic building blocks, the atoms, through the magnetic fields (named magnetic moments) eventually produced by the movement of their unpaired electrons in response to an applied magnetic field (Du Trémolet de Lacheisserie 2005). In this sense, diamagnetic materials—frequently known as non-magnetic—have all their electrons in pairs, so their atoms possess no permanent magnetic moment, resulting in very low magnetic susceptibility ($\chi<0$), which is defined as the magnetization in response to a magnetic field (Pamme 2006). Copper, silver and gold are examples of diamagnetic materials. Paramagnetic materials, like oxygen and platinum salts, have unpaired electrons that align with the external magnetic field direction, therefore, exhibiting positive susceptibility values ($\chi>0$) (Pamme 2006). Once the magnetic field is removed, neither diamagnetic nor paramagnetic materials retain any magnetic properties. On the other hand, ferromagnetic materials (e.g. iron, cobalt and nickel), also called ferromagnets, have unpaired electrons that tend to align with the external magnetic field direction, generating a large magnetic susceptibility ($\chi\gg0$) and, therefore, being strongly attracted to magnetic fields and becoming magnetized (Pamme 2006). This magnetization of ferromagnets is retained once the magnetic field is removed, therefore behaving like permanent magnets. Their strong magnetic properties are also a consequence of the presence of domain regions in the ferromagnetic materials separated by boundaries called domain walls (multi-domain materials), which ensure keeping an overall lower energy state. As the volume of the material decreases, it may reach a critical diameter below which it becomes unfavourable to keep the domain walls, and single-domain particles are created (Dutz and Hergt 2013). Whenever the size of the magnetic particles falls between 1 and 100 nm at least in one dimension, they are called MNPs.

Specifically, MNPs made of ferri- (Fe^{3+}) or ferro- (Fe^{2+}) magnetic materials below a critical size value (typically ~10–20 nm diameter) may exhibit, at room temperature, an unique magnetic property known as superparamagnetism (Bedanta and Kleemann 2009); this critical diameter varies between different materials. When exposed to an external magnetic field, the atomic magnetic moments of superparamagnetic iron oxide nanoparticles (SPIONs) align along the field direction, achieving high susceptibility (Lu et al. 2007). Once the magnetic field is removed, SPIONs behave like a non-magnetic material exhibiting no magnetic memory (i.e., no remanence), which minimizes the interactions between any two MNPs, yielding stable colloidal dispersions (Pamme 2006). SPIONs are, therefore, preferable materials for a number of applications in the biomedical

field, namely for tumour imaging, magnetic targeting, targeted drug-delivery, magnetofection, and MHT (Zhao et al. 2013). Some nanoparticle clusters (multi-core nanoparticles) cannot be described by a specific behaviour, rather sharing characteristics of both ferrimagnetic and superparamagnetic nanoparticles, being also interesting materials for MHT induction (Dutz and Hergt 2014).

2.2.1. Requirements for biomedical applications

The main requirements for the biomedical application of MNP preparations are low toxicity, ability to escape the reticulo-endothelial system (RES) and low protein adsorption (Yang et al. 2012). Therefore, when optimizing iron oxide nanoparticles (IONPs) for their use in biomedical applications, some issues need to be addressed namely their size, stability in biofluids (tendency for aggregation and protein corona formation), possible toxicity, pharmacokinetics and pharmacodynamics within the body (Yang et al. 2012), as well as the specificity for target tissues.

Size

The size of the MNPs is an important factor to consider for *in vivo* or clinical studies. MNPs sized above 200 nm are rapidly taken up by the RES and accumulate in the liver and spleen; on the other hand, MNPs sized below 6 nm are filtered by the kidney (Bychkova et al. 2012). Furthermore, there are natural differences between the neovasculature of tumours (defective and leaky) and that from normal tissues, which lead to increased supply of nutrients and oxygen to the tumour site. While tumour vasculature fenestrations can be hundreds of nanometres in size, normal vessels openings' are generally less than 10 nm (Iyer et al. 2006). This phenomenon has practical implications as nanoparticles sized above 10 nm can extravasate and accumulate in the tumour, but not in the normal tissues. Also, the slow venous return and lower lymphatic clearance characteristic of tumours, favour MNPs' retention in the tumour (Stylianopoulos 2013). This extensive leakage and low clearance are known as the enhanced permeability and retention (EPR) effect, characteristic of many solid tumours (Iyer et al. 2006).

At a cellular level, the upper size limit consensually considered for nanoparticle uptake through endocytosis is 500 nm (Rejman et al. 2004, Bychkova et al. 2012). As already mentioned, nanoparticles sized above 200 nm are generally uptaken by specialized cells of the RES through phagocytosis, a specific type of endocytosis (Saptarshi et al. 2013).

Surface coating stabilization

Apart from their unusual electronic, optical and magnetic properties, the usefulness of nanoparticles predominantly arises from their small size and large surface area (Yang et al. 2012). In the case of bare IONPs, these characteristics, along with their metallic composition, contribute to a high degree of chemical instability and reactivity to air, resulting in surface oxidation and, consequently, loss of magnetism (Wu et al. 2015). This issue may be surpassed by providing the IONPs with a coating layer that limits the access of oxygen to the highly reactive core surface. In this sense, a core-shell type of nanoparticles is the most common one, whereby a highly reactive iron oxide core is protected by an organic (e.g. polymer) or inorganic (e.g. silica, carbon, gold) shell (Figure 7). Alternatively, IONPs can be dispersed or embedded in an organic/ inorganic matrix forming composites where the nanoparticles are fixed in space (Lu et al. 2007).

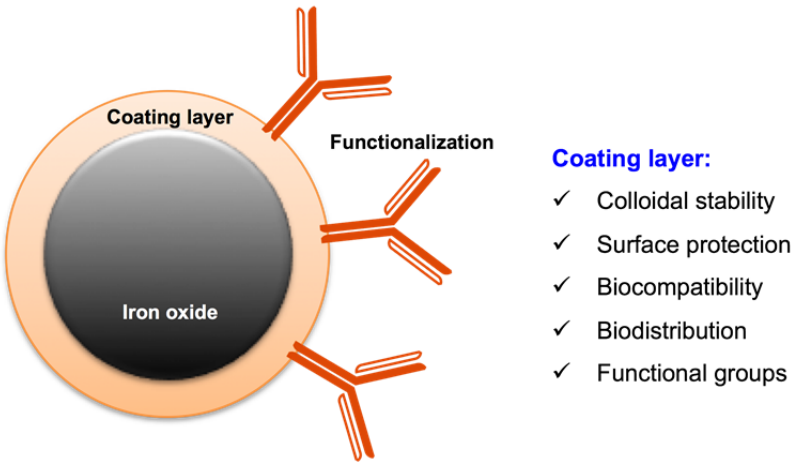

Figure 7 - Schematic representation of a core-shell iron oxide nanoparticle.
The iron oxide magnetic core is embedded in a coating layer that provides the IONPs with protection, stability, biocompatibility and the possibility of functionalization with targeting ligands (e.g. antibodies), while affecting their biodistribution profile.

The most studied protective coatings, so far, are silica or polymers, in particular, poly(ethylene glycol) (PEG) and dextran (and its derivatives). Other polymers include poly(acrylic acid) (PAA), alginate and chitosan, among others (Yoffe et al. 2013). Different coating materials are described in detail in a recent review by Wu *et.al* (Wu et al. 2015). Besides being an important step towards lower IONP degradability, surface coating also brings other advantages such as increased colloidal stability and biocompatibility (Figure 7). Furthermore, in an *in vivo* context, the chosen coating can minimize opsonisation, affecting the circulation half-life of nanoparticles and, consequently, their biodistribution. Such effects can be observed when using PEGylated nanoparticles (Albanese et al. 2012).

The selected coatings provide the nanoparticles with different surface charges that vary depending on the medium's pH (Vilas-Boas et al. 2015). Studies suggest that surface charge may also influence nanoparticle's uptake, with positively charged nanoparticles being more internalized than negatively charged ones, while neutral nanoparticles were not internalized (Villanueva et al. 2009, Bychkova et al. 2012). These different internalization rates result in higher toxicity of the positively charged nanoparticles and lower toxicity, as well as prolonged half-life, of negatively charged ones; neutral nanoparticles are considered the most biocompatible.

Specific coatings also provide the IONPs with reactive groups (e.g. carboxylic groups that stabilize the particles by electrostatic repulsion) that allow particle functionalization or conjugation with biomolecules, such as proteins, to actively pinpoint specific tissues or biological targets (Yoffe et al. 2013). The term "functionalization" is sometimes used meaning "surface coating" [e.g. (Wu et al. 2008)] but, in this work, "surface coating" and "functionalization" refer to different layers of the IONPs (Figure 7).

Conjugation with biomolecules

A targeted use of IONPs in cancer diagnosis and treatment is generally preferred and desirable in order to diminish or avoid the possible side effects on healthy body tissues. While the EPR effect is considered a passive targeting strategy, the active targeting is a strategy that requires a ligand (conjugated to the MNP) directed to a cell-surface receptor, which in many cases results in efficient internalization of targeted MNPs by receptor-mediated endocytosis (Pirollo and Chang 2008). Active targeting can be controlled by the use of safe and stable surface coatings and by providing the IONPs with targeting molecules such as proteins, like streptavidin (STR) or antibodies [e.g., anti-EGFR, Herceptin], or peptides, DNA or RNA (Sperling and Parak 2010). Although STR is not a targeting molecule to be used in cancer recognition it may be used as an intermediate for high affinity binding of antibodies, similarly to staphylococcal Protein A (PA) (Martins et al. 2012).

There are a number of strategies to achieve nanoparticle conjugation, depending on the chemical functional group present on the IONPs, generally carboxylic (–COOH) or amine ($–NH_2$) groups. Among them, one of the most widely used is the so-called EDC crosslinking chemistry. It consists of a water-soluble carbodiimide (1-ethyl-3-(-3-dimethylaminopropyl) carbodiimide hydrochloride, EDC) that activates the carboxylic groups (generally from the IONPs) to an unstable intermediate that will react with the primary amine groups (generally from the protein to bind). The efficiency of this reaction is

increased in the presence of a chemical modification reagent, *N*-hydroxysulfosuccinimide (sulfo-NHS), that converts the activated carboxyl groups in amine-reactive NHS esters, more stable for bioconjugation with primary amines by means of a new amide bond (Sperling and Parak 2010). A schematic representation of the EDC-sulfo-NHS crosslinking reaction is provided in Figure 8.

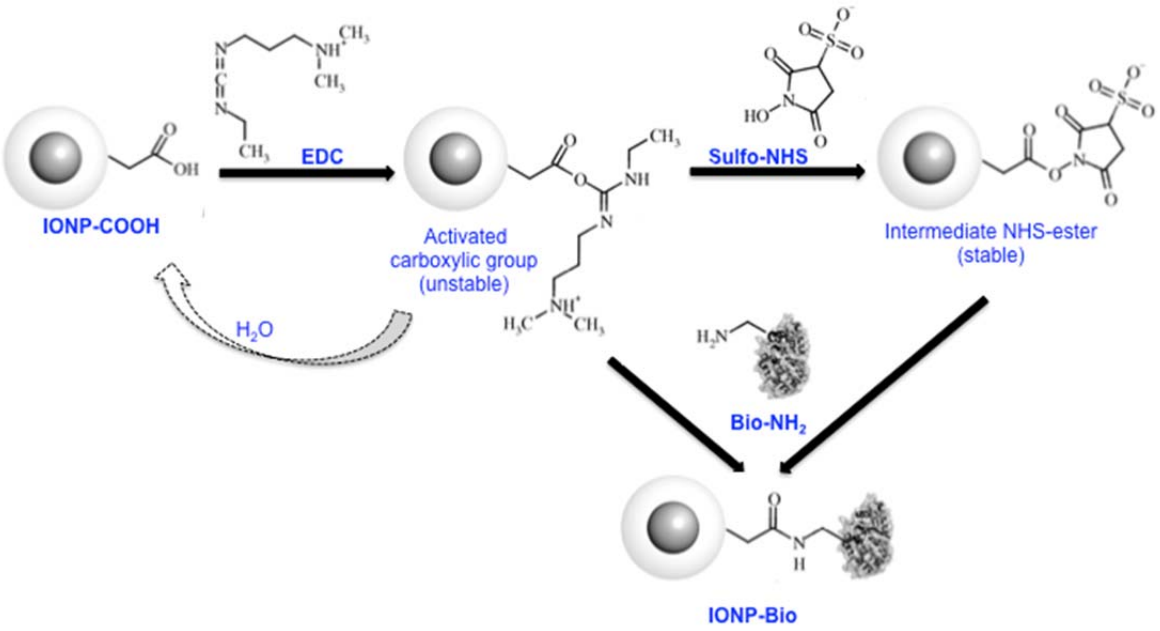

Figure 8 - Schematic representation of the EDC-sulfo-NHS crosslinking chemistry for IONPs functionalization with biomolecules.
Adapted from (Sperling and Parak 2010)

Tumour accumulation and internalization

While it's known that the functionalization, the surface coating, and the size of the nanoparticles play a role in their biodistribution and cell uptake, the different contribution of each factor is still not clear. Some studies using functionalized nanoparticles reached contrasting conclusions on the effect of the targeting biomolecule in tumour accumulation and cell uptake. For example, the use of Herceptin-conjugated PEGylated nanoparticles (ca. 100 nm), compared to non-targeted ones, did not result in more efficient accumulation in the tumour, but resulted in enhanced internalization by the tumour cells (Kirpotin et al. 2006). These nanoparticles' efficient accumulation has been ascribed to the presence of PEG as coating agent, which prolonged their circulation time, therefore, contributing for efficient tumour accumulation through the EPR effect (Pirollo and Chang 2008). On the other hand, a more recent study on the influence of size, targeting and PEGylation on the IONPs biodistribution and tumour accumulation *in vivo*, reported no influence of PEG on

tumour accumulation (NDong et al. 2015). Contrarily to the *in vitro* studies, where the cellular homing was mainly dependent on the targeting moiety, the key determinant factor for tumour accumulation of IONPs *in vivo* was the IONPs size. In fact, the 100 nm IONPs, both targeted and non-targeted, PEGylated and non-PEGylated, were similarly cleared from the blood and accumulated in the liver. On the other hand, the smaller IONPs (ca. 30 nm) accumulated significantly more in the tumour than the 100 nm IONPs, an effect further enhanced by the presence of the targeting moiety (NDong et al. 2015). Another study suggested that targeted polymeric nanoparticles accumulated more in tumours overexpressing the cancer target, while for tumours with lower expression the effect was mainly dependent on the nanoparticle's size (Lee et al. 2010). These conflicting results highlight the need for more studies to further establish the influence of these variables in the accumulation of nanoparticles in the tumour.

Nanoparticle's endocytosis is thought to be a two-step process that starts with nanoparticle's adhesion to the cell surface followed by nanoparticles internalization (Lesniak et al. 2013). Besides the size limitation, the adhesion to cells and subsequent uptake of nanoparticles depends on the presence of targeting moiety, which may trigger receptor-mediated endocytosis (Pirollo and Chang 2008). The protein adsorption layer (known as protein corona) formed by the proteins in the medium where nanoparticles interact with cells (e.g. blood proteins *in vivo*, serum proteins *in vitro*) contributes for lower adhesion, consequently resulting in lower uptake. However, if a targeting moiety is present on the nanoparticles, the adhesion of the nanoparticles to the cells will fully depend on the target recognition (Lesniak et al. 2013). The adhesion of MNPs, particularly, can be improved by means of the external contribution of a static magnetic field, to magnetically concentrate the MNPs and promote MNPs internalization (magnetofection) (Prijic et al. 2012, Ma et al. 2015).

2.2.2. How do MNPs produce heat under an AMF?

The heat generation by MNPs exposed to an AMF, i.e., the conversion of electromagnetic to thermal energy, is governed by different mechanisms, depending, mainly, on the size of the MNPs used. For multi-domain IONPs (e.g. ferromagnets) submitted to AMF, heat production arises mainly from hysteresis losses, i.e., the energy dissipated during a magnetization cycle. The higher the saturation magnetization (Ms) of the MNPs, the bigger amount of heat is dissipated (Figure 9). When the AMF is removed, these MNPs behave as permanent magnets, keeping some magnetization (remanent magnetization), as opposed to SPIONs that display no remanent magnetization after AMF removal (Figure 9) (Hervault and Thanh 2014).

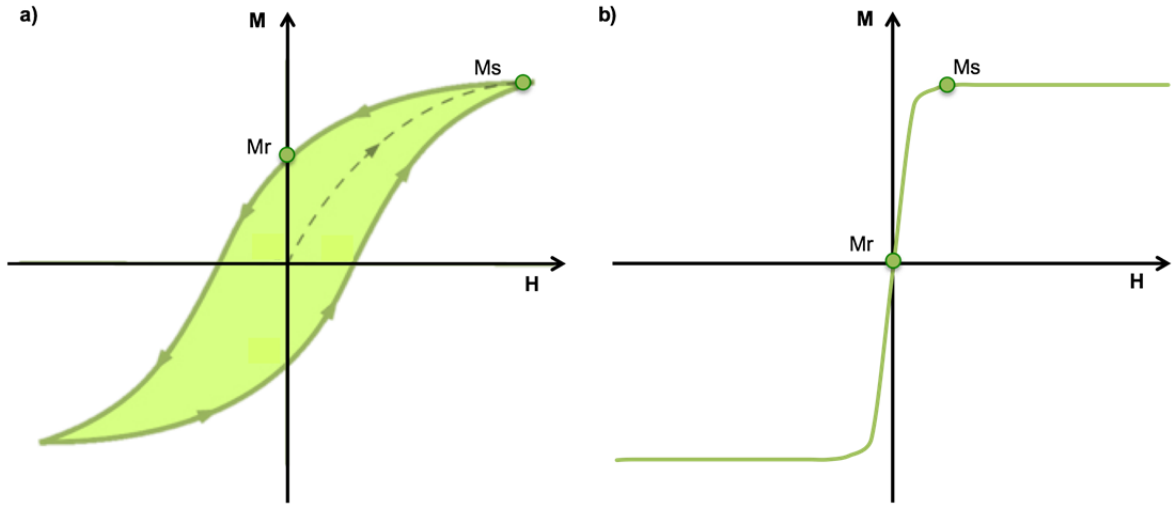

Figure 9 - Dependence of magnetization (M) on the applied magnetic field amplitude (H). a) Typical hysteresis loop of a multi-domain IONP, showing the area that represents the energy dissipated during a magnetization cycle, where Ms is the saturation magnetization and Mr is the remanent magnetization. b) Typical magnetization curve for SPION, showing the absence of remanent magnetization (Mr) when the AMF is removed.

For single-domain MNPs (including SPIONs), heat generation is due to two different modes of relaxation losses known as Néel and Brownian relaxation. Néel relaxation derives from the orientation of the magnetic moments in the same direction as the applied AMF, for each field oscillation. Brownian relaxation comes from the friction of the whole particle's rotation in its dispersing medium (Lee et al. 2015). Therefore, the contribution of each relaxation mode for heat dissipation will depend on the size and mobility of the MNPs: while Néel relaxation varies exponentially with the core volume, being more significant for small diameters, Brownian relaxation varies linearly with the viscosity of the solvent and the hydrodynamic volume of the MNPs (Khandhar et al. 2011). As an example, in tumour tissue, the internalization of MNPs by cancer cells prevents Brownian relaxation from occurring, so only Néel relaxation will contribute to heat generation (Dutz and Hergt 2014).

The heating ability of different MNPs to be used for magnetic hyperthermia is commonly described by the specific absorption rate (SAR), also known as specific loss power, which is the quantification of power dissipation of magnetic nanomaterials under a specific AMF ($W \cdot g^{-1}$):

$$SAR = \frac{C}{m_{Fe}} \frac{\Delta T}{\Delta t}$$

being C the specific heat capacity of the sample, m_{Fe} is the iron mass per unit volume, and $\Delta T/\Delta t$ the initial slope of the T *vs.* time curve (Hervault et al. 2016). SAR is affected

by a number of parameters, such as size, size distribution, chemical composition, concentration, and also frequency (f) and amplitude (H) of the applied AMF. Clustering MNPs seems to improve their SAR with respect to the individual SPIONs composing the magnetic nanoclusters (MNCs) (Maity et al. 2011). The potential of MNPs to be used in hyperthermia applications is often defined by their SAR value. However, care must be taken while comparing SAR values due to the wide range of different equipment available for AMF application, and the diversified protocols for SAR quantification (Hervault and Thanh 2014).

2.2.3. Use of iron oxide nanoparticles in the clinical context

The use of IONPs in the clinical context is currently a reality, in particular as iron-replacement therapies (e.g. Ferrisat, DexFerrum or Ferumoxytol). Other formulations have also been approved as imaging agents by the FDA or the EMA (e.g. Feridex I.V., Resovist, Combidex, among others), but the majority of them has, curiously, been discontinued in the US and European markets (Anselmo and Mitragotri 2016), as their diagnostic utility was not demonstrated in the pivotal studies (Wang 2015). Several clinical trials are currently ongoing, assessing MNP formulations for diagnosis or therapy in many different conditions. As an example, the FDA approved drug Ferumoxytol is being tested as an enhanced contrast agent for magnetic resonance imaging (MRI) in some types of cancer and multiple sclerosis (NIH 2015).

2.3. *In vitro* MHT studies

For the MNPs to be approved for *in vivo* or clinical trials their potentiality needs first to be tested *in vitro*, in cancer and/or normal cell models, to have an initial impression on the tolerability and toxicity of the MNPs and the selected AMF conditions. Accordingly, many reports in the literature refer to the use of MHT to kill cancer cells *in vitro*.

Establishing comparisons between *in vitro* MHT studies can be a challenge due to the widely different conditions used by different authors, which in some cases is aggravated by the lack of information concerning a certain aspect of the procedure. Tables 2 and 3 compile examples of *in vitro* MHT studies, presenting the most relevant parameters that may have contributed for the observed outcome. Amongst them, we highlight the cell line that was tested, the IONPs' characteristics (namely, the coating employed, the size, and initial concentration), the targeting system (if applicable), the AMF parameters, and the reported T reached. Different cell lines may have distinct susceptibilities to heat, meaning that similar T profiles may lead to varying outcomes in

unrelated cells. One major contributing factor for such differences may be the divergent induction of HSP synthesis amongst cell lines (Hildebrandt et al. 2002). As explained in section 2.2.1., the targeting moiety and the characteristics of the nanoparticles will have an impact on their interaction with cells (and subsequent internalization). The importance of the concentration of MNPs used for the MHT test is related to the possible secondary effects that may derive from it lately, in an *in vivo* context. The reached *T* is a vital element to be disclosed in an MHT study due to the obvious impact it may have in the observed outcome. Another parameter that is also important to refer is the time-point at which cell viability levels are assessed. In fact, evaluating cell viability levels right after MHT application may lead to deceiving results, particularly if high enough *T* has not been reached or maintained for enough time. The heat insult may cause a sudden deregulation in cellular metabolism, which can be recovered if the stimulus is removed and conditions are favourable (Hildebrandt et al. 2002). In this section, we will discuss and review some *in vitro* reports on MHT, using targeted or non-targeted nanoparticles, either in a mono-therapeutic context or in combination with other therapies, primarily focusing on the observed outcome after MHT application.

2.3.1. *In vitro* non-targeted MHT studies

Many of the reports found in the literature concerning *in vitro* MHT refer to the use of either plain or surface-coated nanoparticles in many different cell lines. Table 2 compiles a number of these studies, specifying for each of them the parameters that mostly influence the observed outcome after MHT, which will be our primary focus.

Amongst the selected reports on non-targeted *in vitro* MHT, some studies stand out due to the attained low cell viability levels. As an example, Qu *et al.* reported 10 % MCF-7 (breast cancer) cell viability 24 h after using low concentrations of iron oxide nanoclusters doped with manganese and/or zinc ions for MHT. The observed low cytotoxicity in the absence of AMF and the elevated MHT efficiency show great potential for further *in vivo* studies using these magnetic nanoclusters (MNCs) (Qu et al. 2014). Sadhukha and co-workers described similar MHT efficiencies (around 10 % cell viability) in breast (MDA-MB-231) and lung (A549) cancer cell lines after a 30 min MHT treatment. The lower field amplitude used in this study, compared to the previous one, was compensated by a higher magnetite dose. Less prominent cell viability results were reported in the same study, whenever AMF was applied for shorter periods and lower *T* was reached (Sadhukha et al. 2013a). A study developed by Oh and co-workers used similar conditions: approximate amounts of magnetic material, comparable AMF conditions, and the same breast cancer model. Depending on the applied magnetic field amplitude,

distinct *T* was reached and, consequently, distinct cell death pathways were activated. While 42 °C led to an apoptotic pathway, reaching 52 ºC led to cell death through a necrotic pathway. Surprisingly, although a *T* of 52 ºC is expected to lead to complete cell death, both *T* resulted in similar cell viability levels (ca. 20 %) (Oh et al. 2016). A study by Guardia *et al.* describes the use of PEGylated nanocubes with very high SAR values to kill epidermoid carcinoma cells (KB cells) with a 1 h AMF application. The observed outcome strongly varied from 0–75 % cell viability, depending on the iron amount internalized by the cells, which further influenced the reached *T*. Complete cell death was reported when the *T* of 65 ºC was reached (Guardia et al. 2012), which may be a risky *T* to achieve in a clinical situation. A very interesting *in vitro* study addressed the influence of the tumour size, simulated by prostate cell clusters, on the efficiency of MHT (Hedayati et al. 2013). These authors concluded that a minimum of 250,000 cells, loaded with 200 pg of iron each, is required to reach 41.3 ºC, the lowest *T* that produced a cytotoxic effect. If translated to an *in vivo* situation, a minimum tumour size of 1 mm^3 would be required for an efficient MHT treatment (Hedayati et al. 2013), which may imply the failure of MHT to treat microscopic tumours or metastasis. These observations are, in fact, in agreement with Rabin's theoretical calculations that show that the "intracellular hyperthermia" concept firstly introduced by Gordon (Gordon et al. 1979) had no biophysical basis, as the cell membranes could not prevent heat conduction (Rabin 2002). Curiously, many of the reported studies do not refer to the concept of intracellular hyperthermia, in the sense that AMF is applied right after adding the magnetic materials to the cells. In fact, for the intracellular version of hyperthermia to be considered, a cells-plus-MNPs-incubation-time is necessary to allow particle's internalization. Therefore, in these studies, the outcome is independent of the interaction of MNPs and cells (e.g. (Maity et al. 2011, Sadhukha et al. 2013a, Qu et al. 2014, Ma et al. 2015, Oh et al. 2016)).

A number of studies combine MHT with chemotherapy in a synergistic way. Alvarez-Berrios et al. tested carboxymethyldextran-coated MNPs to perform MHT in breast (MDA-MB-468), colorectal (Caco-2) and ovarian (A2780) cancer cells lines. Depending on the applied field amplitude, two different T were reached (43 or 45 ºC), consequently yielding two distinct outcomes. In particular, the breast cancer cell line seemed more resistant to the effects of heat. These authors, therefore, potentiated the MHT effects in combination with the proteasome inhibitor, bortezomib (Alvarez-Berrios et al. 2014). To explore the potentiality of IONPs as drug carriers, Quinto *et al.* synthesized phospholipid-PEG coated IONPs loaded with doxorubicin for combined MHT and chemotherapy in a human cervical cancer cell line (HeLa). They observed an additional decrease on cell viability from ca. 55 % to ca. 30 %, still leaving some margin for improvement (Quinto et al. 2015).

Many other authors found lower MHT efficiency in a mono-therapeutic context but explored MHT effects in combination treatments. In this sense, Espinosa *et al.* developed MNPs that generate heat in response to AMF and to laser excitation, the so-called photothermal therapy (PTT). When performing only MHT, the samples reached 40 ºC, resulting in low MHT efficiency (75 % cell viability in a human ovarian cancer cell line, SKOV-3). This effect was potentiated by the bimodal approach that led to an enhancement of the treatment efficiency to only 15 % cell viability due to the higher *T* reached, 50 ºC (Espinosa et al. 2016). The same group had previously developed magnetic liposomes that are also responsive to photodynamic therapy (PDT) due to the inclusion of a photosensitizer agent. Both therapies resulted very effective either alone or in combination (Di Corato et al. 2015). Another example of double-effector MNPs was provided by Yoo *et al.* using MNPs that combine heating ability with enhanced ROS production. Cell viability decreased from 75 to 35 % when passing from mono-therapy to the combined approach (Yoo et al. 2012). In an interesting study, Yin and colleagues enhanced MHT efficiency by combining it with miRNA delivery to promote cell death through apoptosis. MNPs internalization was intensified by magnetofection, a magnetically-promoted incorporation of MNPs into cells. The AMF application resulted in an increase in *T* to 43 ºC, directly resulting in 60 % cell viability. This result was improved to 34 % cell viability in the combination therapy (Yin et al. 2014). Ma *et al.* observed that a static magnetic field can reduce the heating ability of MNPs under an AMF. By combining an alternating with a static magnetic field, these authors reduced the MHT effects in a surrounding area, while restricting the MHT effect to a specific area of interest. Although the reported MHT efficiencies in this *in vitro* study were modest, the proposed strategy shows great potential for *in vivo* applications (Ma et al. 2015).

The *in vitro* studies discussed herein suggest that the MHT efficiency in a mono-therapeutic context may be rather limited, therefore needing to be combined with other therapies to further enhance the treatment's outcome.

Table 2 - Conditions used, and outcome observed, in *in vitro* studies using magnetically-induced hyperthermia alone or combined with chemotherapeutic agents.

Cell line	MNPs			Incubation time (h)	[Fe] sample	MNPs excess removal (Y/N)	Magnetic field			Reported T (ºC)	% Cell viability (h after MHT)	Obs.	Reference
	Coating	Size nm (technique)	Initial conc. ($g \cdot L^{-1}$)				F (kHz)	H ($kA \cdot m^{-1}$)	Time (min)				
A549	-	17.3±8.1 (XRD)	15	1	NR	N	750	0.8	10	47	35 (0) LDH	When using Pt-Fe-HAP for MHT=20% cell viability	(Tseng et al. 2014)
A549; MDA-MB-231	Myristic acid + pluronic F127	12±3 (TEM); ~185 (DLS)	1.5 (Fe_3O_4)	0	NA	N	386	6	5, 15, 30	43–46	~60, ~30, ~10, resp. (2) LDH	Similar efficiency for both cell lines; no colonies formed two weeks after MHT	(Sadhukha et al. 2013a)
DU-145	Starch	~108 (DLS)	0.015, 0.075, 0.1, 0.15 (Fe)	16–24	5, 70, 105, 199 pg/cell, resp.	Y	150	88	30	37–49.1	<10 for T>43ºC (10–14 days) clonogenic survival assay	PDL as facilitator of MNPs uptake; different reached T according to cell pellet size and iron/cell	(Hedayati et al. 2013)
HeLa	Phospho lipid-PEG	~14 (TEM)	0.1 (Fe)	0	NA	N	355	24	60	43–46	~55 (24) MTT	When using DOX-MNPs=32% cell viability	(Quinto et al. 2015)
Jurkat	PMAO-PEG	12, 13 or 16 (TEM); ~20 (DLS)	0.49, 0.6 and 0.6, resp.	0.25	NA	N	373	14	15	38.5, 39.8 and 43.5, resp.	50, 30 and 30, resp. (0.5) ATP levels	If normalized to cells+MNP-AMF, cell viability= 40, 70 and 85%, resp. Optimization of MNP size to enhance MHT	(Khandhar et al. 2012)
KB	Pullulan acetate	~10 (TEM); 25.8±6.1 (DLS)	NR	0	NR	N	100	10.4	20	45 or 47	45ºC=45, 47ºC=20 (24) MTT	L929 (normal) cell viability without AMF application=90%	(Gao et al. 2010)
KB	PEG	19±3 (TEM); 37±11 (DLS)	1 (Fe)	24	25–170 pg/cell 1.3–5.4 g Fe/L	Y	110	20	60	43	0–75 (NR) TB	2–4 g Fe/L to reach 40–45ºC=50% cell viability; at 5 g Fe/L reach 65ºC=0% cell viability	(Guardia et al. 2012)
MCF-7	triethylene glycol: triethanol amine	~44 (TEM)	0.5 (Fe)	0	NA	N	240	89	60	45	25 (48) MTT	Nanoclusters also suitable for MRI i*n vivo*; for the unclustered 10nm MNPs=40% cell viability	(Maity et al. 2011)
MCF-7	MgO	~75 (TEM)	2 mM	2	8 mM	Y	765	20	15	41–45	NR	MNPs cytotoxicity: 2mM=80% and 8mM=55% cell viability (SRB)	(Chalkidou et al. 2011)
MCF-7	Chitosan	20–30 (TEM)	1	0	NA	N	267	24	120	44–45	60 (1) TB	L929 (normal)=93% cell viability	(Thorat et al. 2014)
MCF-7; MCF-7/ADR	mPEG−PCL	~100 (TEM & DLS)	0.2 (MNCs); 0.1 (MNPs)	0	NA	N	114	115	15	NR	10 (24) MTT	$MnFe_2O_4$/MNC *vs.* $Mn_{0.6}Zn_{0.4}Fe_2O_4$/MNC, both with similar MHT efficiencies, in both cell lines. Use low AMF exposure times	(Qu et al. 2014)

Table 2 - Conditions used, and outcome observed, in *in vitro* studies using magnetically-induced hyperthermia alone or combined with chemotherapeutic agents.

Cell line	MNPs			Incubation time (h)	[Fe] sample	MNPs excess removal (Y/N)	Magnetic field			Reported T (ºC)	% Cell viability (h after MHT)	Obs.	Reference
	Coating	Size nm (technique)	Initial conc. ($g \cdot L^{-1}$)				F (kHz)	H ($kA \cdot m^{-1}$)	Time (min)				
MDA-MB-231	PEG bis (amine)	~15 (TEM)	0.2	5	NR	N	500	37.4	60	43±1	75 (NR) WST-8	When using GdTx-MNPs for MHT=36% cell viability (GdTX as sensitizer to MHT)	(Yoo et al. 2012)
MDA-MB-231	Chitosan	~18 (TEM); ~90 (DLS)	1.5 (Mn and Fe)	0	NA	N	307	50 (then to 20 or 35)	30	42 or 52, resp.	22.5 and 18, resp. (24) Annexin-V/Pi	24, 48 and 72h incubation with MNPs yielded 100, 112 and 146 pg Fe/cell; for MHT42 apoptosis and for MHT52 necrosis	(Oh et al. 2016)
MDA-MB-468; Caco-2; A2780	Carboxy methyl dextran	69±4 (TEM)	3.8	0	NA	N	233	29.4 or 34.7	30	43 or 45, resp.	MDA-MB-468 43ºC=50, 45ºC=30; Caco-2 43ºC=35, 45ºC=15; A2780 43ºC=25, 45ºC=5 (48) TB	Reported enhanced effects of bortezomib in combination with MHT (cell viability lower than 20% in all cases).	(Alvarez-Berrios et al. 2014)
SKOV-3	Liposomes	150 (TEM); 200 (DLS)	0.5–5 mM (Fe)	1–4	~20 pg/cell (for the 5mM Fe)	Y	700	24	30	NR	10 (12) AlamarBlue	When combined with PDT=0% cell viability; missing MNP conc. of reported cell viability data	(Di Corato et al. 2015)
SKOV-3	Gallol-PEG	~20 (TEM)	0.2 mM (Fe)	2	~6 pg/cell	Y	520	20	10	38–40	75 (NR) AlamarBlue	When combined with PTT=15% cell viability and T=50 ºC	(Espinosa et al. 2016)
SMMC-7721	-	17±2 (TEM)	1	0	NA	N	50	34	40	42, 44 and 44.3	75.4, 61.5 and 53.6 (24) MTT	Application of a static magnetic field to limit the heating to a restricted area	(Ma et al. 2015)
U87-EGFRvIII	PEI	77±11 (DLS)	0.01	5	NR	Y	225	5	45	44.1	60 (24) MTS; 80 in spheroids	Magnetofection was used to facilitate MNPs uptake; if combined with let-7a miRNA=34% cell viability (45% in spheroids)	(Yin et al. 2014)

NA – not applicable; NR – not reported; resp. – respectively
TEM – transmission electron microscopy; DLS – dynamic light scattering; XRD – x-ray diffraction; MNCs – magnetic nanoclusters; MNPs – magnetic nanoparticles; HAP – hydroxyapatite
PEG – poly(ethylene glycol); PEI – poly(ethylenimine); PMAO - poly(maleic anhydride-alt-1-octadecene); mPEG-PCL - monomethoxy-terminated poly(ethylene glycol)-b -poly-(ε-caprolactone)
Cell viability tests – TB – trypan blue exclusion; MTT - 3-(4,5-dimethylthiazol-2-yl)-2,5-diphenyltetrazolium bromide reduction; MTS - 3-(4,5-dimethylthiazol-2-yl)-5-(3-carboxymethoxyphenyl)-2-(4-sulfophenyl)-2H-tetrazolium reduction; SRB – sulforhodamine B binding; WST-8 - 2-(2-methoxy-4-nitrophenyl)-3-(4-nitrophenyl)-5-(2,4-disulfophenyl)-2H-tetrazolium reduction
PDT – photodynamic therapy; PTT – photothermal therapy.

2.3.2. *In vitro* targeted MHT studies

Molecular targeting, along with the surface-receptor expression levels, has been described as the main factor affecting MNPs binding to cells in an *in vitro* situation (NDong et al. 2015). The overexpression of some surface-receptors in cancer cells compared to normal cells allows differential interaction of MNPs directed to that receptor by means of an antibody, a peptide sequence, or a ligand protein, a concept known as active targeting. In this sense, the preferential accumulation (and possible internalization) of MNPs in cancer cells provides a robust strategy to kill cancer cells with minimal predicted effects in normal cells. Table 3 collects some features of *in vitro* studies directed to selected cancer targets.

Liao *et al.* developed alginate-coated IONPs functionalized with D-Galactosamine (D-Gal), to specifically target liver cancer cells. These authors observed enhanced MHT efficiency of targeted, compared to non-targeted, MNPs in HepG2 cells, decreasing cell viability levels from 60 %, with non-targeted, to an impressive 5 % with D-Gal-MNPs (Liao et al. 2015). Unfortunately, a correlation between the observed outcome and the *T* reached during MHT cannot be established due to lack of data concerning the observed *T*. Moreover, some doubts remain concerning this particular targeted strategy, as some studies report the asialoglycoprotein receptor, to which D-Gal binds to, to be widely expressed in normal hepatocytes (Shi et al. 2013). Similarly high MHT efficiency was observed in a study using very low MNPs' concentration for MHT mediated by Luteinizing Hormone–Releasing Hormone (LHRH)-targeted MNPs (Taratula et al. 2013). In this case, the samples reached 44 ºC and a 5 % cell viability rate of ovarian cancer cells expressing the LHRH receptor was reported. Interestingly, significantly lower internalized iron amount was necessary in this study (ca. 15 pg Fe/cell), as opposed to the previous one (ca. 365 pg Fe/cell) (Liao et al. 2015), to lead to such prominent effect. This fact can be a consequence of the different number of cells used in the experiments (5× higher in (Taratula et al. 2013)) and/or possible distinct surface expression levels of each receptor.

The folate receptor is a promising target for cancer treatment as it appears to be overexpressed in many cancer types with limited expression in healthy tissues (Zwicke et al. 2012). Some groups have been investing in the development of MNPs functionalized with folate/ folic acid for actively targeted MHT in recent years (Sivakumar et al. 2013, Sadhasivam et al. 2015, Gupta et al. 2016). The reported outcomes were very distinct, ranging from 20–65 % cell viability levels, with no reference to the achieved *T* (Sivakumar et al. 2013, Gupta et al. 2016), which hampers comparisons and prevents conclusions regarding MHT efficiency. In any case, these authors found improvements to their strategy

when combined with chemotherapeutic drugs, either 5-fluouracyl (Sivakumar et al. 2013), or doxorubicin (Gupta et al. 2016). A study by Sadhasivam *et al.* describes a significant increase in lactase dehydrogenase (LDH) leakage, compatible with cell death, for ovarian cancer cells (HeLa) reaching 43–45 ºC after a 10-min AMF application (Sadhasivam et al. 2015). Interestingly, normal fibroblasts were not affected under similar conditions.

The human epidermal growth factor receptor 2 (HER2, also known as ERBB2) is an oncogene found to be overexpressed in nearly 20–30 % of the breast tumours. $HER2^+$ breast cancers are recognised as more aggressive and more deadly, with improved prognosis since Trastuzumab, a blocking antibody, was introduced in the clinical context [reviewed in (Mitri et al. 2012)]. Therefore, targeting the HER2 receptor for MHT studies seems a promising approach that some research groups have been developing (Ito et al. 2004, Zhang et al. 2011, Mi et al. 2012). These studies have used the same breast cancer cell model, SK-BR-3, known to overexpress the HER2 receptor, and tested MNPs with resembling sizes (100–150 nm), providing an opportunity for comparison. Widely distinct outcomes were reported, attaining 25–60 % cell viability, depending on the AMF conditions and *T* reached. While Zhang *et al.* reported keeping the *T* around 37 ºC by the application of an intermediate AMF power, leading to a modest decrease to 60 % cell viability (Zhang et al. 2011), Ito and co-workers' study using lower AMF power, observed a *T* rise to 42.5 ºC consequently showing significantly higher efficiency (down to 25 % cell viability) (Ito et al. 2004). In the study performed by Mi *et al.* the concept of "targeting" may be controversial, because the excess of free MNPs was not removed prior to MHT (Mi et al. 2012). Therefore, in this particular situation, the MHT effect (30 % cell viability) cannot be solely attributed to the targeting strategy, as it depended not only on the bound MNPs but also on the ones that remained in suspension. It is, therefore, expectable that applying the same treatment to normal cells (i.e., with low or absent HER2 positivity) may lead to similar cytotoxic outcome. Unfortunately, this is not the only study in which there has been this misunderstanding. Although some studies provide information on the behaviour of normal cells exposed to similar MHT conditions (Sadhasivam et al. 2015, Thomas et al. 2015), others fail to remove the excess of MNPs primarily incubated with cells without testing normal cells (Mi et al. 2012, Sivakumar et al. 2013, Kruse et al. 2014). This fact may have serious implications on the observed outcome that may, therefore, be fallaciously enhanced by the presence of MNPs that are not necessarily interacting with the cells. Thomas *et al.* targeted the CD44 receptor, in SCC7 murine cells, using hyaluronic-acid-conjugated MNPs. The *T* increase to 42 ºC during 10 min led to interesting MHT efficiency (30 % cell viability) while keeping normal (CD44 negative) cells undamaged (Thomas et al. 2015). Noteworthy for future studies, Kruse *et al.* used

CREKA—a tumour homing peptide—functionalized MNPs to target the fibrin-associated plasma proteins mostly present in the interstitial space within tumours. These authors reported additive effects when combining the chemotherapeutic agent, cysplatin (Kruse et al. 2014).

Other interesting targets that have been tested for targeted MHT include the cancer stem cell marker, CD90 (Yang et al. 2016), the $\alpha\vee\beta3$ integrin receptors (Shah et al. 2014), and EGFR (Domenech et al. 2013). Yang and co-workers used antibody-functionalized MNPs to target the CD90 receptor in cancer stem cells and to separate them from the CD90 negative counterparts using magnetic-activated cell sorting (MACS). The cells targeted with MNPs were then submitted to a 1-h AMF application leading to increased *T* (44 ºC) and 30 % cell viability. These authors suggested that these MNPs, reported as thermosensitive magnetoliposomes, are also suitable for MRI purposes (Yang et al. 2016). Shah and colleagues proposed targeting $\alpha\vee\beta3$ integrin receptors in glioblastoma cells (U87MG) using MNPs functionalized with tumour homing peptide, iRGD (arginine-glycine-aspartic acid). The MNPs' uptake was enhanced using magnetofection and the MHT was proposed as a strategy to enhance the intracellular delivery of a mitochondria-targeting pro-apoptotic peptide. The reached *T* was not reported and cell viability levels decreased to 40 % in the combined treatment, which corresponds to a discrete increase of the effect obtained in the absence of MHT (Shah et al. 2014), leaving margin for some criticism on whether a "magnetic hyperthermia" effect was effectively observed.

The EGFR is a well know target in many cancer treatment modalities, being the first cancer target against which monoclonal antibodies were developed, cetuximab and panitumumab, to be used in metastatic colorectal and head and neck cancer therapy (Martinelli et al. 2009). Domenech *et al.* have taken advantage of the overexpression of this receptor in breast cancer cells to test MNPs conjugated to its natural ligand, the epidermal growth factor (EGF), for MHT purposes. A 25 % decrease in cell viability was reported for cancer cells targeted with EGF-MNPs and submitted to an AMF for 1h, without significantly damaging normal cells that followed the same protocol. Temperature changes were not reported (Domenech et al. 2013). A previous study from the same group targeted EGFR using MNPs conjugated to an anti-EGFR antibody observing a prominent reduction of cell viability to 5 % after AMF application during 2 h. In this report, a *T* rise was not detected and the authors hypothesized the effects to be due to the rotation of the MNPs under the AMF that led to mechanical damage. Also noteworthy in this study, the targeted MNPs exhibited significant cytotoxicity even without AMF application (down to 40 % cell viability), which decreases the contribution of the AMF effect to the observed outcome (Creixell et al. 2011).

As for the non-targeted MHT *in vitro* studies, the targeted MHT strategies described herein showed limited treatment efficiency, which could be enhanced by a combination with chemotherapeutic drugs. In fact, for the only study performed in GBM cells, targeted-MHT efficacy was limited to a 60 % reduction in cell viability. Noteworthy, studies in normal cells are lacking to assure the treatment's selectivity and safety, as less than one third of the studies tested the same targeted strategy in normal (control) cell lines.

Table 3 - Conditions used, and outcome observed, in *in vitro* studies using targeted magnetic hyperthermia alone or combined with chemotherapeutic agents

Functionalization	Cell line	MNPs			Incubation time (h)	[Fe] sample	MNPs excess removal (Y/N)	Magnetic field			Reported T (ºC)	% Cell viability (h after MHT)	Obs.	Reference
		Coating	Size (nm)	Initial conc. ($g \cdot L^{-1}$)				F (kHz)	H ($kA \cdot m^{-1}$)	Time (min)				
Anti-CD90[a]	Huh7	PEG	10–20 (TEM); 130±4.6	0.34 (Fe)	1	NA	Y	200	NR	60	44	30 (24) MTT	Thermosensitive magnetoliposomes; $CD90^+$ separated from $CD90^-$ by MACS and then treated with MHT	(Yang et al. 2016)
Anti-EGFR[a]	MDA-MB-468; MCF-7	Carboxy methyl dextran	14±3 (TEM); 78±8 (DLS)	5.0	1, 6, 10	13–21 pg/cell	Y	233	37.5	120	ND	5 (120) TB	T rise not detected; cell viability with EGF-MNPs<40%	(Creixell et al. 2011)
CREKA[b]	A549	Dextran	5–13 (TEM);	3 (Fe_3O_4)	NA	NA	N	292	58	30	NR	40 (48 & 72) Calcein-AM	Incubation suspended cells+NP; reported additive effects of cysplatin to 20% cell viability after 72h	(Kruse et al. 2014)
EGF[a]	MDA-MB-231	Carboxy methyl dextran	61±29 (DLS)	0.3 (Fe_3O_4)	2	1.75 pg/cell	Y	233	42	60	Kept below 37	75 (48) CellTiter-Blue	184-B5 (normal) cell viability unchanged. Reported the effects to derive from ROS production	(Domenech et al. 2013)
Folate[b]	MCF-7; G1	Carboxy methyl cellulose	100–150 (TEM); 80–200 (DLS)	2 and 4	NA	NA	N	305	18	60	NR	20 (24) TB	If combined with 5-FU=5% cell viability	(Sivakumar et al. 2013)
Folate[a]	HeLa (FR+)	PEG	84.9 (TEM)	0.5	1	0.3 $g \cdot L^{-1}$	N	750	0.8	10	43–45	-	Reported LDH values of 0.76 compared to 0.45 for untreated control; human fibroblasts not affected	(Sadhasivam et al. 2015)
Folic acid[b]	HeLa	Poly acrylic acid	8–10 (TEM)	2	24	≈250 pg/cell (24h inc. w/ 0.3 $g \cdot L^{-1}$)	Y	265	27	10	NR	65 (24) SRB	When using DOX loaded FA-MNPs=50% cell viability; DOX-FA-MNPs+AMF=10% cell viability	(Gupta et al. 2016)
Galactose[a]	HepG2	Alginate	109.1–146.9 (HD)	0.5	4	364.4 pg/cell	Y	780	19	20	NR	5 (18) MTT	Only applicable for hepatic tumours	(Liao et al. 2015)

Table 3 - Conditions used, and outcome observed, in *in vitro* studies using targeted magnetic hyperthermia alone or combined with chemotherapeutic agents.

Functionalization	Cell line	MNPs			Incubation time (h)	[Fe] sample	MNPs excess removal (Y/N)	Magnetic field			Reported T (ºC)	% Cell viability (h after MHT)	Obs.	Reference
		Coating	Size (nm)	Initial conc. ($g \cdot L^{-1}$)				F (kHz)	H ($kA \cdot m^{-1}$)	Time (min)				
Herceptin[a]	SK-BR-3	Dextran	138±7.6 (DLS)	28.6 pg Fe_3O_4/ cell	4	16.5 pg Fe_3O_4/ cell	Y	360	9.6	30	42.5	25 (24) TB	Cell viability recovered after 5 days in culture. When AMF was repeated 24h after, cell viability <10% after 5 days	(Ito et al. 2004)
Herceptin[a]	SK-BR-3	Dextran	≈100 (DLS)	0.1	3	≈28 pg/cell	Y	163	35.8	20	Kept below 37	60 (6) Live-dead kit	HMEC (normal) cells >90% cell viability	(Zhang et al. 2011)
Herceptin[b]	SK-BR-3	PLA-TPGS/ TPGS-COOH	155.2±0.17 (DLS)	0.86; (177ug Fe)	24	NA	N	240	42	20 or 30	NR	30 (12) MTT	If combined with docetaxel=10% cell viability	(Mi et al. 2012)
Hyaluronic acid[a]	SCC7 (CD44+)	None *vs.* PEG	10–20 (TEM); 81–272 (DLS)	0.1	1	NA	N	368	1	10	42	30 (24) MTS	For SAR experiments, $2g \cdot L^{-1}$ reached 42ºC; CD44- cell viability unchanged	(Thomas et al. 2015)
iRGD[b]	U87-EGFRvIII; MDA-MB-231	PEI+ PEG	46.8±2.3 (DLS)	0.02	24	NR	Y	300	5	45	NR	40 (48) MTS	Magnetofection to facilitate MNPs uptake; MHT as enhancer of peptide therapeutics	(Shah et al. 2014)
LHRH peptide[b]	A2780/AD	PMAO+ PEI+ PEG	≈40 (TEM) ≈90 (DLS)	0.015 (Fe)	12	14.9 pg/cell	Y	393	33.5	30	44	5 (48) Calcein-AM	Similar cell viability achieved with DOX loaded LHRH-MNPs combined with MHT at 40ºC	Taratula et al. 2013)

NA – not applicable; ND – not detected; NR – not reported;
TEM – transmission electron microscopy; DLS – dynamic light scattering; MACS – magnetic-activated cell sorting; MNPs – magnetic nanoparticles
LHRH – Luteinizing Hormone–Releasing Hormone
PEG – poly(ethylene glycol); PEI – poly(ethylenimine); PMAO - poly(maleic anhydride-alt-1-octadecene); PLA-TPGS - poly(lactide)-D-a-tocopheryl poly(ethylene glycol) succinate; TPGS-COOH – carboxyl group-terminated TPGS;
Cell viability tests – TB – trypan blue exclusion; MTT - 3-(4,5-dimethylthiazol-2-yl)-2,5-diphenyltetrazolium bromide reduction; MTS - 3-(4,5-dimethylthiazol-2-yl)-5-(3-carboxymethoxyphenyl)-2-(4-sulfophenyl)-2H-tetrazolium reduction; SRB – sulforhodamine B binding
[a]Monotherapeutic context
[b]Combination with chemotherapeutic agents

2.4. *In vivo* MHT studies

In vivo studies on MHT refer to the use of MNPs that are injected into *in vivo* animal models previously inoculated with tumorigenic cells, which grow into tumours in a few days. Besides the different types and configurations of MNPs used (individual or organized in clusters or sticks), and the different tumours to treat (origin, size), variations are also found in the route of administration, normally intratumoural (IT) or intravenous (IV) injection. The administration route leads to differential distribution and accumulation of the magnetic materials, and a balance needs to be found between the effective tumour treatment and the appearance of secondary effects due to particle accumulation in vital organs, such as the liver, spleen and lungs. A collection of the most relevant aspects of some *in vivo* studies is provided in Table 4.

Andreas Jordan and co-workers successfully treated malignant rat gliomas using magnetic hyperthermia (Jordan et al. 2006). They administered aminosilane-coated MNPs by IT injection and controlled the applied AMF to produce an increase in tumour's *T* to 43–47 ºC, in two AMF applications. The reported outcomes varied from a 1.7 to a 4.5× increase in the mean survival of the treated rats, respectively, depending on the reached intratumoural *T*. Interestingly, these authors tested, similarly and in parallel, dextran-coated MNPs that spread into the surrounding tissue shortly after MNPs injection, leading to inefficient tumour heating. On the other hand, the authors claim the aminosilane MNPs to specifically interact with the tumour cells forming deposits that allow consecutive MHT treatments after MNPs injection (Jordan et al. 2006). Ohno *et al.* had previously reported similar results with the same *in vivo* model using carboxymethylcellulose-coated MNPs, organized in a thin stick-type, directly introduced in the tumour, also a glioma. An average 3× increase in the mean rat's survival was observed using a 3-cycle protocol reaching 44.4 ºC (Ohno et al. 2002). Drake *et al.* also performed a 3-cycle protocol in an *in vivo* MHT study using dextran-coated MNPs in BALB/c mice bearing colon tumours. They observed a significant 80 % reduction in the tumour's size by day 3 post-MHT, and a delay in tumour's growth after this time-point. Unfortunately the reached *T* was not reported.

Huang *et al.* successfully treated squamous cell carcinomas inoculated in NCr nude mice with a tumour ablation efficiency of 78–90 %, without reporting secondary effects. The intravenously injected PEGylated MNPs accumulated with a 16:1 tumour to non-tumour surroundings ratio, and the application of high power AMF led to an increase in the tumours' *T* to 60 ºC in 2 min (42 ºC in the muscle that accumulated MNPs). These authors defended that the rapid increase to an ablative *T*, compared to longer heating periods at

lower *T*, protects the tumour surroundings from heat dissipation, decreasing the probability of secondary effects (Huang and Hainfeld 2013). A major concern regarding IV injection strategies may be the high accumulation of MNPs in the liver (higher than the tumour), which limits the treatment of tumours located in the vicinity of this organ.

Contrasting with the previous study that defended rapid tumour ablation, Yang *et al.* observed complete tumour elimination in 27 % of the MHT treated mice, 70 days after IT injection with non-targeted MNPs. Three AMF cycles were necessary to achieve this result. Notably, when using anti-CD90 targeted MNPs, instead of the non-targeted ones, a significant increase to 78 % complete tumour elimination was observed. The tumours in this study were formed from liver cancer stem cells ($CD90^+$) isolated from a hepatocellular carcinoma cell line by MACS. Therefore, the authors claim MHT to be efficient in cancer stem cell elimination (Yang et al. 2016), showing that, if overall magnetic content would not be an issue for effective MHT (Hedayati et al. 2013), it would be useful for elimination of isolated cells that may spread from the tumour. Also using targeted MNPs, Baldi *et al.* used an EGFR-targeted nanocarrier for *in vivo* hyperthermia purposes and found a 1.7× increased mean survival of the treated animals, after five successive IT injections and AMF application cycles (Baldi et al. 2014). Unfortunately, this study lacks statistical power due to the very small size of the animal groups. Sadhukha and co-workers also reported on the use of EGFR-targeted MNPs (using a peptide) with a very peculiar application: to be inhaled for the localized treatment of lung cancer with MHT. Bioluminescent tumours were generated, using luciferase-transfected-A549 cells, and tumour growth was followed through the luminescence signal. After inhalation, the MNPs were allowed to target and redistribute within the lungs, before a single MHT cycle was performed during 30 min, which resulted in a significant impairment in tumour growth rate (Sadhukha et al. 2013b). Although *T* and overall MNPs dosage details are not provided, this seems a very interesting and promising approach for the local treatment of lung cancer.

The accumulation efficiency of passive *vs.* active targeting was compared by Xie *et al.* using PEG-phospholipid MNPs (either non-targeted or RGD-modified) as an *in vivo* theranostic agent, i.e., as a contrast agent for MRI and as a heating agent for MHT. Interestingly, they found that one single IV injection dose of MNPs does not result in accumulation of enough magnetic material to produce tumour heating. Therefore, 6 repeated IV injections were performed followed by 15 MHT 30-min-sessions, which resulted in a delay in tumour growth. This discrete outcome is related to the insufficient tumoural heat reported, derived from poor MNPs accumulation within the tumour (Xie et al. 2016). This fact can be related to the targeting strategy itself, which aims at the tumour vasculature instead of the tumour cells. This study provides a true example of the

difficulties encountered to reach satisfactory tumour accumulation of MNPs, after IV administration, so that enough heat is generated locally for an efficient MHT treatment. Other authors have previously reported on the challenges of effective MNPs' delivery to the entire tumour with active targeting (Kirpotin et al. 2006, Pirollo and Chang 2008).

The combination of MHT with other therapeutic strategies was also tested in and *in vivo* context. Yoo and co-workers conducted an experiment in nude mice bearing breast tumours submitted to a 30-min AMF application (1 cycle) that heated the tumours to 43 ºC. These authors found that, although the tumour's size initially regressed after MHT, it would still regrow after some days because tumour elimination was not complete. Therefore, they developed MNPs combined with an agent that depletes the reducing metabolites in cancer cells, GdTX, predisposing them to the damaging effects of ROS, and leading to complete apoptotic tumour regression 8 days after MHT (Yoo et al. 2012). Combining MHT with gene therapy targeting α-fetoprotein in human liver carcinomas, Yuan *et al.* reported a more than 90 % reduction in the tumour size, relative to control, 28 days after a 2-cycle MHT treatment that increased the tumour's *T* to more than 42 ºC for nearly 50 min. Consistently with a synergistic effect, the combined therapy was significantly more efficient than each therapy independently (Yuan et al. 2014). Worth mentioning, although controlled tumour growth was possible in this study, complete tumour elimination was not found, which may result in tumour relapse at longer time-points.

A group from Japan was the first to describe anti-tumour immunity after magnetically-induced hyperthermia treatment. They implanted two glioma tumours in opposite flanks of the same rat and injected magnetic cationic liposomes (MCLs) in only one of them. Twenty-eight days after the treatment, which caused the tumour's *T* to increase to 45 ºC, both tumours had disappeared. They verified that the hyperthermia treatment to one of the tumours led to the recognition of tumour antigens by the rat's immune system (Yanase et al. 1998). Later, Kawai *et al.* also described anti-tumour immunity in their attempts to treat prostate cancer induced in rats, also using MCLs. The 30 min-application of an AMF raised the intratumoural *T* to 45 ºC and inhibited tumour growth. They reported the presence of immunocytes in the tumours of treated rats, which may have been recruited by the release of HSP70 from the treated cells (Kawai et al. 2005). More recently, Toraya-Brown and co-workers showed that the hyperthermia-induced immunologic response might be *T* dependent (Toraya-Brown et al. 2014). In fact, and in disagreement with the previous studies (Yanase et al. 1998, Kawai et al. 2005), when primary tumours were heated to 45 ºC for 20 min, although complete tumour destruction was observed, the secondary tumour continued to grow like in the control mice. On the other hand, heating

the primary tumour to 43 ºC for 30 min produced complete, or incomplete but significant—depending on the type of tumour and mice—tumour elimination. At the same time, the secondary tumour's growth rate decreased as a result of the intense immunostimulation, in particular $CD8^+$ T-cells recruitment and activation (Toraya-Brown et al. 2014).

In most of the *in vivo* studies described herein, MHT resulted in increased animal survival due to decreased tumour growth. This incomplete tumour regression seems to be related to inhomogeneous distribution of the MNPs after the IT injection. In agreement with the *in vitro* studies, combination of MHT with another treatment modalities resulted in enhanced efficacy. The few studies reporting complete tumour elimination corresponded to the cases in which temperatures equal to or above 45 ºC led to complete cell destruction.

Only a fifth of the *in vivo* studies described in this review refer to the use of targeted MNPs, while only one seventh use the IV route for MNPs injection, evidencing the need for more *in vivo* studies addressing these issues.

Table 4 - *In vivo* studies using passive or active targeted anti-cancer MHT

Cell line (number of cells)	*In vivo* model	Initial tumour size	MNPs			MNPs inj. mode	Magnetic field					T (ºC)	Outcome	Obs.	Reference
			Coating	Size (nm)	Initial amount		Time after inj.	F (kHz)	H ($kA \cdot m^{-1}$)	Time (min)	Cycles				
Human breast cancer MDA-MB-231 (NR)	NR (nude mice)	100 mm^3	PEG bis (amine)	~15 (TEM)	75 µg MNPs	IT	0	500	37.4	30	1	43	Incomplete tumour regression day 8; tumour regrowth day 12	When using GdTx-MNPs for MHT = tumour eliminated within 8 days	(Yoo et al. 2012)
Human chronic myeloid leukaemia K562/A02 (1×10^7)	BALB/c mice	950±150 mm^3	Oleic acid + Pluronic F-127	18.4± 1.8 (TEM)	22 µg MCLs/g body weight	IT	0	219	10.5–310	40	1	~42	40 % decrease relative tumour volume	If combined with DNR + 5-BrTet=80 % decrease relative tumour volume and decreased P-gp expression	(Ren et al. 2012)
Human epidermoid carcinoma A431 (5×10^6)	SCID female mice	200–400 mm^3 (calc.)	PLGA-*b*-PEG	77.8± 2.1 (DLS)	400–800 µL of 4.5 mg Fe_3O_4/mL, days 16,17,18, 19,and 22	IT	0	173	25	30	5	5–6 inc.	1.7× inc. MS	hEGFR-targeted MNPs; observed increased T in subsequent treatments; *in vivo* biodistribution after IV injection shows higher accumulation in the liver and lungs, than tumour	(Baldi et al. 2014)
Human hepato carcinoma HepG2 (1×10^6)	BALB/c female mice	50 mm^3	PEI	20–30 (TEM)	1 mg MNPs/ cm^3 tumour	IT	0	230	NR	60	2	42–44	~70 % or ~92 % reduction tumour volume 28 days after MHT, resp. MHT and MHT+gene therapy	Combination of MHT with gene therapy targeting α-fetoprotein in hepatocarcinoma	(Yuan et al. 2014)
Human liver cancer stem cells Huh7 $CD90^+$ (2×10^4)	NOD/ SCID mice	600 mm^3	PEG	10–20 (TEM); 130±4.6	NR	IT	24 h	200	NR	60	3	NR	27.3±9.8% complete tumour regression 70 days after injection	When using Anti-CD90-MNPs=78±19.1% complete tumour regression 70 days after injection; rectal T<40ºC	(Yang et al. 2016)
Human lung squamous carcinoma A549-Luc (1×10^6)	Fox Chase SCID female mice	0.5×10^6 photons/s	Myristic acid + pluronic F127	369±34 (DLS)	NR	IH	7 days	386	6	30	1	NR	Reduction in tumour growth rate over 1 month after MHT; reduced tumour weight	No significant side effects; inhalation led to higher tumour MNPs accumulation than other organs	(Sadhukha et al. 2013b)
Mouse breast cancer 4T1 (5×10^6)	BALB/c female mice	50–80 mm^3 (calc.)	PEG	54.6 (DLS)	6×30 µg Fe/g body weight (every other day)	IV (tail vein)	30 min	390	2.6	30	15	Passive: 38.7–42.5; Active: 39.6–44.1	59 % apoptotic cells; delayed tumour growth	Passive *vs.* active targeting ($\alpha\vee\beta3$ integrin –targeted MNCs); studied bioaccumulation in the main organs; combined MRI and MHT; no obvious toxicity	(Xie et al. 2016)
Mouse colon carcinoma CT-26 (1×10^6)	BALB/c mice	200–300 mg (calc.)	Dextran	13.2± 3.1 (TEM)	0.2 mL of 16 $g \cdot L^{-1}$	IT	0	52	20	30	3	NR	Day 3: reduced size by 20 %; day 10: 500 mg	Day 3: CT doubled size; day 10: CT 1500 mg	(Drake et al. 2007)

Table 4 - *In vivo* studies using passive or active targeted anti-cancer MHT

Cell line (number of cells)	*In vivo* model	Initial tumour size	MNPs			MNPs inj. mode	Magnetic field					T (ºC)	Outcome	Obs.	Reference
			Coating	Size (nm)	Initial amount		Time after inj.	F (kHz)	H ($kA \cdot m^{-1}$)	Time (min)	Cycles				
Mouse colon carcinoma CT-26 (1×10^5) or mouse melanoma B16F10 (1.25×10^5)	BALB/c or C57BL/6 mice	5×6 mm (2 tumours/ mouse)	BNF-Starch	100 (TEM)	140 µg Fe	ID	0	167.5	36–44	20 or 30	1	42.5–43 for 30 min; 44.5–45 for 20 min	43ºC = Complete elimination of treated CT26 tumour in BALB/c in 5 days + untreated tumour grew slower than CT; incomplete elimination of treated B16 tumour in C57BL/6 + untreated tumour grew slower than CT; 45ºC = complete elimination of treated B16 tumour in C57BL/6 + no effect in the untreated tumour	Hyperthermia-induced immunologic response at 43 but not at 45ºC; immunologic response was not observed for Lewis lung carcinoma tumours, even at 43ºC; rectum T=35.5–37ºC	(Toraya-Brown et al. 2014)
Mouse squamous cell carcinoma SCC7 (2×105)	NCr nude mice	~150 mm3	PEG	11.3± 2.3 (TEM) 23.8± 0.1 (DLS)	1.7 g Fe/Kg body weight	IV (tail vein)	24 h	980	38	2	1	60	Complete tumour ablation in 78–90 % cases	Muscle w/ MNPs T=42ºC; Muscle w/o MNPs T= 36ºC; Liver uptake > tumour's; 16:1 MNP ration tumour to non-tumour	(Huang and Hainfeld 2013)
Rat prostate cancer PLS10 (1×10^6)	F-344 Fisher male rats	5–6 mm	Lipid membrane[a]	10 nm (TEM)	2 g MCLs	IT	30 min	118	30.6	30	1	45	Suppressed tumour growth; no disappearance	Rectum T=38ºC; reported anti-tumour immunity (CD4, CD8 activation)	(Kawai et al. 2005)
Rat glioma RG-2 (1×10^5)	F-344 Fisher male rats	3–4 mm	Aminosilane	15 (TEM)	20 µL of 2 mol Fe/L	IT	0	100	18 max	40	2	43–47	1.7–4.5× inc. MS, depending on T	Rectum T=36–37ºC	(Jordan et al. 2006)
Rat glioma T-9 (1×10^7)	F-344 Fisher female rats	13–18 mm	Lipid membrane[a]	10	3 mg Fe_3O_4	IT	24 h	118	30.6	30	3	43	89 % complete treated tumours regression + complete regression of untreated tumours; no tumour regrowth during 3 months	2 tumours implanted per rat, only one received MCL and AMF, both disappeared. Long-lasting anti-tumour immunity was reported; rectum and other tumour T=35–37ºC	(Yanase et al. 1998)
Rat glioma T-9 (5×10^6)	F-344 Fisher female rats	NR (eighth day)	Carboxy-methyl cellulose	NA	3.3 mg Fe_3O_4	IT	24 h	89	30	30	3	44.4	3× inc. MS (44.2±10.9 *vs.* 14.4±1.5 of the CT)	Rectum T did not change; a variation of MNPs is used, named "stick-type magnetite"	(Ohno et al. 2002)

[a]Lipid membrane: N-(a-trimethylammonioacetyl) didodecyl-D-glutamate chloride, dilauroylphosphatidylcholine and dioleoylphosphatidylethanolamine at a molar ratio of 1:2:2

NR – not reported; CT – control; -Luc – Luciferase transfected; TEM – transmission electron microscopy; DLS – dynamic light scattering; MACS – magnetic-activated cell sorting; MNPs – magnetic nanoparticles; MCLs – magnetite cationic liposomes; DNR, daunorubicin; 5-BrTet, 5-bromotetrandrine; LHRH – Luteinizing Hormone–Releasing Hormone

PEG – poly(ethylene glycol); PEI – poly(ethylenimine); PLGA - poly(D,L-lactide-co-glycolide)

Administration routes: IT – intratumoural; IV - intravenous; IH – inhalation; ID – intradermal

2.5. Clinical studies

The first clinical trials testing MHT to treat cancer were performed in Japan in the 90's, using metallic implants consisting of FePt alloys. The magnetic heaters were locally implanted into gliomas of 24 patients during surgery or stereotactically, and heated under a 240 kHz AMF, for 60 min, two to three times a week, in combination with external irradiation and, eventually, chemotherapy. The treatment efficiency depended on tumour localization with tumours located in the thalamus or the basal ganglia responding better (45.5 % of the cases) than the ones located in the cortical or subcortical region (23.1 % of the cases) (Kobayashi and Kida 1990).

The subsequent clinical studies took place nearly fifteen years after, in Europe, under Jordan's A. supervision, and already used MNPs as heat mediators (aminosilane-coated MNPs) for the treatment of locally recurrent prostate cancer or recurrent GBM (Johannsen et al. 2005, Johannsen et al. 2007, Maier-Hauff et al. 2007, Maier-Hauff et al. 2011). A study including 22 patients with many different types of solid tumours found some limitations in MHT application, namely the insufficient increase in *T* and inhomogeneous MNPs distribution. On the other hand, this study showed that the MNPs stay in the injection site for at least a month, what would allow repetition of the AMF application in cycles (Wust et al. 2006). In parallel, a phase I clinical trial studied the feasibility, toxicity and quality of life in 10 prostate cancer patients, with IT injected MNPs, weekly receiving an AMF cycle (100 kHz, 2–15 kA/m, 60 min) for six weeks (Johannsen et al. 2007). Hyperthermic to ablative intratumoural *T* were reached (up to 55 ºC), which sometimes resulted in heating of adjacent tissues up to 44 ºC causing some discomfort manageable with local cooling. The small number of participants in the study and the disparities between the patients' characteristics prevented taking clear conclusions on the MHT outcome. Low systemic toxicity was observed and the quality of life was temporarily impaired during, and up to three months after, MHT. The authors concluded that, although feasible, the technique required further refinements, including a combination with radiotherapy, which was not addressed in this study (Johannsen et al. 2007).

The first trial attesting the feasibility and tolerability of nanoparticle-induced MHT on recurrent GBM treatment included 14 patients that received 0.1–0.7 mL of MNPs intratumourally, and were subjected to 4–10 AMF cycles. The resulting intratumoural *T* consequently varied from 42.4–49.5 ºC, with minor or no side effects reported (Maier-Hauff et al. 2007). Later, the efficacy and safety of MHT for GBM treatment was established, in combination with radiotherapy, in a complex study with 59 patients. The aminosilane-coated MNPs were instilled into the tumour, under neuro-navigational control,

along with a thermometry catheter to monitor intratumoural *T*. The amount of injected MNPs varied with the tumour size (assessed by computed tomography (CT) scan in the beginning of the study), and the median peak *T* reached 51.2 ºC. The MHT treatment, always combined with radiotherapy, resulted in a gain in the mean overall survival after recurrence of 7.2 months, and of 8.6 months in the mean overall survival after first diagnosis, both considered "remarkable" by the authors. Regrettably, forty-seven of the 59 patients died within the course of the study. The reported adverse side effects were described as "moderate" and varied from sweating and general sensation of warmth, to tachycardia, headaches and convulsions (Maier-Hauff et al. 2011). Such complex studies, dealing with such limited patient prognosis, seem very difficult to accomplish.

MagForce is currently developing another clinical trial in Germany to further establish the efficacy of MHT in GBM treatment (MagForce 2016b). There seems to be one more on-going clinical trial on MHT ("unknown" status, not verified in more than two years), which aims at studying the fate of MNPs after IT injection on prostate cancer patients with a previously planned surgery to remove their tumours (NIH 2014). The authors will use MRI and CT to assess MNPs location, and also histologically analyse the tumour specimens after surgery. In case the MNPs remain at the injection site, then the next step will be running a similar study in which the MHT treatment is actually performed as cancer therapy.

No studies with targeted MNPs or IV injection of MNPs have been clinically developed, so far, leaving the door open for future improvements in MHT for cancer treatment.

2.6. Final considerations

The use of MHT for the treatment of cancer is currently a reality, in particular for GBM.

While some of the *in vitro* studies discussed herein show very appealing results, testing new and refined materials for increased heating abilities and low cytotoxicity, others show limited efficacy suggesting that improvements can be made. The addressed targeted strategies, mainly studied *in vitro*, offer the possibility of autonomously directing the MNPs towards the tumour after an IV injection, a perspective that should be further refined *in vivo*. While directed strategies have been tested in a variety of tumours, targeted MHT strategies for leukaemia and GBM treatment, however, have not been explored so far, particularly targeting CXCR4. Most of the *in vivo* MHT studies have tested IT injection of MNPs. The IT *vs.* IV MNPs' injection is possibly one of the most dividing issues for *in vivo* MHT testing, as a balance needs to be encountered between safety and

efficiency. While the IT injection seems safer because of the limited access of MNPs to other tissues, questions arise concerning the (in)homogeneity of MNPs' dispersion within the tumour, resulting in non-uniform *T* elevation throughout the tumour that may lead to inefficient outcome. On the other hand, the less explored IV injection appears as a more "natural" way by which active or passive targeting allow the MNPs to meet the tumours, independently of their size and location. However, the MNPs allocation to tissues other than the tumour, in particular the liver, spleen, kidney and lungs, must be regarded with caution. In any case, the results from some *in vivo* studies are exciting, in particular when the development of anti-tumour immunity contributed for the observed outcomes, providing an encouraging perspective for future clinical trials on targeted MHT. The current use of nanoparticle-induced MHT for GBM treatment is so far still limited to direct injection of non-targeted nanoparticles into the tumour mass, providing inhomogeneous MNP distribution, and consequent death from tumour regrowth.

Notwithstanding the encouraging results obtained with the *in vitro* and, above all, *in vivo* studies, MHT for cancer treatment is still underexplored, particularly using directed strategies that may allow selective tumour targeting, with minor effects in normal cells.

Objectives of this thesis

The use of MHT for cancer treatment is still far from reaching its full potential and a long path needs to be explored towards the achievement of an efficient anticancer strategy, with minimal expected side effects. The use of functionalized, targeted, nanomaterials is one improvement that can be made, but the dependence of treatment efficiency on the amount of magnetic material associated to cells is a difficult challenge. This dissertation aims at the development of a magnetically-mediated hyperthermia strategy using functionalized nanoparticles to target cancer cells. Specifically, the objectives of this thesis are:

- ⇒ To study and optimize magnetic nanoparticle's functionalization with biomolecules;
- ⇒ To functionalize magnetic nanoparticles with antibodies against a surface receptor overexpressed in many types of cancer cells, the chemokine receptor CXCR4;
- ⇒ To study the interaction between magnetic nanoparticles functionalized with anti-CXCR4 antibodies and cancer *vs.* normal cells *in vitro*;
- ⇒ To optimize a magnetically-mediated hyperthermia strategy using anti-CXCR4-functionalized nanoparticles to target cancer cells *in vitro*, with emphasis on cytotoxicity studies – the poof-of-concept;
- ⇒ To apply and tailor the developed strategy to distinct *in vitro* tumour models with different expression levels of the selected marker;
- ⇒ To ensure the safety of the MHT treatment developed in terms of cytotoxicity against normal cells.

CHAPTER II

Experimental Section, Results and Partial Discussions

MANUSCRIPT I

Unsubmitted manuscript

Manuscript I

Optimizing magnetic nanoparticle's functionalization with biomolecules for targeted magnetically-induced hyperthermia in cancer cells

Authors

Vânia Vilas-Boas[a,b,*], Begoña Espiña[b], Verónica Martins[b], Yury Kolen'ko[b], Manuel Bañobre-Lopez[b], Paulo Freitas[b] and Félix Carvalho[a,*]

Affiliations

UCIBIO-REQUIMTE, Laboratory of Toxicology, Biological Sciences Department, Faculty of Pharmacy, University of Porto, Rua Jorge Viterbo Ferreira, 228, 4050-313 Porto, Portugal

[b]International Iberian Nanotechnology Laboratory, Av. Mestre José Veiga, s/n, 4715-330 Braga, Portugal

*corresponding authors emails: vvilasboas@ff.up.pt and felixdc@ff.up.pt :

Abbreviations

AMF – alternating magnetic field
BCA – bicinchoninic acid
BSA – bovine serum albumin
CD – circular dichroism
CP – co-precipitation
EDC – 1-ethyl-3-[3-dimethylaminopropyl]carbodiimide hydrochloride
Fab – antibody-binding fragment
FBS – fetal bovine serum
Fc – fragment crystallisable
FITC – fluorescein isothiocyanate
FTIR – Fourier Transformed Infrared spectroscopy
HBSS +/+ – Hanks balanced saline solution w/ calcium and magnesium salts
HT – hydrothermal
IgG – immunoglobulin G
IR – infrared
LSCM – laser scanning confocal microscope
MNP – magnetic nanoparticle
MHT – magnetic hyperthermia
NHS – N-hydroxysulfosuccinimide
PA – Protein A
PAA – poly(acrylic acid)
pAb – polyclonal antibody
PB – Presto Blue™
PS – protein solution
RT – room temperature
S – supernatant
SA – sodium acetate
SAR – specific absorption rate
STR – streptavidin
T – temperature
W – wash

Abstract

The use of functionalized nanomaterials in the biomedical field has gained significant importance in recent years, in particular with biomolecules that direct the nanomaterials to target tissues/cells. In this study, the functionalization of *in house* synthesized poly(acrylic acid)-coated magnetic nanoparticles (MNPs) was optimized for different model proteins, using the EDC-Sulfo-NHS crosslinking chemistry. The functionalization efficiency was quantified by protein quantification methods such as Bradford, UV-vis spectrometry and circular dichroism, and the interaction between the protein and the MNPs was examined by Fourier Transformed Infrared spectrometry. After the optimization, satisfactory coverage of the MNPs surface was achieved and the as-obtained Streptavidin- or Staphylococcal Protein A-functionalized MNPs (STR– or PA–MNPs, respectively) were further conjugated with an anti-CXCR4 antibody targeting tumour cells, and then used for magnetic hyperthermia experiments with cancer cells *in vitro*. The observed results depended on the MNPs concentration used for the studies, with the highest concentration of MNPs leading to more than 75 % reduction in cell viability. PA–MNPs displayed higher stability than STR–MNPs in terms of aggregation as shown by microscopy studies; the aggregation in these functionalized MNPs induced a higher increase in hyperthermia studies.

From the obtained results, we may assume that successful immobilization of distinct proteins was observed, reaching satisfactory levels of biomolecules per MNP. The immobilized proteins retained functionality, as supported by the *in vitro* experiments on magnetic hyperthermia using cancer cells.

1. Introduction

Magnetic nanoparticles (MNPs) are often covered by coating layers that protect the reactive metallic core and provide the MNPs with stability and biocompatibility, while being a source of chemical groups for additional functionalization (Wu et al. 2015). Amongst the variety of possible organic coatings, poly(acrylic acid) (PAA) has gained wide interest in the recent years, due to the extensive number of functional groups and the stability it confers, while considered biologically safe (Prijic et al. 2012, Iversen et al. 2013, Couto et al. 2015).

The conjugation of MNPs with biomolecules is a challenging, yet very interesting, step that supplies the MNPs with recognition abilities, i.e., the possibility of identifying a specific target and binding to it. In most cases, the biomolecules used for MNPs functionalization are proteins (or peptides), including enzymes, antibodies, receptor-ligands and affinity proteins [(such as streptavidin (STR), or protein A (PA)] (Minelli et al. 2010). In particular, STR forms one of the strongest, non-covalent, biological bonds with biotin, with high affinity, specificity and stability. As a tetrameric protein, STR has four known binding sites for biotin. Therefore, when in solution, STR can bind up to 4 biotin molecules, but when immobilized in a surface, this number drops due to steric hindrance (Quevedo et al. 2016). Biotinylated antibodies can be effectively immobilized on MNPs coated with STR. This is one of the most used strategies for the generation of immuno-targeted MNPs.

The *Staphylococcus aureus*-derived PA is a 42 kDa protein known to bind the fragment crystallisable (Fc) region of antibodies (e.g. IgG), with varying affinities, depending on the host and, where applicable, the immunoglobulin's subclass (Kronvall et al. 1970). Five possible binding sites of IgG to PA have been described (Moks et al. 1986), but steric hindrance between IgG molecules prevents more than 2 IgG to bind 1 PA simultaneously (Yang et al. 2003, Mu et al. 2015). Interestingly, this is an oriented binding through the Fc region of the antibody, leaving the antibody's region of specific recognition (antibody-binding fragment, Fab) free to interact with its target.

Functionalized MNPs have a wide range of applications in catalysis and in biomedicine, namely, for magnetic separation, magnetic drug delivery and magnetic hyperthermia (MHT) (Lu et al. 2007). MHT is a cancer treatment based on the heat produced by MNPs under an alternating magnetic field (AMF) (Banobre-Lopez et al. 2013). It is currently approved to treat a highly aggressive type of brain tumours, named glioblastoma, in combination with radiotherapy (MagForce 2016), but there's margin for therapy improvement, namely by using targeted magnetic particles. Therefore, the use of

a selective moiety holding the MNPs capable of target recognition and binding, holds great potential for increased selectivity and safety of MHT for the treatment of cancer.

In this study we evaluate diverse functionalization pathways with the final goal of immobilizing antibodies on the surface of MNPs for effective targeting of cancer cells in *in vitro* targeted MHT studies.

2. Materials and methods

Dulbecco's Modified Eagle's Medium – high glucose (DMEM), Roswell Park Memorial Institute medium (RPMI-1640), trypan blue solution, sodium pyruvate, sodium bicarbonate, penicillin (10,000 U/mL) and streptomycin (10,000 µg/mL), herein referred to as Pen-Strep, sodium acetate, bovine serum albumin (BSA), streptavidin (STR), Protein A (PA), were purchased from Sigma-Aldrich, Inc. (St. Louis, MO, USA). Fetal bovine serum (FBS) was purchased from HyClone UK, Ltd (Northumberland, England, UK). Pierce™ Coomassie Plus (Bradford) Assay Kit, Micro BCA™ Protein Assay Kit, Pierce™ Biotin-Fluorescein Conjugate (Biotin-FITC), 1-ethyl-3-[3-dimethylaminopropyl]carbodiimide hydrochloride (EDC), biotin-conjugated anti-Campylobacter polyclonal antibody, biotin-conjugated anti-Salmonella polyclonal antibody and Sulfo-N-hydroxysulfosuccinimide (Sulfo-NHS) were purchased from ThermoFisher Scientific (Cambridge, UK). Biotinylated anti-human-CXCR4 monoclonal antibody (clone 12G5), biotinylated mouse IgG2a (clone MOPC-173) and low endotoxin, azide-free anti-human-CXCR4 antibody (clone 12G5) were purchased from BioLegend Inc. (San Diego, CA, USA).

2.1. Cell culture

Human glioblastoma cells, LN229 (ATCC® CRL-2611™), and human acute lymphoblastic leukaemia cells, Jurkat (ATCC® TIB-152™), were purchased from the American Type Culture Collection (Manassas, VA, USA). These cell lines were grown in DMEM high glucose or RPMI-1640, respectively, both supplemented with 10 % FBS, 1 % Pen-Strep and maintained in a controlled atmosphere at 37 ºC and 5 % CO_2.

2.2. Specific absorption rate estimations

The specific absorption rate (SAR) is the power absorbed per mass of magnetic material in watts per kilogram (in W/kg). Accurate measurement of SAR is essential for quantifying the heating efficiency of MNPs' suspensions for applications in anti-cancer MHT. Three nanoparticle's suspensions were tested to assess their magnetic

hyperthermia performance: PAA-CP (ca. 13 nm diameter core), PAA-HT-Na and PAA-HT (ca. 18 nm diameter core, in both cases). The samples were obtained using distinct synthesis methods: CP refers to “co-precipitation” while HT stands for “hydrothermal” method (Kolen’ko et al. 2014). The PAA-HT-Na sample was obtained using sodium hydroxide instead of ammonia (used for PAA-HT) as precipitation agent.

The MHT performance of those samples was evaluated using an AMF of 869 kHz and 225 Oe (18 $kA \cdot m^{-1}$). MNPs were diluted in cell culture medium to the same final magnetite concentration (0.5 $g \cdot L^{-1}$) in a 1 mL sample volume. All samples were contained in a glass vial and placed at the mid-point of a water-cooled copper coil of a DM 100 system (nB nanoScale Biomagnetics). Each sample’s temperature (*T*) was recorded using an optical-fibre-based thermometer.

The SAR of each sample was calculated using the following equation:

$$SAR = \frac{C}{mFe}\frac{\Delta T}{\Delta t}$$

where C is the heat capacity of water (4.184 $J \cdot K^{-1} \cdot g^{-1}$), mFe is the mass (g) of iron in 1 mL of sample, and ΔT is the *T* variation in the Δt time interval.

2.3. MNPs’ conjugation with proteins

The selected MNPs’ formulation was washed using a permanent magnet to remove the excess of free PAA and recovered in the same volume of ultrapure water (Milli-Q®, Merck Millipore, Darmstadt, Germany). Subsequently, and according to the manufacturer’s instructions, EDC was added to the MNPs followed by equal volume of sulfo-NHS and the suspension was incubated for 15–30 min, at room temperature (RT), with agitation. The MNPs were then magnetically separated to remove the excess of EDC and sulfo-NHS, resuspended in the protein solution (PS), and incubated at 4 ºC, for 3 h, with agitation. The PS concentration corresponded to, at least, 5× the amount of protein calculated to fulfil the MNPs’ surface area (calculated for each protein as described in supplementary data). The MNPs were again magnetically separated, the supernatant (S) was collected to further quantify the free protein, and the MNPs were washed with the same volume of Milli-Q. A subsequent magnetic separation allowed the collection of this washing volume (W) and the MNPs were further resuspended in a 2 % dilution of bovine serum albumin (BSA) in ultrapure water. Whenever the magnetic separation of the MNPs was not possible due to low magnetic susceptibility, a centrifugation step was performed (12,000 *g*, 5 min). A schematic representation of sample’s collection for protein quantification is provided in Figure 1.

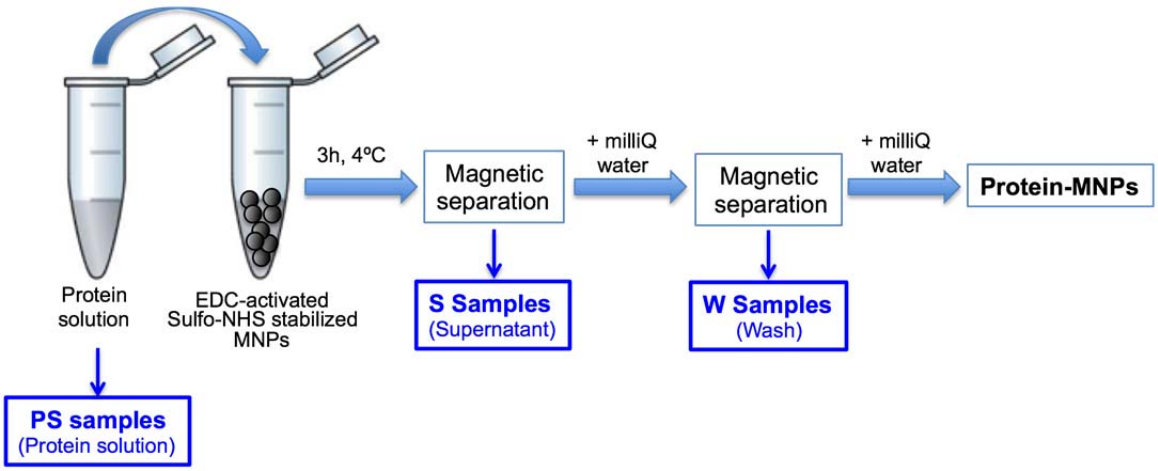

Figure 1 – Schematic representation of sample collection during MNPs functionalization with proteins, after the MNPs activation and stabilization with EDC-Sulfo-NHS.

The parameters subjected to optimization were:

EDC-Sulfo-NHS concentration: different concentrations of these reagents were tested (EDC = 12, 6, 1.2 and 0.6 g·L^{-1}; Sulfo-NHS = 33, 16.5, 3.3 and 1.65 g·L^{-1});

Protein coupling buffer: ultrapure water, sodium acetate (SA) pH=4.5 and SA pH=4;

Tested proteins: BSA, STR, Protein A and polyclonal antibodies (anti-Campylobacter or anti-Salmonella).

2.4. Protein quantification

2.4.1. Coomassie Plus (Bradford)

Ten microliters of the corresponding protein standard or sample were mixed with 300 µL of Coomassie Plus reagent, in duplicates or triplicates, and incubated for 10 min, in the dark. The absorbance was measured at 595 nm using a microplate reader (Synergy H1, BioTek Instruments). The amount of protein immobilized on the MNPs was estimated by subtracting the amount of unbound protein (measured in S and W) from the measured starting amount of protein, PS.

2.4.2. Micro-BCA

Protein standards were prepared considering the linearity range of this assay (2 and 40 µg·mL^{-1}). Standards or diluted samples were incubated, in a 96-well microplate, with an equal volume of a mixture of the reagents A, B and C, according to the manufacturer's instructions, for 2 h at 37 ºC. After cooling the microplate to RT, the absorbance was read at 562 nm using a microplate reader (Synergy H1, BioTek Instruments). As for the

Bradford assay, the amount of protein immobilized on the MNPs was estimated by subtracting the amount of unbound protein (measured in the supernatant S and washes W) from the measured starting amount of protein, PS.

2.4.3. Absorbance at 280 nm

This is a widely used protein quantification method due to its simplicity and the non-destructive use of the samples. For this purpose, a NanoDrop 2000c (Thermo Scientific) spectrophotometer was used to read 2 µL of each sample, in duplicates.

2.4.4. Circular dichroism

Circular dichroism (CD) measurements followed a previously established protocol (Fears et al. 2013). Briefly, the collection of the UV absorbance and the CD spectra was performed simultaneously over the range of 190–260 nm, in a 1-mm path-length quartz cuvette, using a Jasco J-815 spectropolarimeter. Each scan was acquired at a rate of 20 $nm \cdot min^{-1}$, under controlled *T* conditions (20 ºC) and represents the average of 3 accumulations. Raw ellipticity values (mdeg) were converted to molar ellipticity (Mol. Ellip.; $deg \cdot cm^2 \cdot dmol^{-1}$) using a previously described methodology (Fears et al. 2013).

2.5. Fourier Transformed Infrared Spectroscopy (FTIR) studies

The samples concerning functionalized MNPs were prepared as previously described in the section 2.3. A sample of MNPs conjugated with BSA, the MNPs before functionalization, and a BSA sample were prepared. All the samples were dried, at 37 ºC, overnight. Potassium bromide was used as reference material for the FTIR analysis. The IR spectra (1800–400 cm^{-1}) were collected in transmission mode using a Nicolet 6700 spectrometer (Thermo Scientific).

2.6. *In vitro* magnetic hyperthermia treatments in two cancer cell models

LN229 cells were detached using trypsin, while Jurkat cells were kept in suspension; both cell lines were washed with the appropriate cell culture medium, and the cell density and viability was counted in a haemocytometer using trypan blue exclusion method. Cells ($2–2.5 \times 10^6$ per test condition) were incubated with MNPs (functionalized or not with antibodies), to a final concentration of magnetite of 0.2 or 0.5 $g \cdot L^{-1}$, for 1 h, at 37 ºC, under constant shaking. A centrifugation step (125 *g*, 5 min, RT) was performed to separate the free MNPs from the mixture, and the samples were then recovered in 1 mL of cell culture medium. All samples were transferred to glass vials and placed at the mid-point of a

water-cooled copper coil of a DM 100 system (nB nanoScale Biomagnetics). Each sample's temperature was recorded using an optical-fibre-based thermometer.

2.7. Cytotoxicity evaluation after MHT

2.7.1. Presto Blue metabolization

After AMF application to the cell samples, Presto Blue™ reagent (PB) was added at a 1:10 dilution, following the manufacturer's instructions. Following exposure for 30–60 min, the samples were centrifuged at 850 *g*, for 5 min, at 4 ºC, to collect the supernatant, whose fluorescence was measured, at 590 nm emission and 560 nm excitation wavelengths, in a microplate reader (Synergy H1, BioTek Instruments).

2.7.2. Laser scanning confocal microscopy

After MHT application, cells were seeded in 8-well μ-dishes with treated surface for adherent cells (Ibidi, Martinsried, Germany) and incubated at 37 °C, 5 % CO_2 and humidified atmosphere for 24 h. Prior to live cell imaging, samples were labelled with phycoerythrin (PE)-labelled Annexin-V (2 μL of stock solution), during 30 min, and counterstained with Hoechst 33342 (final concentration1 $\mu g \cdot mL^{-1}$), during 10 min, at 37 °C. Samples were then washed with Hanks Balanced Saline Solution with calcium and magnesium salts (HBSS +/+) before imaging. Fluorescence images were collected using a laser scanning confocal microscope (LSM 780, Carl Zeiss) simultaneously using 405 (for Hoechst 33342) and 561 nm (for PE) excitation lasers.

3. Results and discussion

3.1. Selection of the magnetic nanoparticle formulation

Three distinct MNP dispersions, different in capping/stabilizing agent and/or synthesis method—PAA-CP, PAA-HT (Kolen'ko et al. 2014) and PAA-HT-Na—were compared regarding their MHT performance to select the most appropriate to proceed for the functionalization studies. Figure 2a shows the curves of *T* versus time for each of the three MNPs' formulations when diluted to the same final magnetite concentration ($0.5\ g \cdot L^{-1}$) and exposed to the same AMF. The equipment used for the AMF application (Figure 2b) is composed of an applicator module, holding a water-cooled copper coil with the centred sample holder and the optical fibre *T*-probe, and a controller module for the selection of the AMF parameters, and the monitoring and analysis of the experiments.

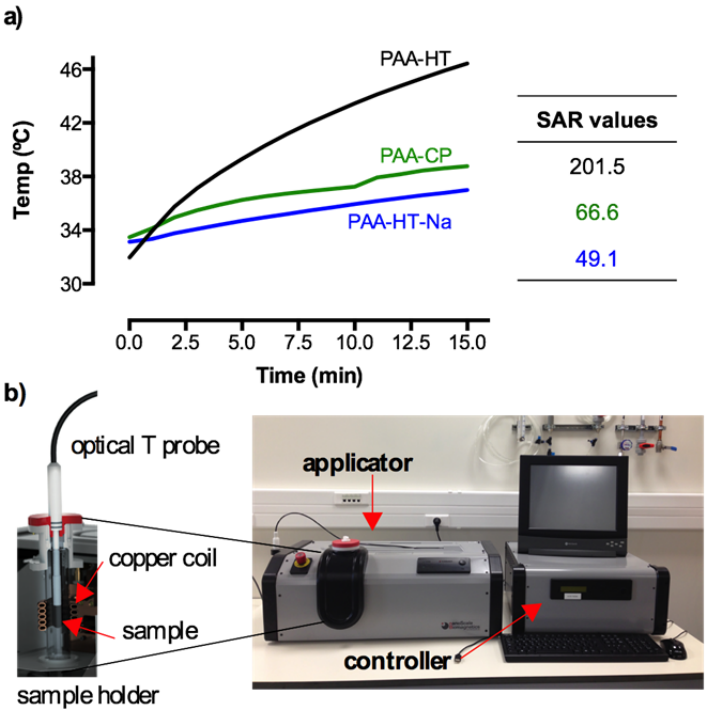

Figure 2 - Magnetic hyperthermia performance of different PAA-coated MNPs. Samples diluted to 0.5 g/L [magnetite] in cell culture medium were submitted to AMF (869 kHz, 18 kA/m) for 15 min, using the equipment in b). The detail shows a transverse section of the sample holder. The samples' *T* at each minute was collected using an optical *T* probe. SAR values for each sample are provided in the table. Adapted from (Biomagnetics)

Sample PAA-HT presented the best performance in heating ability at the tested magnetite concentration, increasing the medium's *T* to 46 ºC in less than 15 min (Figure 2a). Accordingly, this sample exhibited the highest SAR value, as denoted in Figure 2a, which was 3–4× bigger than the ones calculated for the other samples. This distinctive performance of PAA-HT sample for MHT purposes led to its selection for further optimization of the functionalization. Therefore, all the other tests further presented in this work were performed using PAA-HT MNPs, also simply called MNPs hereinafter.

3.2. MNPs' functionalization

The widely used EDC-Sulfo-NHS crosslinking chemistry was optimized for the functionalization of the MNPs with biomolecules. This chemistry takes advantage on the carboxylic groups (–COOH) provided by the PAA-coating of the MNPs to activate and bind them to the amine groups ($–NH_2$) of proteins (Sperling and Parak 2010). The collection of samples for the evaluation of the functionalization efficiency was described in the Methods section and summarized in Figure 1.

3.2.1. Optimization with Bovine Serum Albumin

Due to its abundance and low price, BSA was used as a model protein for the optimization procedure. This protein has been described to increase the stability and biocompatibility of nanoparticles tested as drug carriers for biomedical applications (Jenita et al. 2014). The theoretical number of BSA molecules that fits the surface of 18-nm-core MNPs was calculated to be 40 BSA molecules per MNP (as described in supplementary data, taking into account the biomolecule's parking area, but not steric or electrostatic interactions). We started by testing different concentrations of EDC and Sulfo-NHS to select the one that would be efficient without appreciably affecting the stability of the MNPs (Figure 3).

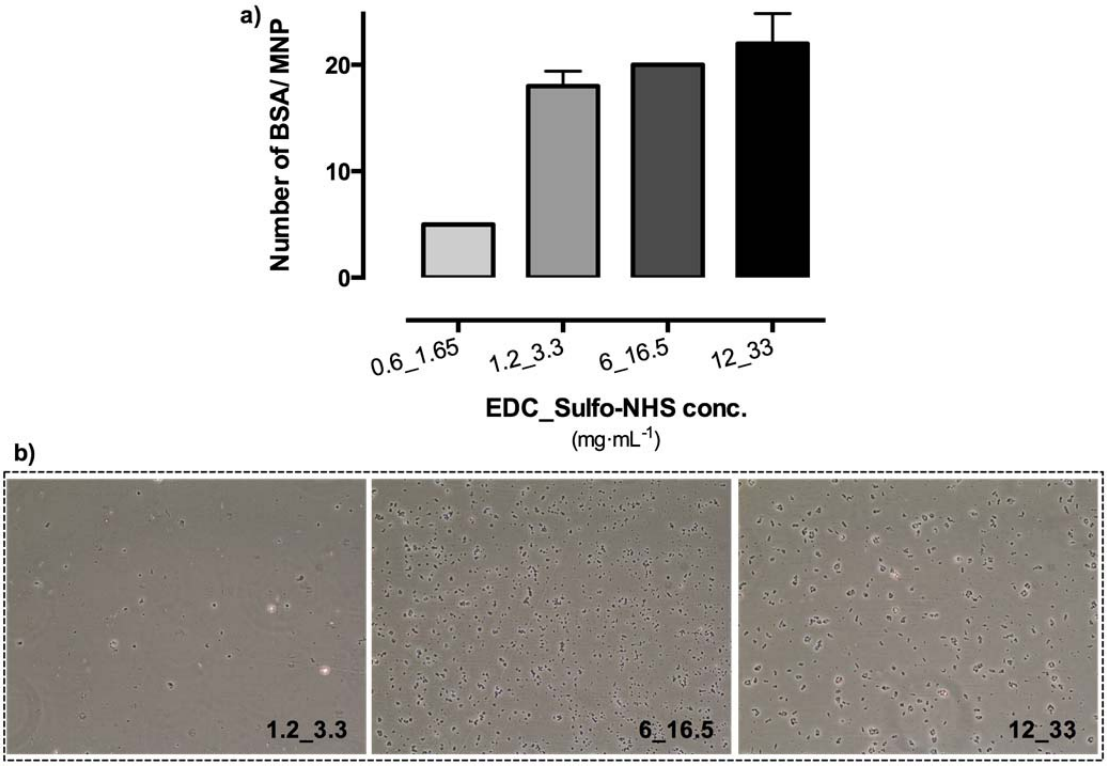

Figure 3 - Dependence of BSA immobilization on EDC-Sulfo-NHS concentration.
Different concentrations of EDC-Sulfo-NHS were tested for BSA immobilization on MNPs. a) The estimated number of BSA per MNP, quantified with Coomassie Plus reagent, was plotted for each EDC-Sulfo-NHS concentration. b) Representative optical micrographs (100× magnification) of the as-obtained MNPs showing that when using higher EDC-Sulfo-NHS more (and bigger) MNP aggregates are observed.

The lowest tested concentration of EDC-Sulfo-NHS resulted in less efficient protein immobilization (~5 BSA per MNP) than the higher concentrations, which reached average levels of 20 BSA per MNP. Others have previously achieved efficient BSA immobilization on bare iron oxide MNPs using EDC as coupling agent (Mehta et al. 1997). When the

reagents were not used, no BSA binding was observed. Achieving similar protein binding efficiencies, the concentrations of 1.2 and 3.3 mg·mL^{-1} were chosen due to the resulting higher stability and lower MNPs' aggregation (Figure 3b). Similar dependency of MNPs' aggregation on the EDC concentration has been previously reported (Wang and Lee 2003). The concentration of BSA to be incubated with the activated MNPs also influenced the immobilization efficiency, with higher concentration resulting in higher amount of protein immobilization (Figure 4). While increasing surface coverage of 47, 78 and 184 % (taken the theoretical estimation as 100 %) were observed with increasing initial BSA concentrations, the highest tested concentration in this study resulted in more than 70 BSA molecules per MNP, which far overcomes the calculated theoretical value of 40 BSA per MNP, suggesting the formation of additional protein layers. Wang *et al*. used similar EDC concentrations (2 mM ~ 1.3 mg·mL^{-1}) for the efficient immobilization of avidin, quantifying the unreacted protein using a Bradford protein assay. These authors also reported a dependency of the immobilization efficiency on the protein concentration (Wang and Lee 2003). Nevertheless, in the reports by Wang *et al.* and Mehta *et al*. the number of biomolecules per MNP was not calculated (Mehta et al. 1997, Wang and Lee 2003), preventing conclusions regarding the formation of extra layers of biomolecules.

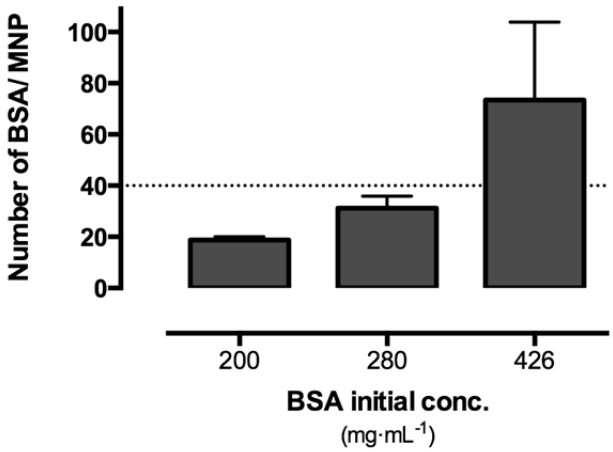

Figure 4 - Dependence of BSA immobilization on BSA initial concentration.
The estimated number of BSA per MNP was plotted for each initial BSA concentration (dashed line represents the theoretical value calculated for BSA fitting on 18-nm-MNPs).

BSA isoelectric point has been reported to be ca. 4.9 (Galisteo-Gonzalez and Molina-Bolivar 2014); therefore, the use of a buffer with a pH slightly below BSA's isoelectric point would favour the initial interaction of the protein with the carboxylic groups of the MNPs due to the overall net positive charge. Therefore, BSA immobilization was also tested

using SA buffers at pH=4.5 and pH=4.0 as coupling buffers, but the observed binding efficiency was lower than when using ultrapure water as vehicle (data not shown).

The MNPs samples were analysed before and after BSA immobilization using FTIR, and the obtained spectra are shown in Figure 5.

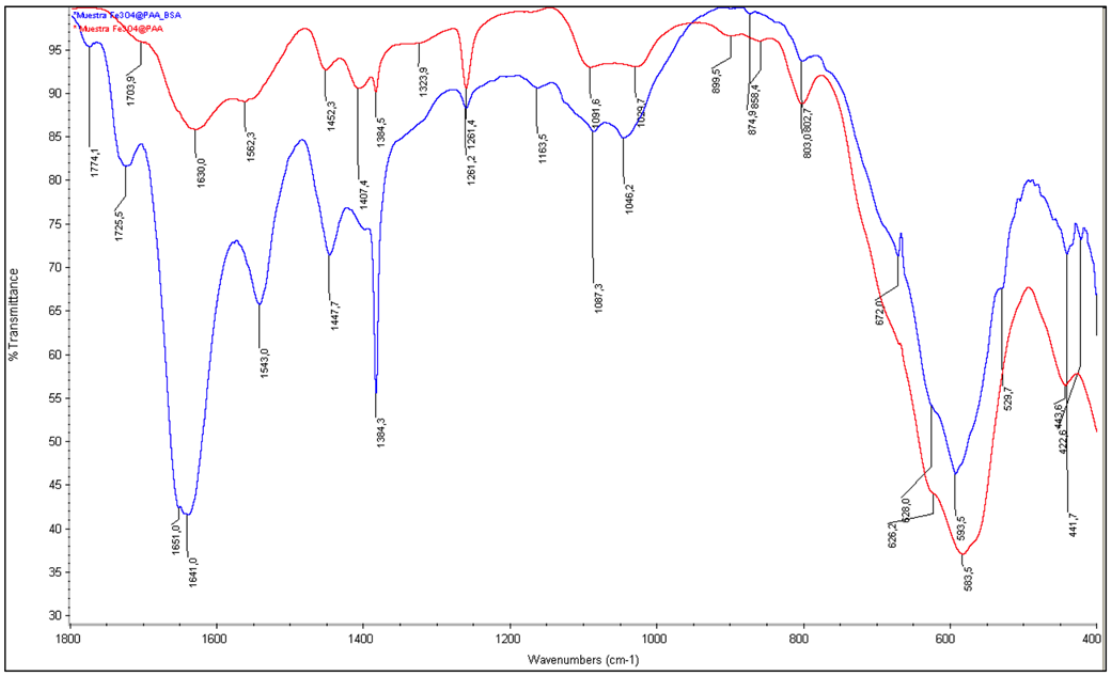

Figure 5 – Fourier transformed infrared spectra of PAA-MNPs before and after BSA immobilization.
Red spectrum – PAA–HT; blue spectrum – PAA–HT–BSA.

The FTIR data supported the interaction of PAA with the iron oxide nanoparticles (red bands at 583.5 and 444 cm^{-1}), despite the presence of a small amount of free PAA, i.e., not interacting with the magnetite core (red band at 1703.9 cm^{-1}) (Lin et al. 2005). Furthermore, the effective interaction between BSA and the carboxylic groups from PAA was confirmed, due to the appearance of amide bonds (blue bands at 1641 and 1543 cm^{-1}) different from the ones found in the spectra of HT–PAA (red bands at 1630 and 1562 cm^{-1}) and BSA-only (1648 and 1540 cm^{-1} (Peng et al. 2004)).

3.2.2. MNPs functionalization with streptavidin, protein A or antibodies

Using the optimized settings for functionalization of MNPs, the process was repeated for STR, PA and pAb, and the relative efficiency was calculated quantifying the free protein (Figure 6). In particular, a Bradford assay (Coomassie Plus reagent) was used for the estimation of STR and pAb, and for PA the quantification was performed using circular dichroism (CD). The theoretical values calculated for the fitting of STR, PA and pAb

molecules were 44, 192 and 27, respectively (see supplementary data) and the observed estimated protein immobilization values were 30.4±3.6, 161.0±60.3 and 25.7±4.0 molecules per MNP, respectively, suggesting satisfying MNP-surface coverage with the proteins. These values represent 69, 84 and 95 % surface coverage, respectively, for STR, PA and pAb (Figure 6).

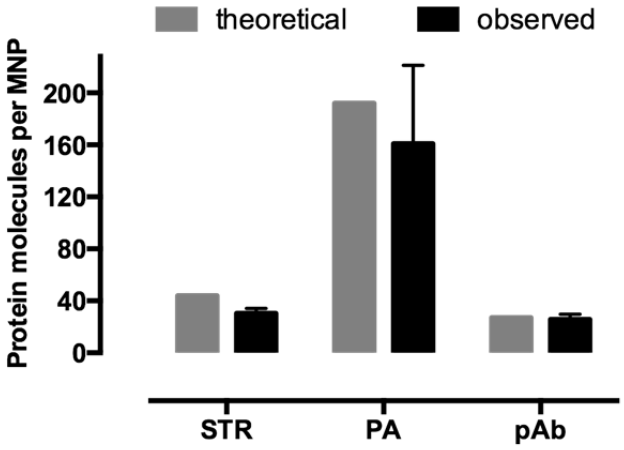

Figure 6 – Efficiency of PAA–HT MNPs' functionalization with Streptavidin, Protein A, or polyclonal antibody.
For STR and pAb, the free protein collected from the MNPs (in the supernatants and washing steps) was quantified using Coomassie Plus reagent. PA was quantified by circular dichroism. The number of protein molecules immobilized per MNP was estimated and compared with the maximum theoretical values.

STR and PA are interesting proteins that enable the binding of antibodies with high affinity to obtain targeted MNPs. In particular, STR binds with elevated affinity to biotin, which in turn can be linked to antibodies. This is considered the strongest non-covalent biological interaction known, being widely used for a number of different cellular and molecular assays (Holmberg et al. 2005). We tested the ability of the as-STR-functionalized MNPs to bind a biotin-conjugated polyclonal antibody (pAb) and estimated an average of 30 pAb per MNP, which corresponds to ca. 1 pAb per STR (data not shown). Interestingly, when not using the EDC-Sulfo-NHS reagents for the functionalization, a residual amount of 10 STR per MNP was found, contrarily to BSA that would not bind at all. Adding fluorescein isothiocyanate (FITC)-labelled biotin (Biotin-FITC) to these samples resulted in a calculated average 4–5 biotin molecules per STR in the MNPs' samples (data not shown). The fact that the four biotin-binding sites in these STR molecules are available for interaction with biotin shows that the STR's functionality is retained after immobilization, but is also suggestive of weak interaction between the STR and the MNPs.

Regarding PA, curiously, the protein failed to react with the Coomassie Plus reagent and it was not possible to establish a proper calibration curve (Figure S1). When using the micro-BCA (bicinchoninic acid) protein assay a standard curve was obtained (Figure S1, R^2=0.9962), but interferences were found when reading the S samples, possibly due to contaminating and residual nanoparticles contributing for the absorbance readings. Proteins are known to absorb at the 280 nm and, less commonly, in the far ultraviolet (UV), at 195–205 nm (Kelly et al. 2005, Fears et al. 2013). Particularly, the immobilization of PA on the surface of MNPs has been previously quantified by measuring the absorbance at 280 nm (Mu et al. 2015). However, for the work described herein, the measurements at 280 nm performed on a NanoDrop spectrophotometer encountered similar challenges as for the micro-BCA assay: a standard curve was obtained (Figure S1, R^2=0.9925) and the PS sample's concentration could be estimated but significant interferences were found for the S samples.

As previously referred, another standard, though not so common, method for protein quantification is protein absorbance in the far UV, at 195 nm. As for the previous methods, a linear correlation was found for the standards (Figure 7a), but real samples may have some interference at this wavelength. Therefore, a more protein-specific method, i.e., circular dichroism (CD), was necessary, as it can be related to the protein's structure, concentration, etc. In fact, measurements of CD signals in the far UV can give quantitative estimates of secondary structure (α-helix and β-sheet conformations) comparable to those obtained with X-ray crystallography or NMR (Kelly et al. 2005). Previous studies on the PA's CD spectrum have estimated that PA contains nearly 50 % α-helix structure and 10–20 % β-sheet structures (Sjoholm 1975). The peak positions and shapes within the CD spectra for PA were conserved among the standards and samples, allowing an extrapolation of the sample's concentration from the standard curve. In particular, the signal at 208 nm, correspondent to PA's α-helix structure, in the CD spectrum seemed a convenient feature, as it was not affected by the solvent (water) or by residual amounts of MNPs that may be contaminating in the S samples (Figure 7b). This signal has been previously recommended for the estimation of the α-helical content of proteins (Kelly et al. 2005), but to the best of the authors' knowledge, it's the first time it has been used to estimate the efficiency of PA immobilization on MNPs.

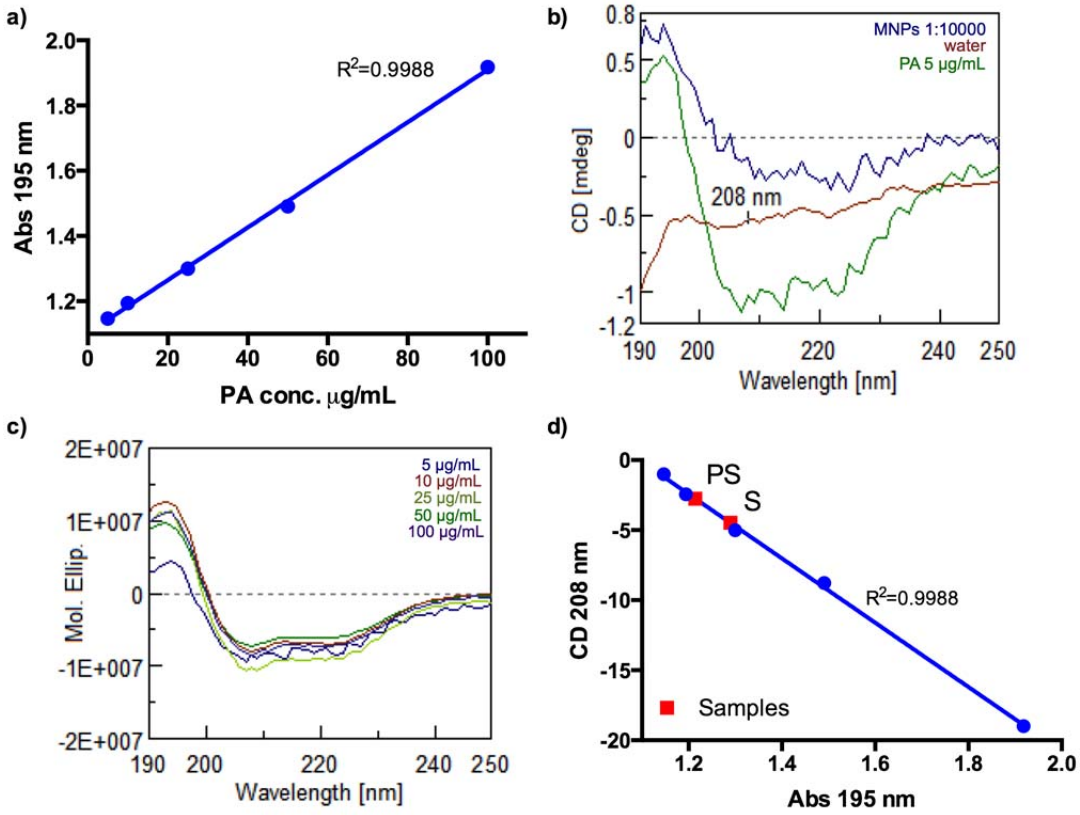

Figure 7 - Protein A quantification in standards and samples after MNPs functionalization. a) A linear correlation was found between PA concentration and the absorbance at 195 nm. b) Circular dichroism spectrum of PA did not suffer interference from water or from traces of MNPs that could be present after MNPs functionalization (S samples). c) The similar and almost superimposing molecular ellipticity curves showed no significant concentration-dependent changes in the protein structure, in particular, at the CD wavelength selected for protein quantification (208 nm). d) The measured absorbance at 195 nm linearly correlated with the CD signal at 208 nm, allowing estimation of PA concentration.

Furthermore, the CD 208 nm signal did not relate to any concentration-dependent structure alteration, as shown by the nearly superimposing molecular ellipticity curves (Figure 7c). A linear correlation was found between the CD 208 nm signal and the absorbance at 195 nm obtained in the same CD spectrometer (Figure 7d), which finally allowed the interpolation of the samples' (PS and S) PA concentration. The results indicated a satisfactory coverage of the MNPs surface with an average 161 PA molecules per MNP (Figure 6), corresponding to 84 % of surface coverage with protein, which can further bind the Fc region of IgG, leaving the Fab free for antigen recognition.

The optimized functionalization strategy successfully allowed the immobilization of a polyclonal antibody directly at the MNPs surface (Figure 6, pAb). This direct immobilization of antibodies on MNPs has the advantage of being simple and fast, and readily applicable to polyclonal antibodies, dramatically cheaper than their monoclonal

counterparts. For monoclonal antibodies, however, this approach can become nearly unaffordable due to the excess of protein required to favour the coupling chemistry. Moreover, the random orientation of the antibody molecules landing on the MNP's surface, and the use of relatively aggressive reagents, may hamper the antibodies' functionality to some extent (Peluso et al. 2003). Whenever direct immobilization is not an option, the antibody immobilization via STR or PA affinity may be favourable as it requires less amount of antibody.

3.3. Assessing protein functionality after immobilization using magnetic hyperthermia experiments in cancer cells

As an example of a biomedical application, the STR–MNPs were conjugated with a biotinylated-anti-CXCR4 antibody, simply by adding the IgG solution to the STR-MNPs, at a ratio of 3 IgG/MNP, and tested in MHT experiments with cancer cells. In fact, CXCR4 is a chemokine receptor that is overexpressed in many types of cancer cells, being therefore an interesting target for cancer diagnosis and treatment (Zlotnik 2006). For these tests a human glioblastoma cell line, LN229, was used in which CXCR4 overexpression was confirmed (Manuscript 3). The conditions to be used for the MHT experiments were selected on the basis of the heating performance of the unconjugated MNPs and the respective outcome in another human glioblastoma cell line (Manuscript 2, supplementary data). Cells in suspension were incubated with the obtained CXCR4–STR–MNPs at a final magnetite concentration of 0.2 $g \cdot L^{-1}$ and then centrifuged to remove the excess of free MNPs. The *T* profile of these samples during AMF application (2 cycles, 499 kHz, 24 $kA \cdot m^{-1}$, 1h each) is shown in Figure 8a. The *T* profile of samples containing LN229 cells incubated with CXCR4–STR–MNPs were clearly distinguishable from the ones containing MNPs without antibody, due to the higher *T* reached during MHT. This fact is a strong indicator that the linker protein retained its functionality after immobilization (Jung et al. 2008), binding to the antibody that, in turn, recognised and bound to cells. Although the *T* did not rise above 37 ºC in any case, surprisingly, some decreases in the metabolic rate of the cells (Presto Blue™, Figure 8b) were observed for the samples containing MNPs without antibody, particularly after MHT.

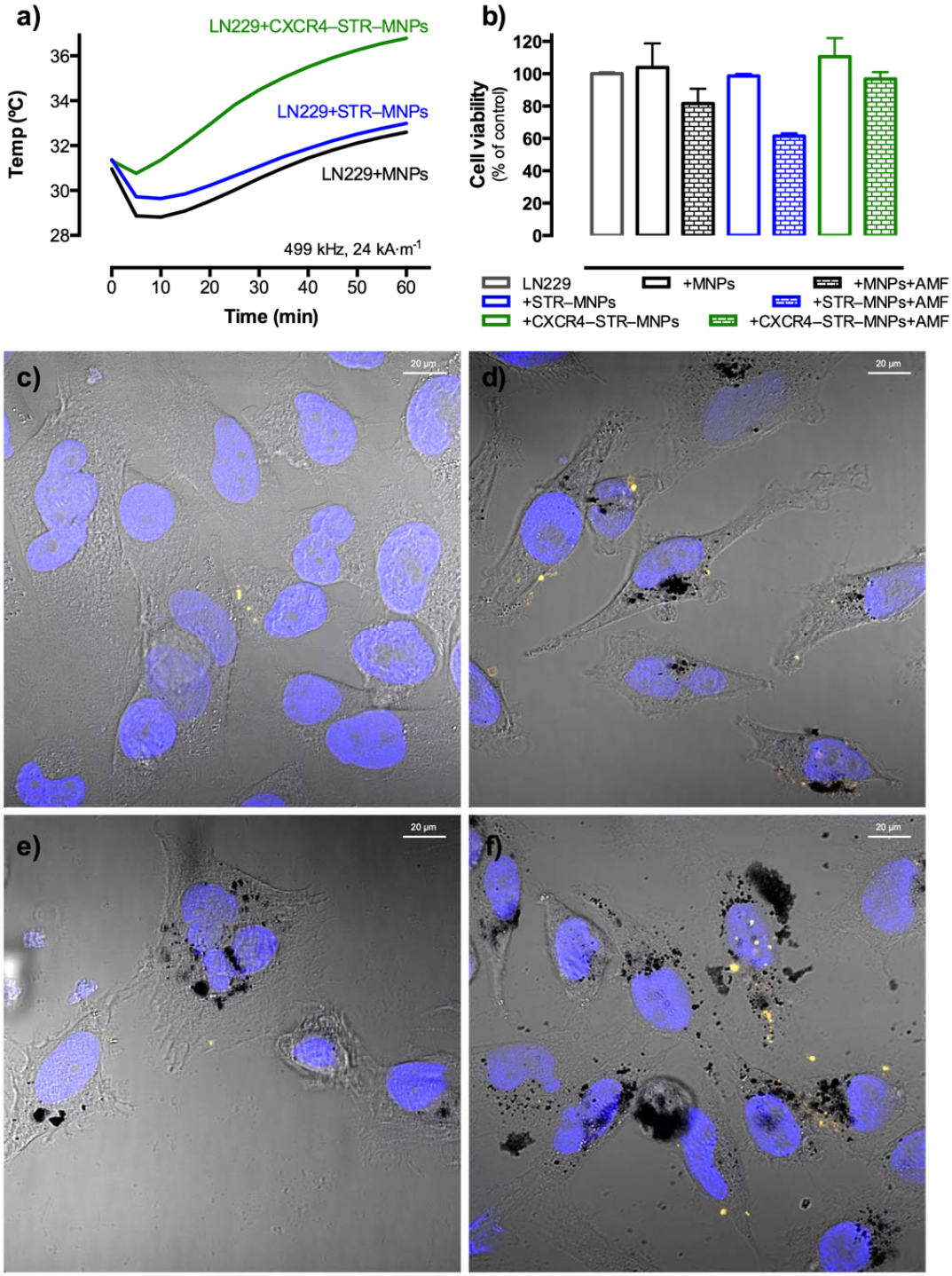

Figure 8 – Magnetic hyperthermia experiment using LN229 cells incubated with MNPs, or STR–MNPs, or CXCR4–STR–MNPs.
a) Heating profiles. b) The effects on cell viability were evaluated using PrestoBlue reagent, right after AMF application. Laser scanning confocal microscopy images showing Hoechst 33342 labelling of the nucleus (blue) and Annexin-V staining (yellow) in cells-only (c), cells with MNPs (d), cells with STR–MNPs (e), and cells with CXCR4–STR–MNPs (f), 24 h after MHT.

Hypothesizing that this decreased metabolic rate could be a transitory effect of the MHT protocol, as these samples were kept at *T* bellow the physiological ones, the

samples were imaged the following day, with laser scanning confocal microscopy (LSCM), to check for apoptosis signals, using Annexin-V (Figure 8c–f). Annexin-V binds to the phosphatidylserine residues that translocate to the outer leaflet of the cell membrane at the onset of apoptosis (Koopman et al. 1994). The cells exhibited a normal shape, at this time-point, indicating that the results of PB after MHT were not due to an irreversible cytotoxic effect. The levels of Annexin-V staining did not vary significantly between samples (Figure 8c–f, yellow staining), indicating that the different treatments did not produce significant toxicity in LN229 cells.

Subsequently, we compared the efficiency of the STR–MNPs to the PA–MNPs, conjugated with anti-CXCR4 antibody, in MHT experiments with Jurkat cells. This *in vitro* model of acute lymphoblastic leukaemia is widely used for mechanistic studies due to its easy manipulation, and it widely expresses CXCR4 (Baribaud et al. 2001). As control samples, an isotype control antibody (i.e., an antibody from the same host and IgG subtype) was used instead of the anti-CXCR4 antibody used for the test samples. Unlike the previous MHT experiments, AMF parameters were adjusted so that the samples heat to the maximum possible *T* within the first half (30 min) of the treatment, then keeping this *T* during the second half (Manuscript 2). The heating profiles varied principally according to the linker protein used for antibody's attachment to the MNPs, i.e., STR or PA. In this sense, the samples with STR–MNPs, overall heated more than the ones with PA–MNPs with the same antibody, but PA–MNPs allowed a clearer distinction between the *T* curves of the control and test samples (Figure 9a), also providing evidence on the maintenance of PA's (and antibody's) functionality after immobilization. In agreement with the observed *T* profiles, the cell viability levels 24 and 72 h after MHT were considerably lower when STR was used as the linker biomolecule, resulting in less than 10 % viable cells 72 h after MHT (Figure 9b).

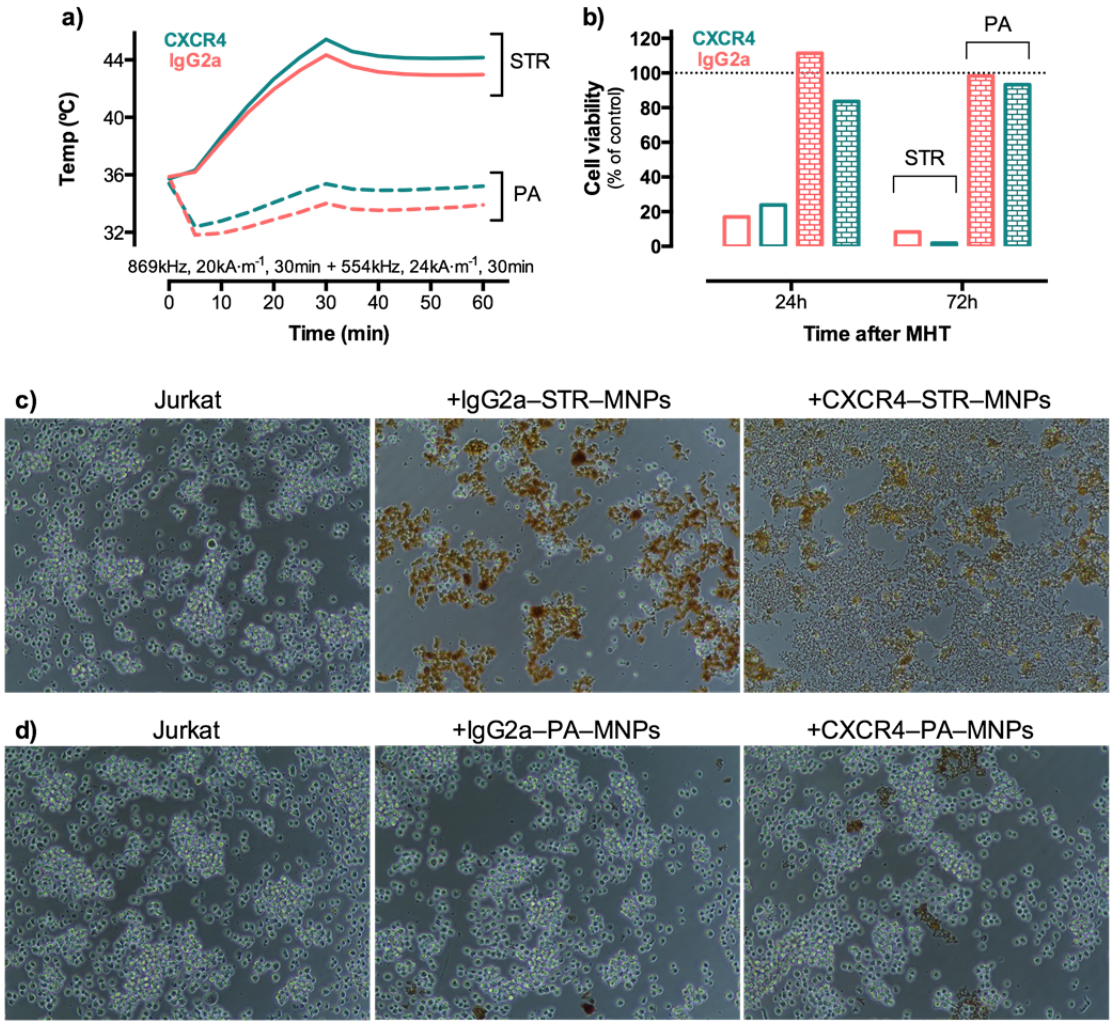

Figure 9 – Comparing MHT efficiency using STR– or PA–MNPs further conjugated with an anti-CXCR4 antibody, in Jurkat cells.
a) Heating profiles b) Cellular metabolic rate 24 and 72 h after MHT. Samples bearing STR–MNPs (c) or PA–MNPs (d) were imaged 72 h after MHT using optical microscopy, under a 100× magnification.

The optical microscopy images collected 72 h after MHT show noteworthy aggregation of STR–MNPs, mostly with the isotype control antibody, but also with anti-CXCR4 antibody (Figure 9c). The PA–MNPs also display some aggregation but to a relatively lower extent (Figure 9d). Knowing that antibodies may have more than one biotin per antibody molecule, and that each STR can bind more than one biotin molecule, crossed interactions may occur in which the same antibody molecule may be shared between different STR–MNPs, resulting in big agglomerates of MNPs (Garanger et al. 2009) (Figure 10). In order to avoid this effect an excess of antibodies should be added to conjugate with the STR immobilized in the MNPs surface, meaning a high cost of the functionalization and preventing its use. In the case of PA–MNPs, however, such

aggregation was not observed, probably due to the oriented binding of the antibody, through its Fc region, to the PA on the MNPs (Figure 10).

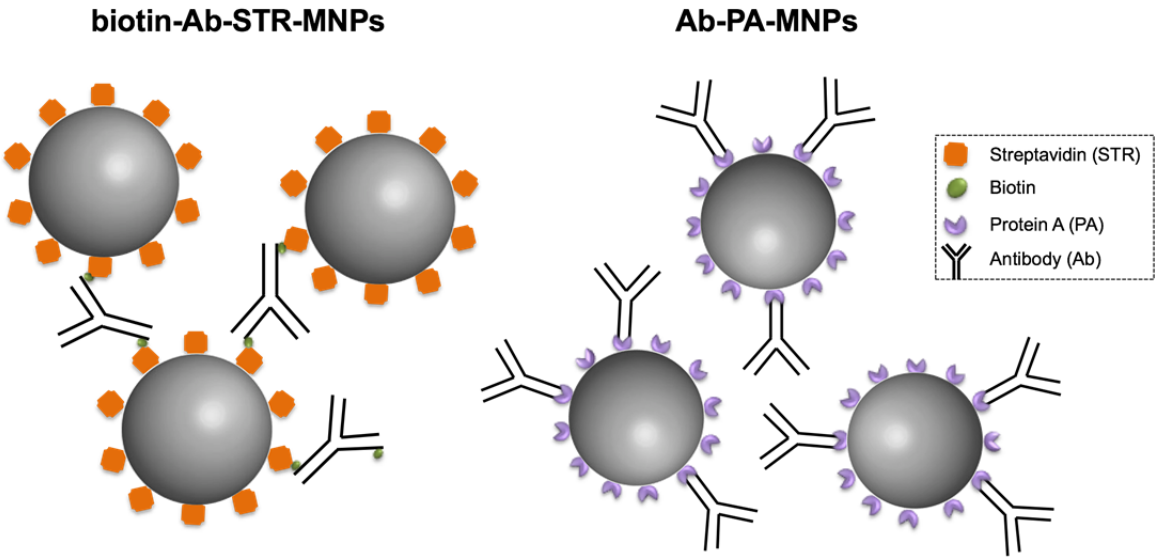

Figure 10 – Schematic representation of magnetic nanoparticle's functionalization with antibodies, using streptavidin (STR) or Protein A (PA) as linker proteins.

Overall, the obtained results indicate that, despite the lower *T* reached when using PA–MNPs, using PA as the linker protein for antibody attachment is a strategy less prone to MNPs' aggregation, and consequently, with less risk of unspecific binding and toxicity. We believe that the MHT efficiency of this strategy may be improved by using bigger MNPs that are magnetically more efficient (higher saturation magnetization).

4. Conclusions

This work describes the challenges of the optimization of protein binding to MNPs. Successful immobilization of distinct proteins was accomplished, reaching satisfactory levels of biomolecules per MNP. The immobilized proteins retained functionality, as supported by the *in vitro* experiments on magnetic hyperthermia using cancer cells. These experiments showed that the higher level of aggregation of STR–MNPs might be contributing for the observed higher temperatures, and consequent low cell viability levels, in particular in the control samples. On the other hand, PA–MNPs appear to be more stable and, therefore, more suitable for biomedical applications.

5. Acknowledgements

V. V.-B. acknowledges Fundação para a Ciência e Tecnologia (FCT, Portugal) for her PhD fellowship (grant SFRH/BD/82556/2011). This work received financial support from project NORTE-01-0145-FEDER-000024, supported by Norte Portugal Regional Operational Programme (NORTE 2020), under the PORTUGAL 2020 Partnership Agreement, through the European Regional Development Fund (ERDF). This work also received co-funding from European Regional Development Fund (ERDF) and Northern Regional Operational Program, Projects ON2-RH-INTEGRATION and NORTE-45-2015-02 Nanotechnology based functional solutions

6. Conflict of interest:

The authors declare that they have no competing interests.

7. References

Banobre-Lopez M, Teijeiro A and Rivas J. 2013. Magnetic nanoparticle-based hyperthermia for cancer treatment. *Rep Pract Oncol Radiother* **18**(6): 397-400.

Baribaud F, Edwards TG, Sharron M, Brelot A, Heveker N, Price K, Mortari F, Alizon M, Tsang M and Doms RW. 2001. Antigenically distinct conformations of CXCR4. *J Virol* **75**(19): 8957-8967.

NanoScale Biomagnetics. "Nanoscale biomagnetics - instrumentation for your ideas." Retrieved Dezember 2016, from http://www.nbnanoscale.com/.

Couto D, Sousa R, Andrade L, Leander M, Lopez-Quintela MA, Rivas J, Freitas P, Lima M, Porto G, Porto B, Carvalho F and Fernandes E. 2015. Polyacrylic acid coated and non-coated iron oxide nanoparticles are not genotoxic to human T lymphocytes. *Toxicol Lett* **234**(2): 67-73.

Fears KP, Petrovykh DY and Clark TD. 2013. Evaluating protocols and analytical methods for peptide adsorption experiments. *Biointerphases* **8**(1): 20.

Galisteo-Gonzalez F and Molina-Bolivar JA. 2014. Systematic study on the preparation of BSA nanoparticles. *Colloids Surf B Biointerfaces* **123**: 286-292.

Garanger E, Weissleder R and Josephson L. 2009. A multifunctional single-attachment-point reagent for controlled protein biotinylation. *Bioconjug Chem* **20**(1): 170-173.

Holmberg A, Blomstergren A, Nord O, Lukacs M, Lundeberg J and Uhlen M. 2005. The biotin-streptavidin interaction can be reversibly broken using water at elevated temperatures. *Electrophoresis* **26**(3): 501-510.

Iversen NK, Frische S, Thomsen K, Laustsen C, Pedersen M, Hansen PB, Bie P, Fresnais J, Berret JF, Baatrup E and Wang T. 2013. Superparamagnetic iron oxide polyacrylic acid coated gamma-Fe_2O_3 nanoparticles do not affect kidney function but cause acute effect on the cardiovascular function in healthy mice. *Toxicol Appl Pharmacol* **266**(2): 276-288.

Jenita JL, Chocalingam V and Wilson B. 2014. Albumin nanoparticles coated with polysorbate 80 as a novel drug carrier for the delivery of antiretroviral drug-efavirenz. *Int J Pharm Investig* **4**(3): 142-148.

Jung Y, Jeong JY and Chung BH. 2008. Recent advances in immobilization methods of antibodies on solid supports. *Analyst* **133**(6): 697-701.

Kelly SM, Jess TJ and Price NC. 2005. How to study proteins by circular dichroism. *Biochimica Et Biophysica Acta-Proteins and Proteomics* **1751**(2): 119-139.

Kolen'ko YV, Bañobre-López M, Rodríguez-Abreu C, Carbó-Argibay E, Sailsman A, Piñeiro-Redondo Y, Cerqueira MF, Petrovykh DY, Kovnir K, Lebedev OI and Rivas J. 2014. Large-scale synthesis of colloidal Fe_3O_4 nanoparticles exhibiting high heating efficiency in magnetic hyperthermia. *The Journal of Physical Chemistry C* **118**(16): 8691-8701.

Koopman G, Reutelingsperger CP, Kuijten GA, Keehnen RM, Pals ST and van Oers MH. 1994. Annexin V for flow cytometric detection of phosphatidylserine expression on B cells undergoing apoptosis. *Blood* **84**(5): 1415-1420.

Kronvall G, Grey HM and Williams RC, Jr. 1970. Protein A reactivity with mouse immunoglobulins. Structural relationship between some mouse and human immunoglobulins. *J Immunol* **105**(5): 1116-1123.

Lin CL, Lee CF and Chiu WY. 2005. Preparation and properties of poly(acrylic acid) oligomer stabilized superparamagnetic ferrofluid. *J Colloid Interface Sci* **291**(2): 411-420.

Lu AH, Salabas EL and Schuth F. 2007. Magnetic nanoparticles: Synthesis, protection, functionalization, and application. *Angewandte Chemie-International Edition* **46**(8): 1222-1244.

MagForce. (2016). "Nanotherm® therapy information for the treatment of brain tumors." Retrieved December 2016, from http://www.magforce.de/en/patienten/beschreibung-der-therapie.html.

Mehta RV, Upadhyay RV, Charles SW and Ramchand CN. 1997. Direct binding of protein to magnetic particles. *Biotechnol Tech* **11**(7): 493–496.

Minelli C, Lowe SB and Stevens MM. 2010. Engineering nanocomposite materials for cancer therapy. *Small* **6**(21): 2336-2357.

Moks T, Abrahmsen L, Nilsson B, Hellman U, Sjoquist J and Uhlen M. 1986. Staphylococcal protein A consists of five IgG-binding domains. *Eur J Biochem* **156**(3): 637-643.

Mu X, Tong Z, Huang Q, Liu B, Liu Z, Hao L, Zhang J, Gao C and Wang F. 2015. Nano-magnetic immunosensor based on staphylococcus protein A and the amplification effect of HRP-conjugated phage antibody. *Sensors (Basel)* **15**(2): 3896-3910.

Peluso P, Wilson DS, Do D, Tran H, Venkatasubbaiah M, Quincy D, Heidecker B, Poindexter K, Tolani N, Phelan M, Witte K, Jung LS, Wagner P and Nock S. 2003. Optimizing antibody immobilization strategies for the construction of protein microarrays. *Anal Biochem* **312**(2): 113-124.

Peng ZG, Hidajat K and Uddin MS. 2004. Adsorption of bovine serum albumin on nanosized magnetic particles. *J Colloid Interface Sci* **271**(2): 277-283.

Prijic S, Prosen L, Cemazar M, Scancar J, Romih R, Lavrencak J, Bregar VB, Coer A, Krzan M, Znidarsic A and Sersa G. 2012. Surface modified magnetic nanoparticles for immuno-gene therapy of murine mammary adenocarcinoma. *Biomaterials* **33**(17): 4379-4391.

Quevedo PD, Behnke T and Resch-Genger U. 2016. Streptavidin conjugation and quantification - a method evaluation for nanoparticles. *Anal Bioanal Chem* **408**(15): 4133-4149.

Sjoholm I. 1975. Protein A from staphylococcus aureus. Spectropolarimetric and spectrophotometric studies. *Eur J Biochem* **51**(1): 55-61.

Sperling RA and Parak WJ. 2010. Surface modification, functionalization and bioconjugation of colloidal inorganic nanoparticles. *Philosophical Transactions of the Royal Society a-Mathematical Physical and Engineering Sciences* **368**(1915): 1333-1383.

Wang TH and Lee WC. 2003. Immobilization of proteins on magnetic nanoparticles. *Biotechnology and Bioprocess Engineering* **8**(4): 263-267.

Wu W, Wu ZH, Yu T, Jiang CZ and Kim WS. 2015. Recent progress on magnetic iron oxide nanoparticles: Synthesis, surface functional strategies and biomedical applications. *Science and Technology of Advanced Materials* **16**(2).

Yang L, Biswas ME and Chen P. 2003. Study of binding between protein A and immunoglobulin G using a surface tension probe. *Biophys J* **84**(1): 509-522.

Zlotnik A. 2006. Chemokines and cancer. *Int J Cancer* **119**(9): 2026-2029.

Supplementary data

Protein A quantification – unsuitable methodologies

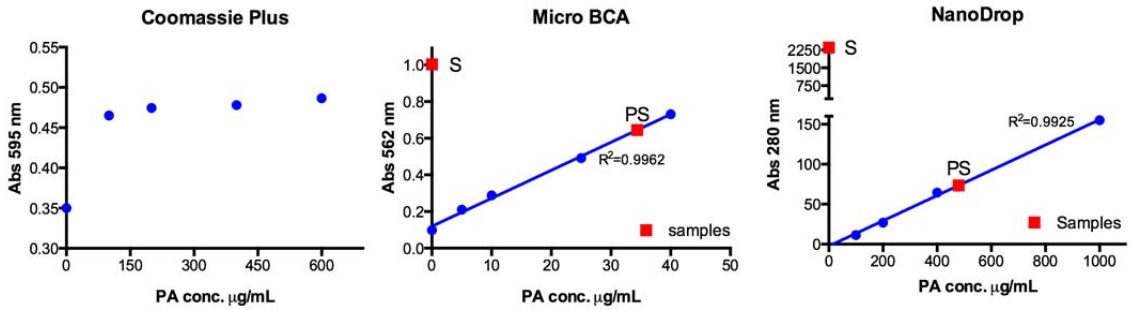

Figure S 1 – Different protein quantification methods tested for PA quantification. Coomassie Plus reagent failed to react with PA and a proper calibration curve could not be established. Although it was possible to establish a calibration curve using Micro BCA (bicinchoninic acid) and protein absorbance at 280 nm (using a NanoDrop spectrophotometer), interferences were detected in the S samples that prevented PA quantification.

Calculation of protein fitting on MNPs surface

The number of protein molecules per unit volume was calculated:

$$Prot\ molec\ per\ L = \frac{mC \times N_a}{M}$$

where mC is the mass concentration (g·L^{-1}), N_a is the Avogadro constant and M is the molecular weight (g·moL^{-1}).

The mass, in grams, of each MNP can be calculated:

$$m = \rho \times \frac{4}{3}\pi r^3$$

where ρ is the density (g·cm^{-3}) and r is the radius of the MNP (cm). Knowing the magnetite concentration (Fe_3O_4mC, g·L^{-1}) of the MNPs, the number of MNPs per unit volume can be roughly estimated:

$$MNP\ per\ L = \frac{Fe_3O_4mC}{m}$$

The number of protein molecules that fit the surface of a MNP was calculated considering the average diameter of the protein and the surface area of the MNP as follows:

$$Prot\ per\ MNP = \frac{4\pi {r_1}^2}{\pi {r_2}^2}$$

where r_1 corresponds to the MNPs' radius and r_2 is the average protein radius.

MANUSCRIPT II

Under review

Manuscript II

Combining the Iron Loading of CXCR4-Targeted and Non-Targeted Nanoparticles to Efficiently Kill Jurkat Cells via Unassisted Magnetically-Induced Hyperthermia

Authors:

Vânia Vilas-Boas[a, b, *], Begoña Espiña[b], Yury V. Kolen'ko[b], Manuel Bañobre-Lopez[b], José Alberto Duarte[c], Verónica Martins[b, #], Dmitri Y. Petrovykh[b], Paulo Freitas[b] and Félix Carvalho[a*]

Affiliations:

[a]UCIBIO-REQUIMTE, Laboratory of Toxicology, Biological Sciences Department, Faculty of Pharmacy, University of Porto, Rua de Jorge Viterbo Ferreira, 228, 4050–313 Porto, Portugal

[b]International Iberian Nanotechnology Laboratory, Av. Mestre José Veiga s/n, 4715-330 Braga, Portugal

[c]CIAFEL, Faculty of Sports, University of Porto, R. Dr. Plácido da Costa 91, 4200-450 Porto, Portugal

* corresponding authors email: vvilasboas@ff.up.pt and felixdc@ff.up.pt

[#] present address: Magnomics, Parque Tecnológico de Cantanhede, Núcleo 04, Lote 2 3060-197 Cantanhede | PORTUGAL

Abbreviations:

ALL – Acute Lymphoblastic Leukaemia

AMF – Alternating magnetic field

AnV–FITC – Annexin-V conjugated with Fluorescein isothiocyanate

BSA – Bovine serum albumin

FBS – Foetal bovine serum

IC – Isotype control

JK – Jurkat cells

LDH – Lactate dehydrogenase

MHT – Magnetic hyperthermia treatment

MNP – Magnetic nanoparticle

MP – Magnetic particle

PBS – Phosphate buffer saline solution

Pi – Propidium iodide

RFU – Relative fluorescence units

SAR – Specific absorption rate

SPION – Super-paramagnetic iron oxide nanoparticle

STS – Staurosporine

T – Temperature

Tc – Constant (plateau) temperature

Abstract:

We describe an *in vitro* anti-cancer treatment strategy that uses a combination of targeted and non-targeted magnetic (nano)particles to kill Jurkat cells *via* magnetically-induced hyperthermia. Jurkat cells are an *in vitro* model of human acute T-cell leukaemia, a hematopoietic cancer that kills around 65 % of the affected adults. Cells are incubated with (non-targeted) poly(acrylic acid)-coated magnetic nanoparticles, followed by incubation with magnetic particles functionalized with anti-CXCR4 antibody, to target the CXCR4 receptor that is highly expressed in these cells. After removing the excess of free (non-interacting) particles, an alternating magnetic field (AMF) is applied to produce magnetic hyperthermia treatment (MHT). This study shows that complete cancer cell death is achieved only when a necrotic, rather than apoptotic, pathway is followed. As expected in this strategy of using two particle populations, this lethal MHT outcome could only be attributed to the combined iron loading resulting from both specific (targeted) and nonspecific (non-targeted) particle populations. This controlled strategy is a rare example of using MHT in a mono-therapeutic context to achieve complete cell death after a 1-h exposure to AMF, making it a promising approach for leukaemia treatment that minimizes potential side effects.

Keywords: magnetic hyperthermia; CXCR4; nanoparticles; cancer treatment; leukaemia

1. Introduction

Susceptibility of cancer cells to different drugs or treatments is commonly evaluated using Jurkat cells as *in vitro* models (Finlay et al. 1993, Black et al. 2016, Daglioglu and Okutucu 2016). These easily handled suspension cells are particularly appropriate models for studies of targeted treatments because Jurkat cells are immortalized T-lymphocytes collected from a patient with Acute Lymphoblastic Leukaemia (ALL), which in clinical oncology typically requires long and aggressive treatments (Inaba et al. 2013). After successful experimental treatments, the Fas-receptor up-regulation in Jurkat cells can be readily exploited to provide a positive control for apoptotic cell death pathway (Kolenko et al. 1999).

The chemokine receptor CXCR4 is a natural choice for targeting Jurkat cells that are known to overexpress it (Crazzolara et al. 2001). The specificity and effectiveness of targeting CXCR4 in ALL cells has been demonstrated using its antagonist AMD3100, which reduced the growth and proliferation of ALL, while having no impact on normal haematopoiesis (Juarez et al. 2007). Potential clinical significance of targeting CXCR4 is emphasized by its association with greater invasive potential and organ infiltration in childhood ALL (Crazzolara et al. 2001). In a more general context, CXCR4 is highly expressed in many other types of tumour cells (Zlotnik 2006), opening possibilities for extending CXCR4-targeting treatments developed using Jurkat cells to other types of cancer.

Magnetic hyperthermia treatment (MHT) is a cancer therapy (Banobre-Lopez et al. 2013) which is currently under phase II clinical trials for glioblastoma treatment (MagForce 2016). MHT exploits the local heat generated by magnetic nanoparticles (MNPs) under an external alternating magnetic field (AMF). Phase I clinical trials showed MHT to be well tolerated with moderate side effects (Wust et al. 2006, Johannsen et al. 2007), and the results collected from the phase II clinical trials on glioblastoma patients were encouraging, leading to a 7.2 to 8.6 months increase in overall survival (Maier-Hauff et al. 2011). Targeting strategies with functionalized nanoparticles, e.g. with antibodies (Zhang et al. 2011) or peptides (Sadhukha et al. 2013), have been proposed in order to improve MHT outcome (Sadhukha et al. 2013, Kruse et al. 2014, Liao et al. 2015, Sadhasivam et al. 2015). Our work pursues a similar volumetric targeting concept, whereby the targeted particles are preferentially retained in the volume with high concentration of cancerous cells.

Mono-therapeutic apoptotic MHT has been characterized in a recent review as “basically ineffective” and “insufficient for cancer treatment” (Lee et al. 2015). The

apparent practical limit on the effectiveness of MHT is encountered despite highly efficient targeting, whether evaluated by the fraction of retained particles or by the concentration of particles associated with individual targeted cells. Accordingly, MHT has been typically used in combination with other therapies (Shah et al. 2014, Yin et al. 2014, Yuan et al. 2014, Espinosa et al. 2016, Hervault et al. 2016), including stereotactic radiotherapy (Maier-Hauff et al. 2011), or anticancer drugs (Kim et al. 2015, Quinto et al. 2015). We hypothesize that instead of supplementing MHT by other therapies it may be possible to enhance the effectiveness of a "pure" MHT strategy by further increasing the total iron loading, which would increase the temperature achieved during MHT and result in 100 % lethal outcome for cancer cells in the targeted volume. Given the apparent limit on iron loading that can be achieved using a single population of targeted (specific) particles, we propose to augment the iron loading by adding a second non-targeted (nonspecific) particle population. As an example, this work describes the development of a therapeutic strategy based on the combined use of both CXCR4-targeted (specific) and non-targeted (nonspecific) magnetic nanoparticles to produce cytotoxic magnetic hyperthermia in leukaemia cells in a mono-therapeutic context, by ensuring that lethal temperatures are reached under an AMF.

2. Materials and Methods

2.1. Reagents

All reagents used in this study were of analytical grade or of the highest grade available. Fetal bovine serum (FBS) was purchased from HyClone UK, Ltd, Northumberland, England, UK. Penicillin (10,000 $U \cdot mL^{-1}$) and streptomycin (10,000 $\mu g \cdot mL^{-1}$), herein referred to as Pen-Strep, RPMI-1640 cell culture medium, sodium pyruvate, nicotinamide adenine dinucleotide reduced form (NADH), triton x-100, caspase-3 fluorimetric substrate N-Acetyl-Asp-Glu-Val-Asp-7-amido-4-methylcoumarin (Ac-DEVD-AMC), 4-(2-Hydroxyethyl)piperazine-1-ethanesulfonic acid (HEPES), 3-[(3-cholamidopropyl)dimethylammonio]-1-propane-sulfonate hydrate (CHAPS), dithiothreitol (DTT), ethylenediaminetetraacetic acid (EDTA), KH_2PO_4, $K_2HPO_4.3H_2O$, CaCl2, NaCl, glycerol, staurosporine (STS) from Streptomyces sp., propidium iodide (Pi), glutaraldehyde solution (25 % in water), hydrochloric acid, sodium cacodylate trihydrate, calcein-AM solution and bovine serum albumin (BSA) were purchased from Sigma-Aldrich, Inc. (St. Louis, MO USA). BD Pharmingen™ FITC labelled Annexin-V (AnV–FITC) was purchased from BD Biosciences (USA). Anti-human CXCR4, clone 12G5, low endotoxin, azide-free monoclonal antibody produced in mouse, and its matched isotype-control,

mouse anti-human monoclonal IgG2a were purchased from BioLegend Inc. (San Diego, CA, USA).

2.2. Cell culture

Human acute T-cell leukaemia cell line Jurkat, clone E6.1, (ATCC® TIB-152™) was purchased from the American Type Culture Collection (Manassas, VA, USA). This cell line was grown in RPMI-1640 medium supplemented with 10 % FBS, 1 % Pen-Strep and maintained in a controlled atmosphere at 37 ºC and 5 % CO_2.

2.3. Incubation of cells with nanoparticles for *in vitro* magnetic hyperthermia

Poly(acrylic acid)-coated magnetic nanoparticles (SPION), with an average iron-oxide core diameter of 17.9 ± 4.4 nm were synthesized and characterized as previously described (Kolen'ko et al. 2014). Two million cells per test condition were resuspended in 1 mL of a 0.362 $g \cdot L^{-1}$ [Fe] SPION suspension in cell culture medium (final sample volume 1 mL), for 2 h, with mild agitation. Samples were then centrifuged at 125 *g* for 5 min and resuspended in 1 mL of a 0.264 $g \cdot L^{-1}$ [Fe] suspension of dextran-coated 250 nm magnetic particles (09-20-252 Nanomag®-D, Micromod Partikeltechnologie GmbH, Rostock, Germany), in 2 % BSA, for 1 h, at 37 ºC, with mild agitation (final sample volume 1 mL). These particles have covalently bound protein-A at their surface, and were previously incubated with CXCR4 or IC antibodies, for 1 h, at 37 ºC, with agitation, to obtain functionalized particles (MP–CXCR4 or MP–IC, respectively). Samples were then centrifuged at 125 *g* for 5 min, washed with cell culture medium, centrifuged again, recovered in 1 mL cell culture medium and transferred to glass vials, previously blocked with BSA, for the MHT experiments. Incubations using only SPION (2 h, 37 ºC, in cell culture medium) or only MP–CXCR4 (1 h, 37 ºC, in 2 % BSA) were also performed.

2.4. Magnetic hyperthermia treatment

The application of the alternating magnetic field (AMF) to the samples described in the preceding section was performed using a magnetic field generator (DM 100, nB nanoScale Biomagnetics, Zaragoza, Spain) operating at 869 kHz and 20 $kA \cdot m^{-1}$ for 30 min, followed by another 30 min period at 554 kHz and 24 $kA \cdot m^{-1}$. The temperature (*T*) of the suspension was measured using an optical temperature probe included in the equipment and the average constant *T* reached in the second step of AMF was called *Tc*. For SAR determination, temperature increases under the same AMF conditions were recorded for suspensions of only SPIONs and only MP in cell culture medium, as

previously suggested (Wildeboer et al. 2014). After AMF application, cells were seeded and subsequently tested to determine the levels of cell viability at successive points in time.

2.5. TEM for SPION uptake studies

Samples were prepared following a previously established protocol (Fraga et al. 2013). Briefly, JK cells with SPION were pelleted at 300 *g* for 5 min, fixed with 2.5 % glutaraldehyde in 0.1 M sodium cacodylate buffer pH 7.4, for 2 h, and rinsed with cacodylate buffer 0.1 M. Samples were then post-fixed in 2 % osmium tetroxide, dehydrated with graded ethanol, embedded in Epon and further placed 2 to 3 days at 60 ºC to promote resin polymerization. Ultrathin (100 nm) sections, contrasted with uranylacetate and lead citrate, were then prepared on cupper grids (300 Mesh) for TEM analysis (Zeiss EM10A, Carl Zeiss, Oberkochen, Germany).

2.6. Confirming specific (targeted) interactions

After incubating cells with MP–CXCR4 or MP–IC, samples were incubated with atto-633 labelled anti-mouse antibody produced in goat (Sigma-Aldrich, Inc., St. Louis, MO USA), for 30 min, at 37 ºC. Samples were further incubated with calcein-AM 0.4 μM, for flow cytometry studies, or calcein-AM 1 μM and then seeded in 8-well μ-slide (Ibidi, Martinsried, Germany) for laser scanning confocal microscopy using a Zeiss LSM 780 confocal microscope. For flow cytometry studies, a S3™ cell sorter (Bio-Rad Laboratories, Hercules, CA), equipped with 488 nm and 561 nm lasers, was used as a flow cytometer to acquire the fluorescence signals in logarithmic mode. JK cell population was defined setting a polygon gate according to their light scattering properties (forward *vs.* side scatter plot) excluding cell debris. Fluorescence due to calcein was followed in FL-1 channel, and atto-633 fluorescence was collected in FL-4. FCS files were analysed using ProSort™ software.

2.7. Iron quantification with inductively coupled plasma optical emission spectroscopy (ICP-EOS)

Cells were incubated with SPION only, MP–CXCR4 only, SPION+MP–CXCR4 or SPION+MP–IC following the procedure and described in section 2.3. For the ICP measurements, samples were digested with 1 mL hydrochloric acid, for 24 h, and then diluted with milli-Q® water (Millipore) to a final volume of 50 mL. Measurements were performed in triplicates, in an ICPE-9000 Multitype ICP Emission Spectrometer (Shimadzu).

2.8. Assessment of MHT-induced cytotoxicity

The effects from the MHT were assessed by flow cytometry using Annexin-V (AnV–FITC) and propidium iodide (Pi) labelling. Caspase-3 activity was assessed using a fluorimetric substrate. Cellular metabolic activity was estimated using PrestoBlue® reduction assay and membrane damage was evaluated through the LDH leakage assay. The anticancer drug staurosporine (STS) was used at 2.5 µM for 1 h as a positive control for apoptotic cell death.

2.8.1. Annexin-V & propidium iodide labelling for flow cytometry

The translocation of phosphatidylserine residues from the inner to the outer leaflet of the cell membrane is considered one of the earliest events of apoptosis (Koopman et al. 1994). A previously described protocol was used with minor modifications (Valente et al. 2012). Briefly, two hours after MHT, 2×10^5 cells were collected in cell culture medium, washed with PBS and resuspended in 200 µL of Annexin-V binding buffer (diluted from the 10x stock solution: 0.1 M HEPES, pH 7.4; 1.4 M NaCl; 25 mM $CaCl_2$) in 2 % BSA, with or without 5 µL of FITC-labelled Annexin-V (AnV–FITC), and kept for 20 min, at room temperature, in the dark. Cells were centrifuged at 210 *g*, 5 min, at 4 ºC and immediately analysed. Propidium iodide (Pi, 1 $\mu g \cdot mL^{-1}$) was used to detect membrane damage in these samples.

Flow cytometry parameters were set as described in section 2.6, using positive and negative controls. Fluorescence collected in FL-1 channel (green fluorescence from AnV–FITC) was plotted *vs.* the one collected in FL-3 channel (red fluorescence from Pi), and the percentage of positive cells for each channel (or both) estimated after establishing the quadrants based on the controls. For each sample, at least 15,000 gated events were counted and distinguished as living cells (AnV–$FITC^-$/Pi^-, lower left quadrant); apoptotic cells (AnV–$FITC^+$/Pi^-, upper left quadrant); late stage apoptosis or necrotic cells (AnV–$FITC^+$/Pi^+, upper right quadrant), and necrotic cells (AnV–$FITC^-$/Pi^+, lower right quadrant).

2.8.2. Caspase-3 activity assay

After MHT, at least 1×10^6 cells per well were seeded in 6-well plates and incubated at 37º C with a controlled atmosphere with 5 % CO2. Cells were collected 24 h after AMF application to check the activation status of caspase-3 protein. Cells were collected on ice, centrifuged at 850 *g*, for 5 min, at 4 ºC, washed with PBS and resuspended in 35 µL of a lysis buffer (50 mM HEPES, 0.1 mM EDTA, 1.63 mM CHAPS supplemented with 1 mM

DTT before using). After vigorously vortexing the samples, these were kept at -80 ºC until analysis.

On the day of analysis, samples were thawed on ice, vortexed and left to equilibrate for 10 min on ice before centrifugation at 16,000 *g*, for 10 min, at 4 ºC. The supernatant was collected to new tubes and the pellet was discarded. For each assay, 10 µL of this supernatant were mixed with 90 µL of an assay buffer (50 mM HEPES, 100 mM NaCl, 1 mM EDTA, 1.63 mM CHAPS, 10 % glycerol supplemented with 10 mM DTT before using), containing 14.8 µM fluorimetric substrate (Ac-DEVD-AMC), and the kinetic reading was immediately started. A Synergy H1 microplate reader (BioTek Instruments, Bad Friedrichshall, Germany) was used to perform the kinetic readings (at 37 ºC; excitation at 380 nm, emission at 460 nm), which lasted for 3 h with successive readings at each 10 min. The amount of protein loaded per well was estimated using Coomassie Plus (Bradford) Protein kit (Thermo Fisher Scientific, Inc., Rockford, IL USA) following manufacturer's instructions. Caspase-3 activity was expressed as the slope of the curve obtained plotting the protein corrected-fluorescence signals *vs.* time ($RFU \cdot \mu g^{-1} \cdot min^{-1}$).

2.8.3. Metabolic rate assay

After MHT, cells were seeded in 96-well plates (15,000 cells per well) and cell viability was assessed 24 and 72 h after AMF application by the addition of 10 µL PrestoBlue® cell viability reagent (Molecular Probes™, Carlsbad, CA) to each well. After incubation at 37 ºC for 3 h, fluorescence signals were collected using a microplate reader (Synergy H1, BioTek Instruments) with excitation wavelength at 560 nm and emission wavelength at 590 nm.

2.8.4. Lactate dehydrogenase (LDH) leakage assay

LDH activity in the cell culture medium was assessed spectrophotometrically following the decrease in absorbance of nicotinamide adenine dinucleotide reduced form (NADH) during the reduction of pyruvate to lactate, as an indicator of membrane disruption, i.e., cell death. A previously described protocol was used with minor modifications (Barbosa et al. 2014). Briefly, after MHT, 20,000 cells were seeded per well in 96-well plates and LDH leakage was assessed 24 and 72 h after AMF application. Fifty µL of cell culture medium were collected per well (to measure extracellular LDH content) and replaced by 50 µL of a 0.5 % triton X-100 solution in cell culture medium (to induce cell lysis). After incubating for 1 h, at 37 ºC, 25 µL of cell culture medium were collected to a new plate, for LDH measurements after the full kill. The collected medium

was mixed with 200 µL of reagent solution containing 0.21 mM NADH, dissolved in LDH buffer (33.3 mM KH_2PO_4 and 66.7 mM $K_2HPO_4.3H_2O$, pH 7.4). The reaction was started with 25 µL sodium pyruvate (22.7 mM, prepared in LDH buffer) and the kinetic conversion of NADH into NAD^+ was followed for 5 min, at 340 nm, in a microplate reader (Synergy H1, Bio-Tek Instruments). The final volume of reaction in each well was previously set to 275 µL with LDH buffer. Final results of LDH released into the extracellular medium (LDH leakage), were expressed as cell death values calculated as previously described (Barbosa et al. 2014).

2.9. Statistical analysis

All data are presented as mean±standard deviation (SD), except when stated otherwise, of at least three independent experiments performed in triplicate whenever possible. Normality of the data distribution was assessed applying three tests: KS normality test, D'Agostino and Pearson omnibus normality test and Shapiro-Wilk normality test. Differences between the average *Tc* were estimated using ordinary two-way ANOVA followed by Dunnett's multiple comparisons post test. In the AnV–FITC/ Pi double staining, PrestoBlue® and LDH experiments, differences between controls and treatments at each time-point were estimated using ordinary two-way ANOVA followed by Tukey's multiple comparisons test. For the caspase-3 activity experiments, the change of the protein corrected-fluorescence signal with incubation time ($RFU \cdot \mu g^{-1} \cdot min^{-1}$) was determined by linear regression analysis for each control or treatment and plotted as caspase-3 activity values. Differences in caspase-3 activity values were estimated using one-way ANOVA (Kruskall-Wallis) followed by Dunn's multiple comparisons test. P values under 0.05 were considered statistically significant.

3. Results and discussion

3.1. Selecting AMF parameters

For practical implementation of the strategy where each of the two nanoparticle populations controls one of the factors contributing to the overall MHT efficiency, it is critical to ensure that neither population alone produces lethal heating under AMF (Figure 1).

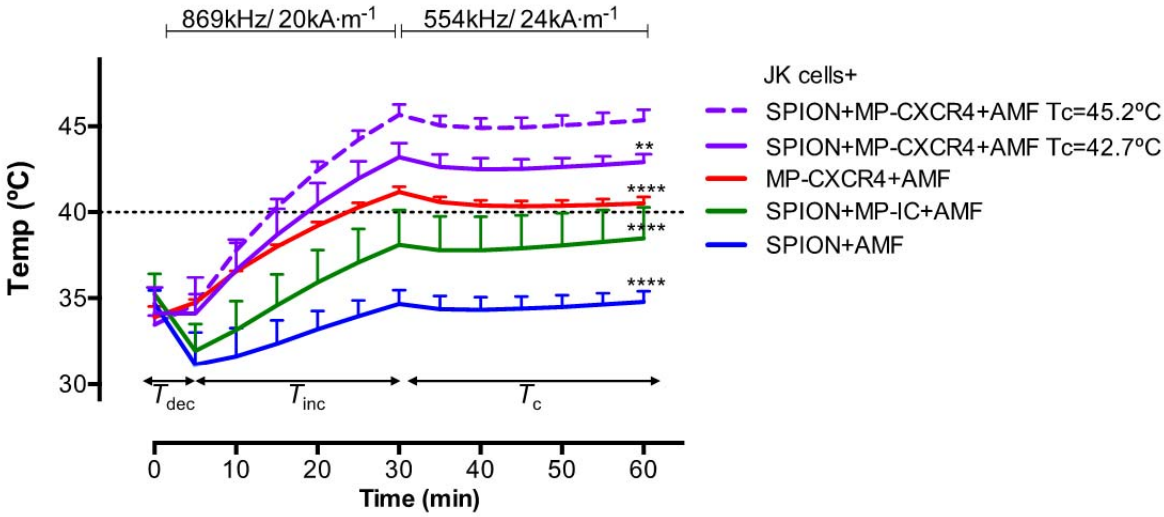

Figure 1 – Heating profiles of Jurkat cells incubated with SPION and/or antibody-functionalized MPs.
The samples were submitted to an alternating magnetic field for 1 h, as outlined in the graph, until a constant temperature (*T*c) was reached. The graph shows an initial sample's chilling due to lack of thermal insulating system (T_{dec}), followed by a *T* increase after the thermal barrier is overcome (T_{inc}), and a final stabilization phase for the last 30 min of MHT (*T*c). When a combination of SPION and CXCR4-functionalized MPs were used, average *T*c of 42.7 or 45.2 ºC were observed. The curves represent the mean±SD of two to four independent experiments. Differences between the average *Tc* were estimated using ordinary two-way ANOVA followed by Dunnett's multiple comparisons test. **p<0.01 JK+SPION+MP–CXCR4+AMF Tc=45.2ºC *vs.* JK+SPION+MP–CXCR4+AMF Tc=42.7ºC; ****p<0.0001 JK+SPION+MP–CXCR4+AMF Tc=45.2ºC *vs.* any of the other tested conditions.

After an optimization of AMF parameters (Figures S1 and S2 in SI†), the heating profile in our experiments matched that recommended in a recent review for optimal MHT (Dutz and Hergt 2014). AMF was applied following a two-step process, whereby temperature (*T*) mainly rises during the first AMF step (30 min, 869 kHz, 20 kA·m^{-1}) (T_{inc}) and stabilizes in the second AMF step (30 min, 554 kHz, 24 kA·m^{-1}) at a constant temperature (*Tc*) that depends on the particles used and their functionalization.

A minor artefact related to a limitation of our equipment, during the initial phase, a decrease of temperature can be observed for all samples (T_{dec}), due to the time needed for the heating to be effective after placing the samples, pre-incubated at 37 ºC, inside the coil. This artefact would not be applicable in a living organism.

3.2. Two nanoparticle populations

The two independent particle populations of our MHT strategy were implemented by design to have specific (targeted) and nonspecific (non-targeted) interactions, respectively, with cancer cells.

For the specifically interacting population, we functionalized protein-A-modified 250 nm magnetic particles with an anti-CXCR4 antibody (MP–CXCR4) that is able to recognize and target the highly overexpressed CXCR4 in JK cells (Figure S3 in SI†). Although some nonspecific retention of particles was observed, the surface targeting of JK cells with these functionalized particles (JK+MP–CXCR4) was confirmed by flow cytometry and laser scanning confocal microscopy, whereby antibodies attached to the MPs were labelled with fluorescent secondary antibodies (Figure 2).

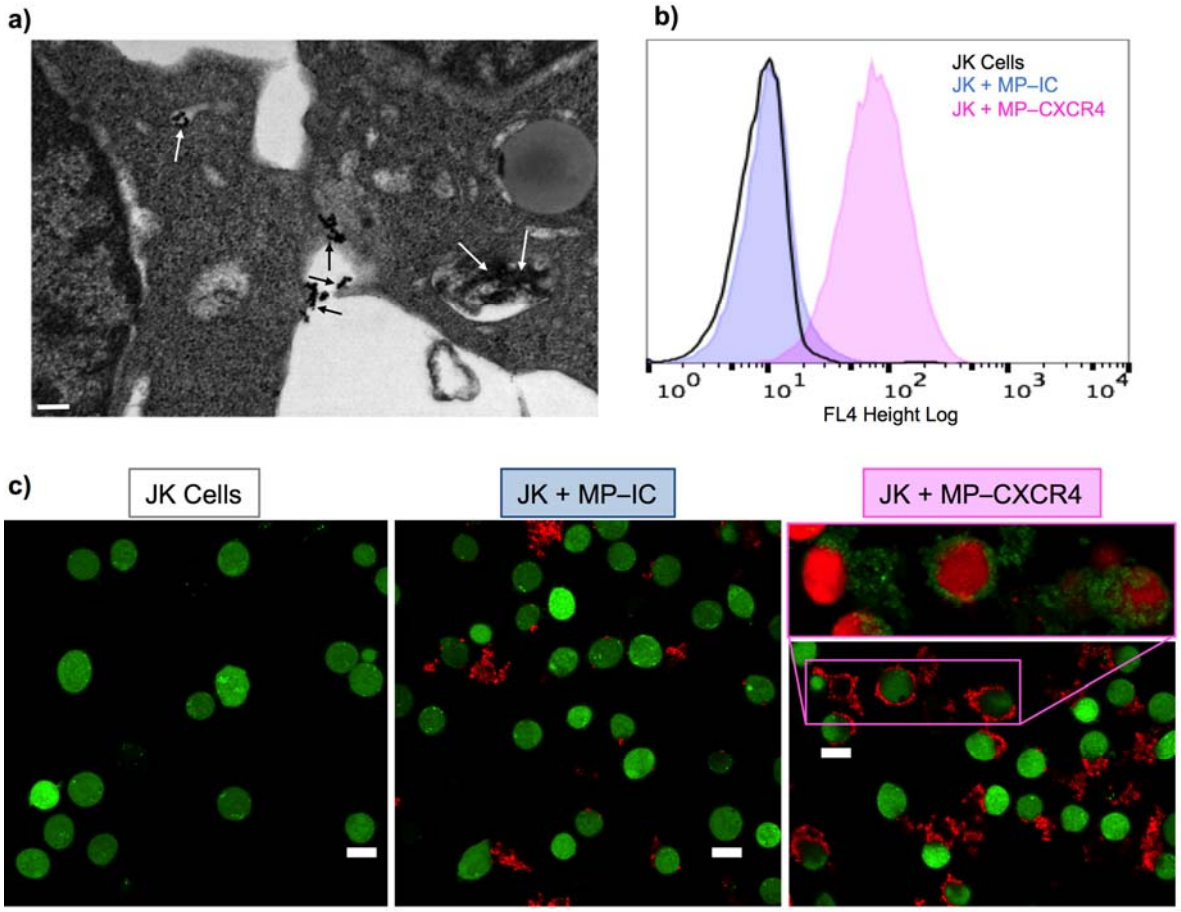

Figure 2 – Studying the interaction between SPIONs, MPs and cells.
a) Transmission Electron Microscopy (TEM) micrograph showing Jurkat cells (JK) with SPION internalized in endosomal compartments (white arrows) or adherent to the cell membrane (black arrows). Scale bar is 200 nm. JK cells labelled with calcein-AM were incubated with IC- or CXCR4-functionalized particles and analysed using **b)** flow cytometry and **c)** laser scanning confocal fluorescence microscopy. A fluorescently labelled secondary antibody (atto-633 IgG) was used to detect the antibodies attached to the particles. Flow cytometry measurements (b) show an increase in the mean fluorescence intensity emitted by JK cells (selected as calcein-positive events) on the atto-633 detection channel (FL4) when using CXCR4-functionalized particles, indicating these particles are recognising and binding to these cells. These results were further confirmed by laser scanning confocal fluorescence microscopy (c), which showed JK cells (staining green) surrounded by CXCR4-functionalized particles (staining red, right panel). Scale bar is 10 µm The insert shows a zoomed 3D detail of the selected area, with reversed colouring for better visualization.

Both techniques (Figure 2b and c) showed increased fluorescence in cells targeted with MP–CXCR4 in comparison to cells only (JK) and cells with MP–IC (MPs functionalized with an isotype control antibody, IC). The complex 3D microstructures formed by agglomerates of fluorescently labelled MP–CXCR4 particles around the JK cells are highlighted in the 3D view inset (Figure 2c, right panel). This targeted association of MP–CXCR4 particles with JK cells was further corroborated by ICP-OES results (Table 1) that showed retention of 92.4 % of the MP–CXCR4 particles by JK cells, after incubation followed by removal of free particles.

As the nonspecifically interacting population, 18-nm-core super-paramagnetic iron oxide nanoparticles (SPIONs) were used in this work because of their efficient heating ability. SPIONs were synthesized and characterized as previously reported (Kolen'ko et al. 2014). Unlike the specific MP–CXCR4 particles, only 2.4 % of these nonspecific SPIONs become associated with JK cells after incubation followed by removal of free particles (Table 1). This modest uptake is corroborated by TEM imaging that shows only a minimal number of SPIONs associated with the cell membrane (Figure 2a, black arrows), in contrast to the extensive adsorption and agglomeration of MP–CXCR4 particles at JK cell surfaces (Figure 2c, right panel). Uptake of some SPIONs into endosomal compartments in JK cells is also evident in the TEM image (Figure 2a, white arrows).

For either particle population independently, the *Tc* reached under AMF was relatively low: 34.5 ºC for the JK+SPIONs and 40.5 ºC for the JK+MP–CXCR4 samples (Figure 1). The MHT treatment did not induce perceptible cytotoxicity in the presence of SPIONs alone (Figure S4 in SI†). The higher *Tc* reached for JK+MP–CXCR4 samples lead to an increase of caspase-3 activity, however it did not produce a significant effect on viability of targeted cells (Figure S4 in SI†). Given the >90 % retention of the MP–CXCR4 particles by JK cells, further optimization of the targeting is unlikely to increase the iron loading sufficiently to produce significant cytotoxicity in targeted cells. Conversely, supplementing the specific MP–CXCR4 particles with a second (nonspecific) SPION population opens the possibility for a more substantial increase in iron loading and the associated effectiveness of MHT. The high SAR of our SPIONs (261 $W \cdot g^{-1}$ *vs.* 220 $W \cdot g^{-1}$ for MP–CXCR4 particles), under the AMF conditions used in this work, further supports the practicality of the two-population strategy.

3.3. Sequential incubation with two nanoparticle populations

The incubation procedure involved four steps: first, a 2 h-incubation of cells with SPIONs (0.362 $g \cdot L^{-1}$ Fe); second, removing the excess of free SPIONs; third, a 1 h-

incubation with MP–CXCR4 (0.264 $g \cdot L^{-1}$ Fe); and fourth, removing the excess of free MPs. Following the two washing steps, the total iron concentration during AMF application was measured using ICP-OES and calculated to be 0.309 $g \cdot L^{-1}$ (≈ 5.5 mM) in the JK+SPION+MP–CXCR4 samples and 0.168 $g \cdot L^{-1}$ (≈ 3.0 mM) in the JK+SPION+MP–IC samples (Table 1). This represents nearly 50 and 27 %, respectively, of the total initial iron amount these samples were exposed to (0.626 $g \cdot L^{-1}$, ≈ 11.2 mM, Table 1).

Table 1 – Iron quantification by Inductively Coupled Plasma - Optical Emission Spectrometry

Sample	Initial Fe [$g \cdot L^{-1}$]	Average Fe/ sample [$g \cdot L^{-1}$]	% particle retention[a]
JK+SPION	0.362	0.0087±0.0043	2.4
JK+MP-CXCR4	0.264	0.2440±0.0254	92.4
JK+SPION+MP-CXCR4	0.626	0.3090±0.0042	49.4
JK+SPION+MP-IC	0.626	0.1680±0.0212	26.8

[a]The percentage of particle retention was calculated as 100× ratio between the average Fe/ sample and the respective initial Fe, for each sample. Results are mean±SD of two independent experiments.

Flow cytometry data obtained after co-incubation of cells and nanoparticles (Figure 3) indicate that both particle populations interact with the cells, showing different light scattering properties (in forward scatter, FSC, and side scatter, SSC, detectors) depending on the type of particles. Similar data have been previously interpreted as a proof of cell-particle interactions (Poirier et al. 2014).

Figure 3 clearly shows the movement of the gated events up on the SSC-Height axis, related to cell granularity or internal complexity, from a JK cells-only sample (31.1 ± 4.9) to JK+SPIONs (73.4 ± 0.6; $p<0.0001$), and then to JK+MP–CXCR4 (135.0 ± 7.6; $p<0.0001$). When a combination of both particles was used, features of both scattering patterns of cell-particle events were observed, reaching an intermediate SSC value (90.1 ± 11.8; $p<0.0001$ *vs.* JK+MP–CXCR4). Observing evidence of interactions with both types of particles, in particular, indicates that SPIONs associated with the cells during the first step do not block the subsequent MP–CXCR4 interaction with the cell surface.

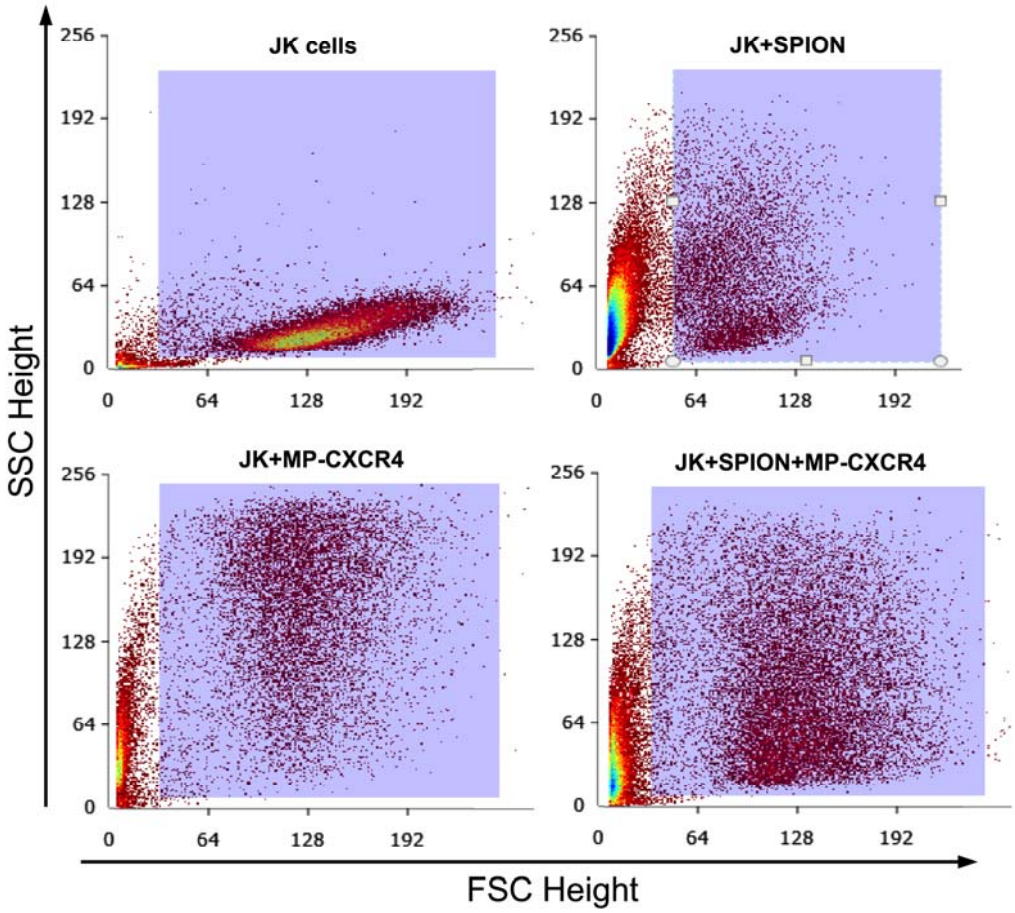

Sample	FSC Height	SSC Height
JK cells	121.4 ± 8.2	31.1 ± 4.9
JK+SPION	80.9 ± 1.7	73.4 ± 0.6****
JK+MP-CXCR4	101.8 ± 9.3	135.0 ± 7.6****
JK+SPION+MP-CXCR4	105.8 ± 6.5	90.1 ± 11.8****

Figure 3 – Light scattering properties of Jurkat cells incubated with SPION and/or antibody-functionalized MPs.
Flow cytometry data showing changes in light scattering properties due to the presence of different nanoparticles, alone or in combination, an indication of interaction between particles and cells. The mean±SD values collected by the forward and side scatter detectors, from three independent experiments, are presented in the table. Differences were estimated using ordinary two-way ANOVA followed by Tukey's multiple comparisons test. ****p<0.0001 *vs.* JK cells only or the selected sample

3.4. MHT outcome

As expected, the cytotoxic effects of MHT were observed only after cells were treated with a combination of both nanoparticle populations (Figures 4 and 5). In other words, a lethal MHT outcome could only be attributed to the combined iron loading resulting from both specific and nonspecific interactions. This exclusive attribution is supported by the

absence of significant cytotoxicity in all negative controls (Figures 4 and 5): whenever AMF was not applied (JK+SPION+MP–IC and JK+SPION+MP–CXCR4 samples) or the matched IC antibody was used (JK+SPION+MP–IC+AMF samples). In particular, no significant effects on cell viability were observed in all the negative controls that included only the putatively nonspecific SPIONs (Figure S4). As a positive control, STS, yielded apoptotic signatures in the assays, in agreement with previous reports (Ullal and Pisetsky 2010). Given the complexity of the samples systematically compared in these measurements, we have to evaluate the results based on the aggregate parameters, such as heating curves, *Tc* values, and cell death outcomes.

3.5. Apoptotic *vs.* necrotic outcome

Serendipitously, after MHT experiments we observed both apoptotic and necrotic outcomes that strongly correlated with the average reached *Tc*: 42.7 ºC and 45.2 ºC, respectively (Figure 1, purple curves).

In the first outcome group (n=4, *Tc*=42.7 ºC), results suggest the cell death pathway to be predominantly apoptotic, as caspase-3 activity was significantly induced (Figure 4a, $p<0.05$). Unexpectedly for a classical apoptotic pathway, we found only low levels of AnV^+ cells for JK+SPION+MP–CXCR4+AMF Tc=42.7ºC samples (Figure 4b), which could be related to an interference of the MNPs with the standard AnV assay. The positive control for an apoptotic cell death, STS, clearly increased the number of AnV^+ cells, representing the apoptotic pathway (Figure 4b and c).

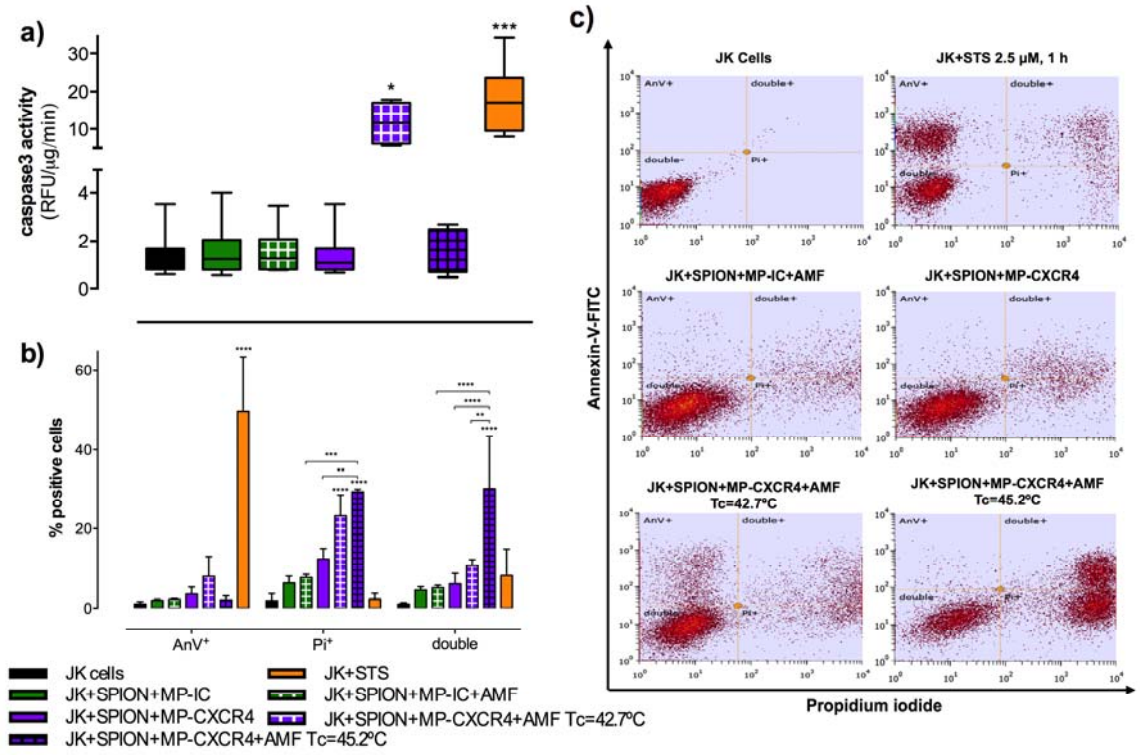

Figure 4 – Apoptosis-induction studies after MHT.
a) An induction of caspase-3 activity was observed in JK+SPION+MP–CXCR4+AMF samples when *Tc* was 42.7 ºC and in the tested positive control for apoptosis, staurosporine (STS). Differences between each treatment and untreated control were estimated using ordinary two-way ANOVA followed by Tukey's multiple comparisons test. **b)** and **c)** Incubation with AnV–FITC and Pi dyes was performed 2 h after AMF application. The percentage of cells staining positive for each dye individually or together are shown for each treatment/ control. A significant increase in Pi^+ cells was observed in JK+SPION+MP–CXCR4+AMF samples, compared to all tested controls, independently of the average reached *Tc*. When an average 45.2 ºC were reached, a significant increase in the double stained events was also observed, showing a total of around 60% dead cells, as short as 2 h after MHT treatment. STS induced a significant increase in the percentage of AnV^+ cells, as expected in an apoptotic cell death pathway. Values are mean+SD of at least three independent experiments. Differences were estimated using one-way ANOVA (Kruskal-Wallis) followed by Dunn's multiple comparisons test. *p<0.05; **p<0.01, ***p<0.001 and ****p<0.0001 *vs.* untreated cells or *vs.* the referred control.

In the second outcome group, for which *Tc* reached 45.2 ºC (*n*=4), a more destructive scenario was observed, as illustrated in Figure 4c by representative plots of AnV and Pi double staining to study apoptosis. In this outcome group, nearly 60 % of the cells stained either Pi or Pi and AnV double positive, as early as 2 h after MHT (Figure 4b and c), indicating cell membrane damage. These results, along with the lack of caspase-3 activation, are indicative of a necrotic pathway for cell death. Furthermore, cell viability dropped to zero in these samples, 72 h after MHT (Figure 5), demonstrating the high effectiveness of the treatment.

Notably, when an apoptotic pathway was activated (i.e. JK+STS and JK+SPION+MP–CXCR4+AMF Tc=42.7ºC samples) a slightly different outcome was

registered, as cell death was significant but not complete. This fact suggests treatments that induced necrotic pathway to be more effective than the apoptotic pathway, in terms of cancer cell death in the present study, in agreement with previous conclusions about insufficient effectiveness of apoptotic MHT (Lee et al. 2015).

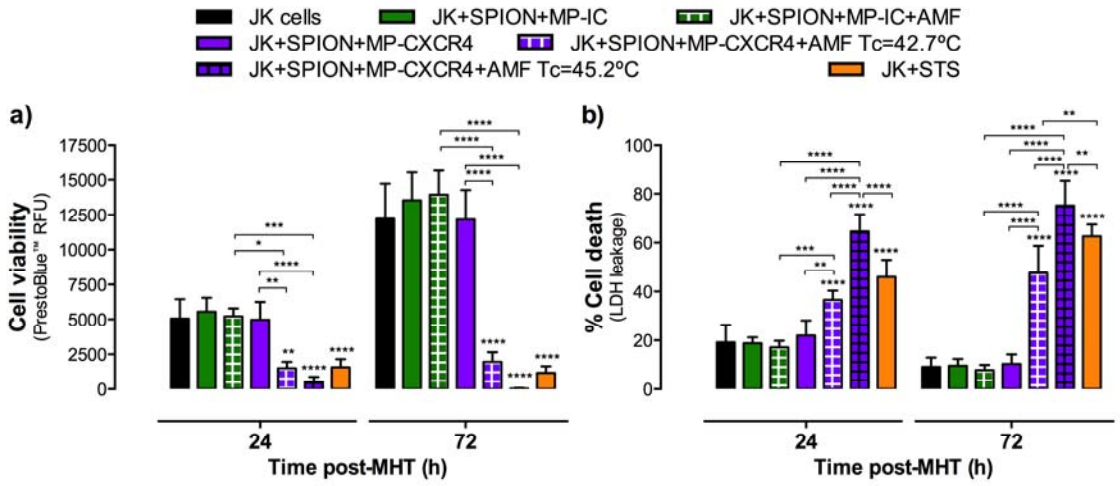

Figure 5 - Cell viability and cell death rates after AMF application.
a) PrestoBlue® reagent was used to measure cellular metabolic activity after AMF application and the emitted fluorescence was compared as a measure of cell viability. Clearly significant differences in cell viability were observed for the JK+SPION+MP–CXCR4+AMF samples when compared to all the tested controls, in both studied time-points (24 and 72 h post-MHT), and independently of the reached *Tc*. Cell viability values after 72 h drastically dropped to zero when the highest *Tc* was achieved. **(b)** Accordingly, the LDH leakage assay results showed a significant increase in cell death levels in JK+SPION+MP–CXCR4+AMF samples. Results are mean+SD of at least four independent experiments performed in triplicate. Differences were estimated using ordinary two-way ANOVA, followed by Tukey's multiple comparison *post* test. *p<0.05; **p<0.01; ***p<0.001 and ****p<0.0001 *vs.* untreated cells or *vs.* the referred sample.

Observing different outcomes under identical initial conditions may seem counterintuitive, however, as previously reported (Guardia et al. 2012), the natural variability of the cell-nanoparticle system, including differences between batches of particles and antibodies, can lead to different plateau *T*. This natural variability highlights a speculative advantage of using two independent particle populations, whereby insufficient specific iron loading could be augmented by the nonspecific population as necessary.

3.6. Comparative MHT efficiency

Despite the extensive literature on MHT, none could be directly compared to our work because, first, only a few reports refer to the use of MHT in leukaemia cells (Giustini et al. 2011, Ren et al. 2012), and second, CXCR4-targeting MNPs have only been previously reported as MRI contrast agents for pancreatic cancer, i.e., in a context of cancer diagnostics (He et al. 2012, Zevon et al. 2015). Accordingly, the following discussion will

rely on comparisons to studies that used cell lines, targeting and operating conditions different from ours.

The variety of criteria to evaluate the practicality and efficiency of the proposed MHT notwithstanding, we find that our treatment compares very favourably to those reported in the literature. For example, *in vitro* MHT studies using CREKA-functionalized MNPs reported a 60 % decrease in cell viability under AMF conditions similar to ours (Kruse et al. 2014). Considering the required iron concentration provides an insightful context for this impressive result. In our work AMF was applied after removing the excess free particles that are not associated with the cells. We note that in reference (Kruse et al. 2014) the AMF was applied without removing the excess of free particles and, thus, the total iron concentration was more than 7× higher than that used in our work (2.2 *vs.* 0.3 $g \cdot L^{-1}$, respectively). Other studies using functionalized MNPs observed similar MHT efficiency outcomes, however, a quantitative comparison in terms of iron concentration is not possible because only overall mass-concentration of nanoparticles was reported (Liao et al. 2015, Sadhasivam et al. 2015).

In an example using non-targeted nanoparticles, Guardia and co-authors reported a 50–100 % decrease in cell viability *in vitro* in an experiment using magnetic nanocubes (Guardia et al. 2012). The heating power provides an important basis for the comparison of different AMF protocols for MHT. Specifically, the heating power is an increasing function of the product of the field amplitude H and the frequency f ($H \cdot f$ product), which therefore provides a quantitative index of the heating power for a given AMF protocol. In terms of the overall heating efficiency, in both reference (Guardia et al. 2012) and our work, samples reached 43 ºC after a 1 h AMF application. This suggests an approximately linear effect of both AMF power and iron concentration on the heating efficiency, as we used 8× higher $H \cdot f$ product (the maximum of 17.4×10^9 *vs.* 2.2×10^9 $A \cdot m^{-1} \cdot s^{-1}$) and a 6.5–13× lower iron concentration (0.309 *vs.* 2.0–4.0 $g \cdot L^{-1}$ Fe, respectively) to achieve a similar Tc. In terms of the cell death outcome, in our strategy decreasing cell viability from ca. 15 % to ca. 0 % (after 72 h) required an increase of T of only 2.5 ºC, whereas with magnetic nanocubes a T increase of 22 ºC (up to 65 ºC), and a concomitant increase in iron concentration to 5 $g \cdot L^{-1}$ (16× higher than the one used in this work), was reported for reaching 100 % cell death (Guardia et al. 2012). In our approach, a shorter incubation time (3 h *vs.* 24 h) was sufficient to reach this outcome. Another previous study that reported SAR values comparable to ours while using AMF with a lower $H \cdot f$ product similarly relied on a proportionally higher total iron concentration (Hayashi et al. 2013).

We find the outlook for our strategy of combining specific and nonspecific populations of nanoparticles for MHT to be promising both in terms of efficiency and the potential range of applications. As discussed above, the efficiency of MHT—evaluated via either heating or cell death outcome—achieved in our strategy favourably compares to those reported in the literature (Giustini et al. 2011, Guardia et al. 2012, Kruse et al. 2014). Furthermore, our strategy could enhance other implementations of MNP-based cancer therapies. First, it provides a straightforward approach to reaching cytotoxic magnetic hyperthermia whenever specific (targeted) iron content alone is insufficient, particularly in a mono-therapeutic regimen. Second, it suggests the possibility of a broader (e.g., tissue-wide or even systemic) application of non-targeted nanoparticles, combined with a more localized and/or targeted strategy. Crucially, the localization of cytotoxic MHT under this strategy remains defined by the specific (targeted) particles, i.e., unaffected by the supplemental nonspecific particle population. Furthermore, a lower (and more easily manageable) concentration of each component would be required. Finally, our strategy can directly benefit from all the enhancements of MHT that have been proposed in the literature, including a combination of hyperthermia with chemotherapy agents (Kim et al. 2015, Quinto et al. 2015), or with photothermal therapy (by taking advantage of both magnetic and photothermal properties of iron oxide nanoparticles) (Espinosa et al. 2016), or by confining the MHT region using a static magnetic field (Ma et al. 2015).

4. Conclusions

This work describes an efficient *in vitro* magnetic hyperthermia methodology to achieve complete death of Jurkat cells using a combination of CXCR4-targeted and non-targeted magnetic nanoparticles. As expected in our strategy, this lethal MHT outcome could only be attributed to the combined iron loading resulting from both specific (targeted) and nonspecific (non-targeted) particle populations. This controlled strategy is a rare example of using MHT in a mono-therapeutic context to achieve complete cell death after a 1-h exposure to AMF, therefore proving its promise for future *in vivo* evaluations.

5. Acknowledgements

V. V.-B. acknowledges Fundação para a Ciência e Tecnologia (FCT, Portugal) for her PhD fellowship (grant FRH/BD/82556/2011). This work received financial support from project NORTE-01-0145-FEDER-000024, supported by Norte Portugal Regional

Operational Programme (NORTE 2020), under the PORTUGAL 2020 Partnership Agreement, through the European Regional Development Fund (ERDF)".

B. E. acknowledges the co-funding from European Regional Development Fund (ERDF); and Northern Regional Operational Program, Projects ON2-RH-INTEGRATION and NORTE-45-2015-02 Nanotechnology based functional solutions.

6. Conflict of interest:

The authors declare that they have no competing interests.

†***Supporting Information (SI)****:* Supporting Information is available, reporting on the optimization of AMF parameters and the expression of CXCR4 in Jurkat cells.

7. References

Banobre-Lopez M, Teijeiro A and Rivas J. 2013. Magnetic nanoparticle-based hyperthermia for cancer treatment. *Rep Pract Oncol Radiother* **18**(6): 397-400.

Barbosa DJ, Capela JP, Silva R, Vilas-Boas V, Ferreira LM, Branco PS, Fernandes E, Bastos Mde L and Carvalho F. 2014. The mixture of "ecstasy" and its metabolites is toxic to human SH-SY5Y differentiated cells at in vivo relevant concentrations. *Arch Toxicol* **88**(2): 455-473.

Black M, Barsoum IB, Truesdell P, Cotechini T, Macdonald-Goodfellow SK, Petroff M, Siemens DR, Koti M, Craig AWB and Graham CH. 2016. Activation of the PD-1/PD-l1 immune checkpoint confers tumor cell chemoresistance associated with increased metastasis. *Oncotarget* **7**(9): 10557-10567.

Crazzolara R, Kreczy A, Mann G, Heitger A, Eibl G, Fink FM, Mohle R and Meister B. 2001. High expression of the chemokine receptor CXCR4 predicts extramedullary organ infiltration in childhood acute lymphoblastic leukaemia. *Br J Haematol* **115**(3): 545-553.

Daglioglu C and Okutucu B. 2016. Synthesis and characterization of AICAR and DOX conjugated multifunctional nanoparticles as a platform for synergistic inhibition of cancer cell growth. *Bioconjug Chem* **27**(4): 1098-1111.

Dutz S and Hergt R. 2014. Magnetic particle hyperthermia - a promising tumour therapy? *Nanotechnology* **25**(45): 452001.

Espinosa A, Di Corato R, Kolosnjaj-Tabi J, Flaud P, Pellegrino T and Wilhelm C. 2016. Duality of iron oxide nanoparticles in cancer therapy: Amplification of heating efficiency by magnetic hyperthermia and photothermal bimodal treatment. *ACS Nano* **10**(2): 2436-2446.

Finlay GJ, Marshall E, Matthews JH, Paull KD and Baguley BC. 1993. In vitro assessment of n-[2-(dimethylamino)ethyl]acridine-4-carboxamide, a DNA-intercalating antitumour drug with reduced sensitivity to multidrug resistance. *Cancer Chemother Pharmacol* **31**(5): 401-406.

Fraga S, Faria H, Soares ME, Duarte JA, Soares L, Pereira E, Costa-Pereira C, Teixeira JP, de Lourdes Bastos M and Carmo H. 2013. Influence of the surface coating on the cytotoxicity, genotoxicity and uptake of gold nanoparticles in human HepG2 cells. *J Appl Toxicol* **33**(10): 1111-1119.

Giustini AJ, Gottesman RE, Petryk AA, Rauwerdink AM and Hoopes PJ. 2011. Kinetics and pathogenesis of intracellular magnetic nanoparticle cytotoxicity. *Proc SPIE Int Soc Opt Eng* **7901**.

Guardia P, Di Corato R, Lartigue L, Wilhelm C, Espinosa A, Garcia-Hernandez M, Gazeau F, Manna L and Pellegrino T. 2012. Water-soluble iron oxide nanocubes with high values of specific absorption rate for cancer cell hyperthermia treatment. *ACS Nano* **6**(4): 3080-3091.

Hayashi K, Nakamura M, Sakamoto W, Yogo T, Miki H, Ozaki S, Abe M, Matsumoto T and Ishimura K. 2013. Superparamagnetic nanoparticle clusters for cancer theranostics combining magnetic resonance imaging and hyperthermia treatment. *Theranostics* **3**(6): 366-376.

He Y, Song W, Lei J, Li Z, Cao J, Huang S, Meng J, Xu H, Jin Z and Xue H. 2012. Anti-CXCR4 monoclonal antibody conjugated to ultrasmall superparamagnetic iron oxide nanoparticles in an application of MR molecular imaging of pancreatic cancer cell lines. *Acta Radiol* **53**(9): 1049-1058.

Hervault A, Dunn AE, Lim M, Boyer C, Mott D, Maenosono S and Thanh NT. 2016. Doxorubicin loaded dual pH- and thermo-responsive magnetic nanocarrier for combined magnetic hyperthermia and targeted controlled drug delivery applications. *Nanoscale* **8**(24): 12152-12161.

Inaba H, Greaves M and Mullighan CG. 2013. Acute lymphoblastic leukaemia. *Lancet* **381**(9881): 1943-1955.

Johannsen M, Gneveckow U, Taymoorian K, Thiesen B, Waldofner N, Scholz R, Jung K, Jordan A, Wust P and Loening SA. 2007. Morbidity and quality of life during thermotherapy using magnetic nanoparticles in locally recurrent prostate cancer: Results of a prospective phase i trial. *Int J Hyperthermia* **23**(3): 315-323.

Juarez J, Dela Pena A, Baraz R, Hewson J, Khoo M, Cisterne A, Fricker S, Fujii N, Bradstock KF and Bendall LJ. 2007. CXCR4 antagonists mobilize childhood acute lymphoblastic leukemia cells into the peripheral blood and inhibit engraftment. *Leukemia* **21**(6): 1249-1257.

Kim HC, Kim E, Jeong SW, Ha TL, Park SI, Lee SG, Lee SJ and Lee SW. 2015. Magnetic nanoparticle-conjugated polymeric micelles for combined hyperthermia and chemotherapy. *Nanoscale* **7**(39): 16470-16480.

Kolen'ko YV, Bañobre-López M, Rodríguez-Abreu C, Carbó-Argibay E, Sailsman A, Piñeiro-Redondo Y, Cerqueira MF, Petrovykh DY, Kovnir K, Lebedev OI and Rivas J. 2014. Large-scale synthesis of colloidal Fe_3O_4 nanoparticles exhibiting high heating efficiency in magnetic hyperthermia. *J Phys Chem C* **118**(16): 8691-8701.

Kolenko V, Uzzo RG, Bukowski R, Bander NH, Novick AC, Hsi ED and Finke JH. 1999. Dead or dying: Necrosis versus apoptosis in caspase-deficient human renal cell carcinoma. *Cancer Res* **59**(12): 2838-2842.

Koopman G, Reutelingsperger CP, Kuijten GA, Keehnen RM, Pals ST and van Oers MH. 1994. Annexin V for flow cytometric detection of phosphatidylserine expression on B cells undergoing apoptosis. *Blood* **84**(5): 1415-1420.

Kruse AM, Meenach SA, Anderson KW and Hilt JZ. 2014. Synthesis and characterization of CREKA-conjugated iron oxide nanoparticles for hyperthermia applications. *Acta Biomater* **10**(6): 2622-2629.

Lee N, Yoo D, Ling D, Cho MH, Hyeon T and Cheon J. 2015. Iron oxide based nanoparticles for multimodal imaging and magnetoresponsive therapy. *Chem Rev* **115**(19): 10637-10689.

Liao SH, Liu CH, Bastakoti BP, Suzuki N, Chang Y, Yamauchi Y, Lin FH and Wu KC. 2015. Functionalized magnetic iron oxide/alginate core-shell nanoparticles for targeting hyperthermia. *Int J Nanomedicine* **10**: 3315-3328.

Ma M, Zhang Y, Shen XL, Xie J, Li Y and Gu N. 2015. Targeted inductive heating of nanomagnets by a combination of alternating current (AC) and static magnetic fields. *Nano Res* **8**(2): 600-610.

MagForce. (2016). "A new study to validate nanotherm™ therapy and build confidence within the specialist medical community." Retrieved August 2016, from http://www.magforce.de/en/studien.html.

Maier-Hauff K, Ulrich F, Nestler D, Niehoff H, Wust P, Thiesen B, Orawa H, Budach V and Jordan A. 2011. Efficacy and safety of intratumoral thermotherapy using magnetic iron-oxide nanoparticles combined with external beam radiotherapy on patients with recurrent glioblastoma multiforme. *J Neurooncol* **103**(2): 317-324.

Poirier M, Simard JC, Antoine F and Girard D. 2014. Interaction between silver nanoparticles of 20 nm (AgNP20) and human neutrophils: Induction of apoptosis and inhibition of de novo protein synthesis by AgNP20 aggregates. *J Appl Toxicol* **34**(4): 404-412.

Quinto CA, Mohindra P, Tong S and Bao G. 2015. Multifunctional superparamagnetic iron oxide nanoparticles for combined chemotherapy and hyperthermia cancer treatment. *Nanoscale* **7**(29): 12728-12736.

Ren Y, Zhang H, Chen B, Cheng J, Cai X, Liu R, Xia G, Wu W, Wang S, Ding J, Gao C, Wang J, Bao W, Wang L, Tian L, Song H and Wang X. 2012. Multifunctional magnetic Fe_3O_4 nanoparticles combined with chemotherapy and hyperthermia to overcome multidrug resistance. *Int J Nanomedicine* **7**: 2261-2269.

Sadhasivam S, Savitha S, Wu CJ, Lin FH and Stobinski L. 2015. Carbon encapsulated iron oxide nanoparticles surface engineered with polyethylene glycol-folic acid to induce selective hyperthermia in folate over expressed cancer cells. *Int J Pharm* **480**(1-2): 8-14.

Sadhukha T, Wiedmann TS and Panyam J. 2013. Inhalable magnetic nanoparticles for targeted hyperthermia in lung cancer therapy. *Biomaterials* **34**(21): 5163-5171.

Shah BP, Pasquale N, De G, Tan T, Ma J and Lee KB. 2014. Core-shell nanoparticle-based peptide therapeutics and combined hyperthermia for enhanced cancer cell apoptosis. *ACS Nano* **8**(9): 9379-9387.

Ullal AJ and Pisetsky DS. 2010. The release of microparticles by jurkat leukemia T cells treated with staurosporine and related kinase inhibitors to induce apoptosis. *Apoptosis* **15**(5): 586-596.

Valente MJ, Henrique R, Vilas-Boas V, Silva R, Bastos Mde L, Carvalho F, Guedes de Pinho P and Carvalho M. 2012. Cocaine-induced kidney toxicity: An in vitro study using primary cultured human proximal tubular epithelial cells. *Arch Toxicol* **86**(2): 249-261.

Wildeboer RR, Southern P and Pankhurst QA. 2014. On the reliable measurement of specific absorption rates and intrinsic loss parameters in magnetic hyperthermia materials. *J Phys D Appl Phys* **47**(49).

Wust P, Gneveckow U, Johannsen M, Bohmer D, Henkel T, Kahmann F, Sehouli J, Felix R, Ricke J and Jordan A. 2006. Magnetic nanoparticles for interstitial thermotherapy--feasibility, tolerance and achieved temperatures. *Int J Hyperthermia* **22**(8): 673-685.

Yin PT, Shah BP and Lee KB. 2014. Combined magnetic nanoparticle-based microRNA and hyperthermia therapy to enhance apoptosis in brain cancer cells. *Small* **10**(20): 4106-4112.

Yuan C, An Y, Zhang J, Li H, Zhang H, Wang L and Zhang D. 2014. Magnetic nanoparticles for targeted therapeutic gene delivery and magnetic-inducing heating on hepatoma. *Nanotechnology* **25**(34): 345101.

Zevon M, Ganapathy V, Kantamneni H, Mingozzi M, Kim P, Adler D, Sheng Y, Tan MC, Pierce M, Riman RE, Roth CM and Moghe PV. 2015. CXCR-4 targeted, short wave infrared (SWIR) emitting nanoprobes for enhanced deep tissue imaging and micrometastatic cancer lesion detection. *Small* **11**(47): 6347-6357.

Zhang J, Dewilde AH, Chinn P, Foreman A, Barry S, Kanne D and Braunhut SJ. 2011. Herceptin-directed nanoparticles activated by an alternating magnetic field selectively kill HER-2 positive human breast cells in vitro via hyperthermia. *Int J Hyperthermia* **27**(7): 682-697.

Zlotnik A. 2006. Chemokines and cancer. *Int J Cancer* **119**(9): 2026-2029

Supporting Information (SI)

Combining the Iron Loading of CXCR4-Targeted and Non-Targeted Nanoparticles to Efficiently Kill Jurkat Cells via Unassisted Magnetically-Induced Hyperthermia

Vânia Vilas-Boas*, Begoña Espiña, Yury V. Kolen'ko, Manuel Bañobre-Lopez, José Alberto Duarte, Verónica Martins, Dmitri Y. Petrovykh, Paulo Freitas and Félix D. Carvalho*

Optimization of AMF parameters

The MHT experiments were performed using a DM 100 nB nanoScale Biomagnetics AMF applicator equipped with an optical temperature probe. The influence of the different combinations of AMF parameters on cell viability was initially studied in order to select the conditions that would lead to higher MHT efficiency. To do so, U87MG cells (ATCC® HTB-14™, cultivated in a controlled atmosphere containing 5 % CO2, at 37 ºC, in Eagle's Minimum Essential Medium + 10 % Hyclone FBS) were detached using trypsin, incubated with SPIONs and submitted to different combinations of frequency and field amplitude, as shown in Figure S1. These preliminary results suggested that submitting the samples to temperatures (*T*) above 40 ºC for longer periods increased MHT efficiency. Cell viability data were obtained using PrestoBlue® cell viability reagent.

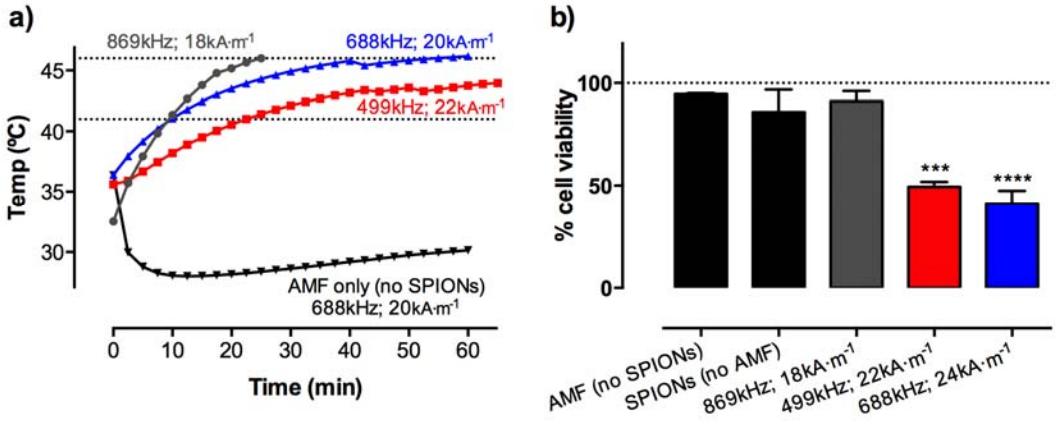

Figure S1 – Optimization of AMF parameters for efficient MHT. a) Different AMF parameters were tested to evaluate the most efficient MHT conditions to be applied in our study. b) Viability tests indicate that submitting the samples to *T* above 40 ºC for longer period of time (red and blue curves) leads to more significant reductions in cell viability, to around 50 %. The AMF (688 kHz, 20 kA·m^{-1}) or the SPIONs-only did not significantly impair cell viability. Differences were estimated using one-way ANOVA (Kruskal-Wallis test) followed by a Dunn's multiple comparisons test. ***p<0.001 and ****p<0.0001 *vs.* untreated cells (100% line in the graph).

Based in the preliminary results reported above, further tests were performed to select the final conditions to be used in the work herein presented. Our *in vitro* model of T-cell leukaemia, Jurkat cells (JK), was used for these optimization studies. Two different protocols were established using a two-step procedure: A - 869 kHz, 20 kA·m^{-1}, 30 min + 554 kHz, 24 kA·m^{-1}, 30 min, or B – 554 kHz, 24 kA·m^{-1}, 30 min + 869 kHz, 20 kA·m^{-1}, 30 min. Figure S2 shows the heating profiles obtained when applying protocols A or B to JK cells previously incubated for 1 h, with MP–CXCR4, after removing the excess of free MPs by centrifugation (125 *g*, 5 min).

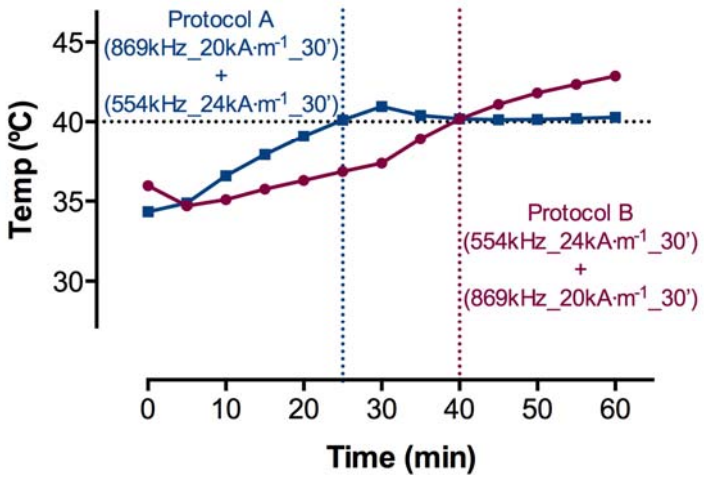

Figure S2 – Selection of AMF parameters for efficient MHT on Jurkat cells. Two different 1 h AMF protocols were tested: protocol-A – 30 min at 554 kHz, 24 kA·m^{-1}, followed by 30 min at 869 kHz, 20 kA·m^{-1}; protocol-B – 30 min at 554 kHz, 24 kA·m^{-1}, followed by 30 min at 869 kHz, 20 kA·m^{-1}. In protocol-A 40 ºC are reached in 25 min and *T* is kept above this level throughout the rest of the protocol. Protocol-B needed more time to reach 40 ºC (40 min), which may limit the exposure time to high and damaging *T*.

The heating curve from protocol-A shows that a high *T* (above 40 ºC) is reached in the first half of the protocol, which is kept in the second half of the AMF application as a consequence of a decrease in the overall AMF power. Following protocol-B, in turn, leads to a lower *T* (than protocol-A) in the end of the first half of the procedure, which further increases in the second half of the protocol due to the overall increase AMF power. Although a higher absolute *T* is reached at the end of protocol-B application, protocol-A reached 40 ºC in 25 min and the *T* was kept above this threshold for efficient MHT for at least 35 min. These findings suggest protocol-A to be the most suitable, amongst the tested, to be applied in the subsequent work.

CXCR4 expression in Jurkat cells

Surface expression of CXCR4 receptor in JK cells was assessed by flow cytometry after incubating ca. 2.5×10^5 cells with 5 µL PE-conjugated mouse anti-human monoclonal CXCR4 antibody (clone 44717, R&D Systems, Abingdon, UK) for 30 min, at 37 ºC, in the dark, in 2 % BSA. In parallel, samples with the matched isotype control (IC) antibody (PE-conjugated mouse anti-human monoclonal IgG2b, ImmunoTools GmbH, Friesoythe, Germany) were prepared to depict unspecific staining. After this incubation period, cells were washed with cold PBS and kept on ice, in the dark, until flow cytometry analysis. Flow cytometry parameters were set as described in section 2.6 of the main text. Fluorescence due to CXCR4–PE was followed in FL-2 channel, and 7-AAD's (BD Pharmingen™, BD Biosciences, USA) fluorescence (followed on FL-4 channel) was used to exclude dead cells from the analysis. FCS files were analysed using ProSort™ software. The results confirmed that, as expected, Jurkat cells are highly CXCR4 expressing cells (Figure S3).

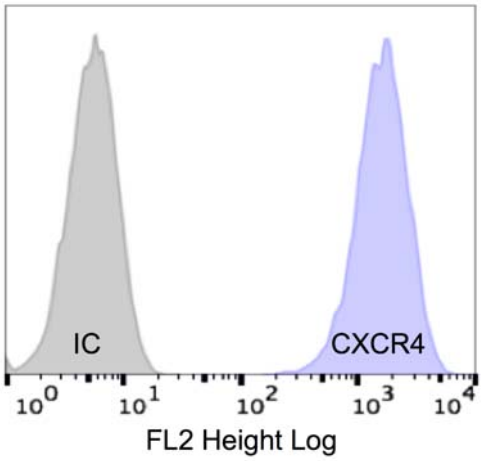

Figure S3 – **Overexpression of CXCR4 in Jurkat cells.**
The expression of CXCR4 in JK cells was assessed by flow cytometry using a PE-labelled anti-CXCR4 antibody. The results were plotted against a PE-labelled isotype control (IC) antibody histogram to better demonstrate the high expression levels of the receptor in this cell line.

Figure S4 presents the kinetic readings of caspase-3 activity and cell viability levels for Jurkat cells with the each particle population independently, after exposure to the selected AMF conditions (protocol-A, Figure S2). As stated in the main text of this work, MHT performed on JK+SPION+AMF samples did not produce cytotoxicity signatures. For the JK+MP–CXCR4+AMF samples, caspase-3 activity was significantly induced ($p<0.01$, Figure S4) but failed to produce a significant reduction in cell viability levels.

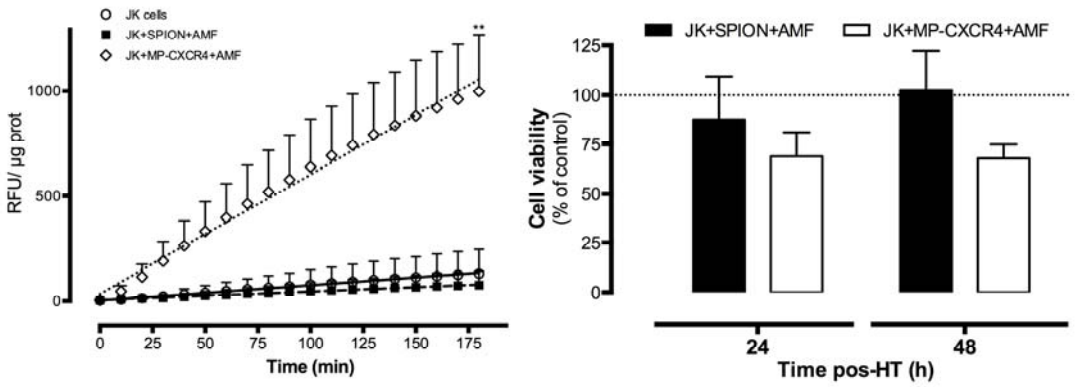

Figure S4 - Caspase-3 and cell viability assays after MHT application when only one type of particles was used.
When using SPION only, average Tc was kept around 34.5 ºC (see Figure 1), which is not expected to affect cell viability. Indeed, caspase-3 activity did not significantly change, and cell viability was not significantly impaired, comparing to cells-only control (100 % dashed line). When using only MP–CXCR4, the average Tc was 40.5 ºC (see Figure 1), which could yield some toxicity in cancer cells. An evident increase in caspase-3 activity was observed in this case (**p<0.01 vs. untreated cells), but cell viability did not decrease more than 35 %. Differences between the observed caspase-3 slopes were estimated using repeated measures two-way ANOVA followed by Dunnett's multiple comparisons test; differences between treated and untreated cell viability rates in both time-points were estimated using ordinary two-way ANOVA followed by Dunnett's multiple comparisons test.

MANUSCRIPT III

Unsubmitted manuscript

Manuscript III

A mono-therapeutic magnetic hyperthermia treatment to kill glioblastoma cells based on CXCR4 targeting

Authors

Vânia Vilas-Boas[a,b,*], Begoña Espiña[b], Yury V. Kolen'ko[b], Manuel Bañobre-Lopez[b], Marina Brito[b], Verónica Martins[b,#], José Alberto Duarte[c], Dmitri Petrovykh[b], Paulo Freitas[b] and Félix Carvalho[a*].

Affiliations

[a]UCIBIO-REQUIMTE, Laboratory of Toxicology, Biological Sciences Department, Faculty of Pharmacy, University of Porto, Rua de Jorge Viterbo Ferreira, 228, 4050–313 Porto, Portugal

[b]International Iberian Nanotechnology Laboratory, 4715-330 Braga, Portugal

[c]CIAFEL, Faculty of Sports, University of Porto, 4200-450 Porto, Portugal

[#]current address: Magnomics, Parque Tecnológico de Cantanhede, Núcleo 04, Lote 2 3060-197 Cantanhede | PORTUGAL

*corresponding authors email: vvilasboas@ff.up.pt and felixdc@ff.up.pt

Abbreviations:

7-AAD – 7-aminoactinomycin D

AMF – Alternating magnetic field

AnV–PE – Annexin-V labelled with phycoerythrin

BSA – Bovine serum albumin

DMEM – Dulbecco's modified essential medium

DMEM/ F-12 – Dulbecco's modified Eagle's medium with nutrient mixture F-12

EDTA - ethylenediaminetetraacetic acid

FBS – Fetal bovine serum

GBM – Glioblastoma multiforme

HEPES – 4-(2-Hydroxyethyl)piperazine-1-ethanesulfonic acid

HIV – Human Immunodeficiency Virus

HBSS – Hanks balanced saline solution with (+/+) or without (-/-) calcium and magnesium ions

IC – Isotype control

ICP-OES – Inductively-Coupled-Plasma – Optical Emission Spectrometry

LDH – Lactate dehydrogenase

MHT – Magnetic hyperthermia

MNP – Magnetic nanoparticle

MP – Magnetic particle

PBS – Phosphate buffer saline solution

RIPA – Radioimmunoprecipitation assay

RT – Room temperature

SD – standard deviation

T – Temperature

T_c – Constant temperature

TEM – Transmission electron microscopy

T_{max} – Maximum temperature

Abstract:

The cell-surface expression levels of a selected target often hamper the development of an efficient targeted strategy to treat cancer. In the case of magnetic hyperthermia (MHT) treatments, this phenomenon limits the accumulation of magnetic material by cancer cells, which is crucial for the achievement of lethal temperatures and, therefore, treatment effectiveness. Herein, we describe the optimization of a highly effective MHT treatment, combining targeted and non-targeted nanoparticles, applied to an *in vitro* model of glioblastoma multiforme (GBM) expressing intermediate levels of a selected surface target, the chemokine receptor, CXCR4.

The CXCR4 at the surface of LN229 cells (*in vitro* model of human GBM) was targeted using immuno-modified magnetic particles, after a boost of magnetic material was provided to cells using non-functionalized nanoparticles. Under specific alternating magnetic field conditions the sample's temperature increased, leading to cell death. A model of human kidney normal cells (HK-2) was used as control.

MHT treatment resulted in significantly different temperature profiles between GBM and normal cells, leading to extensive levels of cancer cell death as briefly as 2 h after MHT. HK-2 cells were kept practically undamaged during the same procedure. Using an isotype control antibody attached to the particles, instead of anti-CXCR4, further confirmed the role of the targeting system in this strategy.

The proposed methodology was highly effective in killing GBM cells, following a necrotic pathway. The dramatic difference between the outcomes for cancer and normal cells, treated under the same conditions, suggests that undesirable side effects could be minimized in future applications for GBM treatment.

Keywords: cancer treatment; glioblastoma; nanoparticles; magnetic hyperthermia; CXCR4

1. Introduction

Glioblastoma multiforme (GBM) is a tumour of the brain that arises from astrocytes, being the most frequent (around 52% of all primary brains tumours) (AANS 2015) and aggressive type of brain tumours. Despite the therapeutic efforts to overcome it (surgery, chemotherapy and radiotherapy), 95 % of the patients die within 12 to 15 months after diagnosis (Bleeker et al. 2012). This very poor prognosis for GBM patients highlights the need for more efficient and safer treatments.

Nearly twenty years have passed since CXCR4, a chemokine receptor known to be a co-receptor for Human Immunodeficiency Virus (HIV) infection of CD4 cells (Feng et al. 1996), was found to be overexpressed in GBM, compared to normal brain tissue (Sehgal et al. 1998). An association was established between CXCR4 expression and tumour proliferation, aggressiveness, metastatic ability and resistance to chemotherapy (Rempel et al. 2000, Rubin et al. 2003, Ehtesham et al. 2006, Redjal et al. 2006, Zagzag et al. 2006). These facts make CXCR4 an appealing target to be used in cancer treatment. Initially developed to prevent HIV from infecting susceptible cells, the CXCR4 antagonist, AMD3100 (Plerixafor), prevented tumour recurrence in a mouse model of xenografted GBM (Kioi et al. 2010), and was recently suggested to be included in the adjuvant treatment of GBM in association with other drugs (Rios et al. 2016).

The local heat generated by magnetic nanoparticles (MNPs) under an external alternating magnetic field (AMF), called magnetic hyperthermia (MHT), is currently being exploited to destroy cancer cells or sensitize them to other treatments, such as radiation (MagForce 2016). MHT treatment of a number of different cancer types showed to be well tolerated, with moderate side effects, in phase I clinical trials (Wust et al. 2006, Johannsen et al. 2007). Phase II clinical trials in GBM patients were encouraging, showing a 7.2 to 8.6 month increase in overall survival (Maier-Hauff et al. 2011), but there's still margin for treatment improvement. Until now, literature on this topic mostly suggests MHT as a sensitizing therapy in combination with stereotactic radiotherapy (Maier-Hauff et al. 2011), with chemotherapy (Kim et al. 2015, Quinto et al. 2015), or other therapies (Yin et al. 2014, Yuan et al. 2014, Di Corato et al. 2015), which is mostly due to insufficient effectiveness of MHT in a mono-therapeutic context. The use of functionalized nanomaterials, often with monoclonal antibodies (Zhang et al. 2011), that can target specific molecules at the cancer cell membrane has been regarded as a means to improve MHT outcome and safety profile. As previously discussed by our group (Manuscript 2), this targeted MHT strategy is dependent on the amount of target molecule available at the cell surface (limiting the

targeted binding of functionalized MNPs), as well as on the cell's iron loading (limiting MHT efficiency).

This work describes the optimization and application of an MHT therapeutic strategy based on the combined use of both CXCR4-targeted and non-targeted magnetic nanoparticles to kill glioblastoma cells expressing intermediate levels of CXCR4.

2. Materials and methods

2.1. Reagents

All reagents used in this study were of analytical grade or of the highest grade available. Fetal bovine serum (FBS) was purchased from HyClone UK, Ltd, Northumberland, England, UK. Penicillin (10,000 $U \cdot mL^{-1}$) and streptomycin (10,000 $\mu g \cdot mL^{-1}$), herein referred to as Pen-Strep, Dulbecco's modified Eagle's medium (DMEM) with 4.5 $g \cdot L^{-1}$ glucose, sodium pyruvate, nicotinamide adenine dinucleotide reduced form (NADH), triton x-100, 4-(2-Hydroxyethyl)piperazine-1-ethanesulfonic acid (HEPES), ethylenediaminetetraacetic acid (EDTA), KH_2PO_4, $K_2HPO_4.3H_2O$, $CaCl_2$, NaCl, glycerol, and bovine serum albumin (BSA) were purchased from Sigma Inc., St. Louis, MO USA. Dulbecco's modified Eagle's medium with nutrient mixture F-12 (DMEM/ F-12) and GlutaMAX™, trypsin 0.25 %-EDTA, fungizone (250 $\mu g \cdot mL^{-1}$) and human transferrin (4 $mg \cdot mL^{-1}$) were purchased from Gibco Laboratories (Lenexa, KS, USA). Anti-mouse IgG-peroxidase polyclonal antibody was purchased from Amersham Pharmacia Biotech (Buckinghamshire, United Kingdom). BD Pharmingen™ Phycoerythrin (PE)-labelled Annexin-V (AnV-PE) and 7-aminoactinomycin D (7-AAD) were purchased from BD Biosciences, USA. Anti-human CXCR4, clone 12G5, low endotoxin, azide-free monoclonal antibody produced in mouse, and its matched isotype-control, mouse anti-human monoclonal IgG2a (IC) were purchased from BioLegend Inc., San Diego, CA, USA.

2.2. Cell culture

Human cell lines from glioblastoma (LN229, ATCC® CRL-2611™) and normal kidney (HK-2, ATCC® CRL-2190™) were purchased from the American Type Culture Collection (Manassas, VA, USA). LN229 cells were grown in DMEM (high glucose) medium supplemented with 10 % FBS and 1 % Pen-Strep, and HK-2 cells were grown in DMEM/F12 Glutamax™, supplemented with 10 % FBS, 1 % Pen-Strep, 2.5 $\mu g \cdot mL^{-1}$ fungizone and 5 $\mu g \cdot mL^{-1}$ human transferrin. Both cell lines were maintained at 37 ºC, in a controlled atmosphere of 5 % CO_2.

2.3. CXCR4 expression in LN229 and HK-2 cells assessed by western blot

Approximately 1.0×10^6 per well were seeded in 6-well plates and grown for 24 h before being scraped (2 wells per condition) in 1 mL ice-cold PBS and centrifuged at 3,000 rpm, for 5 min, at 4 ºC. Cells were then lysed using ice-cold RIPA buffer (50 mM Tris-HCl pH 8, 150 mM NaCl, 1 % Triton X-100, 0.5 % sodium deoxycholate, 0.1 % SDS, 5 mM EDTA) with 1 % (v/v) protease (cOmplete™, Mini, EDTA-free Protease Inhibitor Cocktail, Roche) and phosphatase (1 mM Na_3VO_4, 1 mM NaF) inhibitors for 30 min at 4 ºC, and centrifuged at 13,000 rpm, 10 min, at 4 ºC. Protein content in the supernatant was quantified using Coomassie Plus (Bradford) Protein kit (Thermo Fisher Scientific, Inc., Rockford, IL USA) and 25 µg of protein were diluted 1:1 in 2 x Laemmli buffer with 5 % β-mercaptoethanol, and heated at 95 ºC, for 5 min. Samples were kept at -20 ºC until analysis.

Samples were loaded in a 4–15 % Mini-PROTEAN® TGX™ Precast Protein Gels (Bio-Rad Laboratories, Hercules, CA, USA) and electrophoretically separated at a constant voltage of 75 V using a Tris-glycine running buffer [25 mM Tris base, 192 mM glycine, and 0.1 % SDS (w/v), pH 8.3]. Proteins were then transferred to a nitrocellulose membrane using a transfer buffer [20 % methanol (v/v) in 25 mM Tris base and 192 mM glycine, pH 8.3] at a constant voltage of 100 V, for 3 h. A Mini-PROTEAN Tetra cell system (Bio-Rad Laboratories, Hercules, CA, USA) was used for the electrophoresis and transfer. Membranes were rinsed in Tris-buffered saline solution [TBS: 20 mM Tris base, 300 mM NaCl, pH 8.0], blocked for 2 h, at room temperature (RT), in blocking buffer [5 % non-fat powdered skim milk (w/v) in Tris-buffered saline solution with 0.05 % Tween 20 (v/v) (TBS-T)] and then incubated overnight, at 4 ºC, with a mouse monoclonal anti-human-CXCR4 antibody (clone 44717, R&D Systems, Abingdon, UK) or an anti-α-tubulin in a 1:2,000 dilution in blocking buffer. After incubation with the primary antibody, membranes were washed three times (10 min each) with TBS-T and incubated with the secondary antibody [anti-mouse IgG peroxidase polyclonal antibody (1:5,000 in blocking buffer)], for 1 h, at RT. Following two more washes in TBS-T (10 min each), bands were revealed using ECL Prime chemiluminescence reagents (Amersham Pharmacia Biotech, Buckinghamshire, United Kingdom), according to the supplier's instructions, and visualized using a G:Box Chemi XT4 (Syngene, Cambridge, UK). Quantification of band intensity was performed using Image J analysis software (NIH, USA). Final results, collected from three independent experiments, represent the ratio between CXCR4 and α-tubulin band intensities.

2.4. Incubation of cells with magnetic nanoparticles

A previously developed protocol was used (Manuscript 2), with some modifications. Three million cells per T25 culture flask were incubated with increasing concentrations of poly(acrylic acid)-coated superparamagnetic nanoparticles (SPIONs), synthesized and characterized by our group (Kolen'ko et al. 2014), in cell culture medium, for 150 min, at 37 ºC. The total initial iron concentration of those SPIONs was 0.176, 0.195, 0.217 or 0.260 $g \cdot L^{-1}$ [Fe]. Excess of free SPIONs was then removed and the cellular monolayer was washed with HBSS (+/+). Concurrently, 250 nm composite dextran iron oxide particles (09-20-252 Nanomag®-D, Micromod Partikeltechnologie GmbH, Rostock, Germany), with protein-A at the surface, were incubated (30 min, at RT, with agitation) with CXCR4 antibody or an isotype control (IC) antibody to obtain functionalized particles designated herein as MP–CXCR4 or MP–IC, respectively. Cells were further incubated with these functionalized particles at 0.264 $g \cdot L^{-1}$ [Fe], in 2 % BSA, for 70 min, at 37 ºC, with mild agitation. Excess of free, functionalized MPs was removed and the cellular monolayer was washed with HBSS (-/-) prior to detachment with trypsin-EDTA solution. Samples containing an average 6×10^6 cells were then centrifuged at 125 *g*, for 5 min, recovered in 1 mL cell culture medium and transferred to glass vials previously blocked with 2 % BSA.

2.5. Magnetic hyperthermia treatment (MHT)

The application of AMF to samples prepared in the previous step was performed using a magnetic field generator (DM 100, nB nanoScale Biomagnetics, Zaragoza, Spain) operating at 869 kHz and 250 Oe (≈ 20 $kA \cdot m^{-1}$) for the first 30 min of the experiment, followed by another 30 min at 554 kHz and 300 Oe (≈ 24 $kA \cdot m^{-1}$). The temperature (*T*) of the suspension was measured using an optical temperature probe included in the equipment and the maximum *T* reached at the end of the first step of AMF was called T_{max} and the average *T* kept thereafter was called *T*c (from "constant *T*"). After AMF application, cells were kept in suspension for the flow cytometry studies or seeded for the subsequent tests.

2.6. Studying the interaction of cells with nanoparticles

2.6.1. Transmission electron microscopy (TEM)

Cells (2×10^6) were incubated with 0.217 $g \cdot L^{-1}$ [Fe] of SPION for 150 min, washed, trypsinized and collected. TEM samples were prepared following the protocol described in Manuscript 2. Briefly, cells were pelleted at 1,000 g, for 5 min, at 4 ºC, fixed with 2.5 % glutaraldehyde in 0.1 M sodium cacodylate buffer pH 7.4 for 2 h, and rinsed with cacodylate buffer 0.1 M. Samples were then post-fixed using 2 % osmium tetroxide, dehydrated with

graded ethanol, embedded in Epon and further placed 2 to 3 days at 60 ºC to promote resin polymerization. Ultrathin (100 nm) sections, contrasted with uranylacetate and lead citrate, were prepared on cupper grids (300 Mesh) for TEM analysis (Zeiss EM10A, Carl Zeiss, Oberkochen, Germany).

2.6.2. Immunostaining for optical microscopy

To study the interaction between cells and antibody-functionalized MPs, 2×10^6 cells were incubated with 0.264 $g\cdot L^{-1}$ [Fe] MP–IC or MP–CXCR4 for 70 min, at 37 ºC, and then washed, trypsinized and collected. Cells were then pelleted at 125 g, for 5 min, at RT, and fixed with paraformaldehyde 4 % in PBS 0.1 M, pH 7.2–7.4, during 24 h. Samples were subsequently dehydrated in graded ethanol, cleared with xylene, and embedded in paraffin following routine procedures. A microtome (Leica Microsystems, Model RM2125) with a disposable stainless steel blade (Leica Microsystems, Model 819) was used to cut 5 µm sections from paraffin blocks. These sections were then floated onto warm water (42–44 ºC), and mounted on silane-coated slides (Sigma, S4651-72EA). After dewaxing with xylene and rehydration with graded alcohol, slides were placed in 10 mM citrate buffer in a pressure cooker during 10 min for antigen retrieval, and subsequently placed in a blocking solution of 3 % BSA during 30 min. The endogenous peroxidases were further blocked with a solution of methanol and hydrogen peroxidase during 30 min. After washing, sections were incubated for 2 h with a sheep anti-mouse antibody conjugated with horseradish peroxidase (Amersham Pharmacia Biotech). SIGMAFAST® DAB with Metal Enhancer Tablets (D0426-50SET, Sigma) was used as substrate during 3 min, according to manufacturer's instructions, and the sections were further counterstained with Mayer's haematoxylin. Optical images were collected using an Inverted Wide-Field Microscope Eclipse Ti-E, Nikon.

2.7. Inductively-Coupled-Plasma–Optical Emission Spectrometry (ICP-OES) for iron quantification

To measure the amount of iron in each sample, after MHT, samples were digested in 1 mL HCl 37 %, at RT, for 72 h, and then analysed by ICP-OES, using an ICPE-9000 Multitype ICP Emission Spectrometer (Shimadzu). Three repeated measurements per sample were performed.

2.8. Assessment of cell viability after MHT

2.8.1. Annexin-V & 7-AAD labelling for flow cytometry and fluorescence microscopy

Double staining with AnV–PE and 7-AAD was performed 2 h after MHT treatment, for flow cytometry, and 20 h after MHT for laser scanning confocal microscopy. For flow cytometry studies, $2x10^5$ cells in 50 µL of Annexin-V-binding buffer (diluted from the 10 x stock solution: 0.1 M HEPES, pH 7.4; 1.4 M NaCl; 25 mM $CaCl_2$), were incubated with or without 2 µL of AnV–PE, and kept for 30 min, at RT, in the dark. Cells were centrifuged at 210 *g*, 5 min, at 4 ºC and immediately analysed. 7-AAD was used to detect membrane damage in these samples. Fluorescence collected in FL2 channel (fluorescence from AnV–PE) was plotted *vs.* the one collected in FL4 channel (fluorescence from 7-AAD), and the percentage of positive cells for each channel (or both) was estimated after establishing the quadrants based on the controls. For each sample, at least 10,000-gated events were collected.

For the laser scanning confocal microscopy (LSCM) studies, after MHT application, cells were seeded in 8-well micro-slides with tissue culture treated surface (µ-slide 8-well ibiTreat, Ibidi, Martinsried, Germany), in 200 µL of cell culture medium, and incubated for 20 h to allow attachment. Two µL of AnV–PE in 18 µL of 10× concentrated AnV-binding buffer (0.1 M HEPES, pH 7.4; 1.4 M NaCl; 25 mM $CaCl_2$) were added to the 200 µL of medium in each well and incubated for 30 min at 37 ºC, in the dark. Two µL of 7-AAD were added to each well and incubated for 10 min, in the same conditions. The medium (with excess of dyes) was removed and the cells were fixed with 4 % paraformaldehyde in PBS, for 15 min, at RT, after which each well was washed twice with HBSS (+/+). The samples were imaged using a laser scanning confocal microscope (LSM 780, Carl Zeiss) using 488 and 514 nm excitation lasers.

2.8.2. Lactate dehydrogenase (LDH) leakage assay

LDH leakage from cells is a consequence of membrane disruption, so LDH activity in the cell culture medium is used as a measure of cell death. A previously described protocol (Manuscript 2) was used. Results from the LDH released into the extracellular medium (LDH leakage) were expressed as cell death values calculated according to a previously described methodology (Barbosa et al. 2014). Cell death from untreated controls was then subtracted so that the presented cell death values translate solely the effects of the treatment.

2.8.3. Metabolic rate assay

Around 15,000 cells per well were seeded in 96-well and cell viability was assessed 24 and 72 h after MHT application by the addition of 10 µL PrestoBlue® cell viability reagent (Molecular Probes™, Carlsbad, CA) to each well. After incubation at 37 ºC for 1 h, fluorescence signals were collected using a microplate reader (Synergy H1, BioTek Instruments) with excitation wavelength at 560 nm and emission wavelength at 590 nm.

2.9. Statistical analysis

All data are presented as mean ± standard deviation (SD), except when stated otherwise, of at least two independent experiments. Normality of the data distribution was assessed applying three tests: KS normality test, D'Agostino and Pearson omnibus normality test and Shapiro-Wilk normality test. Differences on the T_{max} and iron content between tested conditions were estimated using two-way ANOVA followed by Tukey's multiple comparisons test. Multivariate linear regression models were used to estimate the dependence of T_{max} on the initial iron amount. Whenever singular values of two variables were plotted, Spearman's rank correlation was estimated to evaluate the magnitude of the association between those variables (T_{max} and iron loading per sample (mg Fe·mL^{-1}), T_{max} and cell death levels 2 and 24 h after MHT, and between iron loading per sample and cell death levels after 24 h). Correlations were considered significant for $r>0.6$ and $p<0.05$.

All statistical analysis was carried out using GraphPad Prism software v6 (San Diego, CA). P values under 0.05 were considered statistically significant.

3. Results and discussion

This work describes the optimization and application of a MHT-based strategy to kill GBM cells that express intermediate levels of cancer biomarkers. The overexpression of such cancer biomarkers is often sufficient for discrimination from normal cells in a diagnostic context; however, those expression levels may be insufficient for successful targeting in therapeutic context. Our group has previously attempted to kill Jurkat cells, an *in vitro* model of leukaemia expressing high levels of CXCR4, with magnetic hyperthermia using a purely targeted system (anti-CXCR4-functionalized particles). We found that an independent magnetic boost was necessary to reach temperatures that could significantly reduce cell viability; a second population of non-targeted nanoparticles was then successfully used to provide the magnetic boost. In this work we propose the use of a similar strategy applied to GBM cells that express lower levels of that same target receptor.

3.1. Assessing CXCR4 expression levels

CXCR4 expression in LN229 and HK-2 cells was assessed by western blot (Figure 1), using Jurkat cells as a positive control (high expression of CXCR4). As expected, Jurkat clearly presented the highest levels of CXCR4, while LN229 cells expressed intermediate levels of the target receptor, and HK-2 cells (normal cells) presented the lowest levels (Figure 1).

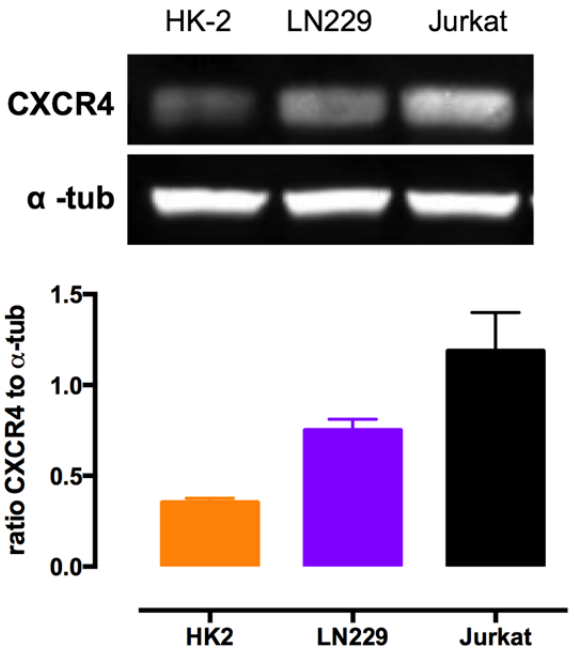

Figure 1 –CXCR4 expression in LN229 and HK-2 cells.
Jurkat cells were used as a positive control of high CXCR4 expression. LN229 cells expressed intermediate CXCR4 levels while HK-2 cells exhibited the lowest levels of that chemokine receptor.

3.2. Magnetically-induced hyperthermia

The optimization and fine-tuning of the hyperthermia strategy presented herein was intended to find the most appropriate conditions to efficiently kill cancer cells. The concentration of MP-CXCR4, the time of incubation of cells with particles, and the number of cells per experiment, had an impact on the observed heating and MHT outcome (Figure S1). Experiments with normal cells were carried in parallel, under the same conditions, to monitor the potential occurrence of side effects in normal cells. Different starting amounts of iron were tested, by changing the amount of the non-targeted (unspecific) nanoparticles, while keeping constant the amount of functionalized nanoparticles. The total iron concentration in all cases was such that the temperature (*T*) reached during MHT could affect LN229 cells but not HK-2 cells. After removing the excess of free nanoparticles by rinsing the monolayer,

cells were detached and submitted to a biphasic AMF, which has been previously tested and optimized to kill Jurkat cells (Manuscript 2). This biphasic AMF consists of a 30 min period at 869 kHz, 20 kA·m^{-1}, after which the maximum *T* (Figure 2, T_{max}) of the MHT is reached, followed by another 30 min period at 554 kHz; 24 kA·m^{-1} that keeps the *T* constant (Figure 2, *T*c) for enough time to produce cytotoxicity (Falk and Issels 2001, Taratula et al. 2013). The heating profiles obtained for the different amounts of SPIONs are presented in Figure 2, independently for each cell type and particle functionalization.

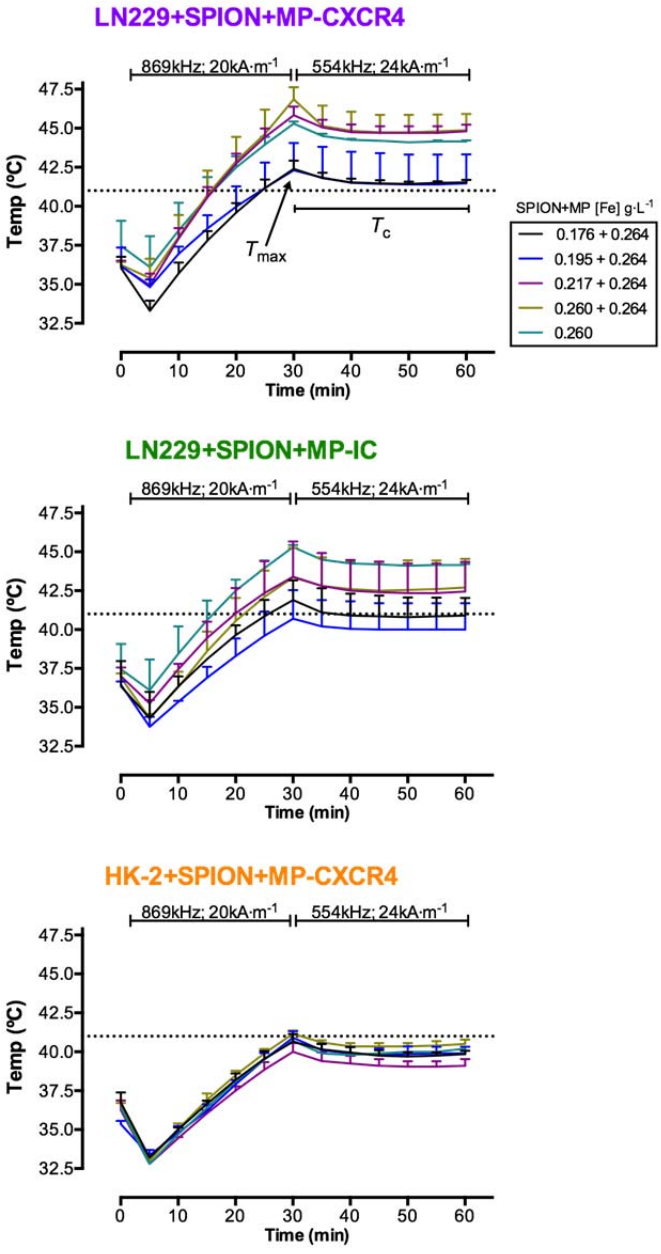

Figure 2 – Heating profiles of LN229 and HK-2 cells when exposed to different concentrations of SPIONs (0.176–0.260 g·L^{-1} Fe) and to CXCR4- or IC-functionalized MPs (0.264 g·L^{-1} Fe).
The dotted line marks 41 ºC, the maximum temperature reached by normal (HK-2) cells, to facilitate comparisons between the cell types or different particle functionalization. T_{max} points the *T* reached at the end of the first heating step. *T*c refers to the average *T* kept thereafter. Results are mean+SD of at least two independent experiments per condition.

The differences in the heating profiles of LN229 (cancer) and HK-2 (normal) cells treated under the same conditions were evident. All HK-2 heating curves reached no more than 41 ºC, considered a safe temperature for normal cells, during the entire AMF application period (30+30 min), independently of the initial amount of SPIONs. For the similarly treated LN229 samples, all the curves clearly overcame this threshold *T* in less than 25 min, and the samples' *T* was kept above this threshold until the end of AMF application. As expected, LN229 samples reached lower *T* when the functionalized particles had the IC antibody, instead of anti-CXCR4. The average maximum temperature (T_{max}) reached for each condition, at the end of the first 30 min, was used for comparison between the experiments and was compiled in Table 1.

Table 1 – Average maximum temperature (T_{max}) reached in MHT experiments using increasing initial iron amounts.

	Initial [Fe] (g·L^{-1})					
Treatment	0.176+0.264	0.195+0.264	0.217+0.264	0.260+0.264	slope	r^2
LN229+SPION+MP–CXCR4	42.4±0.5	42.3±1.8	45.8±0.6	46.9±0.8	10.28	0.84
LN229+SPION+MP–IC	41.9±1.3	40.7±1.8	43.4±2.3	43.4±1.9 *	4.32	0.49
HK-2+SPION+MP–CXCR4	40.7±0.5	40.9±0.4	40.0±0.6 ***	41.2±0.2 ***	0.72	0.09

Results are mean±SD of at least two independent experiments. Differences were estimated using regular two-way ANOVA followed by Tukey's multiple comparisons post test. *p<0.05 and ***p<0.001 *vs.* LN229+SPION+MP–CXCR4 for the same initial iron amount. The slopes obtained from linear regression fitting are also presented along with the goodness of this fit, r^2, which indicates the nearly linear variation between the reached T_{max} and the initial iron amount for the LN229+SPION+MP–CXCR4 samples.

Analysing the slope of the dependence of T_{max} on the initial concentration of the SPIONs indicates three clearly different regimes for the three treatments in Table 1: the strongest dependence (r^2=0.84) was observed for the LN229+SPION+MP–CXCR4 samples, a much weaker dependence (r^2=0.49) for the LN229+SPION+MP–IC, and no dependence (r^2=0.09) for the HK-2+SPION+MP–CXCR4 samples.

For the highest tested iron loading, the T_{max} observed for LN229+SPION+MP–CXCR4 significantly differed from the samples using MP–IC, instead of MP–CXCR4 (Table 1, p<0.05). The mean T_{max} obtained for LN229 cells with MP–CXCR4 was higher than the ones obtained for HK-2 cells under the same conditions, nevertheless, they only reached statistical significance for the two highest tested initial iron amounts (Table 1, p<0.001).

3.3. Interaction of particles with cells

The uptake of SPIONs by both cell lines was confirmed by TEM, as exemplified by the micrographs of LN229+SPIONs or HK-2+SPIONs showing SPIONs internalized in endosomal compartments (Figure 3, red arrows), and not in other organelles or free in the cytoplasm, in both cells lines. Quantification of iron levels in these samples by ICP-OES showed increased uptake for LN229 compared to HK-2 cells (88.27 *vs.* 55.78 pg Fe/cell, respectively), contributing to the observed differences in the reached T_{max}. This intriguing difference in the uptake between a cancer and a normal cell line has been observed and reported before (Rago et al. 2011, Prijic et al. 2012, Sims et al. 2016). Differences in the composition of the cell membrane are believed to play a role in this regard (Rago et al. 2011). Further studies should be conducted to understand whether normal cells, in general, incorporate less non-targeted nanoparticles than cancer cells, as this could indicate a "targeting" system *per se*.

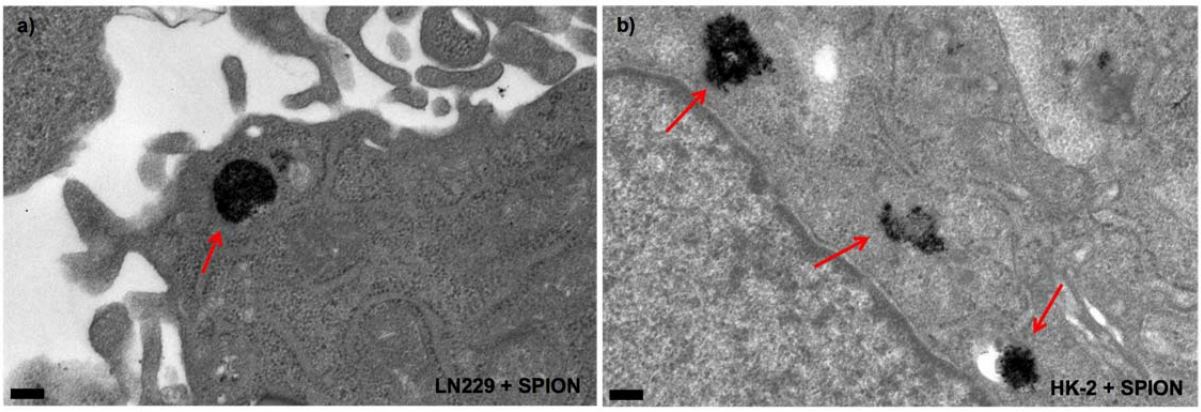

Figure 3 – Uptake of SPION by LN229 and HK-2 cells.
Transmission electron micrographs showing that both LN229 (a) and HK-2 (b) cells uptake SPIONs to endosomal compartments (red arrows). Scale bar is 200 nm.

Using an HRP-labelled secondary antibody, which targets the primary antibody attached to MPs, a bigger amount of MP–CXCR4 was detected interacting with LN229 (Figure 4a) than with HK-2 cells (Figure 4c). These particles were found surrounding the LN229 cell membrane (detail in Figure 4a), almost depicting the shape of the cells, while for the HK-2 cells they distributed randomly and in much less quantity (Figure 4c).

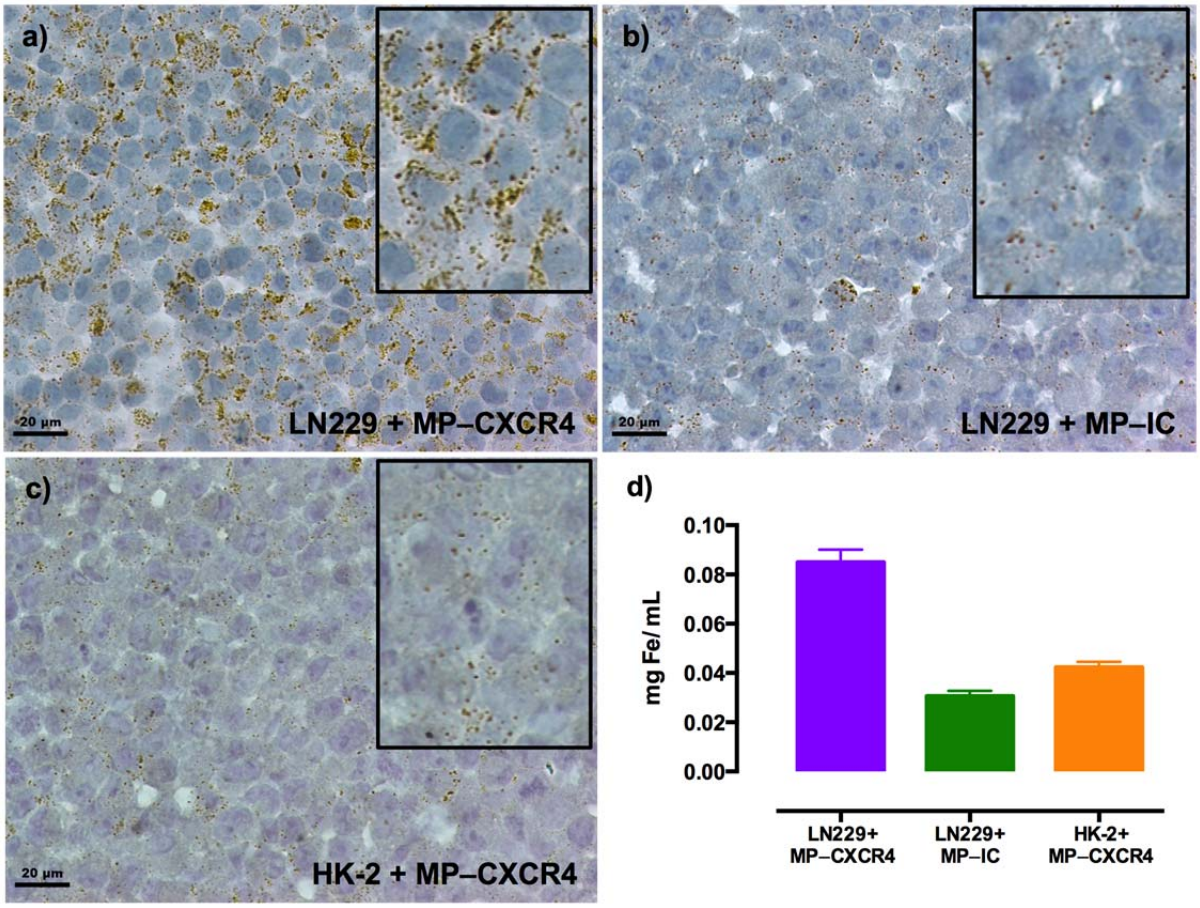

Figure 4 – Interaction of functionalized MPs with LN229 and HK-2 cells.
LN229 cells interact to a bigger extent with (a) CXCR4-targeting than with IC-functionalized (b) particles. Also, LN229 cells (a) interact more than HK-2 cells (c) with CXCR4-targeting nanoparticles. Scale bar is 20 µm. The inserts show details of each picture for better visualization. Iron quantification using ICP-OES (d) confirmed the results obtained using immunocytochemistry.

It was also possible to see some unspecific retention of MP–IC particles in LN229 cells (Figure 4b), which also contributes for the intermediate T_{max} observed for these samples (Table 1). The ability of the targeting particles (MP–CXCR4) to distinguish both cell types was confirmed by the ICP-OES quantification of the iron levels in these samples, which further supported the observed results (Figure 4d). In fact, LN229 cells retained at least the double amount of particles of HK-2 cells. Although these high sensitivity techniques could detect these differences, the temperature profiles of LN229 or HK-2 cells containing only MP–CXCR4 were similar (Figure S2).

Table 2 shows the average calculated iron content per cell in each sample, depending on the initial iron concentration, when using both particle populations.

Table 2 – Average iron content per cell (pg Fe/cell) with increasing initial iron amounts.

	Initial [Fe] ($g \cdot L^{-1}$)			
Treatment	0.176+0.264	0.195+0.264	0.217+0.264	0.260+0.264
LN229+SPION+MP–CXCR4	90.0±4.0	61.7±6.3	106.4±16.5	108.0±28.7
LN229+SPION+MP–IC	80.4±35.8	53.5±0.7	97.7±37.3	77.7±4.2
HK-2+SPION+MP–CXCR4	44.5±16.6 *	53.3±3.6	41.6±13.3 **	38.0±10.2 **

Results are mean±SD of at least two independent experiments. Differences were estimated using regular two-way ANOVA followed by Tukey's multiple comparisons post test. *p<0.05 and **p<0.01 *vs.* LN229+SPION+MP–CXCR4 for the same initial iron concentration.

In agreement with the observed T_{max} results, LN229+SPION+MP–CXCR4 incorporated significantly more iron per cell than HK-2 samples (Table 2, p<0.05). For the highest tested initial iron amount, these samples accumulated nearly 110 pg Fe/cell to reach a T_{max} of 46.9 ºC (Table 1). These values are in line with a previous work by Gupta and co-authors that reported 150 pg Fe/cell in their experiments with folic acid-conjugated nanoparticles for MHT, after a 3 h incubation with DU145 prostate cancer cells (Gupta et al. 2016). Oh *et al.* also reported similar values for MDA-MB-231 breast cancer cells after a long 48-h incubation with non-targeted, chitosan-coated, magnetic particles (Oh et al. 2016). In agreement with the obtained *T* curves (Figure 2), the iron content in HK-2+SPION+MP–CXCR4 samples did not increase as a consequence of increased initial iron amount from either source, almost suggesting that a saturation level for the incorporation of nanoparticles was reached in this cell line.

Interestingly, correlation studies show that the iron content retained by each sample (measured by ICP-OES) positively and significantly correlated with the reached T_{max} (Spearman r=0.74, p=0.0128), for the LN229+SPION+MP–CXCR4 (Figure 5), which was not observed for the control samples.

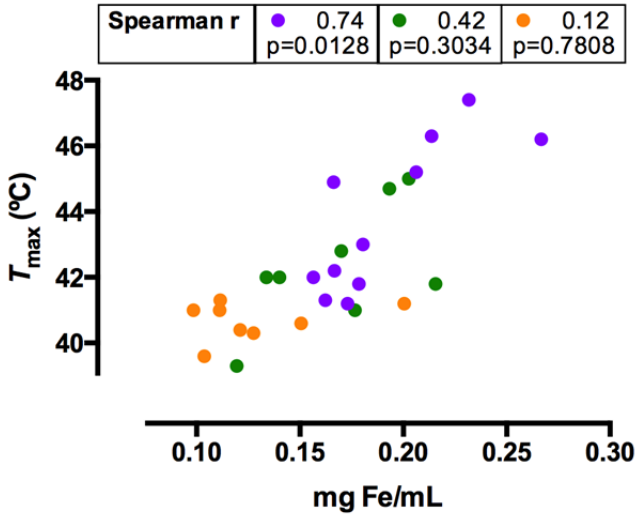

Figure 5 – Iron content per sample and its correlation with T_{max} and cell death after MHT. The amount of iron in each sample was quantified by ICP-OES. Spearman r correlation coefficients and their p-values, for each group of variables, are provided at the top of the respective graph. A significant positive correlation was found between the iron content and the reached T_{max} (a), and the levels of cell death (b), in LN229+SPION+MP–CXCR4 samples.

3.4. Cytotoxic outcome

The cytotoxic effects of MHT on LN229 and HK-2 cells were analysed at different time-points after AMF application. These results are shown in Figure 6.

Two hours after MHT, samples were analysed by flow cytometry (Figure 6a) to study the possibility of apoptotic/necrotic pathways being triggered by MHT. Samples were incubated with AnV–PE and 7-AAD and the amount of cells showing positivity for one or both labels was counted. Contrary to what could be expected for the samples reaching apoptotic temperatures (≈41–43 ºC), our samples exhibited only very low levels of AnV^+-only or double-stained cells, the 7-AAD being the main marker for positivity, whenever the *T* would destroy the membrane and allow this dye to enter the cell. A possible explanation for this observation, is the time-point at which the assessment was performed being too early for this apoptotic marker to be detected, as laser scanning confocal microscopy images taken 24 h after MHT showed increased double positive, round and detached cells for LN229+SPION+MP–CXCR4 compared to HK-2+SPION+MP–CXCR4 samples (Figure 6d). In the absence of a truly apoptotic signature, the events showing positivity were summed and presented as “percentage of dying cells” (Figure 6a), which strongly correlated with the T_{max} for the LN229+SPION+MP–CXCR4 samples (Spearman r=0.96, p=0.0028). For most of these samples, more than 25 % (dashed horizontal line, Figure 6a) of the cells stained positive for both labels, while for the control conditions (LN229+SPION+MP–IC and HK-

2+SPION+MP–CXCR4) remained below this level. A representative dot plot of the event distribution of a LN229+SPION+MP–CXCR4 sample is provided in Figure 6b in comparison with untreated control cells.

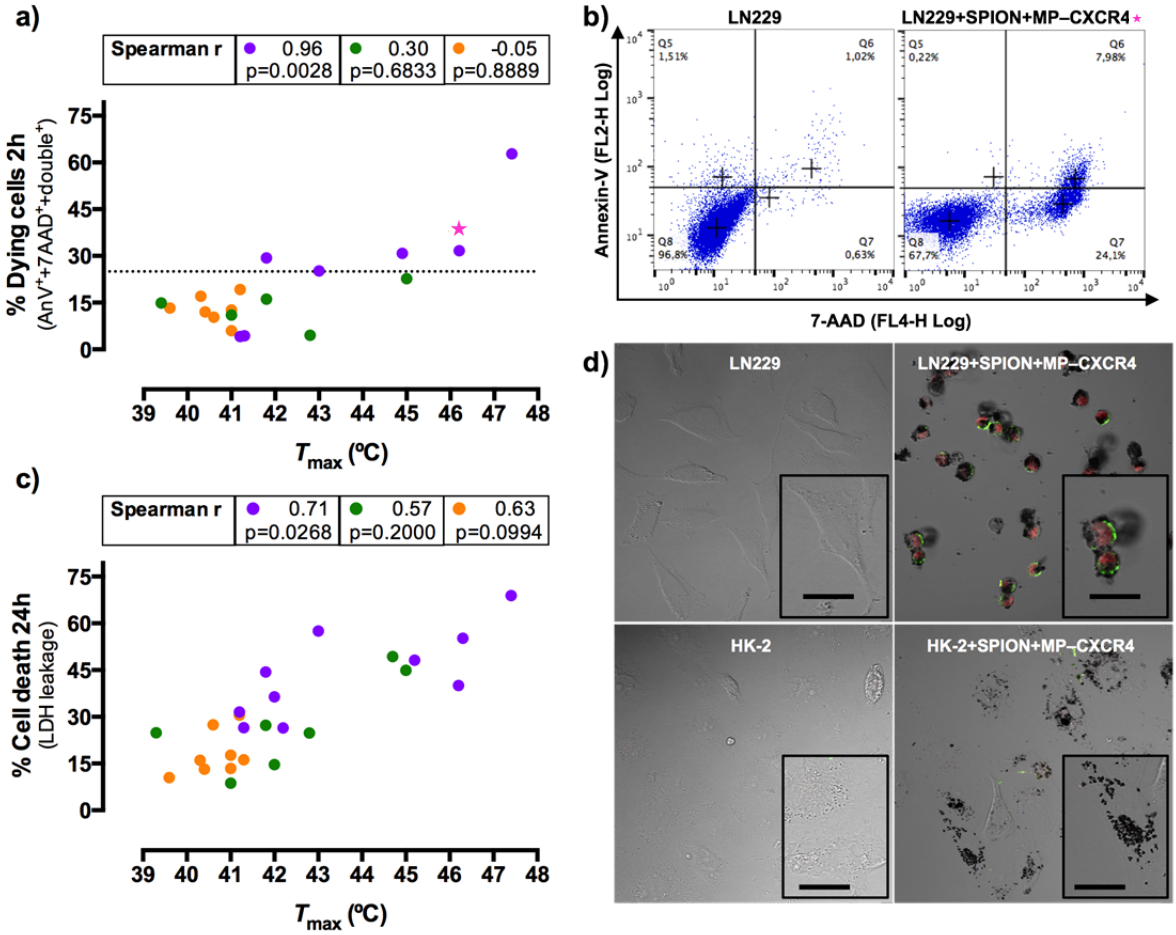

Figure 6 – Individual analysis of cell death/ viability after MHT.
a) Two h after AMF application, samples were stained with Annexin-V and 7-AAD and analysed using flow cytometry. Results are expressed as percentage (%) of dying cells, when positive for any or both fluorescence labellings, are shown for the diverse treatments; LN229+SPION+MP-CXCR4 (violet dots), LN229+SPION+MP-IC (green dots) and HK2+SPION+MP-CXCR4 (orange dots). b) Dot plot of the ★ sample is shown in comparison with untreated cells. "+" represents the mean. c) LDH leakage was evaluated 24 h after MHT as a measure of cell death. Spearman r values with the respective p values are provided for correlation studies. d) Laser scanning confocal micrographs of AnV and 7-AAD labelling of LN229 or HK-2 untreated cells, and 20 h after MHT with SPIONs and MP–CXCR4. Scale bar is 20 μm.

The leakage of lactate dehydrogenase (LDH) to the extracellular medium is a sign of membrane disruption and, consequently, effective cell death. LDH leakage levels were measured 24 h after MHT (Figure 6c), using 0.5 % Triton X-100 as a positive control (92.3±9.1 % cell death for HK-2 cells and 99.3±6.2 % cell death for LN229 cells). In accordance with the percentage of dying cells, cell death levels were equal to or greater

than 25 % for all the LN229+SPION+MP–CXCR4 samples and significantly and positively correlated with the observed T_{max} (Figure 6c, Spearman r=0.71, p=0.0268). On the other hand, cell death was always kept below 20 % for all the HK-2+SPION+MP–CXCR4 samples (Figure 6c).

Although cell death levels never reached 100 %, cell viability experiments after MHT, using a metabolic rate assay, showed that LN229+SPION+MP–CXCR4 samples, treated with the highest initial concentration of SPIONs, have significantly less viable cells than the HK-2 samples treated similarly, exhibiting less than 10 % viable cells 24 h after MHT and practically no viable cells 72 h after MHT (purple bars, Figure 7). This outcome was mainly dependent on the increase in *T*, as the used particles alone did not produce significant toxicity in any of the cell lines (black and grey bars, Figure 7). The AMF alone (i.e. applied to cells without nanoparticles) also did not affect cell viability (Figure S3). These results further support the elevated efficiency and overall safety of our strategy.

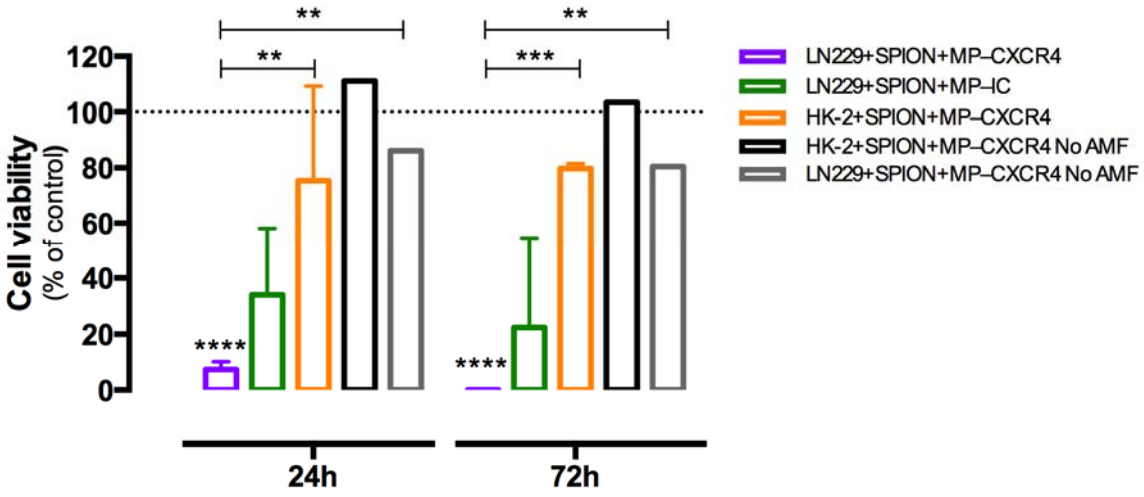

Figure 7 - Cell viability levels after MHT when using the highest tested amount of iron.
LN229 cells targeted with CXCR4-functionalized particles showed significantly lower cell viability than the HK-2 cells treated similarly. No viable cells were observed 72 h after MHT in LN229+SPION+MP–CXCR4 samples. The particles used for the experiments did not significantly affect LN229 and HK-2 cell viability (grey and black bars, respectively). Results are mean+SD. Differences were estimated using regular two-way ANOVA followed by Tukey's multiple comparisons post test. ****p<0.0001 *vs.* untreated cells (dashed line); **p<0.01 and ***p<0.001 *vs.* the referred sample, for the same end-point.

3.5. Comparative MHT outcome

One of the main purposes of this work was showing that the developed strategy may be applied to cells that expressed intermediate levels of the selected target but also, that it may, under similar conditions, differently affect cancer and normal cells. The results now obtained show that the proposed treatment (+SPION+MP–CXCR4) reached higher *T* in cancer than

in normal cells, in particular at the two highest tested initial iron concentrations (Table 1, Figure 2), because cancer cells accumulated more iron, both from non-targeted and from targeted origin, than normal cells (Table 2, Figure 4). The observed increased heating due to MHT lead to significantly increased cell death levels in cancer cells, showing these parameters positively correlated (Figures 5–7). The experiments performed in LN229 using IC-functionalized particles, further supported the role of MP–CXCR4 in the present strategy. The observed differences in cell viability at longer end-points definitely establish this strategy as highly efficient in killing cancer cells, while safe for normal cells.

There are only a few reports in the literature on *in vitro* targeted MHT in a mono-therapeutic context (Liao et al. 2015, Thomas et al. 2015). As an example, Thomas and co-workers, incubated cancer ($CD44^+$) *vs.* normal ($CD44^-$) cells from mouse, during 1 h, with hyaluronic-acid-conjugated particles (to target CD44 antigen) to perform *in vitro* MHT (Thomas et al. 2015). Even though the observed *T* was not specified, these authors reported cell viability levels of ca. 30 % for the cancer cells, without damaging normal cells. In another study, Liao *et al*. targeted liver cancer cells with galactosamine-conjugated nanoparticles to perform targeted *in vitro* MHT (780 kHz, 19 $kA \cdot m^{-1}$, 20 min), reaching desirably low viability levels of liver cancer cells as the ones reported herein (Liao et al. 2015). The application of this approach may be limited by the wide expression of asialoglycoprotein receptors, to which galactosamine binds to, in normal hepatocyte cells, as well (Shi et al. 2013).

In fact, most of the reports on targeted MHT in the literature refer to works in which this strategy was insufficient to kill cancer cells, therefore mainly being used in combination with chemotherapy agents (Mi et al. 2012, Kruse et al. 2014, Gupta et al. 2016). For example, Mi and co-workers developed Herceptin-conjugated nanoparticles and tested their MHT potential in breast cancer cells. The MHT efficiency of these particles, when submitted to AMF, was low (a 40 % reduction in cell viability) and a multimodality nanoparticle system, integrating nanoparticles and docetaxel in a copolymer matrix conjugated with Herceptin, was then proposed with very promising results. The synergistic effects of chemotherapy and targeted MHT lead to cell viability levels similar (lower than 20 % cell viability) to the ones reported herein obtained in a pure MHT context (Mi et al. 2012).

Using AMF parameters very similar to the ones used in this study, Kruse *et al*. described the use of CREKA-functionalized nanoparticles for targeted MHT in a lung cancer cell line. Considerably high initial magnetite concentration (3 mg $Fe_3O_4 \cdot mL^{-1}$ ≈ 2.17 mg $Fe \cdot mL^{-1}$) was necessary to reach *T* from 41–45 ºC during 20 min, which reduced cell viability to 50 %. The MHT strategy was, in the end, improved by an additive effect of cisplatin (Kruse et al. 2014). Another work using folate-conjugated nanoparticles for *in vitro*

targeted MHT reported a 35 % decrease in cell viability 24 h, after application of a 265 kHz and 27 $kA \cdot m^{-1}$ AMF during 10 min. These authors have chosen to use this targeted MHT strategy to sensitize cancer cells for chemotherapy with doxorubicin, further decreasing cell viability levels to around 10 % (Gupta et al. 2016). Combining two different populations of magnetic nanoparticles, the strategy proposed herein reached similar results in a mono-therapy context, and a single MHT session, without the need of using highly cytotoxic, non-selective, chemotherapeutic agents.

4. Conclusions

This work shows a successful application of a combination of non-targeted and targeted nanoparticles to kill glioblastoma cells, expressing intermediate levels of CXCR4, via magnetic hyperthermia, in a mono-therapeutic context. This treatment has proven to be safe for normal cells, which express even lower levels of the selected target, providing a promising strategy to be used in other types of cancer with similar levels of the same, or other, cancer biomarker.

5. Acknowledgements

V. V.-B. acknowledges FCT (Portugal) for her PhD fellowship (grant SFRH/BD/82556/2011). This work received financial support from the European Union (FEDER funds through COMPETE) and National Funds (FCT) through project Pest-C/EQB/LA0006/2013. This work is a result of the project Nanotechnology Based Functional Solutions (NORTE-01-0145-FEDER-000019), supported by Norte Portugal Regional Operational Programme (NORTE2020), under the PORTUGAL 2020 Partnership Agreement, through the European Regional Development Fund (ERDF).

6. Conflict of interest

The authors declare that they have no competing interests.

7. References

American Association of Neurological Surgeons. (October 2015). "Glioblastoma multiforme." Retrieved December 2016, from http://www.aans.org/patient information/conditions and treatments/glioblastoma multiforme.aspx.

Barbosa DJ, Capela JP, Silva R, Vilas-Boas V, Ferreira LM, Branco PS, Fernandes E, Bastos Mde L and Carvalho F. 2014. The mixture of "ecstasy" and its metabolites is toxic to human SH-SY5Y differentiated cells at in vivo relevant concentrations. *Arch Toxicol* **88**(2): 455-473.

Bleeker FE, Molenaar RJ and Leenstra S. 2012. Recent advances in the molecular understanding of glioblastoma. *J Neurooncol* **108**(1): 11-27.

Di Corato R, Bealle G, Kolosnjaj-Tabi J, Espinosa A, Clement O, Silva AK, Menager C and Wilhelm C. 2015. Combining magnetic hyperthermia and photodynamic therapy for tumor ablation with photoresponsive magnetic liposomes. *ACS Nano* **9**(3): 2904-2916.

Ehtesham M, Winston JA, Kabos P and Thompson RC. 2006. CXCR4 expression mediates glioma cell invasiveness. *Oncogene* **25**(19): 2801-2806.

Falk MH and Issels RD. 2001. Hyperthermia in oncology. *International Journal of Hyperthermia* **17**(1): 1-18.

Feng Y, Broder CC, Kennedy PE and Berger EA. 1996. HIV-1 entry cofactor: Functional cDNA cloning of a seven-transmembrane, G protein-coupled receptor. *Science* **272**(5263): 872-877.

Gupta J, Mohapatra J, Bhargava P and Bahadur D. 2016. A pH-responsive folate conjugated magnetic nanoparticle for targeted chemo-thermal therapy and MRI diagnosis. *Dalton Trans* **45**(6): 2454-2461.

Johannsen M, Gneveckow U, Taymoorian K, Thiesen B, Waldofner N, Scholz R, Jung K, Jordan A, Wust P and Loening SA. 2007. Morbidity and quality of life during thermotherapy using magnetic nanoparticles in locally recurrent prostate cancer: Results of a prospective phase I trial. *Int J Hyperthermia* **23**(3): 315-323.

Kim HC, Kim E, Jeong SW, Ha TL, Park SI, Lee SG, Lee SJ and Lee SW. 2015. Magnetic nanoparticle-conjugated polymeric micelles for combined hyperthermia and chemotherapy. *Nanoscale* **7**(39): 16470-16480.

Kioi M, Vogel H, Schultz G, Hoffman RM, Harsh GR and Brown JM. 2010. Inhibition of vasculogenesis, but not angiogenesis, prevents the recurrence of glioblastoma after irradiation in mice. *J Clin Invest* **120**(3): 694-705.

Kolen'ko YV, Bañobre-López M, Rodríguez-Abreu C, Carbó-Argibay E, Sailsman A, Piñeiro-Redondo Y, Cerqueira MF, Petrovykh DY, Kovnir K, Lebedev OI and Rivas J. 2014. Large-scale synthesis of colloidal Fe_3O_4 nanoparticles exhibiting high heating efficiency in magnetic hyperthermia. *The Journal of Physical Chemistry C* **118**(16): 8691-8701.

Kruse AM, Meenach SA, Anderson KW and Hilt JZ. 2014. Synthesis and characterization of CREKA-conjugated iron oxide nanoparticles for hyperthermia applications. *Acta Biomater* **10**(6): 2622-2629.

Liao SH, Liu CH, Bastakoti BP, Suzuki N, Chang Y, Yamauchi Y, Lin FH and Wu KC. 2015. Functionalized magnetic iron oxide/alginate core-shell nanoparticles for targeting hyperthermia. *Int J Nanomedicine* **10**: 3315-3328.

MagForce. (2016). "Nanotherm® therapy information for the treatment of brain tumors." Retrieved December 2016, from http://www.magforce.de/en/patienten/beschreibung-der-therapie.html.

Maier-Hauff K, Ulrich F, Nestler D, Niehoff H, Wust P, Thiesen B, Orawa H, Budach V and Jordan A. 2011. Efficacy and safety of intratumoral thermotherapy using magnetic iron-oxide nanoparticles combined with external beam radiotherapy on patients with recurrent glioblastoma multiforme. *J Neurooncol* **103**(2): 317-324.

Mi Y, Liu X, Zhao J, Ding J and Feng SS. 2012. Multimodality treatment of cancer with herceptin conjugated, thermomagnetic iron oxides and docetaxel loaded nanoparticles of biodegradable polymers. *Biomaterials* **33**(30): 7519-7529.

Oh Y, Lee N, Kang HW and Oh J. 2016. In vitro study on apoptotic cell death by effective magnetic hyperthermia with chitosan-coated $MnFe_2O_4$. *Nanotechnology* **27**(11): 115101.

Prijic S, Prosen L, Cemazar M, Scancar J, Romih R, Lavrencak J, Bregar VB, Coer A, Krzan M, Znidarsic A and Sersa G. 2012. Surface modified magnetic nanoparticles for immuno-gene therapy of murine mammary adenocarcinoma. *Biomaterials* **33**(17): 4379-4391.

Quinto CA, Mohindra P, Tong S and Bao G. 2015. Multifunctional superparamagnetic iron oxide nanoparticles for combined chemotherapy and hyperthermia cancer treatment. *Nanoscale*.

Rago G, Bauer B, Svedberg F, Gunnarsson L, Ericson MB, Bonn M and Enejder A. 2011. Uptake of gold nanoparticles in healthy and tumor cells visualized by nonlinear optical microscopy. *Journal of Physical Chemistry B* **115**(17): 5008-5016.

Redjal N, Chan JA, Segal RA and Kung AL. 2006. CXCR4 inhibition synergizes with cytotoxic chemotherapy in gliomas. *Clin Cancer Res* **12**(22): 6765-6771.

Rempel SA, Dudas S, Ge S and Gutierrez JA. 2000. Identification and localization of the cytokine SDF1 and its receptor, CXC chemokine receptor 4, to regions of necrosis and angiogenesis in human glioblastoma. *Clin Cancer Res* **6**(1): 102-111.

Rios A, Hsu SH, Blanco A, Buryanek J, Day AL, McGuire MF and Brown RE. 2016. Durable response of glioblastoma to adjuvant therapy consisting of temozolomide and a weekly dose of AMD3100 (plerixafor), a CXCR4 inhibitor, together with lapatinib, metformin and niacinamide. *Oncoscience* **3**(5-6): 156-163.

Rubin JB, Kung AL, Klein RS, Chan JA, Sun Y, Schmidt K, Kieran MW, Luster AD and Segal RA. 2003. A small-molecule antagonist of CXCR4 inhibits intracranial growth of primary brain tumors. *Proc Natl Acad Sci U S A* **100**(23): 13513-13518.

Sehgal A, Keener C, Boynton AL, Warrick J and Murphy GP. 1998. CXCR-4, a chemokine receptor, is overexpressed in and required for proliferation of glioblastoma tumor cells. *J Surg Oncol* **69**(2): 99-104.

Shi B, Abrams M and Sepp-Lorenzino L. 2013. Expression of asialoglycoprotein receptor 1 in human hepatocellular carcinoma. *J Histochem Cytochem* **61**(12): 901-909.

Sims LB, Curtis LT, Frieboes HB and Steinbach-Rankins JM. 2016. Enhanced uptake and transport of PLGA-modified nanoparticles in cervical cancer. *Journal of Nanobiotechnology* **14**.

Taratula O, Dani RK, Schumann C, Xu H, Wang A, Song H, Dhagat P and Taratula O. 2013. Multifunctional nanomedicine platform for concurrent delivery of chemotherapeutic drugs and mild hyperthermia to ovarian cancer cells. *Int J Pharm* **458**(1): 169-180.

Thomas RG, Moon MJ, Lee H, Sasikala AR, Kim CS, Park IK and Jeong YY. 2015. Hyaluronic acid conjugated superparamagnetic iron oxide nanoparticle for cancer diagnosis and hyperthermia therapy. *Carbohydr Polym* **131**: 439-446.

Wust P, Gneveckow U, Johannsen M, Bohmer D, Henkel T, Kahmann F, Sehouli J, Felix R, Ricke J and Jordan A. 2006. Magnetic nanoparticles for interstitial thermotherapy - feasibility, tolerance and achieved temperatures. *Int J Hyperthermia* **22**(8): 673-685.

Yin PT, Shah BP and Lee KB. 2014. Combined magnetic nanoparticle-based microRNA and hyperthermia therapy to enhance apoptosis in brain cancer cells. *Small* **10**(20): 4106-4112.

Yuan C, An Y, Zhang J, Li H, Zhang H, Wang L and Zhang D. 2014. Magnetic nanoparticles for targeted therapeutic gene delivery and magnetic-inducing heating on hepatoma. *Nanotechnology* **25**(34): 345101.

Zagzag D, Lukyanov Y, Lan L, Ali MA, Esencay M, Mendez O, Yee H, Voura EB and Newcomb EW. 2006. Hypoxia-inducible factor 1 and VEGF upregulate CXCR4 in glioblastoma: Implications for angiogenesis and glioma cell invasion. *Lab Invest* **86**(12): 1221-1232.

Zhang J, Dewilde AH, Chinn P, Foreman A, Barry S, Kanne D and Braunhut SJ. 2011. Herceptin-directed nanoparticles activated by an alternating magnetic field selectively kill HER-2 positive human breast cells in vitro via hyperthermia. *Int J Hyperthermia* **27**(7): 682-697.

Supplementary data

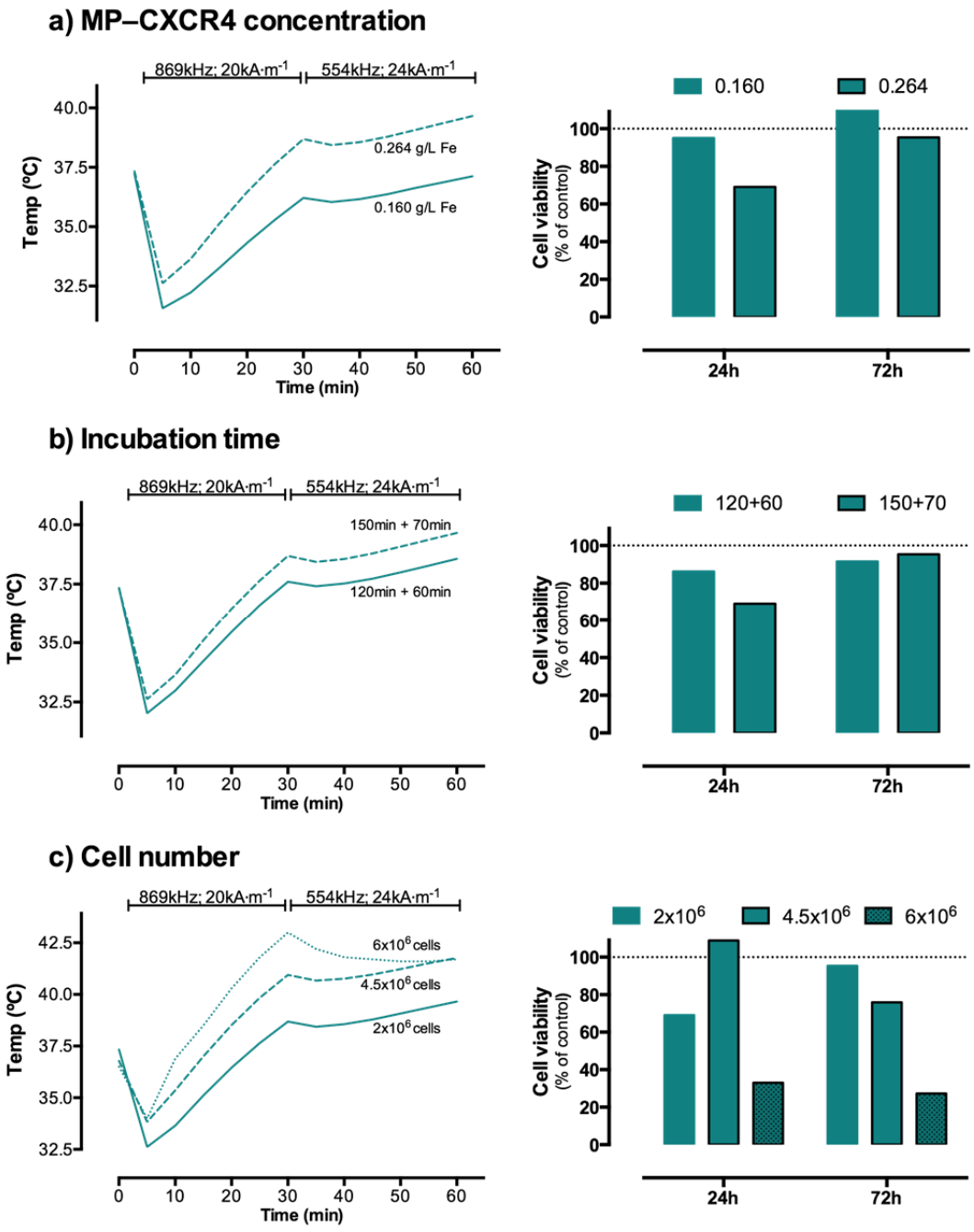

Figure S1 – Different parameters affecting the heating profile and MHT outcome on LN229 cells.
The optimization of the conditions to be used in our experiments indicated a dependence of the heating profile and the MHT outcome (cell viability) on the a) concentration of MP–CXCR4, b) the duration of the incubation period of cells with particles, and c) with the number of cells used per experiments. In every case, the same of amount of SPIONs was used (0.176 g Fe/L). Each comparison is made for experiments in which the only variable is the one referred.

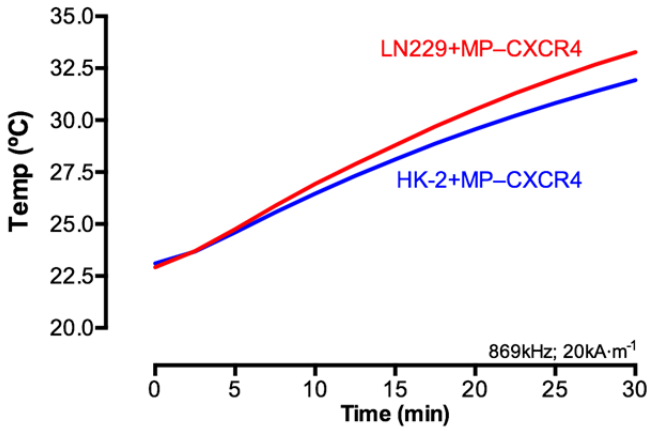

Figure S2 - Heating profile of LN229 and HK-2 cells with targeting particles (MP–CXCR4).
No differences between both cell lines were detected in the temperature profile, when using 2×10^6 cells per condition, despite the increased iron content of LN229 compared to HK-2 cells (Figure 4d of the man text). Results are mean+SD of two independent experiments.

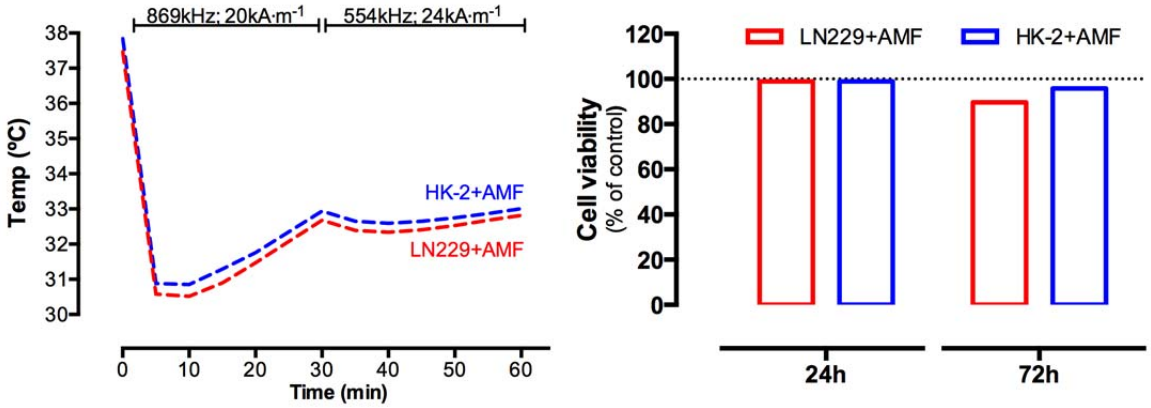

Figure S3 – Applying AMF to cells without magnetic nanoparticles.
Cells without magnetic particles were submitted to AMF (a) and to viability tests after that procedure (b). Results indicate that the used AMF conditions did not produce significant heating and did not significantly affect cell viability of neither cell line.

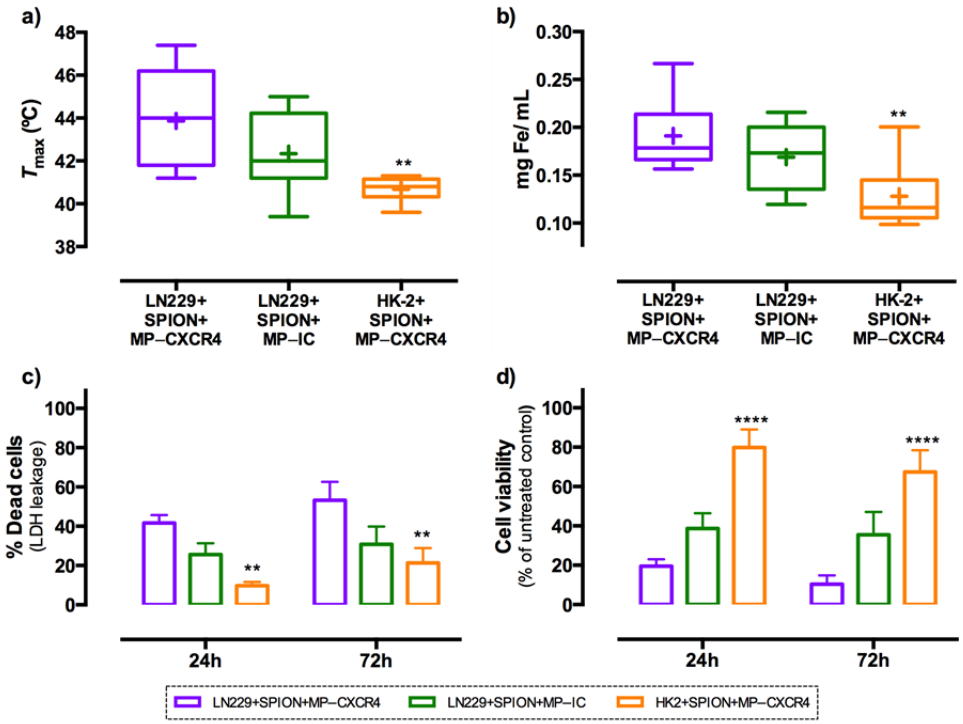

Figure S4 – Overview of MHT efficiency.
Disregarding the different initial concentrations of SPIONs tested in our studies, i.e., considering the results as only being dependent on cell type or particle functionalization, shows that, overall, this strategy produced significantly higher MHT temperatures (a), and significantly increased iron content (b) in cancer cells treated with the SPION and CXCR4-functionalized particles (LN229+SPION+MP–CXCR4), as compared with normal cells subjected to the same treatment (HK-2+SPION+MP–CXCR4). Results are min to max ("+" represents the mean). Differences were estimated using ordinary one-way ANOVA followed by Holm-Sidak's multiple comparisons post test (a) or one-way ANOVA (Kruskal-Wallis) followed by Dunn's multiple comparison post test (b). Similarly, cell death levels (c) were significantly higher for LN229+SPION+MP–CXCR4 samples than the HK-2+SPION+MP–CXCR4 samples, a result corroborated by the significantly lower cell viability levels (d) observed for LN229 cells compared to HK-2 treated similarly. Results are mean+SEM of at least six independent experiments. Differences were estimated using two-way ANOVA followed by Tukey's multiple comparisons post test (c and d). **p<0.01 and ****p<0.0001 *vs.* LN229+SPION+MP–CXCR4 samples.

Interestingly, even when disregarding the differences in the initial SPIONs concentration, the differences between cancer (LN229) and normal (HK-2) cells were evident. Significantly elevated temperatures, higher iron content, increased cell death and lower cell viability were found after MHT was performed in LN229 cells with SPIONs and targeted particles (MP–CXCR4), as compared to the same treatment applied to normal cells. This observation further highlights the elevated efficiency and safety of the proposed MHT strategy.

CHAPTER III

Integrated Discussion and Conclusions

Integrated Discussion

This work was devoted to the development of a targeted anticancer therapy based on MHT. Therefore, the workflow of these studies consisted in: first, optimizing the functionalization of the magnetic agents to be used for the MHT studies; second, selecting the cancer target; third, tuning the MHT conditions for optimized heating; and fourth, performing MHT studies with targeted MNPs in *in vitro* cancer models. In this sense, the following discussion will roughly address these issues and integrate the observed results, without the need to strictly follow the mentioned order of events.

1. Functionalization of the MNPs for MHT studies

The attachment of biomolecules to nanomaterials is an important step towards their increased stability, biocompatibility and targeting ability for the MHT studies. The immobilization strategy is selected according to the functional groups present on the particle's surface (Martins et al. 2012). Particularly for this work, we optimized a coupling methodology that takes advantage of the carboxylic groups from the PAA-coated MNPs to covalently bind free amine groups from proteins, known as EDC-Sulfo-NHS coupling chemistry. The protein BSA was used as a model biomolecule due to its low price and its known enhancement of the MNPs' stability and biocompatibility (Jenita et al. 2014). We have previously accomplished direct physisorption of BSA on oleic acid-coated MNPs, which are only soluble in non-polar organic solvents, after promoting their phase transfer to an aqueous solution (Appendix) (Vilas-Boas et al. 2015). Specifically, the phase transfer to aqueous solvents enables the biomedical use of those MNPs, while the BSA further promotes their stability and biocompatibility. Mehta and co-workers were the first to report direct binding of BSA to bare MNPs, reaching high immobilization rates (Mehta et al. 1997), i.e., nearly all the initial amount of BSA was immobilized in the MNPs. Similarly, in their work, Wang *et al.* observed increased efficiency of avidin immobilization for higher initial concentrations of protein, immobilizing nearly 100 % of the initial amount of protein (Wang and Lee 2003). Nevertheless, the rough number of biomolecules per surface area of MNPs was not calculated in these two studies and, therefore, the surface coverage efficiency could not be estimated. In fact, while high protein content may reflect the formation of various protein layers at the MNPs surface (Martins et al. 2012) —which may unnecessarily contribute to loss of functionality with time and increased cost of the process, particularly for expensive biomolecules—low surface coverage may hamper the stability of the MNPs. Therefore, reporting the functionalization efficiency in terms of number of biomolecules per MNP, allows estimating the probability of having successive layers of proteins or low number of immobilized biomolecules. For this purpose, the

available surface area in each nanoparticle was compared to the area that each protein molecule would occupy (parking area). Thus, the number of biomolecules that physically fit each MNP was estimated, similarly to a previous report (Hung et al. 2008). While increasing the initial protein concentration led to increased final amount of protein interacting with the MNPs, as seen by others (Wang and Lee 2003, Mu et al. 2015), these biomolecules were probably forming a double layer around the MNPs at the highest tested initial concentration. Reports on the formation of a double protein layer in the available literature are scarce (Martins et al. 2012).

We observed a dependency of the functionalization efficiency on the coupling agents' (EDC and Sulfo-NHS) concentration (Figure 3, Manuscript 1). While the lowest tested concentration resulted in very low immobilization efficiency, increasing the concentrations of coupling agents led to increasing efficiencies, however accompanied by increased MNPs' aggregation. Using avidin as protein model, Wang and co-workers also observed MNPs' agglomeration and precipitation when using high concentrations of coupling agents (Wang and Lee 2003). The observed agglomeration prohibits the use of these MNPs for biomedical purposes. With this in mind, the selected concentration of coupling agents to be used in further procedures was the one yielding better overall MNPs' stability while keeping satisfactory surface coverage with the protein.

The attachment of antibodies (the targeting agents in this work) to MNPs may be achieved either by direct immobilization of the antibodies through their functional groups, or by using a linker protein such as STR or PA, which allows further high affinity binding of antibodies (respectively, biotinylated or not). The direct immobilization of antibodies is possible for polyclonal antibodies (pAb) but practically unaffordable for many expensive monoclonal antibodies, due to the excess of biomolecule required to favour the directionality of the coupling chemistry. Furthermore, the random immobilization of the antibody molecules may hamper the antibody's ability to recognize its target, an issue that is also raised when using STR to bind biotinylated antibodies. In fact, we observed considerable aggregation of the STR–MNPs after addition of biotinylated antibodies (Figure 9, Manuscript 1). The tetravalent nature of STR regarding its high affinity ligand, biotin, and the presence of two (or more) biotin molecules per (biotinylated) antibody may lead to cross-interaction between MNPs that can, therefore, share the same antibody molecules (Figure 10, Manuscript 1). Moreover, the presence of biotin in random parts of the antibody may hamper their functionality, particularly if present at the fragment responsible for antigen binding (Fab). These issues are unlikely to occur in PA–MNPs, where the interaction between the antibody and the PA is oriented through the Fc region of the antibody, while keeping the Fab free for antigen recognition and binding (Figure 10,

Manuscript 1). No significant MNPs aggregation was observed for PA–MNPs after antibody immobilization (Figure 9d, Manuscript 1).

Of note, the estimation of PA immobilization was peculiar and rather challenging. While others have previously estimated PA immobilization on MNPs measuring its absorbance at 280 nm (Mu et al. 2015), in this work we noticed some interference, probably arising from the contact with the MNPs, which prevented the used of this methodology. Therefore, PA quantification on the supernatants collected after protein immobilization was performed using CD signal at 208 nm (Figure 7, Manuscript 1). A linear correlation between this signal and the sample's absorbance in the far UV spectrum (at 195 nm) was initially assured, as previously recommended for other proteins (Kelly et al. 2005, Fears et al. 2013). We believe this to be the first report in which the efficiency of PA immobilization on MNPs was assessed using CD.

The reached levels of surface coverage for STR, PA and pAb were very satisfactory (69, 84 and 95 %, respectively), suggesting a broad and immediate applicability of the immobilization strategy optimized in this work to other proteins, resulting in sufficient coverage of the MNPs' surface.

After the immobilization of antibodies, a high degree of aggregation was observed for the STR–MNPs but not for the PA–MNPs, suggesting higher stability of the latter functionalized MNPs. This fact, along with the clear separation between the heating curves of the CXCR4–PA–MNPs and the respective isotype control MNPs, suggests that PA–MNPs are more suitable for biomedical applications, namely MHT, than the STR–MNPs. However, the results suggested that the amount of CXCR4–PA–MNPs that interacted with the cells was insufficient to produce cytotoxicity. Therefore, bigger MNPs, with higher magnetic susceptibility, were used in the subsequent experiments to further increase the heating ability of this targeted strategy.

2. CXCR4 as target for specific MHT of cancer cells

The CXCR4 is a chemokine receptor overexpressed in many types of cancer cells that has been used as part of lymphoma and multiple myeloma treatment (Jagirdar et al. 2015). It has recently been suggested as a target for the treatment of ALL (de Lourdes Perim et al. 2015) and GBM (Terasaki et al. 2011), and its antagonist has been successfully used as an adjuvant in GBM treatment (Rios et al. 2016). Although CXCR4-targeting MNPs have been tested for diagnostic purposes, particularly for magnetic resonance imaging (He et al. 2012, Zevon et al. 2015), using CXCR4-targeted MNPs for MHT cancer treatment has never been proposed or developed to date. Furthermore, the

MHT strategies clinically available so far are limited to the local injection of non-targeted MNPs, resulting in inhomogeneous MNPs' distribution within the tumour and, consequently, variable intratumoural heating. Therefore, many of the studies on targeted MHT show lack of efficiency, which is normally increased by combining chemotherapeutic drugs (Mi et al. 2012, Sivakumar et al. 2013, Taratula et al. 2013, Kruse et al. 2014, Gupta et al. 2016). This combined strategy often results in unwanted side effects of these non-selective drugs. For those reasons, the development of an efficient anti-cancer pure MHT strategy based on CXCR4-targeting would be a significant refinement of the available treatment.

Contrary to the endocytosis of non-targeted MNPs, the magnetic content that cells can bear at their surface is, in theory, limited by the number of surface receptors available for interaction with targeted-MNPs. We chose a widely used *in vitro* model of ALL, Jurkat cells, for the set-up of our MHT strategy due to the elevated expression of that surface receptor in this cell line (Figure S3, Manuscript 2 and (Huang et al. 2014)). For the following studies on adherent cells, a GBM *in vitro* model (LN229 cells) was selected, exhibiting lower levels of surface receptor, but still higher than negative control cell line, the HK-2 cells (Figure 1, Manuscript 3), an *in vitro* model of proximal tubular cells from normal kidney. In this context, CXCR4 expression in LN229 cells was, therefore, categorized as intermediate.

Following the results of the functionalization experiments (Manuscript 1), for our MHT studies, we selected the commercially available dextran composite particles with a diameter of 250 nm (Rudershausen et al. 2002) for further attachment of anti-CXCR4 monoclonal antibodies. These particles are, magnetic beads, also known as cluster-type particles, composed of smaller IONPs embedded in a dextran matrix, with PA covalently bound to their surface. Compared to the previously functionalized MNPs (Manuscript 1), the increased magnetite content of these MPs makes them suitable for experiments that highly depend in the magnetic amount, like MRI and MHT studies (Wabler et al. 2014). In addition, the relative cost of these PA modified MPs was far lower than performing the modification of the 18 nm MNPs used for the functionalization studies.

3. Setting up the MHT conditions

The preliminary tests on the optimization of the MHT conditions [the AMF power, which is proportional to the product of the field amplitude H and the frequency f ($H \cdot f$ product), and the time of exposure] indicated that sustaining the T above 40 ºC for periods longer than 30 min resulted in decreased cell viability (Figure S1, Manuscript 2). These

results are in line with previous publications in which MHT efficiency was enhanced by prolonging the period of exposure to higher *T* (Levi-Polyachenko and Stewart 2011, Taratula et al. 2013). According to these preliminary results, the conditions were tuned to produce a rapid initial increase in the sample's *T*, reaching a maximum *T* at the midterm of the treatment, and then keeping this high *T* for the second half of the treatment (Figure S2, Manuscript 2). Although there are examples in the literature of tuning the AMF power during the experiment to limit the observed T_{max} (Alvarez-Berrios et al. 2014, Oh et al. 2016), we believe this is the first use of a pre-established, two-step, AMF application.

When using CXCR4-targeted MPs only, in Jurkat cells, significant, though insufficient, heating was observed (red, Figure 1, Manuscript 2). Further studies revealed that more than 90 % of the targeted MPs were kept in these samples (Table 1, Manuscript 2), suggesting that an increment of the cell population would not result in increased heating unless simultaneously accompanied by an increase in the amount of targeted MPs.

A boost of magnetic material was then provided to cells to produce increased and, therefore, more efficient, heating, preserving a pure MHT strategy, an approach that had never been tested before. This boost was provided by 18 nm core iron oxide nanoparticles synthesized and fully characterized in house (Kolen'ko et al. 2014). These MNPs were coated with PAA and were used without any other modification, being described herein as non-targeted MNPs or SPIONs. PAA is a hydrophilic polymer that has gained recent interest as coating agent for MNPs due to the presence of many functional groups and the stability it brings to the MNPs' systems (Lin et al. 2005). Although only a few studies addressed the biocompatibility and biodistribution of PAA–MNPs, they interestingly report effects deriving from relevant doses used as contrast agents for imaging procedures (Couto et al. 2016) or in MHT clinical studies (Iversen et al. 2013). These reports consensually showed enhanced accumulation of MNPs mainly in immune cells of the RES of the liver and spleen (Prijic et al. 2012, Couto et al. 2016), but also in the kidneys (Iversen et al. 2013), after intraperitoneal or IV administration. Ding and co-workers studied the continuous biodistribution of gelatin-PAA nanoparticles (ca. 100 nm) loaded with cisplatin (developed for targeted drug release), at different time-points after IV injection. Similar to the previous studies, the nanoparticles accumulated in the spleen, liver and femur (bone marrow) as a consequence of RES clearance. Interestingly, after 22 h, the nanoparticles accumulated in the tumour, as a consequence of the EPR effect (Ding et al. 2012). The EPR effect is a characteristic of solid tumours that derives from the combined hyper-permeability of tumour vasculature, exhibiting pores that may be hundreds of nanometers in size, along with the lack of functional lymphatics that favours nanoparticles' retention (Iyer et al. 2006). This has practical implications since

nanoparticles with sizes above 10 nm (the regular pore size of normal vasculature) extravasate to the tumour but not to the normal tissues, providing a natural, passive targeting, system.

Similarly unanimous is the reported overall biocompatibility of PAA coated nanoparticles (Prijic et al. 2012, Couto et al. 2016), only producing temporary effects in the blood pressure (Iversen et al. 2013), although the triggering of an inflammatory response has also been reported (Couto et al. 2016). At a cellular level, and similar to our findings, PAA–MNPs (i.e., SPIONs) have been found internalized in endosomes (Iversen et al. 2013). The internalization of complexes of PAA–MNPs (200–400 nm) has also been reported, although the bigger size of these complexes suggests that these particles were, most probably, phagocytized (Prijic et al. 2012).

The specific interaction of the targeted MPs with cells was confirmed by flow cytometry and laser scanning confocal microscopy, using a fluorescently labelled secondary antibody targeting the monoclonal antibody of the targeted MPs (Figure 2, Manuscript 2). Interestingly, the interaction of particles with cells induced light scattering changes that could be followed by flow cytometry through the significant differences in the inner complexity (side scatter, SSC, signal) of the analysed events (Figure 3, Manuscript 2). Poirier and co-workers found similar increments in the inner complexity of the cells, which they related to internalization of 20 nm silver nanoparticles (Poirier et al. 2014). Later, a comparable increase in SSC signal was correlated with the iron content of cells, suggesting that flow cytometry studies may be performed to estimate the uptake of SPIONs by mammalian cells (Friedrich et al. 2015). We observed increased inner complexity signals of cells incubated with both types of particles, independently or together, which is a sign of particle internalization in our studies. Even though the threshold size for endocytosis to occur is not perfectly established, there seems to be consensus around the 500 nm upper limit (Rejman et al. 2004, Bychkova et al. 2012). We could not precisely determine whether, in our studies, the CXCR4-targeted MPs were internalized or not by the cells, due to lack of resolution of the light microscopy studies. However, the short time-period of incubation in our study (240–280 min) seems insufficient for the slower rate of internalization of larger particles (dos Santos et al. 2011). Although the internalization of the CXCR4-targeted MPs cannot be excluded in our studies, we believe that the presence of the MPs at the cell surface enhances the roughness of the cell membrane, therefore, producing increased light scattering interpreted as increased inner complexity.

4. The proof of concept: targeted MHT against leukaemia cells

The combination of both non-targeted SPIONs and CXCR4-targeted MPs, in consecutive incubations, and the optimized AMF treatment, resulted in sufficient heating to induce death in Jurkat cells. Noteworthy, in our MHT experiments, the excess of free particles was always removed in every incubation step, to guarantee that only the uptaken SPIONs or interacting MPs would contribute to the observed heating effect. This important step is often missing in many *in vitro* MHT studies (Mi et al. 2012, Sivakumar et al. 2013, Kruse et al. 2014, Sadhasivam et al. 2015, Thomas et al. 2015), which prevents the attribution of the observed effects to the targeting system.

Two distinct outcomes were observed according to the reached *T* (purple, Figure 1, Manuscript 2), which triggered distinct cell death pathways. The activation of apoptosis for *T* up to 43 ºC is a well-known fact, as well as the appearance of necrotic features for higher *T* (Hildebrandt et al. 2002). Although rather unexpected, these distinct *T* profiles may be a result of using different batches of antibodies and particles (Guardia et al. 2012), and even different cell passages.

Interestingly, for the *T* range achieved in our work (42.5–47 ºC), it has been established that a drop of 1 ºC in the *T* can only be compensated by doubling the exposure time to reach similar efficiency. For *T* below this range, the exposure time needs to be multiplied by a factor of 4 (Hildebrandt et al. 2002). These facts demonstrate the importance of using MNPs with increased heating performance for the MHT experiments, which is often measured in terms of SAR values. The MNPs used in our work exhibited high SAR values in our experimental conditions, assuring effective heating and proving appropriate for the MHT tests. Still, comparing these values with the ones reported in the literature is limited by the considerable dependence of SAR values on the equipment and the AMF parameters used for the experiments (Vallejo-Fernandez et al. 2013). The development of a standardized procedure to measure the heating ability of the MNPs could help surpassing this limitation.

Notwithstanding the low levels of Annexin-V positive cells in the samples reaching apoptotic *T* (*T*c=42.7 ºC), the cystein protease, caspase-3, was significantly activated (Figure 4, Manuscript 2), supporting the triggering of an apoptotic pathway in these conditions. On the other hand, the elevated levels of cells with disrupted membrane (Pi and double positive cells) and the absence of caspase-3 activation (Figure 4, Manuscript 2) provide clear indication of necrotic cell death in the samples reaching higher *T* (*T*c=45.2 ºC). Both pathways led to a drastic decline in cell viability and extensive cell death (Figure 5, Manuscript 2), denoting the elevated efficiency of the proposed strategy.

Of note, while the activation of a necrotic pathway resulted in long-term, complete loss of cell viability after MHT, a slight recovery was observed when the apoptotic pathway was triggered, at the later time-point after MHT (Figure 5, Manuscript 2). To overcome this limitation of apoptotic MHT, which has been previously observed (Lee et al. 2015), a second AMF cycle could be performed in an attempt to kill the surviving cells, as done by Ito and co-workers (Ito et al. 2004). These authors observed cell viability recovery after apoptotic MHT in breast cancer cells and could prolong the low cell viability levels when a second AMF cycle was applied 24 h after the first treatment. This approach is also commonly used in an *in vivo* context (some examples in Table 4, General Introduction).

Our results suggest the necrotic pathway to be a more effective cell death mechanism than the apoptotic pathway, and are supportive of previous conclusions on the insufficient efficiency of apoptotic MHT (Lee et al. 2015), particularly in a mono-therapeutic context. There is a wide discussion on whether apoptotic or necrotic pathways should be preferred for cancer treatment (de Bruin and Medema 2008). While apoptosis is considered a more natural process that can be cleaned up by macrophages, the main feature of necrosis is the inflammatory response that normally arises from the spill of the intracellular contents to the extracellular medium through the damaged cell membrane (Proskuryakov et al. 2003). Using an apoptosis-inducing agent to treat cancer may, therefore, seem debatable, and even counterproductive, due to the characteristic apoptosis-resistance of many cancer cells, particularly in solid tumours (de Bruin and Medema 2008). For such approach to be effective, this mechanism of cell death must be restored in these cells, which represents one of the major aims of anti-cancer therapy nowadays (Indran et al. 2011). In fact, the frequent tumour recurrence observed following treatment with an apoptosis-inducing agent led to the search for treatments in which necrosis is induced instead, as a strategy to increase the efficiency of the treatment (Proskuryakov et al. 2003). Particularly for MHT, it is known that reaching T above 43 ºC greatly enhances the treatment's efficiency, possibly due to activation of the necrotic pathways (Hildebrandt et al. 2002). Therefore, it is our conviction that the methodology proposed herein provides strong evidence for the implementation of the concept, demonstrating all the requisites to proceed to further studies in *in vivo* models.

The importance of CXCR4-targeting in the presented strategy was supported by the absence of significant heating of samples in which the CXCR4-targeted MPs were replaced by their IC counterparts (Figure 1, Manuscript 2). In fact, only when the CXCR4-targeted MPs were used, in combination with the non-targeted MNPs, and the AMF was applied, a significant cytotoxic effect was observed (Figure 5, Manuscript 2). Most studies concerning *in vitro* testing of targeted MHT strategies do not test this type of control

antibodies (or peptides), but the same MNPs without the targeting molecule (Mi et al. 2012, Taratula et al. 2013, Kruse et al. 2014, Liao et al. 2015), which seems particularly relevant if simultaneously not testing normal cells. Although the IC antibody would not be used in a clinical situation, it is our conviction that using the MP–IC, instead of MPs without antibody, in parallel to the MP–CXCR4, ensures a more reliable control experiment. This way, the observed effects may be undoubtedly attributable to that particular test antibody, and not to the presence of any antibody that could unspecifically bind to the cells.

5. Application of the developed strategy to adherent cell models

The lower surface expression levels of CXCR4 in adherent cells as compared to Jurkat cells (Figure 1, Manuscript 3) implied the need for further optimization of the developed strategy to be applicable in those cellular models. The observed outcome strongly depended on the concentration of targeted and non-targeted MNPs, the duration of the incubation period, and the cell number to be used in the experiments (Figure S1, Manuscript 3).

In parallel, the same procedure was tested in normal cells to monitor the occurrence of unwanted cytotoxic side effects. In this sense, the ability of MP–CXCR4 to preferentially accumulate in LN229, compared to normal cells, was evident, as suggested by the elevated iron amounts in cancer cells targeted with MP–CXCR4, and further corroborated by optical microscopy studies (Figure 4, Manuscript 3). However, similarly to Jurkat cells, MHT mediated solely by the CXCR4-targeted MPs was insufficient to produce significant elevation of the *T*, generating heating profiles very similar to the HK-2 ones (Figure S2, Manuscript 3). This fact suggested that, unlike Jurkat cells, SPIONs would have more impact than the MP–CXCR4 on the overall heating of GBM cells, due to limited CXCR4 expression. Therefore, increasing amounts of SPIONs were then tested and a dependency of the reached T_{max} on the initial concentration of SPIONs was observed (Figure 2 and Table 1, Manuscript 3). Interestingly, for the normal cell line, HK-2 cells, increasing the initial amount of SPIONs or the presence of the MP–CXCR4 did not produce differences in the observed *T*. Furthermore, cancer cells naturally internalized bigger amounts of SPIONs than normal cells, a fact already noticed by others (Rago et al. 2011, Prijic et al. 2012, Sims et al. 2016). This fact may represent an important advantage if also occurring in an *in vivo* context, along with the EPR effect that also favours MNPs accumulation in tumour tissues (Iyer et al. 2006). These results suggested that, in our study conditions, normal cells might reach a saturation of their endocytic pathways at a faster rate than cancer cells. Differences in cell membrane dynamics and composition

between normal and cancer cells may be on the basis of this contrasting accumulation (Rago et al. 2011), along with their distinct cellular metabolic rate (Bychkova et al. 2012).

Applying the optimized strategy to LN229 versus HK-2 cells resulted in very distinct heating profiles and, consequently, distinct MHT outcome, as expected. The T_{max} exceeded 41 ºC in MP–CXCR4-treated cancer cells, independently of the initial amount of SPIONs. Particularly at the highest tested initial concentration of SPIONs, for which T_{max} overreached 45 ºC, long-lasting and complete loss of cell viability was observed (Figure 7, Manuscript 3). Contrarily to cancer cells, in normal cells, T_{max} remained below (or equal to) 41 ºC, independently of the initial amount of SPIONs, producing limited cytotoxicity. Using MP–IC instead of the MP–CXCR4 in the LN229 cells further strengthened our findings, attributing a noteworthy role for CXCR4-targeting in the proposed methodology. Furthermore, the SPIONs, MPs, and the AMF conditions used in the experiments produced no significant cytotoxic effects by themselves (Figure 5, Manuscript 2; Figures 7 and S3, Manuscript 3).

6. Comparative MHT efficiency

There are only a few studies reporting *in vitro* targeted MHT efficiency comparable to ours, in a mono-therapeutic context (Taratula et al. 2013, Liao et al. 2015). While Taratula *et al.* reported long-lasting decreased cell viability in cells that reached 44 ºC after MHT mediated by LHRH-targeted MNPs (Taratula et al. 2013), Liao *et al.* observed low cell viability levels before the population doubling time was complete, which may be misleading. The latter authors also did not report the achieved *T* and, therefore, we cannot predict if cellular recovery was expected or not (Liao et al. 2015). In any case, the results of our work suggest that the proposed strategy is amongst the most effective *in vitro* MHT procedures reported so far, using a mono-therapeutic MHT approach that requires lower concentration of magnetic material than previous works presenting similar outcomes (Guardia et al. 2012). Guardia and co-workers needed to increase the *T* to 65 ºC to observe complete cell death, which may be a dangerous *T* in a clinical context, especially if maintained during long periods (Guardia et al. 2012). The normal tissues surrounding the tumour may be damaged by the dissipation of heat from the tumour. In their *in vivo* studies, Huang *et al*. observed an increase in the tumour's *T* to 60 ºC but it was limited to an interval of less than 5 min and, therefore, no significant adverse effects derived from it (Huang and Hainfeld 2013). Using non-targeted zinc and manganese-doped nanoclusters, Qu *et al*. reported comparably low levels of cell viability in their *in vitro* MHT studies with breast cancer cells (Qu et al. 2014).

Results similar to ours were observed if combining *in vitro* targeted MHT with doxorubicin (Gupta et al. 2016), docetaxel (Mi et al. 2012), or 5-fluorouracyl (Sivakumar et al. 2013). These chemotherapeutic agents, if not carried by the targeted MNPs, will inevitably produce cytotoxicity in normal cells. The effects of non-targeted MNPs for *in vitro* MHT have also been potentiated by the combination with other therapeutic modalities, this way reaching outcomes similar to ours. A group from the University Paris Diderot combined MHT with photodynamic (Di Corato et al. 2015) and photothermal (Espinosa et al. 2016) therapies for increased efficiency, resulting in cell viability levels similar to the ones observed with our strategy. The need for different equipment for the application of their combination approach (AMF applicator and laser system) may represent a disadvantage compared to a pure MHT strategy that only requires an AMF applicator.

7. Potential applications of the developed methodology

It is our conviction that the potential applications of the approach developed throughout this work go far beyond the models and targets evaluated herein. The overexpression of CXCR4 in many other cancer models, namely breast and prostate (Muller et al. 2001, Taichman et al. 2002), among others, suggest that this strategy may be successfully applied to those types of cancer. Similarly, choosing other target receptors, according to their overexpression, is another thrilling possibility that could be adapted individually to each type of cancer/ receptor overexpression, resembling a “personalized medicine” approach. Also exciting for further *in vivo* studies, is the possibility of allowing the targeted nanoparticles to chemotactically find their targets and accumulate at the tumour site after injection. In particular, for the *in vitro* models addressed in this work, *in vivo* studies shall establish the potential for further clinical developments, as addressed subsequently.

The development of this strategy in an ALL cancer model was primarily a consequence of the overexpression of CXCR4 in that cellular model. Despite this overexpression, the distribution of cancer cells throughout the whole body in the clinical context makes the application of this strategy for leukaemia treatment a real challenge. However, one could take advantage of the magnetic loading of the targeted cells to concentrate the cells in various locations within the body using external magnets, as suggested by Ma *et al.* for hepatocellular carcinoma (Ma et al. 2015). This strategy would allow a localized application of the AMF. The size of the targeted particles would need to be tuned because particles sized above 200 nm are known to be rapidly taken up by phagocytes of the RES and accumulate in the liver and spleen, limiting their half-life in circulation (Bychkova et al. 2012). Similarly to PEG, dextran coating is known to increase

the circulation time of the coated nanoparticles, by surpassing opsonisation (Sharma et al. 2012). Although this characteristic is not yet fully established for PAA coating, the biodegradable nature of that polymer and the presence of flexible hydrophilic chains suggest a prolonged residence time in blood to be possible. Additionally, the pro-apoptotic effects of PAA–MNPs on neutrophils might need to be considered (Couto et al. 2014), as well as the overall ability of the body to manage the iron stores, to avoid iron-related toxicity (Valdiglesias et al. 2016).

Regarding the treatment of GBM, we expect the strategy described and developed herein to be safer than the currently available approach due to the selectivity of the targeted-MNPs. In normal conditions, cells from the nervous system recognizably resist to iron-induced cytotoxic effects by storing it intracellularly in iron-ferritin complexes (Valdiglesias et al. 2016). Therefore, iron-related cytotoxicity derived from the presence of the MNPs is not expected for normal cells. In fact, studies in normal astrocytes showed resistance to iron concentrations, supplied as IONPs, between 0.1 and 4.0 mM (Geppert et al. 2011), which fall within the range of concentrations used in this study. As an example, the possibilities offered by a targeted MHT approach could be explored after an intrathecal injection of the MNPs (Calias et al. 2014), instead of the direct IT injection used so far with non-targeted MNPs (MagForce 2016a). This administration route in the cerebrospinal fluid is already used for some chemotherapeutic drugs, particularly for the treatment of disorders of the central nervous system (Calias et al. 2014), and has been recently tested *in vivo* for the administration of lipid nanoparticles for genetic therapy in Friedreich's ataxia (Nabhan et al. 2016).

Conclusions

From the work performed under the scope of this dissertation some conclusions may be drawn:

⇒ Poly(acrylic acid)-coated iron-oxide nanoparticles synthesized in house could be efficiently functionalized with distinct proteins through the EDC-Sulfo-NHS coupling chemistry.

⇒ Staphylococcal Protein A proved to be a more suitable protein to mediate oriented immobilization of antibodies onto MNPs for biomedical purposes;

⇒ Total magnetic loading, time of exposure, alternating magnetic field parameters, and number of cells, are determining factors for the efficiency of an *in vitro* magnetic hyperthermia treatment;

⇒ A purely targeted MHT strategy to kill cancer cells *in vitro* was found to be poorly efficient. Such inefficiency was surpassed using a second population of non-targeted MNPs, preserving a mono-therapeutic approach;

⇒ The MHT strategy developed herein was further applied to other *in vitro* cell models, namely LN229 cells, with lower CXCR4-expression, reaching similarly high efficiency;

⇒ Sustained temperature raise above 41 ºC for at least 30 minutes induced cell death in Jurkat and LN229 cancer cells through apoptotic (T<43 ºC) or necrotic (T>43 ºC) pathways;

⇒ The triggering of a necrotic pathway was necessary to obtain 100 % loss of cell viability in Jurkat and LN229 cells, using one single application of the described magnetic hyperthermia treatment;

⇒ The MHT strategy described herein resulted in no relevant cytotoxicity in normal cells.

As a final conclusion, we believe the strategy entirely developed through the course of this thesis represents an innovative way of increasing the efficiency of targeted MHT treatments with a boost of magnetic material of a non-targeted origin. This second population was similarly selective for cancer (versus normal) cells due to the higher rate of nanoparticles' internalization by tumour cells, overall resulting in low toxicity in normal cells. The major advantage of our strategy is its elevated efficiency in a mono-therapeutic context, which prevents the need to further combine it with highly toxic chemotherapeutic drugs. Additionally, this work describes a set of new or improved methodologies for nanoparticles' functionalization and characterization, and cell-nanoparticle interaction studies, which can help many other future studies in the emerging nanomedicine field of research.

We are confident that further *in vivo* studies will prove the vast potentiality of this strategy as a therapeutic approach for cancer treatment.

CHAPTER IV

References

References

American Brain Tumor Association (2014). "Brain tumour surgery." Retrieved December 2016, from http://www.abta.org/brain-tumor-treatment/treatments/surgery.html?referrer=http://www.aans.org/patientinformation/conditions and treatments/glioblastomamultiforme.aspx.

American Brain Tumor Association. (2016). "Glioblastoma and malignant astrocytoma." Retrieved December 2016, from http://www.abta.org/secure/glioblastoma-brochure.pdf.

Albanese A, Tang PS and Chan WC. 2012. The effect of nanoparticle size, shape, and surface chemistry on biological systems. *Annu Rev Biomed Eng* **14**: 1-16.

Alvarez-Berrios MP, Castillo A, Rinaldi C and Torres-Lugo M. 2014. Magnetic fluid hyperthermia enhances cytotoxicity of bortezomib in sensitive and resistant cancer cell lines. *Int J Nanomedicine* **9**: 145-153.

Ananta JS, Paulmurugan R and Massoud TF. 2015. Nanoparticle-delivered antisense microRNA-21 enhances the effects of temozolomide on glioblastoma cells. *Mol Pharm* **12**(12): 4509-4517.

Andrade A, Ferreira R, Fabris J and Domingues R (2011). Coating nanomagnetic particles for biomedical applications. Biomedical engineering - frontiers and challenges. P. R. Fazel, InTech.

Anselmo AC and Mitragotri S. 2016. Nanoparticles in the clinic. *Bioengineering & Translational Medicine* **1**: 10-29.

Baldi G, Ravagli C, Mazzantini F, Loudos G, Adan J, Masa M, Psimadas D, Fragogeorgi EA, Locatelli E, Innocenti C, Sangregorio C and Comes Franchini M. 2014. In vivo anticancer evaluation of the hyperthermic efficacy of anti-human epidermal growth factor receptor-targeted PEG-based nanocarrier containing magnetic nanoparticles. *Int J Nanomedicine* **9**: 3037-3056.

Bassan R and Hoelzer D. 2011. Modern therapy of acute lymphoblastic leukemia. *J Clin Oncol* **29**(5): 532-543.

Bedanta S and Kleemann W. 2009. Supermagnetism. *Journal of Physics D-Applied Physics* **42**(1).

Bray F, Jemal A, Grey N, Ferlay J and Forman D. 2012. Global cancer transitions according to the human development index (2008-2030): A population-based study. *Lancet Oncol* **13**(8): 790-801.

Bychkova AV, Sorokina ON, Rosenfeld MA and Kovarski AL. 2012. Multifunctional biocompatible coatings on magnetic nanoparticles. *Russian Chemical Reviews* **81**(11): 1026-1050.

Calias P, Banks WA, Begley D, Scarpa M and Dickson P. 2014. Intrathecal delivery of protein therapeutics to the brain: A critical reassessment. *Pharmacol Ther* **144**(2): 114-122.

Chalkidou A, Simeonidis K, Angelakeris M, Samaras T, Martinez-Boubeta C, Balcells L, Papazisis K, Dendrinou-Samara C and Kalogirou O. 2011. In vitro application of Fe/MgO nanoparticles as magnetically mediated hyperthermia agents for cancer treatment. *Journal of Magnetism and Magnetic Materials* **323**(6): 775-780.

Chen C, Chen L, Yi Y, Chen C, Wu LF and Song T. 2016a. Killing of staphylococcus aureus via magnetic hyperthermia mediated by magnetotactic bacteria. *Appl Environ Microbiol* **82**(7): 2219-2226.

Chen YJ, Fang LW, Su WC, Hsu WY, Yang KC and Huang HL. 2016b. Lapatinib induces autophagic cell death and differentiation in acute myeloblastic leukemia. *Onco Targets Ther* **9**: 4453-4464.

Chudzik B, Miaskowski A, Surowiec Z, Czernel G, Duluk T, Marczuk A and Gagos M. 2016. Effectiveness of magnetic fluid hyperthermia against candida albicans cells. *Int J Hyperthermia* **32**(8): 842-857.

Combs SE, Schulz-Ertner D, Roth W, Herold-Mende C, Debus J and Weber KJ. 2007. In vitro responsiveness of glioma cell lines to multimodality treatment with radiotherapy, temozolomide, and epidermal growth factor receptor inhibition with cetuximab. *Int J Radiat Oncol Biol Phys* **68**(3): 873-882.

Couto D, Freitas M, Costa VM, Chiste RC, Almeida A, Lopez-Quintela MA, Rivas J, Freitas P, Silva P, Carvalho F and Fernandes E. 2016. Biodistribution of polyacrylic acid-coated iron oxide nanoparticles is associated with proinflammatory activation and liver toxicity. *J Appl Toxicol* **36**(10): 1321-1331.

Couto D, Freitas M, Vilas-Boas V, Dias I, Porto G, Lopez-Quintela MA, Rivas J, Freitas P, Carvalho F and Fernandes E. 2014. Interaction of polyacrylic acid coated and non-coated iron oxide nanoparticles with human neutrophils. *Toxicol Lett* **225**(1): 57-65.

Creixell M, Bohorquez AC, Torres-Lugo M and Rinaldi C. 2011. EGFR-targeted magnetic nanoparticle heaters kill cancer cells without a perceptible temperature rise. *ACS Nano* **5**(9): 7124-7129.

da Silva CP, de Oliveira CR, da Conceicao M and de Lima P. 1996. Apoptosis as a mechanism of cell death induced by different chemotherapeutic drugs in human leukemic T-lymphocytes. *Biochem Pharmacol* **51**(10): 1331-1340.

Das V, Bruzzese F, Konecny P, Iannelli F, Budillon A and Hajduch M. 2015. Pathophysiologically relevant in vitro tumor models for drug screening. *Drug Discov Today* **20**(7): 848-855.

de Bruin EC and Medema JP. 2008. Apoptosis and non-apoptotic deaths in cancer development and treatment response. *Cancer Treat Rev* **34**(8): 737-749.

de Lourdes Perim A, Amarante MK, Guembarovski RL, de Oliveira CE and Watanabe MA. 2015. CXCL12/CXCR4 axis in the pathogenesis of acute lymphoblastic leukemia (ALL): A possible therapeutic target. *Cell Mol Life Sci* **72**(9): 1715-1723.

Di Corato R, Bealle G, Kolosnjaj-Tabi J, Espinosa A, Clement O, Silva AK, Menager C and Wilhelm C. 2015. Combining magnetic hyperthermia and photodynamic therapy for tumor ablation with photoresponsive magnetic liposomes. *ACS Nano* **9**(3): 2904-2916.

Ding D, Wang J, Zhu Z, Li R, Wu W, Liu B and Jiang X. 2012. Tumor accumulation, penetration, and antitumor response of cisplatin-loaded gelatin/poly(acrylic acid) nanoparticles. *ACS Appl Mater Interfaces* **4**(3): 1838-1846.

Domanska UM, Kruizinga RC, Nagengast WB, Timmer-Bosscha H, Huls G, de Vries EGE and Walenkamp AME. 2013. A review on CXCR4/CXCL12 axis in oncology: No place to hide. *European journal of cancer (Oxford, England : 1990)* **49**(1): 219-230.

Domenech M, Marrero-Berrios I, Torres-Lugo M and Rinaldi C. 2013. Lysosomal membrane permeabilization by targeted magnetic nanoparticles in alternating magnetic fields. *ACS Nano* **7**(6): 5091-5101.

dos Santos T, Varela J, Lynch I, Salvati A and Dawson KA. 2011. Quantitative assessment of the comparative nanoparticle-uptake efficiency of a range of cell lines. *Small* **7**(23): 3341-3349.

Drake P, Cho HJ, Shih PS, Kao CH, Lee KF, Kuo CH, Lin XZ and Lin YJ. 2007. Gd-doped iron-oxide nanoparticles for tumour therapy via magnetic field hyperthermia. *Journal of Materials Chemistry* **17**(46): 4914-4918.

Drexler HG, Matsuo Y and MacLeod RAF. 2000. Continuous hematopoietic cell lines as model systems for leukemia-lymphoma research. *Leukemia Research* **24**(11): 881-911.

Du Trémolet de Lacheisserie E (2005). Magnetism, from the dawn of civilization to today. Magnetism. E. Du Trémolet de Lacheisserie, D. Gignoux and M. Schlenker, Springer Science & Business Media. **1:** 3-4.

Dutz S and Hergt R. 2013. Magnetic nanoparticle heating and heat transfer on a microscale: Basic principles, realities and physical limitations of hyperthermia for tumour therapy. *Int J Hyperthermia* **29**(8): 790-800.

Dutz S and Hergt R. 2014. Magnetic particle hyperthermia - a promising tumour therapy? *Nanotechnology* **25**(45): 452001.

Elhag R, Mazzio EA and Soliman KF. 2015. The effect of silibinin in enhancing toxicity of temozolomide and etoposide in p53 and PTEN-mutated resistant glioma cell lines. *Anticancer Res* **35**(3): 1263-1269.

Endres MJ, Clapham PR, Marsh M, Ahuja M, Turner JD, McKnight A, Thomas JF, Stoebenau-Haggarty B, Choe S, Vance PJ, Wells TN, Power CA, Sutterwala SS, Doms RW, Landau NR and Hoxie JA. 1996. CD4-independent infection by HIV-2 is mediated by fusin/CXCR4. *Cell* **87**(4): 745-756.

Espinosa A, Di Corato R, Kolosnjaj-Tabi J, Flaud P, Pellegrino T and Wilhelm C. 2016. Duality of iron oxide nanoparticles in cancer therapy: Amplification of heating efficiency by magnetic hyperthermia and photothermal bimodal treatment. *ACS Nano* **10**(2): 2436-2446.

Fears KP, Petrovykh DY and Clark TD. 2013. Evaluating protocols and analytical methods for peptide adsorption experiments. *Biointerphases* **8**(1): 20.

Feng Y, Broder CC, Kennedy PE and Berger EA. 1996. HIV-1 entry cofactor: Functional cDNA cloning of a seven-transmembrane, G protein-coupled receptor. *Science* **272**(5263): 872-877.

Ferlay J, Soerjomataram I, Dikshit R, Eser S, Mathers C, Rebelo M, Parkin DM, Forman D and Bray F. 2015. Cancer incidence and mortality worldwide: Sources, methods and major patterns in Globocan 2012. *Int J Cancer* **136**(5): E359-386.

Ferlay J, Steliarova-Foucher E, Lortet-Tieulent J, Rosso S, Coebergh JW, Comber H, Forman D and Bray F. 2013. Cancer incidence and mortality patterns in europe: Estimates for 40 countries in 2012. *Eur J Cancer* **49**(6): 1374-1403.

Friedrich RP, Janko C, Poettler M, Tripal P, Zaloga J, Cicha I, Durr S, Nowak J, Odenbach S, Slabu I, Liebl M, Trahms L, Stapf M, Hilger I, Lyer S and Alexiou C. 2015. Flow cytometry for intracellular SPION quantification: Specificity and sensitivity in comparison with spectroscopic methods. *Int J Nanomedicine* **10**: 4185-4201.

Gao FP, Cai YY, Zhou J, Xie XX, Ouyang WW, Zhang YH, Wang XF, Zhang XD, Wang XW, Zhao LY and Tang JT. 2010. Pullulan acetate coated magnetite nanoparticles for hyper-thermia: Preparation, characterization and in vitro experiments. *Nano Research* **3**(1): 23-31.

Geppert M, Hohnholt MC, Thiel K, Nurnberger S, Grunwald I, Rezwan K and Dringen R. 2011. Uptake of dimercaptosuccinate-coated magnetic iron oxide nanoparticles by cultured brain astrocytes. *Nanotechnology* **22**(14): 145101.

Gilchrist RK, Medal R, Shorey WD, Hanselman RC, Parrott JC and Taylor CB. 1957. Selective inductive heating of lymph nodes. *Annals of Surgery* **146**(4): 596-606.

Gordon RT, Hines JR and Gordon D. 1979. Intracellular hyperthermia. A biophysical approach to cancer treatment via intracellular temperature and biophysical alterations. *Med Hypotheses* **5**(1): 83-102.

Grazu V, Silber AM, Moros M, Asin L, Torres TE, Marquina C, Ibarra MR and Goya GF. 2012. Application of magnetically induced hyperthermia in the model protozoan crithidia fasciculata as a potential therapy against parasitic infections. *Int J Nanomedicine* **7**: 5351-5360.

Grotzer MA, Neve A and Baumgartner M. 2016. Dissecting brain tumor growth and metastasis in vitro and ex vivo. *J Cancer Metastasis Treat* **2**: 149-162.

Guardia P, Di Corato R, Lartigue L, Wilhelm C, Espinosa A, Garcia-Hernandez M, Gazeau F, Manna L and Pellegrino T. 2012. Water-soluble iron oxide nanocubes with high values of specific absorption rate for cancer cell hyperthermia treatment. *ACS Nano* **6**(4): 3080-3091.

Gupta J, Mohapatra J, Bhargava P and Bahadur D. 2016. A pH-responsive folate conjugated magnetic nanoparticle for targeted chemo-thermal therapy and MRI diagnosis. *Dalton Trans* **45**(6): 2454-2461.

He Y, Song W, Lei J, Li Z, Cao J, Huang S, Meng J, Xu H, Jin Z and Xue H. 2012. Anti-CXCR4 monoclonal antibody conjugated to ultrasmall superparamagnetic iron oxide nanoparticles in an application of MR molecular imaging of pancreatic cancer cell lines. *Acta Radiol* **53**(9): 1049-1058.

Hedayati M, Thomas O, Abubaker-Sharif B, Zhou HM, Cornejo C, Zhang YG, Wabler M, Mihalic J, Gruettner C, Westphal F, Geyh A, Deweese TL and Ivkov R. 2013. The effect of cell cluster size on intracellular nanoparticle-mediated hyperthermia: Is it possible to treat microscopic tumors? *Nanomedicine (Lond)* **8**(1): 29-41.

Hegi ME, Diserens AC, Gorlia T, Hamou MF, de Tribolet N, Weller M, Kros JM, Hainfellner JA, Mason W, Mariani L, Bromberg JE, Hau P, Mirimanoff RO, Cairncross JG, Janzer RC and Stupp R. 2005. MGMT gene silencing and benefit from temozolomide in glioblastoma. *N Engl J Med* **352**(10): 997-1003.

Hervault A, Dunn AE, Lim M, Boyer C, Mott D, Maenosono S and Thanh NT. 2016. Doxorubicin loaded dual pH- and thermo-responsive magnetic nanocarrier for combined magnetic hyperthermia and targeted controlled drug delivery applications. *Nanoscale* **8**(24): 12152-12161.

Hervault A and Thanh NTK. 2014. Magnetic nanoparticle-based therapeutic agents for thermo-chemotherapy treatment of cancer. *Nanoscale* **6**(20): 11553-11573.

Hildebrandt B, Wust P, Ahlers O, Dieing A, Sreenivasa G, Kerner T, Felix R and Riess H. 2002. The cellular and molecular basis of hyperthermia. *Critical Reviews in Oncology Hematology* **43**(1): 33-56.

Huang HS and Hainfeld JF. 2013. Intravenous magnetic nanoparticle cancer hyperthermia. *Int J Nanomedicine* **8**: 2521-2532.

Huang K, Kiefer C and Kamal A. 2014. Novel role for NFAT3 in ERK-mediated regulation of CXCR4. *PLoS One* **9**(12): e115249.

Hung CW, Holoman TRP, Kofinas P and Bentley WE. 2008. Towards oriented assembly of proteins onto magnetic nanoparticles. *Biochemical Engineering Journal* **38**(2): 164-170.

Inaba H, Greaves M and Mullighan CG. 2013. Acute lymphoblastic leukaemia. *Lancet (London, England)* **381**(9881): 1943-1955.

Indran IR, Tufo G, Pervaiz S and Brenner C. 2011. Recent advances in apoptosis, mitochondria and drug resistance in cancer cells. *Biochim Biophys Acta* **1807**(6): 735-745.

Ito A, Kuga Y, Honda H, Kikkawa H, Horiuchi A, Watanabe Y and Kobayashi T. 2004. Magnetite nanoparticle-loaded anti-HER2 immunoliposomes for combination of antibody therapy with hyperthermia. *Cancer Lett* **212**(2): 167-175.

Iversen NK, Frische S, Thomsen K, Laustsen C, Pedersen M, Hansen PB, Bie P, Fresnais J, Berret JF, Baatrup E and Wang T. 2013. Superparamagnetic iron oxide polyacrylic acid coated gamma-Fe_2O_3 nanoparticles do not affect kidney function but cause acute effect on the cardiovascular function in healthy mice. *Toxicol Appl Pharmacol* **266**(2): 276-288.

Iyer AK, Khaled G, Fang J and Maeda H. 2006. Exploiting the enhanced permeability and retention effect for tumor targeting. *Drug Discov Today* **11**(17-18): 812-818.

Jagirdar N, Harvey RD, Nooka A, Flowers C, Kaufman J, Lonial S, Lechowicz MJ, Langston A, Lipscomb C, Gaylor C and Waller EK. 2015. Plerixafor in combination with granulocyte-colony-stimulating factor after chemotherapy increases mobilization efficiency in patients with lymphoma or myeloma: Results of a phase ii clinical trial. *Transfusion* **55**(10): 2351-2357.

Jenita JL, Chocalingam V and Wilson B. 2014. Albumin nanoparticles coated with polysorbate 80 as a novel drug carrier for the delivery of antiretroviral drug-efavirenz. *Int J Pharm Investig* **4**(3): 142-148.

Johannsen M, Gneveckow U, Eckelt L, Feussner A, Waldofner N, Scholz R, Deger S, Wust P, Loening SA and Jordan A. 2005. Clinical hyperthermia of prostate cancer using magnetic nanoparticles: Presentation of a new interstitial technique. *Int J Hyperthermia* **21**(7): 637-647.

Johannsen M, Gneveckow U, Taymoorian K, Thiesen B, Waldofner N, Scholz R, Jung K, Jordan A, Wust P and Loening SA. 2007. Morbidity and quality of life during thermotherapy using magnetic nanoparticles in locally recurrent prostate cancer: Results of a prospective phase I trial. *Int J Hyperthermia* **23**(3): 315-323.

Jordan A, Scholz R, Maier-Hauff K, van Landeghem FK, Waldoefner N, Teichgraeber U, Pinkernelle J, Bruhn H, Neumann F, Thiesen B, von Deimling A and Felix R. 2006. The effect of thermotherapy using magnetic nanoparticles on rat malignant glioma. *J Neurooncol* **78**(1): 7-14.

Kawai N, Ito A, Nakahara Y, Futakuchi M, Shirai T, Honda H, Kobayashi T and Kohri K. 2005. Anticancer effect of hyperthermia on prostate cancer mediated by magnetite cationic liposomes and immune-response induction in transplanted syngeneic rats. *Prostate* **64**(4): 373-381.

Kelly SM, Jess TJ and Price NC. 2005. How to study proteins by circular dichroism. *Biochimica Et Biophysica Acta-Proteins and Proteomics* **1751**(2): 119-139.

Khandhar AP, Ferguson RM and Krishnan KM. 2011. Monodispersed magnetite nanoparticles optimized for magnetic fluid hyperthermia: Implications in biological systems. *Journal of Applied Physics* **109**(7).

Khandhar AP, Ferguson RM, Simon JA and Krishnan KM. 2012. Tailored magnetic nanoparticles for optimizing magnetic fluid hyperthermia. *Journal of Biomedical Materials Research Part A* **100A**(3): 728-737.

Kirpotin DB, Drummond DC, Shao Y, Shalaby MR, Hong K, Nielsen UB, Marks JD, Benz CC and Park JW. 2006. Antibody targeting of long-circulating lipidic nanoparticles does not increase tumor localization but does increase internalization in animal models. *Cancer Res* **66**(13): 6732-6740.

Kobayashi T and Kida Y. 1990. Interstitial hyperthermia of brain tumors by stereotactically implanted heating system. *Stereotact Funct Neurosurg* **54-55**: 514-518.

Kolen'ko YV, Bañobre-López M, Rodríguez-Abreu C, Carbó-Argibay E, Sailsman A, Piñeiro-Redondo Y, Cerqueira MF, Petrovykh DY, Kovnir K, Lebedev OI and Rivas J. 2014. Large-scale synthesis of colloidal Fe_3O_4 nanoparticles exhibiting high heating efficiency in magnetic hyperthermia. *The Journal of Physical Chemistry C* **118**(16): 8691-8701.

Kruse AM, Meenach SA, Anderson KW and Hilt JZ. 2014. Synthesis and characterization of CREKA-conjugated iron oxide nanoparticles for hyperthermia applications. *Acta Biomater* **10**(6): 2622-2629.

Lee H, Fonge H, Hoang B, Reilly RM and Allen C. 2010. The effects of particle size and molecular targeting on the intratumoral and subcellular distribution of polymeric nanoparticles. *Mol Pharm* **7**(4): 1195-1208.

Lee N, Yoo D, Ling D, Cho MH, Hyeon T and Cheon J. 2015. Iron oxide based nanoparticles for multimodal imaging and magnetoresponsive therapy. *Chemical Reviews* **115**(19): 10637-10689.

Lesniak A, Salvati A, Santos-Martinez MJ, Radomski MW, Dawson KA and Aberg C. 2013. Nanoparticle adhesion to the cell membrane and its effect on nanoparticle uptake efficiency. *J Am Chem Soc* **135**(4): 1438-1444.

Levi-Polyachenko NH and Stewart JH. 2011. Clinical relevance of nanoparticle induced hyperthermia for drug delivery and treatment of abdominal cancers. *Open Nanomed. J.* **3**(1): 24-37.

Liao SH, Liu CH, Bastakoti BP, Suzuki N, Chang Y, Yamauchi Y, Lin FH and Wu KC. 2015. Functionalized magnetic iron oxide/alginate core-shell nanoparticles for targeting hyperthermia. *Int J Nanomedicine* **10**: 3315-3328.

Lin CL, Lee CF and Chiu WY. 2005. Preparation and properties of poly(acrylic acid) oligomer stabilized superparamagnetic ferrofluid. *J Colloid Interface Sci* **291**(2): 411-420.

Loynachan CN, Romero G, Christiansen MG, Chen R, Ellison R, O'Malley TT, Froriep UP, Walsh DM and Anikeeva P. 2015. Targeted magnetic nanoparticles for remote magnetothermal disruption of amyloid-beta aggregates. *Adv Healthc Mater*.

Lu AH, Salabas EL and Schuth F. 2007. Magnetic nanoparticles: Synthesis, protection, functionalization, and application. *Angewandte Chemie-International Edition* **46**(8): 1222-1244.

Ma M, Zhang Y, Shen XL, Xie J, Li Y and Gu N. 2015. Targeted inductive heating of nanomagnets by a combination of alternating current (AC) and static magnetic fields. *Nano Research* **8**(2): 600-610.

MacLeod RA and Drexler HG. 2008. Leukaemia cell lines are robust in vitro models. *Br J Haematol* **142**(1): 137-138; author reply 138-141.

MagForce. (2016). "Nanotherm® therapy information for the treatment of brain tumors." Retrieved December 2016, from http://www.magforce.de/en/patienten/beschreibung-der-therapie.html.

MagForce. (2016). "A new study to validate nanotherm™ therapy and build confidence within the specialist medical community." Retrieved December 2016, from http://www.magforce.de/en/studien/neue-glioblastom-studie.html.

Maier-Hauff K, Rothe R, Scholz R, Gneveckow U, Wust P, Thiesen B, Feussner A, von Deimling A, Waldoefner N, Felix R and Jordan A. 2007. Intracranial thermotherapy using magnetic nanoparticles combined with external beam radiotherapy: Results of a feasibility study on patients with glioblastoma multiforme. *J Neurooncol* **81**(1): 53-60.

Maier-Hauff K, Ulrich F, Nestler D, Niehoff H, Wust P, Thiesen B, Orawa H, Budach V and Jordan A. 2011. Efficacy and safety of intratumoral thermotherapy using magnetic iron-

oxide nanoparticles combined with external beam radiotherapy on patients with recurrent glioblastoma multiforme. *J Neurooncol* **103**(2): 317-324.

Maity D, Chandrasekharan P, Pradhan P, Chuang KH, Xue JM, Feng SS and Ding J. 2011. Novel synthesis of superparamagnetic magnetite nanoclusters for biomedical applications. *Journal of Materials Chemistry* **21**(38): 14717-14724.

Martin SJ, Reutelingsperger CP, McGahon AJ, Rader JA, van Schie RC, LaFace DM and Green DR. 1995. Early redistribution of plasma membrane phosphatidylserine is a general feature of apoptosis regardless of the initiating stimulus: Inhibition by overexpression of Bcl-2 and Abl. *J Exp Med* **182**(5): 1545-1556.

Martinelli E, De Palma R, Orditura M, De Vita F and Ciardiello F. 2009. Anti-epidermal growth factor receptor monoclonal antibodies in cancer therapy. *Clin Exp Immunol* **158**(1): 1-9.

Martins SSA, Martins VC, Cardoso FA, Freitas PP and Fonseca LP (2012). Waterborne pathogen detection using a magnetoresistive immuno-chip. Molecular biological technologies for ocean sensing. S. M. Tiqia-Arashiro, Humana Press**:** 263-288.

Mehta RV, Upadhyay RV, Charles SW and Ramchand CN. 1997. Direct binding of protein to magnetic particles. *Biotechnol Tech* **11**(7): 493–496.

Mi Y, Liu X, Zhao J, Ding J and Feng SS. 2012. Multimodality treatment of cancer with herceptin conjugated, thermomagnetic iron oxides and docetaxel loaded nanoparticles of biodegradable polymers. *Biomaterials* **33**(30): 7519-7529.

Mishra R, Das MK, Singh S, Sharma RS, Sharma S and Mishra V. 2016. Articulatin-D induces apoptosis via activation of caspase-8 in acute T-cell leukemia cell line. *Mol Cell Biochem*.

Mitri Z, Constantine T and O'Regan R. 2012. The HER2 receptor in breast cancer: Pathophysiology, clinical use, and new advances in therapy. *Chemother Res Pract* **2012**: 743193.

Mohle R, Bautz F, Rafii S, Moore MA, Brugger W and Kanz L. 1998. The chemokine receptor Cxcr-4 is expressed on CD34+ hematopoietic progenitors and leukemic cells and mediates transendothelial migration induced by stromal cell-derived factor-1. *Blood* **91**(12): 4523-4530.

Moyer HR and Delman KA. 2008. The role of hyperthermia in optimizing tumor response to regional therapy. *International Journal of Hyperthermia* **24**(3): 251-261.

Mu X, Tong Z, Huang Q, Liu B, Liu Z, Hao L, Zhang J, Gao C and Wang F. 2015. Nano-magnetic immunosensor based on staphylococcus protein A and the amplification effect of Hrp-conjugated phage antibody. *Sensors (Basel)* **15**(2): 3896-3910.

Muller A, Homey B, Soto H, Ge N, Catron D, Buchanan ME, McClanahan T, Murphy E, Yuan W, Wagner SN, Barrera JL, Mohar A, Verastegui E and Zlotnik A. 2001. Involvement of chemokine receptors in breast cancer metastasis. *Nature* **410**(6824): 50-56.

Nabhan JF, Wood KM, Rao VP, Morin J, Bhamidipaty S, LaBranche TP, Gooch RL, Bozal F, Bulawa CE and Guild BC. 2016. Intrathecal delivery of frataxin mRNA encapsulated in lipid nanoparticles to dorsal root ganglia as a potential therapeutic for Friedreich's ataxia. *Scientific Reports* **6**.

NDong C, Tate JA, Kett WC, Batra J, Demidenko E, Lewis LD, Hoopes PJ, Gerngross TU and Griswold KE. 2015. Tumor cell targeting by iron oxide nanoparticles is dominated by different factors in vitro versus in vivo. *PLoS One* **10**(2): e0115636.

U.S. National Institutes of Health. (2014). "Clinical trials.Gov." Retrieved December 2016, from

https://clinicaltrials.gov/ct2/show/record/NCT02033447?term=magnetic+hyperthermia&rank=6.

U.S. National Institutes of Health. (April 2015). "Clinicaltrials.Gov." Retrieved December 2016, from https://clinicaltrials.gov/ct2/results?term=magnetic+nanoparticle.

Oh Y, Lee N, Kang HW and Oh J. 2016. In vitro study on apoptotic cell death by effective magnetic hyperthermia with chitosan-coated $MnFe_2O_4$. *Nanotechnology* **27**(11): 115101.

Ohno T, Wakabayashi T, Takemura A, Yoshida J, Ito A, Shinkai M, Honda H and Kobayashi T. 2002. Effective solitary hyperthermia treatment of malignant glioma using stick type CMC-magnetite. In vivo study. *J Neurooncol* **56**(3): 233-239.

Pamme N. 2006. Magnetism and microfluidics. *Lab Chip* **6**(1): 24-38.

Pirollo KF and Chang EH. 2008. Does a targeting ligand influence nanoparticle tumor localization or uptake? *Trends Biotechnol* **26**(10): 552-558.

Poirier M, Simard JC, Antoine F and Girard D. 2014. Interaction between silver nanoparticles of 20 nm (AgNP20) and human neutrophils: Induction of apoptosis and inhibition of de novo protein synthesis by AgNP20 aggregates. *J Appl Toxicol* **34**(4): 404-412.

Prijic S, Prosen L, Cemazar M, Scancar J, Romih R, Lavrencak J, Bregar VB, Coer A, Krzan M, Znidarsic A and Sersa G. 2012. Surface modified magnetic nanoparticles for immuno-gene therapy of murine mammary adenocarcinoma. *Biomaterials* **33**(17): 4379-4391.

Proskuryakov SY, Konoplyannikov AG and Gabai VL. 2003. Necrosis: A specific form of programmed cell death? *Exp Cell Res* **283**(1): 1-16.

Qu Y, Li J, Ren J, Leng J, Lin C and Shi D. 2014. Enhanced magnetic fluid hyperthermia by micellar magnetic nanoclusters composed of $Mn_{(x)}Zn_{(1-x)}Fe_2O_4$ nanoparticles for induced tumor cell apoptosis. *ACS Appl Mater Interfaces* **6**(19): 16867-16879.

Quinto CA, Mohindra P, Tong S and Bao G. 2015. Multifunctional superparamagnetic iron oxide nanoparticles for combined chemotherapy and hyperthermia cancer treatment. *Nanoscale*.

Rabin Y. 2002. Is intracellular hyperthermia superior to extracellular hyperthermia in the thermal sense? *International Journal of Hyperthermia* **18**(3): 194-202.

Rago G, Bauer B, Svedberg F, Gunnarsson L, Ericson MB, Bonn M and Enejder A. 2011. Uptake of gold nanoparticles in healthy and tumor cells visualized by nonlinear optical microscopy. *J Phys Chem B* **115**(17): 5008-5016.

Rejman J, Oberle V, Zuhorn IS and Hoekstra D. 2004. Size-dependent internalization of particles via the pathways of clathrin- and caveolae-mediated endocytosis. *Biochem J* **377**(Pt 1): 159-169.

Ren Y, Zhang H, Chen B, Cheng J, Cai X, Liu R, Xia G, Wu W, Wang S, Ding J, Gao C, Wang J, Bao W, Wang L, Tian L, Song H and Wang X. 2012. Multifunctional magnetic Fe_3O_4 nanoparticles combined with chemotherapy and hyperthermia to overcome multidrug resistance. *Int J Nanomedicine* **7**: 2261-2269.

Rios A, Hsu SH, Blanco A, Buryanek J, Day AL, McGuire MF and Brown RE. 2016. Durable response of glioblastoma to adjuvant therapy consisting of temozolomide and a weekly dose of AMD3100 (plerixafor), a CXCR4 inhibitor, together with lapatinib, metformin and niacinamide. *Oncoscience* **3**(5-6): 156-163.

Rudershausen S, Grüttner C, Frank M, Teller J and Westphal F. 2002. Multifunctional superparamagnetic nanoparticles for life science applications *Eur Cell Mater* **3**: 81-83.

Sadhasivam S, Savitha S, Wu CJ, Lin FH and Stobinski L. 2015. Carbon encapsulated iron oxide nanoparticles surface engineered with polyethylene glycol-folic acid to induce selective hyperthermia in folate over expressed cancer cells. *Int J Pharm* **480**(1-2): 8-14.

Sadhukha T, Niu L, Wiedmann TS and Panyam J. 2013a. Effective elimination of cancer stem cells by magnetic hyperthermia. *Molecular Pharmaceutics* **10**(4): 1432-1441.

Sadhukha T, Wiedmann TS and Panyam J. 2013b. Inhalable magnetic nanoparticles for targeted hyperthermia in lung cancer therapy. *Biomaterials* **34**(21): 5163-5171.

Saptarshi SR, Duschl A and Lopata AL. 2013. Interaction of nanoparticles with proteins: Relation to bio-reactivity of the nanoparticle. *J Nanobiotechnology* **11**: 26.

Schneider U, Schwenk HU and Bornkamm G. 1977. Characterization of EBV-genome negative "null" and "T" cell lines derived from children with acute lymphoblastic leukemia and leukemic transformed non-hodgkin lymphoma. *Int J Cancer* **19**(5): 621-626.

Sehgal A, Keener C, Boynton AL, Warrick J and Murphy GP. 1998. CXCR-4, a chemokine receptor, is overexpressed in and required for proliferation of glioblastoma tumor cells. *J Surg Oncol* **69**(2): 99-104.

Shah BP, Pasquale N, De G, Tan T, Ma J and Lee KB. 2014. Core-shell nanoparticle-based peptide therapeutics and combined hyperthermia for enhanced cancer cell apoptosis. *ACS Nano* **8**(9): 9379-9387.

Sharma A, Madhunapantula SV and Robertson GP. 2012. Toxicological considerations when creating nanoparticle-based drugs and drug delivery systems. *Expert Opin Drug Metab Toxicol* **8**(1): 47-69.

Shi B, Abrams M and Sepp-Lorenzino L. 2013. Expression of asialoglycoprotein receptor 1 in human hepatocellular carcinoma. *J Histochem Cytochem* **61**(12): 901-909.

Shinojima N, Tada K, Shiraishi S, Kamiryo T, Kochi M, Nakamura H, Makino K, Saya H, Hirano H, Kuratsu J, Oka K, Ishimaru Y and Ushio Y. 2003. Prognostic value of epidermal growth factor receptor in patients with glioblastoma multiforme. *Cancer Res* **63**(20): 6962-6970.

Siegel RL, Miller KD and Jemal A. 2015. Cancer statistics, 2015. *CA Cancer J Clin* **65**(1): 5-29.

Signoret N, Oldridge J, Pelchen-Matthews A, Klasse PJ, Tran T, Brass LF, Rosenkilde MM, Schwartz TW, Holmes W, Dallas W, Luther MA, Wells TN, Hoxie JA and Marsh M. 1997. Phorbol esters and SDF-1 induce rapid endocytosis and down modulation of the chemokine receptor CXCR4. *J Cell Biol* **139**(3): 651-664.

Sims LB, Curtis LT, Frieboes HB and Steinbach-Rankins JM. 2016. Enhanced uptake and transport of PLGA-modified nanoparticles in cervical cancer. *J Nanobiotechnology* **14**: 33.

Sivakumar B, Aswathy RG, Nagaoka Y, Suzuki M, Fukuda T, Yoshida Y, Maekawa T and Sakthikumar DN. 2013. Multifunctional carboxymethyl cellulose-based magnetic nanovector as a theragnostic system for folate receptor targeted chemotherapy, imaging, and hyperthermia against cancer. *Langmuir* **29**(10): 3453-3466.

Song CW. 1984. Effect of local hyperthermia on blood-flow and microenvironment - a review. *Cancer Research* **44**(10): 4721-4730.

Sperling RA and Parak WJ. 2010. Surface modification, functionalization and bioconjugation of colloidal inorganic nanoparticles. *Philosophical Transactions of the Royal Society a-Mathematical Physical and Engineering Sciences* **368**(1915): 1333-1383.

Stupp R, Hegi ME, Mason WP, van den Bent MJ, Taphoorn MJ, Janzer RC, Ludwin SK, Allgeier A, Fisher B, Belanger K, Hau P, Brandes AA, Gijtenbeek J, Marosi C, Vecht CJ, Mokhtari K, Wesseling P, Villa S, Eisenhauer E, Gorlia T, Weller M, Lacombe D,

Cairncross JG, Mirimanoff RO, European Organisation for R, Treatment of Cancer Brain T, Radiation Oncology G and National Cancer Institute of Canada Clinical Trials G. 2009. Effects of radiotherapy with concomitant and adjuvant temozolomide versus radiotherapy alone on survival in glioblastoma in a randomised phase III study: 5-year analysis of the EORTC-NCIC trial. *Lancet Oncol* **10**(5): 459-466.

Stupp R, Mason WP, van den Bent MJ, Weller M, Fisher B, Taphoorn MJ, Belanger K, Brandes AA, Marosi C, Bogdahn U, Curschmann J, Janzer RC, Ludwin SK, Gorlia T, Allgeier A, Lacombe D, Cairncross JG, Eisenhauer E, Mirimanoff RO, European Organisation for R, Treatment of Cancer Brain T, Radiotherapy G and National Cancer Institute of Canada Clinical Trials G. 2005. Radiotherapy plus concomitant and adjuvant temozolomide for glioblastoma. *N Engl J Med* **352**(10): 987-996.

Stylianopoulos T. 2013. EPR-effect: Utilizing size-dependent nanoparticle delivery to solid tumors. *Ther Deliv* **4**(4): 421-423.

Taichman RS, Cooper C, Keller ET, Pienta KJ, Taichman NS and McCauley LK. 2002. Use of the stromal cell-derived factor-1/CXCR4 pathway in prostate cancer metastasis to bone. *Cancer research* **62**(6): 1832-1837.

Taratula O, Dani RK, Schumann C, Xu H, Wang A, Song H, Dhagat P and Taratula O. 2013. Multifunctional nanomedicine platform for concurrent delivery of chemotherapeutic drugs and mild hyperthermia to ovarian cancer cells. *Int J Pharm* **458**(1): 169-180.

Terasaki M, Sugita Y, Arakawa F, Okada Y, Ohshima K and Shigemori M. 2011. CXCL12/CXCR4 signaling in malignant brain tumors: A potential pharmacological therapeutic target. *Brain Tumor Pathol* **28**(2): 89-97.

Thomas RG, Moon MJ, Lee H, Sasikala AR, Kim CS, Park IK and Jeong YY. 2015. Hyaluronic acid conjugated superparamagnetic iron oxide nanoparticle for cancer diagnosis and hyperthermia therapy. *Carbohydr Polym* **131**: 439-446.

Thorat ND, Otari SV, Patil RM, Bohara RA, Yadav HM, Koli VB, Chaurasia AK and Ningthoujam RS. 2014. Synthesis, characterization and biocompatibility of chitosan functionalized superparamagnetic nanoparticles for heat activated curing of cancer cells. *Dalton Transactions* **43**(46): 17343-17351.

Toraya-Brown S, Sheen MR, Zhang P, Chen L, Baird JR, Demidenko E, Turk MJ, Hoopes PJ, Conejo-Garcia JR and Fiering S. 2014. Local hyperthermia treatment of tumors induces CD8(+) T cell-mediated resistance against distal and secondary tumors. *Nanomedicine* **10**(6): 1273-1285.

Tseng CL, Chang KC, Yeh MC, Yang KC, Tang TP and Lin FH. 2014. Development of a dual-functional Pt-Fe-HAP magnetic nanoparticles application for chemo-hyperthermia treatment of cancer. *Ceramics International* **40**(4): 5117-5127.

Valdiglesias V, Fernandez-Bertolez N, Kilic G, Costa C, Costa S, Fraga S, Bessa MJ, Pasaro E, Teixeira JP and Laffon B. 2016. Are iron oxide nanoparticles safe? Current knowledge and future perspectives. *J Trace Elem Med Biol* **38**: 53-63.

Vallejo-Fernandez G, Whear O, Roca AG, Hussain S, Timmis J, Patel V and O'Grady K. 2013. Mechanisms of hyperthermia in magnetic nanoparticles. *Journal of Physics D-Applied Physics* **46**(31).

Vilas-Boas V, Guldris N, Carbo-Argibay E, Stroppa DG, Cerqueira MF, Espina B, Rivas J, Rodriguez-Abreu C and Kolen'ko YV. 2015. Straightforward phase-transfer route to colloidal iron oxide nanoparticles for protein immobilization. *RSC Advances* **5**(59): 47954-47958.

Villanueva A, Canete M, Roca AG, Calero M, Veintemillas-Verdaguer S, Serna CJ, Morales Mdel P and Miranda R. 2009. The influence of surface functionalization on the

enhanced internalization of magnetic nanoparticles in cancer cells. *Nanotechnology* **20**(11): 115103.

Wabler M, Zhu WL, Hedayati M, Attaluri A, Zhou HM, Mihalic J, Geyh A, DeWeese TL, Ivkov R and Artemov D. 2014. Magnetic resonance imaging contrast of iron oxide nanoparticles developed for hyperthermia is dominated by iron content. *International Journal of Hyperthermia* **30**(3): 192-200.

Wang TH and Lee WC. 2003. Immobilization of proteins on magnetic nanoparticles. *Biotechnology and Bioprocess Engineering* **8**(4): 263-267.

Wang YX. 2015. Current status of superparamagnetic iron oxide contrast agents for liver magnetic resonance imaging. *World J Gastroenterol* **21**(47): 13400-13402.

Weller M, Rieger J, Grimmel C, Van Meir EG, De Tribolet N, Krajewski S, Reed JC, von Deimling A and Dichgans J. 1998. Predicting chemoresistance in human malignant glioma cells: The role of molecular genetic analyses. *Int J Cancer* **79**(6): 640-644.

Weller M, van den Bent M, Hopkins K, Tonn JC, Stupp R, Falini A, Cohen-Jonathan-Moyal E, Frappaz D, Henriksson R, Balana C, Chinot O, Ram Z, Reifenberger G, Soffietti R, Wick W and European Association for Neuro-Oncology Task Force on Malignant G. 2014. EANO guideline for the diagnosis and treatment of anaplastic gliomas and glioblastoma. *Lancet Oncol* **15**(9): e395-403.

Wu W, He QG and Jiang CZ. 2008. Magnetic iron oxide nanoparticles: Synthesis and surface functionalization strategies. *Nanoscale Research Letters* **3**(11): 397-415.

Wu W, Wu ZH, Yu T, Jiang CZ and Kim WS. 2015. Recent progress on magnetic iron oxide nanoparticles: Synthesis, surface functional strategies and biomedical applications. *Science and Technology of Advanced Materials* **16**(2).

Wust P, Gneveckow U, Johannsen M, Bohmer D, Henkel T, Kahmann F, Sehouli J, Felix R, Ricke J and Jordan A. 2006. Magnetic nanoparticles for interstitial thermotherapy - feasibility, tolerance and achieved temperatures. *Int J Hyperthermia* **22**(8): 673-685.

Wust P, Hildebrandt B, Sreenivasa G, Rau B, Gellermann J, Riess H, Felix R and Schlag PM. 2002. Hyperthermia in combined treatment of cancer. *Lancet Oncology* **3**(8): 487-497.

Xie J, Yan C, Yan Y, Chen L, Song L, Zang F, An Y, Teng G, Gu N and Zhang Y. 2016. Multi-modal Mn-Zn ferrite nanocrystals for magnetically-induced cancer targeted hyperthermia: A comparison of passive and active targeting effects. *Nanoscale*.

Yanase M, Shinkai M, Honda H, Wakabayashi T, Yoshida J and Kobayashi T. 1998. Antitumor immunity induction by intracellular hyperthermia using magnetite cationic liposomes. *Jpn J Cancer Res* **89**(7): 775-782.

Yang H-W, Hua M-Y, Liu H-L, Huang C-Y and Wei K-C. 2012. Potential of magnetic nanoparticles for targeted drug delivery. *Nanotechnology, science and applications* **5**: 73-86.

Yang R, An LY, Miao QF, Li FM, Han Y, Wang HX, Liu DP, Chen R and Tang SQ. 2016. Effective elimination of liver cancer stem-like cells by CD90 antibody targeted thermosensitive magnetoliposomes. *Oncotarget* **7**(24): 35894-35916.

Yin PT, Shah BP and Lee KB. 2014. Combined magnetic nanoparticle-based microRNA and hyperthermia therapy to enhance apoptosis in brain cancer cells. *Small* **10**(20): 4106-4112.

Yoffe S, Leshuk T, Everett P and Gu F. 2013. Superparamagnetic iron oxide nanoparticles (SPIONS): Synthesis and surface modification techniques for use with MRI and other biomedical applications. *Current Pharmaceutical Design* **19**(3): 493-509.

Yoo D, Jeong H, Preihs C, Choi JS, Shin TH, Sessler JL and Cheon J. 2012. Double-effector nanoparticles: A synergistic approach to apoptotic hyperthermia. *Angewandte Chemie-International Edition* **51**(50): 12482-12485.

Yuan C, An Y, Zhang J, Li H, Zhang H, Wang L and Zhang D. 2014. Magnetic nanoparticles for targeted therapeutic gene delivery and magnetic-inducing heating on hepatoma. *Nanotechnology* **25**(34): 345101.

Zevon M, Ganapathy V, Kantamneni H, Mingozzi M, Kim P, Adler D, Sheng Y, Tan MC, Pierce M, Riman RE, Roth CM and Moghe PV. 2015. CXCR-4 targeted, short wave infrared (SWIR) emitting nanoprobes for enhanced deep tissue imaging and micrometastatic cancer lesion detection. *Small* **11**(47): 6347-6357.

Zhang J, Dewilde AH, Chinn P, Foreman A, Barry S, Kanne D and Braunhut SJ. 2011. Herceptin-directed nanoparticles activated by an alternating magnetic field selectively kill HER-2 positive human breast cells in vitro via hyperthermia. *Int J Hyperthermia* **27**(7): 682-697.

Zhao LY, Liu JY, Ouyang WW, Li DY, Li L, Li LY and Tang JT. 2013. Magnetic-mediated hyperthermia for cancer treatment: Research progress and clinical trials. *Chinese Physics B* **22**(10).

Zlotnik A. 2006. Chemokines and cancer. *Int J Cancer* **119**(9): 2026-2029.

Zou YR, Kottmann AH, Kuroda M, Taniuchi I and Littman DR. 1998. Function of the chemokine receptor CXCR4 in haematopoiesis and in cerebellar development. *Nature* **393**(6685): 595-599.

Zwicke GL, Mansoori GA and Jeffery CJ. 2012. Utilizing the folate receptor for active targeting of cancer nanotherapeutics. *Nano Rev* **3**.

RSC Advances

COMMUNICATION

View Article Online
View Journal | View Issue

Cite this: *RSC Adv.*, 2015, **5**, 47954

Received 4th May 2015
Accepted 22nd May 2015

DOI: 10.1039/c5ra08200e

www.rsc.org/advances

Straightforward phase-transfer route to colloidal iron oxide nanoparticles for protein immobilization†

V. Vilas-Boas,[a] N. Guldris,[b] E. Carbó-Argibay,[b] D. G. Stroppa,[b] M. F. Cerqueira,[c] B. Espiña,[b] J. Rivas,[d] C. Rodríguez-Abreu[b] and Yu. V. Kolen'ko*[b]

We report for the first time the effective transfer of hydrophobic oleate-capped iron oxide nanoparticles to an aqueous phase upon treatment with a base bath cleaning solution. We discuss the mechanism of the phase transfer, which involves the elimination of the organic capping agent followed by ionic stabilization of the nanoparticles due to negatively charged Fe–O$^-$ surface species. The resultant superparamagnetic aqueous nanocolloid shows excellent protein immobilization capability.

Iron oxide nanoparticles (NPs) are an important class of nanomaterials with useful magnetic properties, such as high Curie temperature, high saturation magnetization, and many practical biomedical applications. For example, magnetite, Fe_3O_4, and maghemite, γ-Fe_2O_3, NPs are used in cancer therapy *via* magnetic hyperthermia,[1] drug and gene delivery,[2,3] magnetic separation and diagnostics,[4,5] magnetic particle imaging,[6] as well as classical and multimodal magnetic resonance imaging.[7,8] From the perspective of biomedical applications, iron oxide is preferred in the form of colloidally stable aqueous dispersions of monodisperse NPs exhibiting high crystallinity and high saturation magnetization. Control over particle size and shape can be achieved by colloidal synthesis methods such as thermal decomposition[9,10] or hydrothermal/solvothermal routes[11,12] that typically employ readily available oleate (OL) ligand as capping agent. Hence, various iron oxide NPs with tunable size and morphology have been successfully prepared. However, the drawback of the aforementioned colloidal syntheses is that the resultant NPs are hydrophobic and can be well dispersed only in apolar organic solvents. Obviously, such NPs are not suitable for biomedical application, and proper phase transfer into aqueous medium is required to render them water-dispersible.

A variety of phase-transfer protocols have been developed, which work based on electrostatic, steric, or electrosteric repulsions.[13] One strategy consists of ligand exchange, where the hydrophobic surface ligand, typically oleate, is substituted by amphiphilic polymers,[14] surfactants,[15] silica shell,[16] or silane molecules.[17] Another interesting approach is coating hydrophobic NPs by amphiphilic polymers[18,19] or bilayer shells,[20] thus rendering them dispersible in aqueous phase.

For instance, poly(ethylene glycol) (PEG) coated NPs are colloidally very stable in aqueous medium against pH and ionic strength changes, while heating of the dispersion results in NP aggregation as a consequence of low solubility of PEG in water at elevated temperatures.[21,22] NPs transferred into water by using poly(acrylic acid) polymer or tetramethylammonium hydroxide surfactant are charged, which makes them very stable against heating but quite sensitive to ionic strength and pH of the medium. Additionally, polymers, silanes, and surfactants used for phase transfer are expensive and sometimes toxic. Hence, exploring and developing a novel, simple and low cost route to transfer hydrophobic magnetic iron oxide NPs from apolar organic solvent to aqueous medium is certainly required.

Our efforts in phase transfer of monodisperse hydrophobic iron oxide NPs have been directed toward eliminating all organic capping ligands from the surface of the NPs. Specifically, we considered the possibility that elimination of organic capping ligands may be conveniently achieved through treatment of hydrophobic nanocolloids by a base bath cleaning solution, which is an inherent part of any chemical laboratory. We envisioned that, in this way, water-dispersible iron oxide NPs should be formed as a result of ionic stabilization.[23] This straightforward route offers one principle advantage over a traditional polymer and surfactant routes, namely, it produces a nanocolloid free of organic coating, and thus results in a greater content of magnetic material in the final product. To

[a]*UCIBIO-REQUIMTE, Laboratory of Toxicology, Biological Sciences Department, Faculty of Pharmacy, University of Porto, 4050-313 Porto, Portugal*

[b]*International Iberian Nanotechnology Laboratory, 4715-330 Braga, Portugal. E-mail: yury.kolenko@inl.int*

[c]*Center of Physics, University of Minho, Braga 4710-057, Portugal*

[d]*Department of Applied Physics, University of Santiago de Compostela, Santiago de Compostela 15782, Spain*

† Electronic supplementary information (ESI) available. See DOI: 10.1039/c5ra08200e

understand the changes that the nanoparticles undergo during base-bath-assisted phase transfer, we investigated the structure and magnetic properties of the resultant water-dispersible nanocolloids, which we detail in this communication.

OL-capped magnetite nanocolloid (entry OL-HT, Fig. S1a, ESI†) was synthesized by hydrothermal method reported elsewhere.[24] As shown in Fig. 1a, the as-prepared nanocolloid consists of highly crystalline NPs with an average particle diameter of 10.5 ± 5.2 nm with a 95.45% confidence level, *i.e.* 2σ. Treating this hydrophobic nanocolloid with KOH base bath cleaning solution for 24 h at room temperature followed by separation by centrifugation and purification by ethanol provides a brown aqueous nanocolloid (entry OL-HT-BB, Fig. S1b, ESI†) in nearly 70% isolated yield. High-angle annular dark-field scanning transmission electron microscopy (HAADF-STEM) images show that this phase-transfer product consists of many highly crystalline NPs similar to those in the initial OL-HT nanocolloid (Fig. 1b). Additionally, no dramatic changes in particle size or shape are observed with an average particle diameter of OL-HT-BB estimated to be 11.1 ± 5.2 nm. Notably, the NPs are not well separated spatially from each other as in the case of OL-HT NPs, which is most likely due to aggregation during the drying of aqueous NP dispersion on the carbon-coated TEM grid.

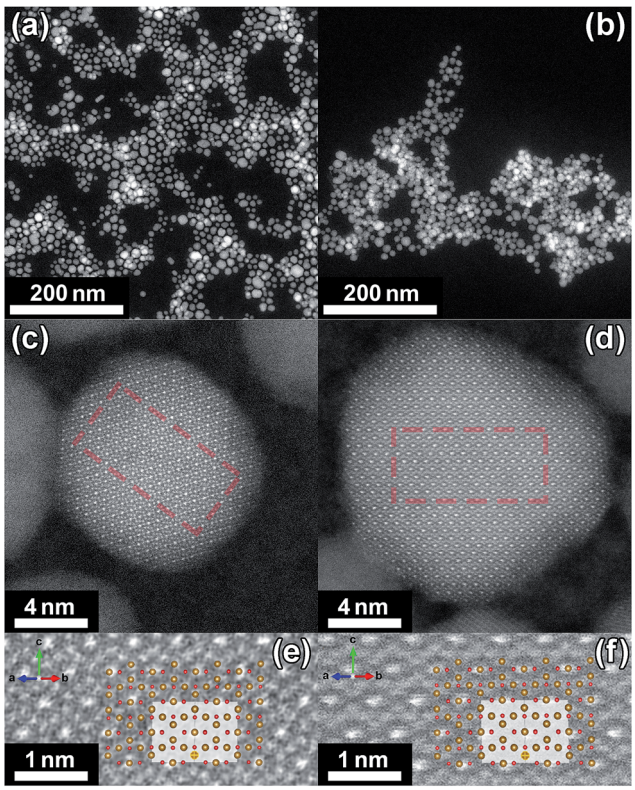

Fig. 1 Comparison of low-magnification, [110] high- and atomic-resolution HAADF-STEM images together with the corresponding structural models (Fe atoms = yellow, O atoms = red) for OL-HT (a, c and e) and OL-HT-BB (b, d and f) nanocolloids. The indicated square areas in (c) and (d) are shown enlarged in (e) and (f), respectively.

To test whether the atomic structure of the NPs is affected during phase transfer, we carried out a morphology characterization using atomic resolution STEM. Fig. 1b and c show a comparison between the HAADF-STEM images of the NPs before and after phase transfer. These data confirm that the atomic structures of the initial and the resultant NPs are comparable. The NPs have cubic inverse-spinel structure type, space group $Fd\bar{3}m$ (Fig. 1e and f). Notably, we cannot conclusively distinguish between Fe_3O_4 and γ-Fe_2O_3 iron oxide phases using our atomic resolution TEM data, or even with electron energy loss spectroscopy (EELS) studies.[25] Specifically, EELS spectra from both OL-HT and OL-HT-BB NPs are extremely similar and the changes in Fe L_3/L_2 ratio and in O proportion are not significant (Fig. S2, ESI†). Therefore, we conclude that Fe_3O_4 and γ-Fe_2O_3 are indistinguishable by the used techniques. This is most likely due to the isostructural nature of these two compounds having similar cubic unit cell parameters ($a = 8.396$ Å for Fe_3O_4 and $a = 8.352$ Å for γ-Fe_2O_3), forming Fe_3O_4–γ-Fe_2O_3 solid solutions.[24]

Next, we investigated the influence of the developed phase-transfer route on the structural properties of the resultant iron oxide NPs. Powder X-ray diffraction (XRD) confirmed that both OL-HT and OL-HT-BB samples have cubic inverse-spinel structure (Fig. S3, ESI†). No remarkable changes are observed after phase transfer. Notably, we were not able to conclusively distinguish between Fe_3O_4 and γ-Fe_2O_3 using XRD, which is consistent with the aforementioned electron microscopy study. γ-Fe_2O_3 and Fe_3O_4 have very similar crystal structures, and the small size of the NPs results in very broad XRD peaks, rendering phase-composition studies difficult. In contrast to XRD, Raman scattering can unambiguously detect the different iron oxide phases, because different polymorphs show distinct Raman-active phonon modes.[26] The main difference between the Raman spectra of Fe_3O_4 and γ-Fe_2O_3 stems from the different position of the most intense A_{1g} phonon modes.[24] We compared the ratio ($R = I(666\ cm^{-1})/I(715\ cm^{-1})$) of the intensity of the A_{1g} mode of Fe_3O_4 to the intensity of the A_{1g} mode of γ-Fe_2O_3. For OL-HT NPs, R is 1.5, indicating the coexistence of both phases, with Fe_3O_4 as the abundant one (Fig. S4a, ESI†). This is in good agreement with our previous studies, wherein we determined that the structure of hydrothermally-synthesized OL-HT NPs is best understood as a Fe_3O_4–γ-Fe_2O_3 solid solution.[19] In contrast to OL-HT, OL-HT-BB has a lower R value of 0.93 (Fig. S4b, ESI†). These data suggest that base-bath-assisted phase transfer leads to the slight oxidation of the initial Fe_3O_4–γ-Fe_2O_3 solid solution NPs to one with large maghemite composition. We speculate that this oxidation within 24 h of the treatment is driven by oxygen from air. It seems clear that the removal of the protective OL capping ligands from the NPs results in direct exposure of their surfaces to the oxidative base-bath conditions.

We employed vibrating sample magnetometry (VSM) at room temperature to investigate the magnetic field dependence of magnetization [$M(H)$] for the iron oxide NPs. The $M(H)$ data in Fig. 2 shows that both nanocolloids exhibit superparamagnetic behaviour without any signature of coercivity, as manifested by the lack of hysteresis loops. The saturation magnetization (M_s) of OL-HT-BB is 72.7 emu g^{-1}, which is just slightly lower than

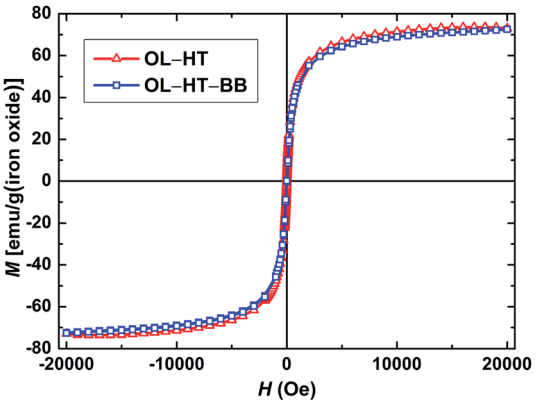

Fig. 2 Room-temperature *M*(*H*) plot for OL-HT and OL-HT-BB nanocolloids.

that of the initial OL-HT (73.8 emu g^{-1}). These large M_s values stem from the high crystallinity and increased particle size.[19,24] The small decrease in M_s after phase transfer correlates well with the observed oxidation of Fe_3O_4–γ-Fe_2O_3 OL-HT into largely γ-Fe_2O_3 OL-HT-BB, since bulk γ-Fe_2O_3 (80 emu g^{-1}) exhibits lower M_s than bulk Fe_3O_4 (92 emu g^{-1}).[27] Nevertheless, the M_s of hydrophilic OL-HT-BB obtained by our newly developed phase-transfer route is superior to that of other Fe_3O_4 or Fe_2O_3 NPs synthesized by the majority of methods,[28,29] and the superparamagnetic state does not change with the phase transfer.

Having investigated structural, microstructural, and magnetic properties before and after phase transfer, we further probed NP capping with the aim of elucidating mechanistic details of our phase-transfer protocol. Thermogravimetric and differential scanning calorimetry analysis (TGA-DSC) of the powdered OL-HT-BB demonstrates that the sample contains only a small amount of organic phase, as shown by *ca.* 2% weight loss between 300 and 750 °C (Fig. S5, ESI†), the temperature range of OL decomposition.[19] Notably, this value is significantly lower compared to the theoretically calculated ones of 9.6% and 18.3% assuming full OL coverage of 11.1 nm iron oxide NPs (Fig. S6, ESI†), evidencing the loss of organic phase. Significant elimination of OL capping after base-bath treatment is also confirmed by Fourier transform infrared spectroscopy (FTIR, Fig. S7, Table S1, ESI†). We presume that the colloidal stability of OL-HT-BB results from the effective cleavage of the OL ligands by KOH from the NP surface in the base bath followed by the formation of ionically-stabilized NPs with negatively charged Fe–O^- surface species.[23]

We tested our hypothesis of the ionic stabilization by conducting Zeta potential measurements at different pH values. OL-HT-BB displays negative Zeta potential of −89 mV at pH 9, −10 mV in phosphate buffer pH 7.4, and +13 mV in MES [(2-(*N*-morpholino)ethanesulfonic acid)] buffer pH 5.1. These results corroborate that the mechanism of our convenient base-bath-assisted phase transfer proceeds through the elimination of the surface capping ligands followed by subsequent formation of negative-charge-surrounded iron oxide NPs.[30] In water at basic pH, the NPs exhibit electrostatic repulsions that render them colloidally stable (Fig. S1b, ESI†). Hence, as-prepared aqueous nanocolloid is pH sensitive and has to be stored at pH ≥ 8.

Aiming at employing magnetic OL-HT-BB for biomedical applications, we examined the potential of our aqueous nanocolloids for proteomic analysis.[31] As a proof-of-concept, we chose to study the immobilization of bovine serum albumin (BSA) protein onto the magnetic NPs. For example, crosslinked BSA-coated iron oxide contrast agents for MRI visualization of intracranial glioma were realized with this reasonably cheap and available protein.[32] In addition, the stability and biocompatibility of the NPs typically improve when loaded with BSA.[33]

We expected our non-coated, charged OL-HT-BB NPs to be suitable for efficient anchoring of protein molecules, and therefore, carried out BSA immobilization experiments. We found that incubation of OL-HT-BB NPs in BSA solution for 3 h at 4 °C (ESI†) led to protein loading of an average of 19 BSA molecules per NP (Fig. 3). This value turned out to be slightly lower than the theoretically estimated 27 BSA/NP assuming monolayer coverage. To elucidate the efficiency of our loading procedure, we also prepared BSA-bearing OL-HT NPs using the known carbodiimide/*N*-hydroxysulfosuccinimide (EDC/sulfo-NHS) method, where BSA is covalently bonded to the NP surface (ESI†). We found that BSA loading using EDC/sulfo-NHS method provides an average 8 BSA/NP (ESI†), which is significantly lower than in the case of OL-HT-BB (Fig. 3).

To characterize BSA binding, we performed an FTIR study of BSA, OL-HT-BB, and BSA-loaded OL-HT-BB samples lyophilized from the respective aqueous dispersions (Fig. 4). The spectrum of BSA-loaded OL-HT-BB features the characteristic amide I, II, and III bands of BSA, as well as the Fe–O band for iron oxide NPs, clearly confirming the presence of the protein on the NP surface. We presume that BSA is physisorbed on the OL-HT-BB NPs, most likely *via* Coulomb forces.[34] Specifically, incubation of OL-HT-BB NPs in BSA solution is carried out in Millipore water at pH 5.3 (ESI†). It is known that the isoelectric point of

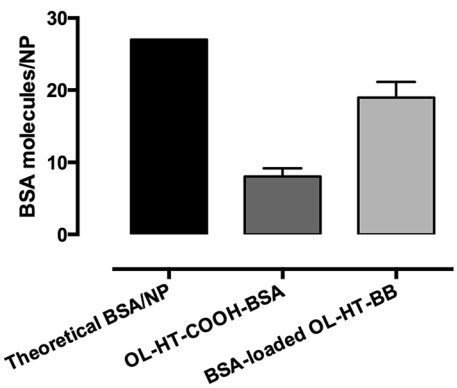

Fig. 3 Comparison of BSA loading through physical adsorption on OL-HT-BB NPs with a covalently bonded control OL-HT-COOH NPs as reference, which indicates significantly higher BSA immobilization in the case of OL-HT-BB NPs ($P < 0.05$).

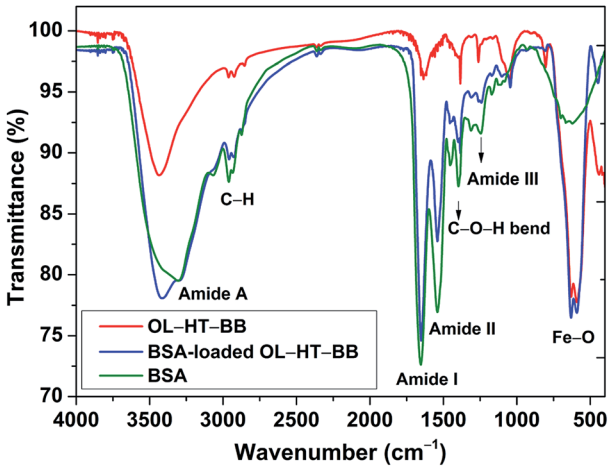

Fig. 4 Comparison of the FTIR spectra of lyophilized OL-HT-BB, BSA-loaded OL-HT-BB and BSA (Table S1, ESI†).

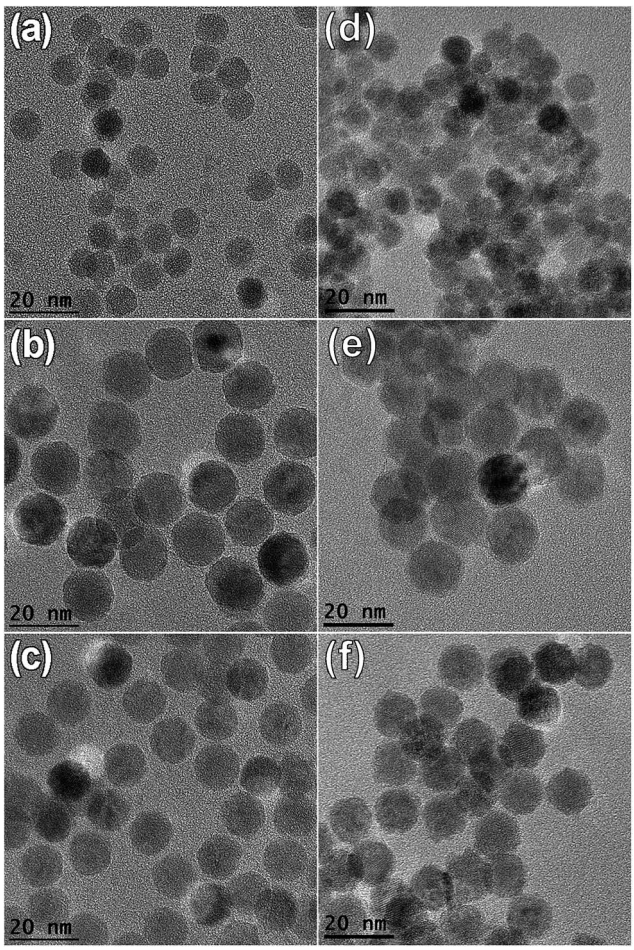

Fig. 5 TEM images showing a series of control phase-transfer experiments for monodisperse iron oxide NPs with sizes of 9.3 ± 1.2 nm (a), 8.7 ± 1.2 nm (b), 13.2 ± 1.1 nm (c), 13.2 ± 1.4 nm (d), 15.8 ± 1.7 (e), and 14.8 ± 1.7 nm (f) prepared by thermal decomposition of $Fe(OL)_3$. Left panels (a, c and e) demonstrate the initial hydrophobic NPs, whereas right panels (b, d and f) show the respective NPs after phase transfer to aqueous media using base-bath treatment. The confidence levels are 95.45%, *i.e.* 2σ.

BSA is at pH = 4.7,[35,36] therefore at this slightly acidic pH of 5.3 the BSA molecules are negatively charged. In contrast, as shown by the aforementioned Zeta potential measurements, the OL-HT-BB NPs at pH 5.3 are positively charged. Consequently, we propose that BSA-loaded iron oxide NPs are formed as a result of electrostatic interactions.

Finally, to extend the use of our convenient phase-transfer route to monodisperse magnetic NPs, we prepared a series of iron oxide NPs using thermal decomposition of $Fe(OL)_3$ complex (ESI†).[9] Monodisperse hydrophobic NPs with average diameters of 9.3 ± 1.2 nm, 13.2 ± 1.1 nm, and 15.8 ± 1.7 nm were synthesized and successfully transferred to aqueous medium without apparent morphological or structural changes (Fig. 5 and S8 (ESI†)). Obviously, our novel phase transfer can be successfully employed to obtain aqueous monodisperse magnetic nanocolloids. Hence, we expect this efficient protocol to find broad application in phase transfer chemistry in the field of nanomedicine.

Conclusions

In summary, we have developed a novel convenient protocol to transfer hydrophobic oleate-capped iron oxide NPs from organic to aqueous phase. Our characterization data provide general evidence of the effective oleate-ligand removal under base-bath conditions followed by formation of ionically-stabilized NPs, rendering them dispersible in aqueous medium. The outstanding physical adsorption of protein by these hydrophilic NPs without the need for functionalization highlights the potential of the system in sample preparation for proteomics. This novel phase-transfer route can be extended to obtain monodisperse aqueous nanocolloids of various materials for further use in biomedical applications.

Acknowledgements

We thank Dr L. M. Salonen and Prof. P. Freitas (INL) for helpful discussions. We also acknowledge the European Regional Development Fund (ON.2 – O Novo Norte Program), the EU FP7 Cooperation Program through the NMP theme (Grant 314212), and the InveNNta project financed by the EU Programme for Cross-border Cooperation: Spain–Portugal (POCTEP 2007–2013) for supporting this work. V. V.-B. acknowledges the FCT (Portugal) for a PhD Fellowship (Grant FRH/BD/82556/2011).

Notes and references

1 M. Johannsen, U. Gneveckow, L. Eckelt, A. Feussner, N. Waldofner, R. Scholz, S. Deger, P. Wust, S. A. Loening and A. Jordan, *Int. J. Hyperthermia*, 2005, **21**, 637–647.
2 S. C. McBain, H. H. P. Yiu and J. Dobson, *Int. J. Nanomed.*, 2008, **3**, 169–180.
3 J. R. Ohlfest, A. B. Freese and D. A. Largaespada, *Curr. Gene Ther.*, 2005, **5**, 629–641.
4 I. Safarik and M. Safarikova, *J. Chromatogr. B: Biomed. Sci. Appl.*, 1999, **722**, 33–53.

5 M. E. Davis, Z. Chen and D. M. Shin, *Nat. Rev. Drug Discovery*, 2008, **7**, 771–782.
6 B. Gleich and R. Weizenecker, *Nature*, 2005, **435**, 1214–1217.
7 J. S. Choi, J. H. Lee, T. H. Shin, H. T. Song, E. Y. Kim and J. Cheon, *J. Am. Chem. Soc.*, 2010, **132**, 11015–11017.
8 Y.-X. J. Wang, *Quant. Imaging Med. Surg.*, 2011, **1**, 35–40.
9 J. Park, K. J. An, Y. S. Hwang, J. G. Park, H. J. Noh, J. Y. Kim, J. H. Park, N. M. Hwang and T. Hyeon, *Nat. Mater.*, 2004, **3**, 891–895.
10 S. H. Sun, H. Zeng, D. B. Robinson, S. Raoux, P. M. Rice, S. X. Wang and G. X. Li, *J. Am. Chem. Soc.*, 2004, **126**, 273–279.
11 T. Taniguchi, K. Nakagawa, T. Watanabe, N. Matsushita and M. Yoshimura, *J. Phys. Chem. C*, 2009, **113**, 839–843.
12 X. Wang, J. Zhuang, Q. Peng and Y. D. Li, *Nature*, 2005, **437**, 121–124.
13 J. Yang, J. Y. Lee and J. Y. Ying, *Chem. Soc. Rev.*, 2011, **40**, 1672–1696.
14 Y. L. Xu, Y. Qin, S. Palchoudhury and Y. P. Bao, *Langmuir*, 2011, **27**, 8990–8997.
15 V. Salgueirino-Maceira, M. A. Correa-Duarte and M. Farle, *Small*, 2005, **1**, 1073–1076.
16 M. Zhang, B. L. Cushing and C. J. O'Connor, *Nanotechnology*, 2008, **19**, 085601.
17 M. Bloemen, W. Brullot, T. T. Luong, N. Geukens, A. Gils and T. Verbiest, *J. Nanopart. Res.*, 2012, **14**, 1100.
18 G. Palui, F. Aldeek, W. T. Wang and H. Mattoussi, *Chem. Soc. Rev.*, 2015, **44**, 193–227.
19 Y. V. Kolen'ko, M. Bañobre-López, C. Rodríguez-Abreu, E. Carbó-Argibay, A. Sailsman, Y. Piñeiro-Redondo, M. F. Cerqueira, D. Y. Petrovykh, K. Kovnir, O. I. Lebedev and J. Rivas, *J. Phys. Chem. C*, 2014, **118**, 8691–8701.
20 A. Prakash, H. G. Zhu, C. J. Jones, D. N. Benoit, A. Z. Ellsworth, E. L. Bryant and V. L. Colvin, *ACS Nano*, 2009, **3**, 2139–2146.
21 A. S. Karakoti, S. Das, S. Thevuthasan and S. Seal, *Angew. Chem., Int. Ed.*, 2011, **50**, 1980–1994.
22 F. Zhang, E. Lees, F. Amin, P. R. Gil, F. Yang, P. Mulvaney and W. J. Parak, *Small*, 2011, **7**, 3113–3127.
23 R. Massart, *IEEE Trans. Magn.*, 1981, **17**, 1247–1248.
24 Y. V. Kolen'ko, M. Bañobre-López, C. Rodríguez-Abreu, E. Carbó-Argibay, F. L. Deepak, D. Y. Petrovykh, M. F. Cerqueira, S. Kamali, K. Kovnir, D. V. Shtansky, O. I. Lebedev and J. Rivas, *J. Phys. Chem. C*, 2014, **118**, 28322–28329.
25 C. Colliex, T. Manoubi and C. Ortiz, *Phys. Rev. B: Condens. Matter Mater. Phys.*, 1991, **44**, 11402–11411.
26 A. M. Jubb and H. C. Allen, *ACS Appl. Mater. Interfaces*, 2010, **2**, 2804–2812.
27 R. M. Cornell and U. Schwertmann, *The Iron Oxides: Structure, Properties, Reactions, Occurences and Uses*, Wiley-VCH, Weinheim, Germany, 2nd edn, 2003.
28 S. Laurent, D. Forge, M. Port, A. Roch, C. Robic, L. V. Elst and R. N. Muller, *Chem. Rev.*, 2008, **108**, 2064–2110.
29 A. H. Lu, E. L. Salabas and F. Schuth, *Angew. Chem., Int. Ed.*, 2007, **46**, 1222–1244.
30 R. Costo, V. Bello, C. Robic, M. Port, J. F. Marco, M. P. Morales and S. Veintemillas-Verdaguer, *Langmuir*, 2012, **28**, 178–185.
31 Y. Li, X. M. Zhang and C. H. Deng, *Chem. Soc. Rev.*, 2013, **42**, 8517–8539.
32 M. A. Abakumov, N. V. Nukolova, M. Sokolsky-Papkov, S. A. Shein, T. O. Sandalova, H. M. Vishwasrao, N. F. Grinenko, I. L. Gubsky, A. M. Abakumov, A. V. Kabanov and V. P. Chekhonin, *Nanomedicine: NBM*, 2015, **11**, 825–833.
33 J. Jenita, V. Chocalingam and B. Wilson, *Int. J. Pharm. Invest.*, 2014, **4**, 142–148.
34 R. V. Mehta, R. V. Upadhyay, S. W. Charles and C. N. Ramchand, *Biotechnol. Tech.*, 1997, **11**, 493–496.
35 S. R. Ge, K. Kojio, A. Takahara and T. Kajiyama, *J. Biomater. Sci., Polym. Ed.*, 1998, **9**, 131–150.
36 S. Salgin, U. Salgin and S. Bahadir, *Int. J. Electrochem. Sci.*, 2012, **7**, 12404–12414.